Image processing in medical ultrasound

Hemmsen, Martin Christian

Publication date:
2011

Document Version
Publisher's PDF, also known as Version of record

Technical University
of Denmark

Image processing in medical ultrasound

Martin Christian Hemmsen

July 2011

DTU Electrical Engineering
Department of Electrical Engineering

Technical University of Denmark
Department of Electrical Engineering
Center for Fast Ultrasound Imaging
DK-2800 Kgs. Lyngby
Denmark

Submitted in partial fulfillment of the requirements for the degree of Doctor of Philosophy at the Technical University of Denmark.

Preface

This Ph.D. dissertation has been submitted to the Technical University of Denmark in partial fulfillment of the requirements for the degree of Doctor of Philosophy.

The work presented in this dissertation is based on the work carried out from August 1st, 2008 to July 31th, 2011 at the Center for Fast Ultrasound Imaging, Department of Electrical Engineering, Technical University of Denmark. It includes three journal papers and four conference papers.

The preparation of this Ph.D. dissertation has been conducted through three years of research. It has taken my skills within mathematical modeling to a whole new level and taught me the physics and science within medical ultrasound imaging and modeling of ultrasound imaging systems. The project has given me the opportunity to travel around the world to attend conferences in Beijing, San Diago, and Rome. A privilege I have valued very much and which has expanded my knowledge within ultrasound. Yet another valuable asset of my study was the opportunity to tutor eight bachelor students in their bachelor thesis projects and two master students during a short course. Further I had the great opportunity to teach students in signal processing and medical imaging through three semesters. It has been a joy to work with, and to share my knowledge within mathematical modeling with professors, colleagues and students at the Center for Fast Ultrasound Imaging.

Martin Christian Hemmsen
Kgs. Lyngby, July 2011

Acknowledgment

First of all, I would like to thank my supervisors, Professor Jørgen Arendt Jensen from the Technical University of Denmark, Ph.D Jacob Kortbæk, and Ph.D Bo Martins from BK Medical ApS., for giving me the opportunity to work with modeling of medical ultrasound systems and for teaching me the scientific disciplines expected at Ph.D. level. They have all exhibited great enthusiasm in driving my results forward and got me to accomplish further than I thought possible.

Furthermore, I would like to thank BK Medical ApS and Sound Technology Inc. for their help and supply of information that made some of this project's simulations and measurements possible.

I would like to thankfully mention my current and former colleagues for numerous discussions, inputs, talks and pleasant travels; amongst others David Bötcher Bæk, Svetoslav Nikolov, Borislav Tomov, Yigang Du, Michael Johannes Pihl, Ye Li, An Pahm, Joachim Rasmussen, Matthias Stuart, Jens Munk Hansen, Kristoffer Lindskov Hansen, Mads Møller Pedersen, and Peter Hansen Furthermore Henrik Laursen and Elna Sørensen for their always very kind help.

Last, but definitely not least, I would like to thank my beloved wife Ann In Hee Hemmsen for her always kind help in correcting my written texts, for listening, supporting, helping, and always being there when I needed her.

Thanks to you all

Abstract

This Ph.D project addresses image processing in medical ultrasound and seeks to achieve two major scientific goals: First to develop an understanding of the most significant factors influencing image quality in medical ultrasound, and secondly to use this knowledge to develop image processing methods for enhancing the diagnostic value of medical ultrasound.

The project is an industrial Ph.D project co-sponsored by BK Medical ApS., with the commercial goal to improve the image quality of BK Medicals scanners. Currently BK Medical employ a simple conventional delay-and-sum beamformer to generate B-mode images. This is a simple and well understood method that allows dynamic receive focusing for an improved resolution, the drawback is that only optimal focus is achieved in the transmit focus point. Synthetic aperture techniques can overcome this drawback, but at a cost of increased system complexity and computational demands. The development goal of this project is to implement, Synthetic Aperture Sequential Beamforming (SASB), a new synthetic aperture (SA) beamforming method. The benefit of SASB is an improved image quality compared to conventional beamforming and a reduced system complexity compared to conventional synthetic aperture techniques. The implementation is evaluated using both simulations and measurements for technical and clinical evaluations.

During the course of the project three sub-projects were conducted. The first project were development and implementation of a real-time data acquisition system. The system were implemented using the commercial available 2202 ProFocus BK Medical ultrasound scanner equipped with a research interface and a standard PC. The main feature of the system is the possibility to acquire several seconds of interleaved data, switching between multiple imaging setups. This makes the system well suited for development of new

processing methods and for clinical evaluations, where acquisition of the exact same scan location for multiple methods is important.

The second project addressed implementation, development and evaluation of SASB using a convex array transducer. The evaluation were performed as a three phased clinical trial. In the first phase, the prototype phase, the technical performance of SASB were evaluated using the ultrasound simulation software Field II and Beamformation toolbox III (BFT3) and subsequently evaluated using phantom and *in-vivo* measurements. The technical performance were compared to conventional beamforming and gave motivation to continue to phase two. The second phase evaluated the clinical performance of abdominal imaging in a pre-clinical trial in comparison with conventional imaging, and were conducted as a double blinded study. The result of the pre-clinical trial motivated for a larger scale clinical trial. Each of the two clinical trials were performed in collaboration with Copenhagen University Hospital, Rigshospitalet, and Copenhagen University, Department of Biostatistic. Evaluations were performed by medical doctors and experts in ultrasound, using the developed Image Quality assessment program (IQap). The study concludes that the image quality in terms of spatial resolution, contrast and unwanted artifacts is statistically better using SASB imaging than conventional imaging.

The third and final project concerned simulation of the acoustic field for high quality imaging systems. During the simulation study of SASB, it was noted that the simulated results did not predict the measured responses with an appropriate confidence for simulated system performance evaluation. Closer inspection of the measured transducer characteristics showed a sever time-of-flight phase error, sensitivity deviations, and deviating frequency responses between elements. Simulations combined with experimentally determined element pulse echo wavelets, showed that conventional simulation using identical pulse echo wavelets for all elements is too simplistic to capture the true performance of the imaging system, and that the simulations can be improved by including individual pulse echo wavelets for each element. Using the improved model the accuracy of the simulated response is improved significantly and is useful for simulated system evaluation. It was further shown that conventional imaging is less sensitive to phase and sensitivity errors than SASB imaging. This shows that for simulated performance evaluation a realistic simulation model is important for a reliable evaluation of new high quality imaging systems.

Abbreviations

BFT3	Beamformation toolbox III
DRF	Dynamic Receive Focusing
HRL	High Resolution Line
HRI	High Resolution Image
IQI	Image Quality Indicators
IQap	Image Quality assessment program
LRL	Low Resolution Line
LRI	Low Resolution Image
SA	Synthetic Aperture
SASB	Synthetic Aperture Sequential Beamforming
SNR	Signal to Noise Ratio
STA	Synthetic Transmit Aperture
STI	Sound Technology Inc.
TOF	Time of Flight
TGC	Time Gain Compensation
VS	Virtual Source
VAS	Visual Analog Scale

x

Contents

CHAPTER

ONE

Introduction

The fundamental purpose of this research project has been to develop an understanding of the most significant factors influencing image quality in medical ultrasound, and to use this knowledge to develop image processing methods for enhancing the diagnostic value of medical ultrasound. Image quality and diagnostic capabilities of medical ultrasound imaging rely to a great extent on the beamformer, which is the primary signal processing task of an ultrasound system. The evolution of ultrasound beamformers from analog into digital implementations have been described by [1] and numerous new variations have lately emerged. With the tremendous improvement in digital hardware and processing power, advanced methods based on Synthetic Aperture (SA) techniques are becoming popular. SA imaging has been a focus of research for almost 3 decades. The research carried out at the Center for Fast Ultrasound Imaging has demonstrated that synthetic aperture focusing not only can be used *in-vivo*, but that it also yields superior B-mode images [2]. In the last years synthetic aperture focusing has moved from the lab to commercial products. Retrospective transmit beamformation (Siemens), zone sonography (Zonare), and multiple angle flash (Verasonics) imaging are just a few of the names used to describe the commercial implementations of synthetic aperture focusing [3].

Recent advances in computer hardware makes it tempting to implement beamforming in computer hardware, but the main obstacle is getting the channel data into the system. The data rate can be reduced using a sparse synthetic transmit aperture [4] reducing the number of acquisitions per second, and another is to use synthetic aperture sequential beamforming (SASB) [5,6] a two-stage beamforming approach.

A major part of this research project has been concerned with implementa-

tion and optimization of ultrasound imaging using SASB and the commercial available ProFocus platform (BK Medical, Herlev, Denmark) for an evaluation of the method. The goal of diagnostic radiology is to provide images of the best technical quality and diagnoses that are as accurate as possible. In [7] Thornbury presents a six-tiered conceptual model for determination of efficacy of diagnostic imaging systems. In this work a methodology for clinical evaluation of image quality was developed. The work has been considered novel and has been submitted for publication and is appended in the chapter titled: Paper III.

Chapter 2 is a continuation of the submitted paper and describes in details how to evaluate image quality both at a technical level, as well as the methodology for determination of the diagnostic efficacy.

Chapter 3 addresses the development and implementation of a versatile research data acquisition system. The project was conducted in collaboration with Svetoslav Ivanov Nikolov (R&D engineer at BK Medical) and Mads Møller Pedersen (Ph.D student at Copenhagen University Hospital). The purpose of the project was to implement a data acquisition system for recording of radio frequency data for development and testing of new imaging methods in both technical and clinical studies. The outcome of the project is documented in journal Paper I and conference Paper III. The developed system has been widely used by bachelor, master, and Ph.D students, resulting in several conference publications.

Chapter 4 presents the theory of SASB imaging and evaluates the technical performance in a comprehensive simulation and measurement parameter study. The simulation study is performed using the simulation software Field II [8, 9] and beamformation toolbox III (BFT3) [10], and the measurement study is performed using a ProFocus scanner and the developed research data acquisition system. A novel implementation of SASB imaging using a convex array has been published in Paper VI.

Chapter 5 is concerned about the clinical evaluation of SASB imaging. The project was conducted in collaboration with Peter Møller Hansen (Ph.D student at Copenhagen University Hospital), Theis Lange (assistant professor at University of Copenhagen), and health care professionals at Copenhagen University Hospital, Department of Radiology. The purpose of the project was to demonstrate that SASB imaging is at least as good as conventional imaging in terms of resolution, contrast, unwanted artifacts, and penetration. SASB imaging was first evaluated in a pre-clinical trial as an initial study and the results have been accepted for publication in Paper V. Subsequently a more thorough investigation was performed in a larger scale clinical trial,

and the result is submitted in the journal Paper II.

Chapter 6 summarizes and addresses the work published in Paper VII and Paper IV. This work focuses on combining Field II with experimentally determined element pulse echo wavelets for an improved simulation model. Field II predicts the received pressure field from a given scatter as the sum of the time convolution between the element two-way spatial impulse response, unique for the location of the scatter relative to the transducer element, and the transducer pulse echo wavelet. By modifying the order of summations and introducing individual element pulse echo wavelets, the model can be improved and physical transducer imperfectness such as variations in element sensitivity, phase, and frequency response can be modeled. The purpose of the work was to improve the Field II model for a reliable simulated system evaluation of high quality imaging systems.

Contributions

The contribution to the field of ultrasound imaging developed during my PhD project period include two submitted journal articles, one early draft journal article, four published conference papers and one published conference abstract as well as eight co-authored conference papers and one co-authored submitted abstract. These are listed as follows:

Journal article

- M. C. Hemmsen, S. I. Nikolov, M. M. Pedersen, M. J. Pihl, M. S. Enevoldsen, J. M. Hansen and J. A. Jensen, "Implementation of a versatile research data acquisition system using a commercially available medical ultra-sound scanner", Submitted to *IEEE Transactions on Ultrasonics, Ferroelectrics and Frequency Control: Special issue on Novel Embedded Systems for Ultrasonic Imaging and Signal Processing*, 2011
- M. C. Hemmsen, P. M. Hansen, T. Lange, J. M. Hansen, M. B. Nielsen and J. A. Jensen, "In Vivo Evaluation of Synthetic Aperture Sequential Beamforming", Submitted to *IEEE Transactions on Ultrasonics, Ferroelectrics and Frequency Control*, 2011
- M. C. Hemmsen and J. A. Jensen, "Simulation of acoustic field for high quality ultrasound imaging", Draft for *IEEE Transactions on Ultrasonics, Ferroelectrics and Frequency Control*

Conference paper and abstract

- M. C. Hemmsen, J.M. Hansen and J. A. Jensen, "Synthetic Aperture Sequential Beamforming applied to medical imaging using a multi element convex array transducer", Submitted to *European Conference on Synthetic Aperture Radar*, 2012, Nuremberg, Germany
- M. C. Hemmsen, P. M. Hansen, T. Lange, J. M. Hansen, M. B. Nielsen and J. A. Jensen, "Preliminary In-Vivo evaluation of Synthetic Aperture Sequential Beamforming", Accepted for presentation at *IEEE International Ultrasonics Symposium*, 2011, Orlando, FL, USA
- M. C. Hemmsen, J. Kortbek, S. I. Nikolov, J. A. Jensen, "Simulation of High Quality Ultrasound Imaging", Presented at *IEEE International Ultrasonics Symposium*, 2010, San Diego, CA, USA
- M. C. Hemmsen, M. M. Pedersen, S. I. Nikolov, M. B. Nielsen and J. A. Jensen, "Ultrasound Image Quality Assessment: A framework for evaluation of clinical image quality", Presented at *SPIE, Medical Imaging*, 2010, San Diego, CA, USA
- M. C. Hemmsen, S. I. Nikolov and J. A. Jensen, "Simulation of high quality ultrasound imaging", Presented at *10th EUROSON*, 2010, Copenhagen, Denmark

Co-authored paper and abstract

- C. B. Jensen, J. Jensen, M. C. Hemmsen, J. M. Hansen and J. A. Jensen, "Compound imaging using Synthetic Aperture Sequential Beamformation", Accepted for presentation to *IEEE International Ultrasonics Symposium*, 2011, Orlando, FL, USA
- A. H. Pham, B. Stage, B. Lundgren, M. C. Hemmsen, M. M. Pedersen and J. A. Jensen, "Simulation of shadowing effects in ultrasound imaging from computed tomography images", Accepted for presentation to *IEEE International Ultrasonics Symposium*, 2011, Orlando, FL, USA
- M. S. Enevoldsen, M. M. Pedersen, M. C. Hemmsen, L. Lönn, K. Henneberg and J. A. Jensen, "Motivation for Use of Patient-Specific Blood Flow Profiles as Inlet Condition in Computational Models", Submitted to *IEEE International Ultrasonics Symposium*, 2011, Orlando, FL, USA

- J. M. Hansen, M. C. Hemmsen and J. A. Jensen, "An object-oriented multi-threaded software beamformation toolbox", Presented at: *SPIE Medical Imaging*, 2011, Lake Buena Vista, FL, USA

- A. H. Pham, B. Stage, M. C. Hemmsen, B. Lundgren, M. M. Pedersen, T. B. Pedersen and J. A. Jensen, "Simulation of ultrasound backscatter images from fish", Presented at *SPIE Medical Imaging*, 2011, Orlando, FL, USA

- M. C. Axelsen, K. F. Røeboe, M. C. Hemmsen, S. I. Nikolov, M. M. Pedersen, M. B. Nielsen and J. A. Jensen, "Evaluation of automatic time gain compensated in-vivo ultrasound sequences", Presented at *IEEE International Ultrasonics Symposium*, 2010, San Diego, CA, USA

- J. A. Jensen, J. Kortbek, S. I. Nikolov, M. C. Hemmsen and B. T. Gueorguiev, "Implementation of Synthetic Aperture Imaging in Medical Ultrasound: The Dual Stage Beamformer Aproach", Presented at *8th European Conference on Synthetic Aperture Radar*, 2010

- M. J. Pihl, S. I. Nikolov, P. Haugaard, M. C. Hemmsen and J. A. Jensen, "Performance of the Transverse Oscillation method using beamformed data from a commercial scanner", Presented at *IEEE International Ultrasonics Symposium*, 2009, Rome, Italy

- M. M. Pedersen, M. C. Hemmsen, J. A. Jensen and M. B. Nielsen, "Research interface for experimental ultra-sound imaging - the CFU grabber project", Presented at *Danish Society of Radiology, Annual meeting*, 2008, Odense, Denmark

CHAPTER

TWO

Performance evaluation

Almost all papers that propose new algorithms include claims about performance. However, frequently the practical value of these claims is limited because of insufficient supporting data or using too vaguely defined performance indicators. This often leads to the questions: So what? Is there any real practical value of the result? The goal for this chapter is to answer the question:

How should the performance of ultrasound imaging systems be determined?

The question is answered by outlining methods and practices that enable researchers to make performance claims that have practical value. There are two important, but quite different, possible definitions of the term ”performance” in this context. One definition of performance is the computation time and hardware demand needed to generate an image. On this dimension, an algorithm that requires less hardware and computation time is better. The other definition of performance relates to the efficacy of the system. On this dimension, a better algorithm is one that improves the probability of benefit to individuals under controlled conditions. Efficacy overlaps partly with the idea of ”effectiveness”, which reflects the use in clinical practice, rather than under controlled conditions. This chapter is concerned with determining the performance of algorithms in this second sense, for guidance of development of new imaging algorithms.

Thornbury describes in [7] a conceptual model that provides a structure to relate efficacy to technology assessment and outcome research. This six-tiered hierarchical model extends from basic laws of physics of imaging (level 1), through clinical use (level 2-4), to patient outcome and societal issues (level 5-6). A key feature is that for an algorithm to be efficacious at a higher level,

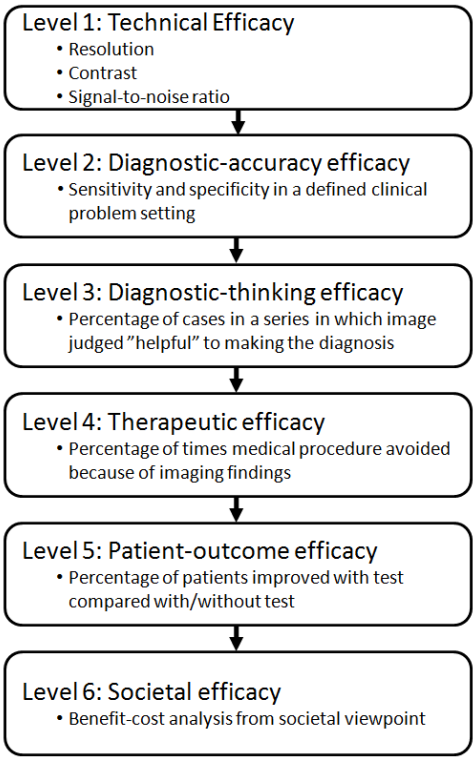

Figure 2.1: A hierarchical model of efficacy. Reproduced from [7].

it must be efficacious at lower levels. The model is shown in Fig. 2.1 and the reader is referred to [7] for a more thorough description of the individual levels.

The model is well suited for a wider perspective of the development of ultrasound imaging systems and for performance evaluation of ultrasound imaging algorithms and modalities. In this work the model is adapted for the purpose of performing a reliable comparison between algorithms. The proposed method is targeted at the continuing development of ultrasound B-mode imaging and performance evaluation at the technical and clinical level.

In the following sections the determination of technical efficacy will be discussed by describing the technical performance indicators used throughout this work, followed by a description of methods and practices for clinical performance evaluation.

2.1 Technical performance indicators

Technical performance indicators or image quality indicators (IQI) are metrics used to determine the technical efficacy. The characteristics for these metrics are that they have a general enough validity for comparison of different systems, provide quantitative results and availability of expected values for interpretation of results. The metrics are useful for an objective evaluation in specification, acceptance testing, and determination of system capabilities. Several international organizations have been involved in the process of defining methods and practices for assessment of quality of medical ultrasound equipment. Examples are the American Institute of Ultrasound in Medicine (AIUM) [11], the American Association of Physicists in Medicine (AAPM) [12, 13], and the International Electrotechnical Committee(IEC) [14]. These efforts have not led to internationally accepted quality standards yet. As a result individual researchers and developers have created their own metrics, some more accepted by the ultrasound community than others. The most used and widely accepted metrics can be described under the following three classifications and will be described in the following subsections:

- System sensitivity and echo detection capability
- Spatial resolution
- Anechoic object detectability

2.1.1 System sensitivity and echo detection capability

System sensitivity and echo detection capability relates to the determination of a systems signal-to-noise ratio (SNR). The penetration depth of a system can be defined as the depth at which usable tissue information disappears and can be estimated from SNR measurements. Typically the depth at which the SNR falls below 0 dB is defined as the penetration depth.

SNR can be measured using a tissue mimicking phantom, in which case the SNR as a function of depth, z, can be determined as the ratio of the signal power, S, to the noise power, N:

$$SNR(z) = \frac{S(z)}{N(z)} = \frac{\mathbb{E}\{x(z)\}^2}{\mathbb{E}\{(x(z) - \mathbb{E}\{x(z)\})^2\}}, \tag{2.1}$$

where $\mathbb{E}$ is the expectation operator, and x is the signal RF value.

In this thesis the signal power will be estimated from M measurements as:

$$S(z) = \left(\frac{1}{M} \sum_{m=1}^{M} x_m(z) \right)^2, \tag{2.2}$$

and the noise power will be estimated as:

$$N(z) = \frac{1}{M} \sum_{m=1}^{M} \left(x_m(z) - \frac{1}{M} \sum_{m=1}^{M} x_m(z) \right)^2. \tag{2.3}$$

It should be noted that this measurement is depending on the actual setting of the overall gain and the overall time-gain-compensation (TGC), both the user specified and any potential system or application TGC. However, if saturation is avoided they do not influence the method. In this thesis the SNR will be estimated for a set of L scan directions and spatial averaging will be employed for a more precise estimate:

$$SNR(z) = \frac{1}{L} \sum_{l=1}^{L} SNR_l(z). \tag{2.4}$$

SNR expressed in dB is calculated in accordance with

$$SNR_{dB}(z) = 10 * log_{10}(SNR(z)). \tag{2.5}$$

2.1.2 Spatial resolution

As ultrasound imaging developed from roots in radar and sonar technology, the natural tendency have been to use the full-width-at-half-maximum (FWHM) method to characterize the spatial resolution [15].

Spatial resolution, also referred to as the resolution cell, determines how closely positioned two reflectors or scattering regions can be to one another and still be identified as separate reflectors. The three dimensional nature of the resolution cell requires determination of the axial, lateral and elevation resolution. The axial resolution is found along the beam's axis and the lateral resolution perpendicular to the beam's axis in the image plane. The elevation resolution is found perpendicular to both the beam's axis and the image plane.

Elevation resolution. Currently most electronically focused 1D transducers have an out-of-slice focus that is achieved by placing an external lens over the array. The elevation resolution, also referred to as the ”slice thickness”, is determined by the geometry of the lens and the transducer resonant frequency [16]. For a circular aperture the beam width at the focal point F can be approximated as:

$$W = \frac{1.22\lambda F}{d}, \tag{2.6}$$

where d is the diameter of the transducer, and λ is the wavelength.

Axial Resolution. The axial resolution depends on the transmitted spatial pulse length or pulse duration, which in turn depends on the electrical pulse and the electro-mechanical impulse response of the transducer. Generally the axial resolution is inversely proportional to the bandwidth of the system [17], and as such a transducer with a high resonant frequency and a broad bandwidth has a short acoustic pulse and good axial resolution. The FWHM can be approximated as:

$$W = \frac{0.66}{\Delta f}, \tag{2.7}$$

where Δf is the -6 dB bandwidth in MHz.

Lateral resolution. The lateral resolution is the only one dependent on the focusing algorithms. There are many ways to determine the lateral resolution [18]. In this thesis the resolution will be stated as the beam width at -6 dB also referred to as FWHM, -20 dB and -40 dB. As the lateral resolution is spatial dependent it will be determined for multiple depths to show the focusing algorithms ability to generate a uniform lateral resolution. The beam width at a given depth will be determined from the beam profile, A, and can be characterized fully from the point spread function:

$$A(x) = \max_{z} I(x, z). \tag{2.8}$$

where x and z is the lateral and axial positions in the log-compressed B-mode image I, see Fig. 2.2.

2.1.3 Anechoic object detectability and contrast resolution

Even though the spatial resolution is a commonly used parameter to quantify performance of ultrasound imaging systems, it can be extremely misleading. The spatial resolution is a well suited quality parameter in radar and sonar imaging, where the targets of interest frequently is highly-reflective targets in

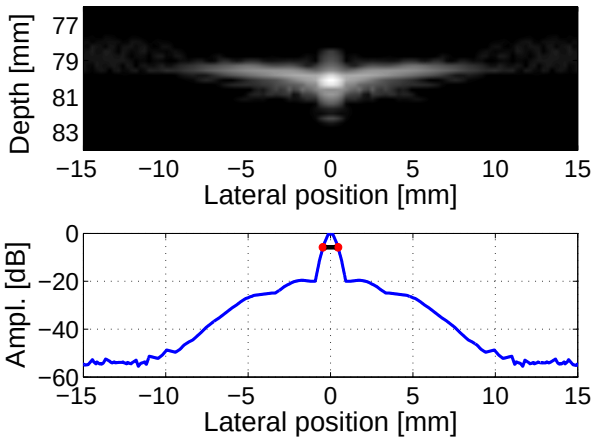

Figure 2.2: Illustration of a B-mode image of a point spread function (top) and lateral beam profile (bottom). The black line and the two read dots indicates the distance FWHM.

a non-backscattering surrounding. However, in medical ultrasound imaging the targets of interest is frequently low-reflective objects like blood vessels or tumors, and are embedded in a continuous back-scattering medium. And as such imaging systems with excellent FWHM beam characteristics, can fail to show tissue detail seen by conventional systems that, by the FWHM criterion, are inferior.

Anechoic object imaging examines the systems ability to detect and accurately display round, negative contrast objects of various sizes. Anechoic object image quality can also be affected by electrical noise, side lobes in the transducer beam, and problems in the image processing hardware.

Contrast analysis has been introduced to diagnostic ultrasound by Smith and Lopez [19] using phantom measurements. Later Smith et al. demonstrated in [20] a parameter

$$C = 20 \log_{10} \left(\frac{M_L}{M_B} \right), \tag{2.9}$$

where M_L is the mean ultrasound signal within a lesion and M_B is the mean echo signal in the surrounding background.

Vilkomerson et al. [15] proposed the concept of "cystic resolution", in which performance was quantified as the size of an anechoic void that produced a given contrast, and was further developed by [21, 22]. Using the developed

parameter in [22] one can compute the contrast at the center of the cysts of different sizes and characterize the system performance as a function of cyst size. The parameter is expressed as

$$C(t) = \sqrt{\frac{1 + SNR^2(t)\left(1 - \frac{E^{in}(t)}{E^{tot}(t)}\right)}{1 + SNR^2(t)}} \tag{2.10}$$

where $E^{tot}(t)$ is the total energy of the point spread function, P, expressed as:

$$E^{tot}(t) = \int_{-\infty}^{\infty} P^2(\vec{x}, t) d\vec{x}, \tag{2.11}$$

and $E^{in}(t)$ is the point spread function energy inside the void, M, expressed as:

$$E^{in}(t) = E^{tot}(t) - \int_{-\infty}^{\infty} P^2(\vec{x}, t) M^2(\vec{x}) d\vec{x}. \tag{2.12}$$

If electronic noise, SNR is neglected and the contrast is only determined at the instant in time, t_0, when the received signal is minimum the expression reduces to the contrast parameter presented in [21]:

$$C_{t_0} = \sqrt{1 - \frac{E^{in}(t_0)}{E^{tot}(t_0)}}, \tag{2.13}$$

referred to as the clutter energy to total energy ratio.

Contrast resolution is another and more commonly used parameter and referrers to the ability to distinguish differences in echogenicity between neighboring soft tissue regions. Ultrasound images contain speckle which makes detecting small echogenicity variations difficult. Tissue contrast resolution may therefore be improved either by reducing speckle variance or by reducing speckle size. Tissue contrast resolution is commonly quantified by Contrast to Noise Ratio (CNR). It expresses simply the fact that detectability increases with increasing object contrast and decreasing speckle variance [21]. CNR is expressed as:

$$CNR = \frac{(\mu_B - \mu_T)^2}{(\sigma_B^2 + \sigma_T^2)}, \tag{2.14}$$

where μ denotes the mean and σ denotes the standard deviation of the log-compressed B-mode image. The subscripts T and B stand for the target and the background, respectively.

2.2 Clinical performance indicators

Clinical performance indicators are metrics used to determine the clinical efficacy. The six-tiered model described by Thornbury in [7] divides the clinical evaluation into three levels, and can in short be described as:

- **Diagnostic-accuracy efficacy** is related to the determination of sensitivity and specificity and is a joint function of image technical quality and interpretation by a human observer.
- **Diagnostic-thinking efficacy** is related to imaging information that may change the physician's diagnostic certainty.
- **Therapeutic efficacy** is related to the determination of influence on the treatment choice.

For development purposes, a good image quality metric provides information for optimization purposes and must therefore be fast to determine and reliable. The major challenge in determining the diagnostic-accuracy efficacy is the need to establish the true (or gold standard) diagnosis. The challenge in determining the therapeutic efficacy is the logistically aspects of planning and managing a series of cases. The diagnostic-thinking efficacy is a good indicator, because it is straightforward to determine and requires only comparison of a series of image sequence pairs, and is the choice of clinical performance indicator used in this thesis.

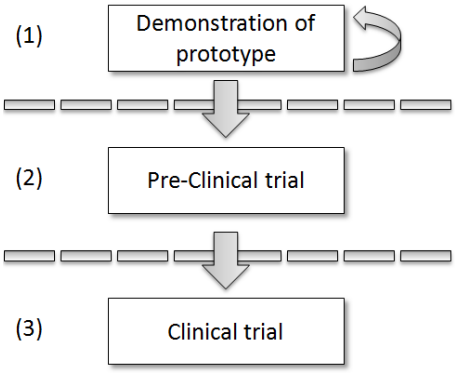

Figure 2.3: Diagram of the clinical evaluation methodology. Figure taken from Paper III.

To obtain a reliable and clinical evaluation the Paper III describes a methodology how to manage and evaluate clinical studies. The methodology describes the process as a three phased study as shown in Fig. 2.3.

The three phases are described as:

- **Demonstration of prototype**, is the stage where developers demonstrate a workable prototype with measurements on phantoms and a few *in-vivo* images. In a collaboration between the developer and the ultrasound specialists, the new method's parameters are iteratively optimized to achieve the best possible setup within safely regulations. Once all parameters are fixed the results may be evaluated, and in case of promising results this stage ends and a pre-clinical study may be designed.
- **Pre-clinical trial**, is the stage where the relevance of a clinical investigation is tested, and the necessary number of patients for the real clinical study is determined. This stage ends and the clinical trial begins when an exact clinical protocol is developed. It describes the method and its parameters in such a degree that the developer is and should be left out in the active part of the following research and should not have any influence on the outcome of the research in either data acquisition, any form of processing of it, or evaluation.
- **Clinical trial**, is the stage of research that determines the statistical significance of the new method. Assessment of the method is performed by a number of ultrasound specialists independent to the method. Furthermore, the assessors must be separated from the specialists performing the ultrasound scanning, blinding them from the acquisition and any form of processing of it.

The methodology ensures the validity of the assessment, as it separates the developer, investigator, and assessor once a research protocol has been established. This separation eliminates any confounding influence on the result from the developer and new processing schemes is not driven by the developers, but by the clinical value.

Other issues to consider is to get a sufficient number of scans under realistic operating conditions for a fair and reliable comparison between methods. This sets certain requirements for the data acquisition system, that has to be able to store data fast to reduce waiting time between scans, and capabilities to acquire data from multiple imaging setups for identical scan location. Such a system is described in Paper I and will be introduced in Chapter 3.

For determination of the diagnostic-thinking efficacy Paper III describes an evaluation methodology using image sequence pairs and software for visualization and data management.

2.2.1 Image quality assessment program

The image quality assessment program (IQap) is designed for assessment of a change in the physician's diagnostic certainty, comparing two imaging systems or configurations. The program is developed based on an earlier publication of a study of clinical evaluation between pairs of sequences [23] and recommended testing procedures according to recommendation 500 from ITU-R [24] for subjective quality assessment. The program implements an evaluation methodology proposed in Paper III. The evaluation methodology states that evaluations should be done blinded and each assessor must sit isolated during the assessment. The assessment consists of two parts - an assessment of the image quality related to the spatial resolution, contrast, noise, formation of unwanted artifacts, and an assessment of penetration depth related to the depth where the anatomic structures are no longer usable for a reliable clinical use. The evaluation procedure is performed in three phases. In the first phase the assessors are introduced to the rating scales and are shown five trial sequences to get acquainted with the task at hand and which types of image sequences to expect. In the second phase the image quality is evaluated, followed by the third phase where the penetration depth is evaluated. The two evaluation phases will be explained in the following.

An important aspect evaluating ultrasound imaging systems is to perform the evaluation in a setup that is as close as possible to the normal situation. This requires that the ultrasound images are being evaluated as a sequence of images, because when evaluating a sequence of noisy images, there is spatio-temporal processing in the human visual system and objects are easier recognized because of temporal processing that acts to reduce the noise. If the evaluation is performed on single images, there is no temporal processing and only spatial visual processing. The images becomes perceptually noisier; objects become more difficult to see; and some disappear altogether. The added temporal dimension of the evaluation involves additional visual processing, and results from evaluating image quality from single images cannot be simply extrapolated to image sequences. Another aspect to consider is to minimize discontinuity at the joints of the image sequence. One possible solution is to display the image sequence in a palindromic display fashion, (reversing the playback order at the ends of the image sequence), and is used in IQap.

Image quality assessment

The presentation method for assessment of image quality combines elements of the simultaneous double stimulus for continuous evaluation (SDSCE) method (ITU BT.500-11, Section 6.4) and the double stimulus continuous quality scale (DSCQS) method (ITU BT.500-11, Section 5).

As with the SDSCE method, each trial involves a split-screen presentation of two paired image sequences, referred to as a sequence pair. One of the image sequences will be the reference sequence, while the other is referred to as the test sequence. The reference sequence could be a conventional setup or the configuration to compare against, and the test sequence is the method or configuration under investigation. Unlike the SDSCE method, observers will be blinded from the configuration or method represented by the two members of the sequence pair and the left-right placement of the movies are randomized. As with the DSCQS method, each assessment session comprises a number of presentations, each with a single observer. Unlike the DSCQS method where the assessor only observes the sequences two times and rates each sequence individually, the assessor is free to observe the sequences until a mental measure of relative quality associated with the sequences is obtained. Figure 2.4 shows a basic test cell illustrating the presentation structure.

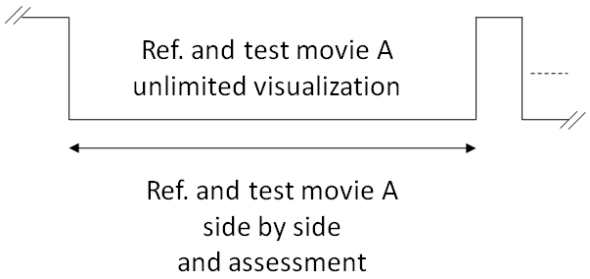

Figure 2.4: Basic test cell illustrating the presentation structure for assessment of image quality. Reference and test sequences are displayed as matching pairs side-by-side with random left-right placement. Assessors are free to observe the stimuli until a mental measure of relative quality associated with the sequences is obtained. Following the assessment of sequence A is evaluation of sequence B. Figure taken from Paper III.

Each of the image sequence pairs is evaluated using a stimulus comparison scale, as described in ITU BT.500-11, Section 6.2. The specific judgment scale used is a non-categorical (continuous) scale, as described in ITU BT.500-11, Section 6.2.4.2, for reference it may be called a Visual Analog Scale (VAS) and

is also described in [25]. During introduction of the assessors to the system and the rating methods, the VAS scale is described with the same number of labels as on the ITU-R categorical comparison scale but with slightly modified labels (better, slightly better, equally good, slightly better, better) to report the existence of perceptible quality differences and allow the random left-right placement of the sequence pairs. After introduction and during assessment the labels are hidden to avoid categorized data and to get a smoother distribution. Figure 2.5 shows the associated VAS for image quality assessment.

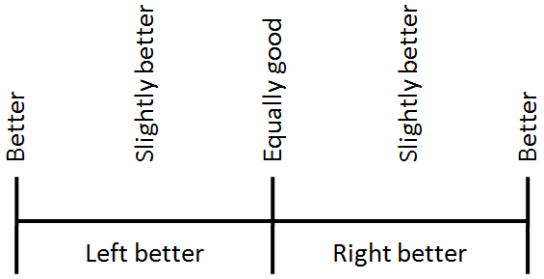

Figure 2.5: Visual analog scale (VAS) for image quality assessment. Figure taken from Paper III.

Each of the assessment trials are presented randomized, blinded, and independently of each other and, in a different random sequence for each assessor. As with the assessment method described in ITU-R TG6/9 [26] Section 7.1.1.3, each sequence pair is assessed two times with different left-right placement. The purpose of presenting the same sequence pair two times is to assess a measure of judgment bias. The following trials are performed for each sequence pair:

Table 2.1: Description of the required trials for each sequence pair under investigation.

Left image	Right image
Reference sequence	Test sequence
Test sequence	Reference sequence

Assessors are instructed to evaluate which of the two presented image sequences that creates a better diagnostic confidence. Figure 2.6 illustrates the graphical user interface (GUI) associated with the rating process of image quality.

Figure 2.6: Illustration of the GUI associated with the rating process. The scale used for scoring is shown in the bottom, and the control panel for navigating the sequences are shown in the lower right corner. The B-mode image shown on the left is generated using SASB and the image on the right using DRF. Figure taken from Paper V.

Penetration depth assessment

The presentation method for assessment of penetration depth combines elements of the double stimulus continuous quality scale (DSCQS) method (ITU BT.500-11, Section 5) and the non-categorical judgment methods (ITU BT.500-11, Section 6.1.4.3).

As with the DSCQS method, each assessment session comprises a number of presentations, each with a single observer. Each presentation involves a randomized individually assessment of the two image sequences from a paired image sequence. The assessor is free to observe the presented sequence until a mental measure of penetration depth associated with the sequence is obtained. Figure 2.7 shows a basic test cell illustrating the presentation structure. As with the assessment of image quality observers are blinded from the configuration or method displayed.

Each of the assessment trials are presented randomized, blinded, and independently of each other, and in a different random order for each assessor. Each of the presented sequences are assessed using a non-categorical judgment method, as described in ITU BT.500-11, Section 6.1.4.2. The judgment method uses a numerical scale, where assessors assign a value to each se-

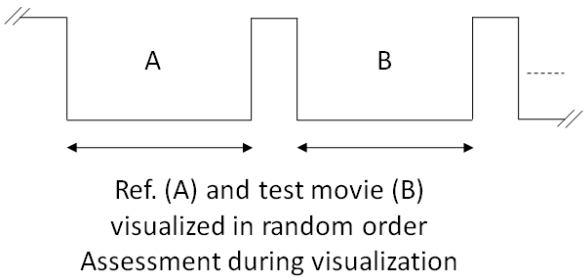

Figure 2.7: Basic test cell illustrating the presentation structure for assessment of penetration depth. Reference and test movies are displayed individually in randomized order. Assessors are free to observe the stimuli until a mental measure of penetration depth associated with the sequences are obtained. Following the assessment of sequence A is evaluation of sequence B. Figure taken from Paper III.

quence, reflecting the penetration depth where the anatomic structures are no longer usable for a reliable clinical use. Figure 2.8 illustrates the GUI associated with the rating process of penetration depth.

Figure 2.8: Illustration of the GUI associated with the assessment of penetration depth. The horizontal red line is placed at the respective depth where the assessor evaluates the image quality no longer usable for reliable diagnostic use. The control panel for navigating the sequences are shown in the lower right corner. The B-mode image shown is generated using SASB. Figure taken from Paper V.

2.3 Discussion

This chapter began by asking the question,

How should the performance of ultrasound imaging systems be determined?

The chapter then focused on a relatively narrow definition of performance, concerned with the clinical and technical efficacy parameters for guidance of new imaging algorithms.

The technical efficacy is related to the fundamental performance indicators, such as, spatial resolution, contrast, and sensitivity. The point spread function is extremely important for image quality as it determines both spatial resolution and contrast. Sensitivity is important primarily because it effects penetration. The section introduced a few good internationally accepted indicators by the ultrasound society and will be used through out this thesis for selection of configurations and objective performance metric.

The clinical efficacy is related to the image information that may change the physician's diagnostic certainty. A methodology was proposed that enables researchers to perform reliable clinical studies. The methodology ensures the validity of the assessment, as it separates the developer, investigator, and assessor in the clinical study. Furthermore, a methodology for the assessment of subjective image quality in terms of diagnostic-thinking and penetration depth was proposed and implemented in the software program IQap. The methodology ensures validity of the assessment, as the performance evaluation is performed blinded and in a side-by-side comparison study between paired image sequences of the same field-of-view. This allows the evaluator to study the image sequences in detail from the two methods at the same time for better comparison.

CHAPTER

THREE

Research data acquisition system

The fundamental requirement evaluating new processing methods, is access to raw ultrasound data. Previously researchers have worked with ultrasound manufacturers to build custom ultrasound systems such as RASMUS [27,28] and SARUS [29], but due to the size of these scanners they are inaccessible in the clinic. Recently, a number of research interface platforms for clinical ultrasound scanners have been developed for systems such as Hitachi HiVision 5500 [30], Siemens Antares [31] and the Ultrasonix 500 [32]. With the introduction of research interface platforms on clinically available scanners it is now possible to acquire and store data.

For a system to be suitable for acquisition of data for clinical evaluations, the system has to keep factors, such as identical transducer, region of interest, and recording time constant on both the reference and the experimental image. Another system requirement is the ability to acquire a sufficient number of scans under realistic operating conditions. Thus, the data acquisition system should be capable of acquiring and storing data fast enough to conduct an ultrasound examination with multiple image sequences. Such a system is developed and presented in Paper I and Paper III. This chapter will introduce the key capabilities of the system.

3.1 System overview

The developed ultrasound research system consists of a commercially available ultrasound scanner (2202 ProFocus equipped with a UA2227 Research Interface, BK-Medical, Herlev, Denmark) and a standard PC. The PC is connected to the scanner using a X64-CL Express camera link (Dalsa, Waterloo, Ontario, Canada), and through an Ethernet link. See Fig 3.1 for an overview of the system setup.

Figure 3.1: Illustration of the data acquisition system setup.

The research interface and the OEM interface on the 2202 ProFocus architecture, allows external devices to control and access data on the scanner. The OEM interface makes it possible to set and read system parameters and can be used to stream processed images. It is basically a substitute of the normal interface: keyboard, track ball, and screen, and enables embedding in 3rd party products as a self-sufficient component. The research interface on the other hand, streams data prior to envelope detection.

Fig. 3.2 illustrates the data flow and the structure of the software and hardware in the system. Raw channel data from the individual transducer elements are sampled and sent to the beamformer. The beamformed data is subsequently optionally time-variant band-pass filtered, time gain compensated, and transformation to baseband I/Q data. The I/Q data is available for streaming through the research interface and for further processing to generate B-mode, CFM, Doppler, and M-mode images. The results of this processing are transferred to the processing engine for subsequent post-processing

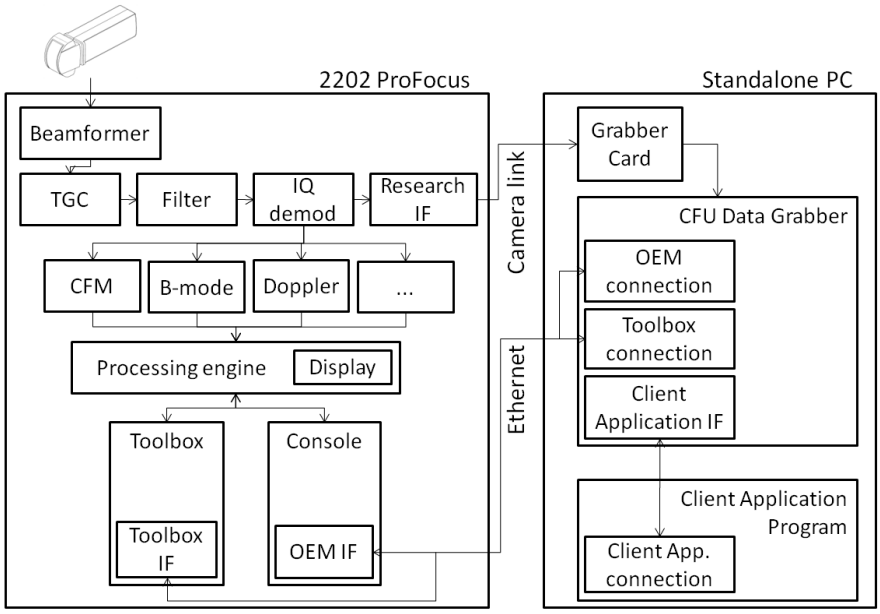

Figure 3.2: Data flow and structure of the software and hardware of the system.

and display. The user interface and the calculation of control parameters are handled by the main application called Console. The system architecture of the 2202 ProFocus makes it possible for several standalone applications to coexist and to interact with the control parameters. One such application is the Toolbox, and it is used for debugging of the system, for prototyping of new algorithms, and for image optimization. One can view the Toolbox as a form of parameter control unit.

The remote control of acquisition and parameters is handled by the application called CFU Data Grabber. The application implements a communication module to the OEM interface and the Toolbox interface. Furthermore, it implements an interface that makes it possible for 3rd party programs, such as Matlab (Mathworks, Natick, MA, USA), to interact with the application.

3.1.1 Data Acquisition

The acquisition of data is controlled via the CFU Data Grabber software and can be performed with a single button click. Alternatively, the acquisition can be issued from 3th party programs such as Matlab. Since many researchers utilize Matlab for data analysis, a SDK (Software development kit) for Matlab

is developed. The SDK implementation allows a flexible manipulation of the control parameters, data acquisition, and automated system performance evaluation.

The data storage time is approximately 15.1 seconds for a 3 sec interleaved B-mode sequence, including complete scanner settings. An interleaved B-mode sequence is a configuration of the scanner where the scan sequence is split into two independent views; view A and view B. Each view is updated simultaneously, and allows for a data acquisition switching between multiple configurations, maintaining identical transducer, scanner, region of interest, and recording time on both views. This allows for acquisition of an experimental and standardized data set for evaluation of new processing methods.

3.1.2 Parameter Control

The system allows manipulation of the control parameters in two ways, either through the Console or using standalone applications such as the Toolbox. The Console is the standard user interface and the main application. Modifications made through the Console are limited to standard clinical use and a set of precalculated and validated control parameter setups. The Toolbox allows manipulation of the full control parameter set. A subset of the parameters available, is described in Table 3.1. These parameters are not available on the normal clinical interface or other typical scanners. The manipulation of the control parameters allows a wide degree of experimentation with the receive and transmit aperture control. Modifications made through the Toolbox can result in non-validated setups and measurements must be performed to ensure the regulation set by the United States Food and Drug Administration FDA [33] is not compromised.

Receive and Transmit Aperture Control

The Receive and transmit aperture control give the user the ability to control the fundamental parameters related to the formation of an echo line. The available parameters span from adjusting the size and growth of the aperture to controlling the weighting of the individual elements. A subset of the parameters are described in the following:

- Aperture growth and dynamic focusing. By default, the system dynamically moves the receive focal point outward and grows the aperture to

optimize echoes received from increasing depths. With the Toolbox, the user is given the control to override this dynamic updating and define a static size and focal position of the receive aperture. Hereafter, the default state is referred to as a dynamic aperture, and the opposite, a static aperture. Of course, once the aperture is made static, the user has to choose a focal position and a size for the aperture.

Table 3.1: Description of a subset of the parameter controls.

Parameter	Description
Dynamic focusing and dynamic apodization	Receive aperture dynamic focusing and aperture growth can be disabled individually. When disabled, receive aperture size and focal position are fixed.
F#	Receive and transmit aperture size can be adjusted individually.
Receive apodization	Receive apodization can be chosen from a fixed list of standard curves such as Hamming, Gaussian, or rectangular apodization or optionally to upload a custom made apodization matrix. If defined as a matrix the apodization can vary between individual beam lines.
Receive time delay profile	Receive time delay profile can be specified individually for each image line when dynamic focusing is disabled.
Line density	The image line density can be chosen from a range of half an element pitch to two element pitch.
Speed of sound	Speed of sound can be specified to match the imaging application.
Excitation waveform	A bipolar excitation waveform can be specified with a time resolution of 8.3 nsec.
Region of interest	The region of interest can be adjusted in all imaging modes.

- Aperture focal position. When the receive aperture is static, the user can adjust the focal position to any depth. The transmit focal position is adjusted independently.
- Aperture size. The user can adjust the aperture size in dimensionless units of F-number.
- Aperture apodization. The user is given the ability to select between a set of predefined receive aperture weight functions, such as Hamming, Gaussian, or rectangular apodization or optionally to upload a custom made apodization matrix. If defined as a matrix, the apodization can vary between individual beam lines.

3.2 Discussion and conclusion

A versatile research data acquisition system is developed and implemented using a commercially available medical ultrasound scanner. The system will allow researchers and clinicians to rapidly develop applications and ease the transition to the clinic for evaluation.

The developed research data acquisition system consists of a standard PC and a ProFocus ultrasound scanner. The system uses an open architecture that allows acquisition of data for experimental research, such as developing new image processing algorithms. With the system, users can tailor the data acquisition to fit their working environment, while still maintain the clinical integrity of using a robust medical device. This will allow researchers and clinicians to rapidly develop applications and move them relatively easy to the clinic for evaluation.

A central part of developing new applications and methods is determination of both technical and diagnostic efficacy. With the system, users can acquire interleaved data sequences switching between an experimental setup and a reference setup. This, in combination with the ability to acquire and store multiple data sets during the same examination, makes the system adequate for clinical trials.

CHAPTER

FOUR

Synthetic Aperture Sequential Beamforming

The basic idea in synthetic aperture techniques is to synthesize a large aperture by moving, or multiplexing, a small active aperture over a larger array [34]. There are several variants of the technique for ultrasonic imaging, that all make it possible to generate images with dynamic focusing during both transmit and receive.

The synthetic aperture focusing technique (SAFT) [35] is the simplest synthetic aperture method, where each time only a single element is used for transmission and reception. Simple transmit and receive electronics is needed, but it requires data memory for all N data recordings. The main disadvantage of SAFT is the low signal-to-noise ratio (SNR) and as a result, a poor contrast resolution. In multi-element synthetic aperture focusing (MSAF) a group of elements transmits and receives signals simultaneously for each emission, which increases acoustic power and signal-to-noise ratio [36].

Synthetic transmit aperture (STA) and Multi-element synthetic transmit aperture are methods where respectively one or a group of array elements transmit a pulse, and all aperture elements receive the echo signals [37, 38]. The advantage of this approach is that full dynamic focusing can be applied to transmit and receive, achieving the highest quality of image. The shortcoming is that N^2 echo recordings are required to synthesize an image. This disadvantage can be overcome to some extent, at the cost of image quality, if a sparse configuration is applied [4]. Significant tissue motion can affect synthetic aperture images, as shown by Nock and Trahey (1992); Karaman et al. (1998) and Gammelmark and Jensen (2003). However, *in vivo* studies of STA

imaging have been published with good results [2].

Recently Kortbek et al. (2009) introduced the concept of Synthetic Aperture Sequential Beamforming (SASB) to overcome the high system requirements of STA imaging. The basic idea in SASB is to create a dual-stage procedure using two separate beamformers. In the initial stage a beamformer using a single focal point in both transmit and receive, creates a virtual source at the fixed focus point. The second stage beamformer creates a set of high resolution image points by combining information from multiple virtual sources, which results in a dynamically expanding array as the image depth increases and a range independent lateral resolution can be obtained. Kortbek et al. evaluated in [6] SASB using a multi element linear array transducer, and showed that the lateral resolution could be made more range independent and improved significantly compared to conventional imaging. In Paper VI SASB was further developed for implementation using convex array transducers and will be the topic of the following section.

4.1 The theory of synthetic aperture sequential beamforming

In conventional dynamic receive focusing (DRF) a new set of delay values is calculated for each focusing point (FP) and applied to the responses of the individual transducer elements which are then summed coherently. The delays are found from the round trip time-of-flight (TOF), which is the propagation time of the emitted wave in its path from the transmit origin, $\vec{r}_e$ to the receive focusing point, $\vec{r}_{fp}$ through the transmit focusing point $\vec{r}_{tfp}$ and return to one of the elements of the receive aperture, $\vec{r}_r$. Fig. 4.1(a) illustrates the time-of-flight calculation for DRF. Assuming the speed of sound c is known, the delay value, t_d for the receiving element with position $\vec{r}_r$ is calculated as

$$t_d(\vec{r}_r) = \frac{1}{c}\Big(\|\vec{r}_{tfp} - \vec{r}_e\| \pm \|\vec{r}_{fp} - \vec{r}_{tfp}\| + \|\vec{r}_r - \vec{r}_{fp}\|\Big), \tag{4.1}$$

where $\|\|$ is the Euclidean norm.

With SASB a first stage beamformer with a fixed receive time-delay profile creates a set of N focused image lines from M emissions. The delay profile is found from the round trip time-of-flight, which is the propagation time of the emitted wave in its path from the transmit origin, to the focusing point through the virtual source (VS), and return to one of the elements of the receive aperture, again through the virtual source (VS). Fig. 4.1(b) illustrates the time-of-flight calculation for the SASB first stage beamformer. The delay

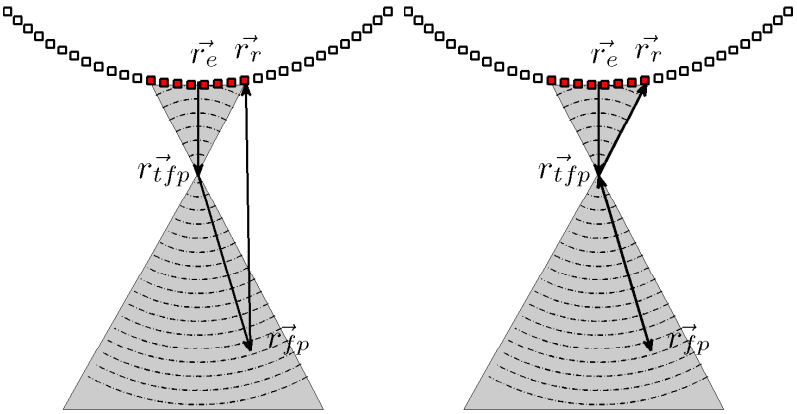

(a) Dynamic receive focus (b) Fixed receive focus

Figure 4.1: Wave propagation path (solid line) for calculating the receive focusing time delays for a focused transmission (a) using dynamic receive focusing and (b) fixed receive focusing. Figure taken from Paper VI.

value for the individual receive elements are calculated as

$$t_d(\vec{r}_r) = \frac{1}{c}\Big(\|\vec{r}_{tfp} - \vec{r}_e\| \pm 2\|\vec{r}_{fp} - \vec{r}_{tfp}\| + \|\vec{r}_r - \vec{r}_{tfp}\|\Big). \tag{4.2}$$

The $\pm$ in (4.1) and (4.2) refer to whether the image point is above or below the transmit focal point.

Each point in the focused image line contains information from a set of spatial positions limited by the opening angle of the virtual source. The opening angle is defined as

$$\alpha = 2\arctan\frac{1}{2F\#}. \tag{4.3}$$

A single image point is therefore potentially represented in multiple first stage focused image lines. A second stage beamformer creates a set of high resolution image points by combining information from multiple first stage focused image lines that contain information from the spatial position of the image point. A single sample, h, representing the image point at the location $\vec{r}_{ip}$ can be expressed as

$$h(\vec{r}_{ip}) = \sum_{k=1}^{K(\vec{r}_{ip})} \mathcal{W}(k, \vec{r}_{ip}) \cdot l_k(t_{d_k}(\vec{r}_{ip})), \tag{4.4}$$

where $l_k(t_{d_k}(\vec{r}_{ip}))$ is the sample at time t_{d_k} from the scan line with propagation direction θ_k. The variable $\mathcal{W}$ is an apodization function with $K(\vec{r}_{ip})$ val-

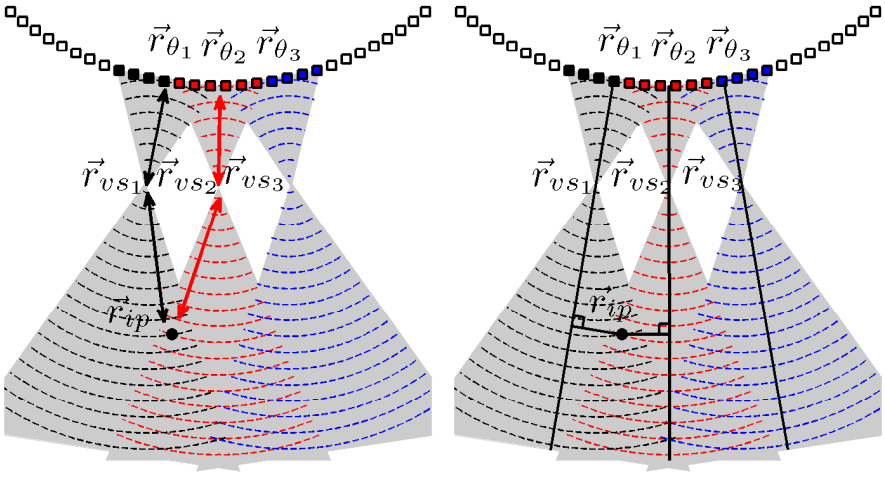

(a) Time-of-flight calculation (b) Apodization weight calculation

Figure 4.2: In (a) and (b) the dashed lines indicate the propagating waves for three multi element emissions. The squares indicate the individual transducer elements. The black dot indicate a specific image point. In (a) the time-of-flight path for the individual emissions from the scan line reference point to the image point and back is illustrated by the arrows. In (b) the calculation of apodization weight is illustrated. Note that the apodization weights are determined based on the shortest distance from the image point to the respective scan lines. In both (a) and (b) note that the third emission shown in blue does not contribute to the image point as it contains no information about the spatial position of the image point due to the limited opening angle. Figure taken from Paper VI.

ues, which controls the weighting of the contribution from each of the first stage scan lines.

The time delay, t_{d_k} for the individual scan lines are found from the round trip time-of-flight, which is the propagation time of the emitted wave in its path from the scan line reference position, $\vec{r}_{\theta_k}$ to the image point $\vec{r}_{ip}$ through the virtual source, $\vec{r}_{VS}$ and return via the same path. Fig. 4.2(a) illustrates the time-of-flight calculation for the SASB second stage beamformer. The delay value for the scan line with reference position $\vec{r}_{\theta_k}$ and VS in $\vec{r}_{VS}$ is calculated as

$$t_{d_k}(\vec{r}_{ip}) = \frac{2}{c}\Big(\|\vec{r}_{VS} - \vec{r}_{\theta_k}\| \pm \|\vec{r}_{ip} - \vec{r}_{VS}\|\Big). \tag{4.5}$$

K is a function of the position of the image point, $\vec{r}_{ip}$ since the number of contributing emissions increases with distance from the virtual sources. The synthesized aperture increases with range resulting in a less range dependent lateral resolution. To determine if a specific first stage scan line contains in-

formation about a given image point one has to evaluate if the image point is within the insonfied area from the virtual source. This can be done by evaluating the angle between the image point, $\vec{r}_{ip}$ and the position of the virtual source, $\vec{r}_{VS_k}$ relative to the scan line direction and is calculated as

$$\Phi = \arccos\left(\frac{\pm(\vec{r}_{ip} - \vec{r}_{VS_k})}{\|\vec{r}_{ip} - \vec{r}_{VS_k}\|} \cdot \frac{\vec{r}_{VS_k} - \vec{r}_{\theta_k}}{\|\vec{r}_{VS_k} - \vec{r}_{\theta_k}\|}\right), \tag{4.6}$$

where $\vec{r}_{\theta_k}$ is the position of the scan line reference position. The $\cdot$ in (4.6) is the dot product and $\pm$ refers to whether the image point is above or below the VS. The sign is positive if the image point is below the VS.

Comparing Φ to half of the scan line opening angle, α, determines if the scan line contains information about the image point or not:

$$f(\vec{r}_{ip}, \vec{r}_{\theta_k}, \vec{r}_{VS_k}) = \begin{cases} 0, & \text{if } \Phi \text{ is } > \frac{\alpha}{2} \\ 1, & \text{if } \Phi \text{ is } \leq \frac{\alpha}{2} \end{cases} \tag{4.7}$$

In the case where $\Phi <= \frac{\alpha}{2}$ the first stage scan line contains information about the image point.

The total number of VS's that contribute to a specific image point can be determined from

$$K(\vec{r}_{ip}) = \sum_{k=1}^{N} f(\vec{r}_{ip}, \vec{r}_{\theta_k}, \vec{r}_{VS_k}), \tag{4.8}$$

where N is the total number of VS's in the scan sequence.

The variable $\mathcal{W}$ in (4.4) is an apodization function determining the weighting of the individual scan lines. The weight for the scan line, l_{θ_k} contributing to image point $\vec{r}_{ip}$ can be calculated from (4.9)

$$\mathcal{W}(k, \vec{r}_{ip}) = \begin{cases} 0.54 - 0.46cos(2n\pi), & \text{if } n \text{ is } \leq 1 \\ 0, & \text{if } n \text{ is } > 0 \end{cases} \tag{4.9}$$

for the case of a desired Hamming apodization, where n can be calculated from

$$n = \frac{d(l_{\theta_k}, \vec{r}_{ip})}{\Delta} + 0.5, \tag{4.10}$$

and is given as the ratio between the shortest distance, $d(l_{\theta_k}, \vec{r}_{ip})$ from the image point, $\vec{r}_{ip}$ to the scan line, l_{θ_k} and a desired aperture width, Δ. The distance $d(l_{\theta_k}, \vec{r}_{ip})$ can be expressed as

$$d(l_{\theta_k}, \vec{r}_{ip}) = \frac{|det([(\vec{r}_{\theta_k} - \vec{r}_{VS_k}), (\vec{r}_{VS_k} - \vec{r}_{ip})])|}{\|\vec{r}_{\theta_k} - \vec{r}_{VS_k}\|} \tag{4.11}$$

where $\vec{r}_{\theta_k}$ is the reference point of the scan line, $\vec{r}_{VS_k}$ is the position of the VS, and $\vec{r}_{ip}$ is the position of the image point all in Cartesian coordinates $(x, z)^T$. det referrers to the determinant. The aperture width Δ can be determined from the desired F# from

$$\Delta = \frac{\sqrt{\|\vec{r}_{VS} - \vec{r}_{ip}\|^2 - d(l_k, \vec{r}_{ip})^2}}{F\#} \tag{4.12}$$

Fig. 4.2(b) illustrates the apodization weight calculation.

4.2 Implementation and beamforming strategy

As mentioned in the introduction of this chapter, one of the shortcomings of full synthetic aperture imaging is that N^2 echo recordings are required to synthesize an image. This requirement is reduced significantly with SASB, due to the sequential beamforming. The major data reduction is achieved by the first stage beamformer. Here M channels of RF data is beamformed to generate a low resolution line, LRL, using a fixed delay and apodization profile. Typically this step also includes a matched filtering and a down conversion to base band, forming a complex signal. Designing a system with a frame rate of 20 frames/s, 192 LRL's pr. frame, 4 bytes pr. sample, and 2000 samples pr. LRL results in a bandwidth of

$$\begin{aligned} datarate &= frames/s \times shots/frame \times bytes/sample \times samples/LRL \\ &= 20 \times 192 \times 4 \times 2000 \\ &\approx 31(MB/s). \end{aligned} \tag{4.13}$$

For comparison, USB 2 has a peak data rate of 60 MB/s and 802.11n has a peak data rate of 75 MB/s. Fig. 4.3 illustrates a block diagram of the first stage beamformer. The first stage beamformer can both be implemented using an analog beamformer or as shown in the figure using a digital beamformer. The advantage of an implementation using an analog beamformer is that only one very high resolution and high speed A/D-converter is needed, where a digital implementation requires N high speed, high resolution A/D-converters. However, the larger flexibility and a more accurate realization is in favor of the digital beamformer.

The second stage beamformer combines a set of LRL's to form a high resolution line, HRL. For each sample in the HRL, a sample from each of those LRL's, which contain information from the HRL sample spatial position is

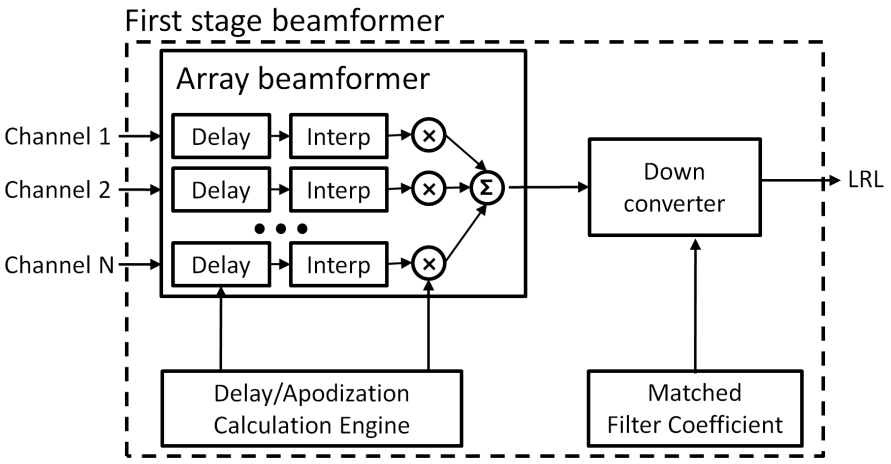

Figure 4.3: Block diagram of the first stage beamformer. The beamformer has N input channels for local storage in the beamformer. The fixed delay and apodization of each channel is controlled by the delay and apodization calculation engine. After beamforming the signal is matched filtered and down converted, generating a LRL.

weighted and summed to form the sample value. Potentially each LRL can contribute to all the sample values of all HRL's, and as such for all samples in each HRL it must be determined which LRL's that contribute. The second stage beamformer has the complexity of a general dynamic receive focusing beamformer. For each sample in the HRL's the delay profile must be calculated. Apodization is also a desirable requirement for suppression of off-axis energy lobes. As the number of contributing LRL's increases with the distance from the virtual sources a dynamic apodization is needed. Fig. 4.4 illustrates a block diagram of a 64 channel second stage beamformer, capable of producing 3 output lines in parallel.

Designing a system there are certain considerations to be made between the desired number of HRL's, number of output lines, and the number of input channels. The first consideration is the maximum number of HRL's that can be generated, if the beamformer is applied a single time pr. emission and is determined from:

$$N_{HRL} = N_{output\ lines} \times N_{input\ channels}. \tag{4.14}$$

If the beamformer is applied N times during each emission the maximum number of HRL's is increased by a factor of N. The number of times the

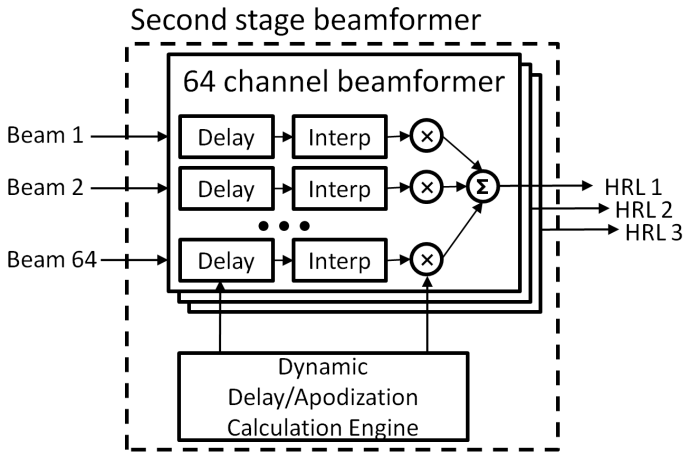

Figure 4.4: Block diagram of the second stage beamformer. The beamformer has 64 input channels for local storage in the beamformer. The delay and apodization of each channel is controlled by the dynamic delay and apodization control unit. The beamformer can generate 3 output lines.

beamformer has to be applied at each emission can be determined from:

$$N_{pass} = \left\lceil \frac{N_{HRL}}{N_{output\ lines} \times N_{input\ channels}} \right\rceil . \tag{4.15}$$

Another consideration is the maximum number of HRL's that can be created, without adding multiple output lines, and can be determined from:

$$N_{HRL} = N_{input\ channels}. \tag{4.16}$$

If the desired number of HRL's is larger than the number of input channels a memory is needed to hold the sum of the intermediate output lines from the beamformer. This memory must be able to hold the number of HRL's times the number of samples pr. HRL.

For a system design continuing the example from above. The desired number of HRL's is 192, with 2000 samples pr. line. Such a system can be implemented using a 64 channel beamformer that can generate 3 output lines. In this case a memory is needed to store the intermediate HRL's because the total number of HRL's is larger than the number of input channels. The memory needed must be able to hold 192 times 2000 samples (1.5 MB).

Fig. 4.5 illustrates the beamforming strategy used in the example. After each emission a single LRL is created and saved in the memory of the second stage

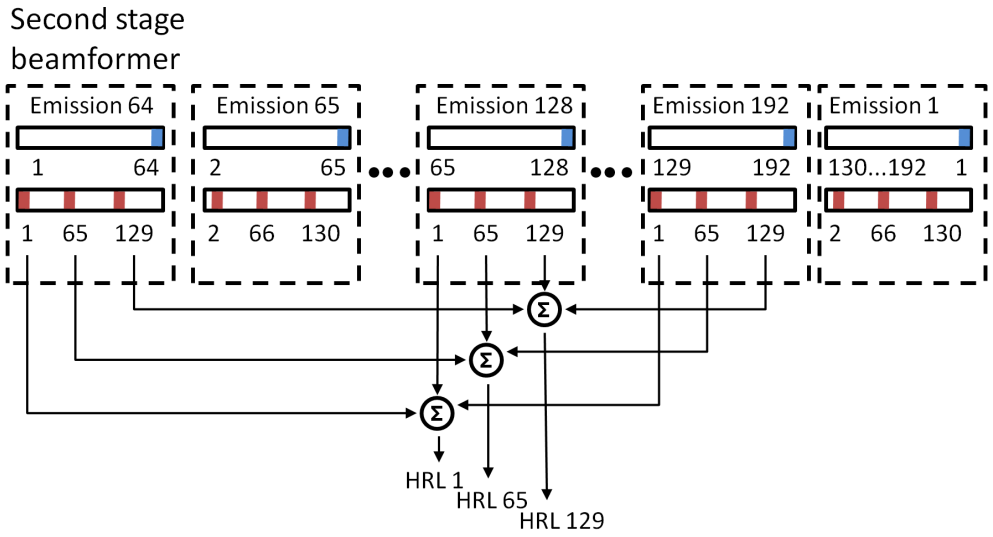

Figure 4.5: Second stage beamforming strategy. The blue marker indicate the latest LRL stored in the memory of the second stage beamformer (first-in-first-out principle is used). The red markers indicate the three intermediate HRL's generated by the second stage beamformer. Each HRL is a sum of 3 intermediate HRL's.

beamformer using the principle of first-in-first-out. Once the data has been saved to memory the beamformer starts to beamform 3 lines. In the case where the current emission is no. 64, the memory of the second stage beamformer is filled with LRL 1 through 64 and the beamformer can create three intermediate HRL's, e.g. 1, 65 and 129. They are intermediate results, because they have to be updated with the beamformed value from LRL's 65 through 192. The next time the HRL's 1, 65 and 129 will be updated is following emission 128, where the beamformer memory will be filled with LRL's 65 through 128. The final update will happen following emission 192.

4.3 Simulated system performance evaluation

In this section SASB is investigated using the simulation software Field II to acquire RF data and BFT3 to beamform data. The purpose of the section is to demonstrate SASB imaging using convex array transducers, and to evaluate the technical performance for a number of configuration to determine good configurations for comparison with conventional imaging. The technical performance indicators presented in Chapter 2.1 will be evaluated.

The simulation study is performed using a phantom consisting of 14 evenly distributed stationary point targets. The points are placed in the center of the phantom (x=0, y=0), in the range from 10 mm to 140 mm, see Fig. 4.6(a). This phantom is used to investigate the spatial resolution, the cystic resolution, and the clutter energy to total energy ratio.

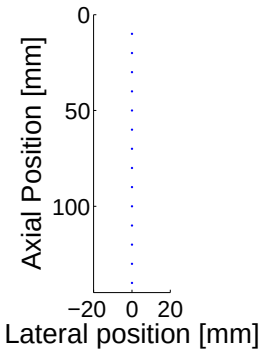

(a)

Figure 4.6: Visualization of the point target simulation phantom. Each of the blue dots indicate a point scatterer.

The simulations are made with a model of a commercially available Sound Technology Inc. (STI) abdominal 3.5 MHz probe with a room-temperature vulcanization (RTV) lens, see Table 4.1 for a summary of the transducer parameters.

Table 4.1: Transducer parameters

Transducer Parameters (STI - 3ML 3.5CLA192)		
Pitch	0.33	mm
Elevation focus	65	mm
Number of elements	192	
Radius of curvature	60	mm
Field of view (FOV)	60.5	^{o}
Bandwidth at -6 dB	85	%
Acoustic layer thickness	1.037	mm

4.3.1 Setup

The parameters which are the most decisive for the performance of SASB imaging are the depth of the virtual source, and the number of active elements in the first stage beamformer. A parameter study is done by varying

the depth of the virtual source with values from 10 mm to 100 mm in steps of 10 mm, and the number of active elements are varied by changing the F# from 1 to 3.5 in steps of 0.5. The study is done with a fixed set of transducer parameters and processing parameters shown in Table 4.2.

Table 4.2: Simulation parameters

Parameter	Value
Field II	
Sampling frequency	120 MHz
Speed of sound	1540
No. mathematical elements in x	7
No. mathematical elements in y	15
BFT3	
Sampling frequency	15 MHz
Speed of sound	1540
Interpolation	Cubic-spline
Scanner setting	
Max. no. of active elem.	64
Excitation pulse	Manufacturer specified 5 MHz pulse
Field of view (FOV)	60.5^o
Angle between scan lines	$0.1576\ ^o$
Length of scan lines	146.13 mm
No. of emissions	384
No. of scan lines	384
1st stage processing	
Transmit sub-aperture	Symmetric
Transmit apodization	Boxcar
Transmit F#	1,1.5,2,2.5,3,3.5
Transmit focal depth	10,20,30,40,50,60,70,80,90,100 mm
Receive sub-aperture	Same as transmit
Receive apodization	Gauss (α: 0.4)
2st stage processing	
Number of image lines	384
Field of view (FOV)	$60.5\ ^o$
Angle between image lines	$0.1576\ ^o$
Apodization	Gauss (α: 0.4)

In the following simulation studies a measured element pulse echo response from the center element is used as the combined excitation waveform and the two-way element impulse response. The used excitation pulse is a manufacturer specified pulse with a center frequency of 5 MHz. The element pulse echo response is measured using a custom made phantom. The phantom is

designed such that a transducer can be fixated and moved in the x-z coordinate system using two Newport high-resolution micrometers. By moving the transducer in the x-z coordinate system the transducer can be placed such that an identical distance from all the transducer elements to the surface of the phantom is obtained. At this position the distance from the elements to the surface of the phantom is identical to the elevation focus of the transducer. This ensures that the surface of the return pulse match the curvature of the generating element and the spatial impulse response is a Dirac impulse.

Grating lobes arise in SASB imaging in a combination of the angle between first stage scan lines, the opening angle of the virtual sources, and the wavelength of the transmitted pulse. All of these parameters can be controlled in SASB to prevent grating lobes. For a fair comparison between configurations and to avoid significant grating lobes, 384 first stage scan lines are used in all of the following simulations.

The technical performance indicators are calculated based on the simulated beamformed RF-data and B-mode images. The B-mode images are created by envelope detection of the beamformed RF-data, followed by a log-compression to a dynamic range of 60 dB, and subsequently scan converted using bilinear interpolation. Before scan conversion the images are TGC corrected according to depth to obtain homogeneous images. The images created for investigation of the point spread function is normalized such that each of the local maximum of the point spread functions has a value of 0 dB.

4.3.2 Simulation results

In this section the lateral resolution, cystic resolution, and clutter energy to total energy ratio is investigated. Each of the performance parameters will be investigated with different configurations of SASB. For each configuration, data from the generated B-mode image is extracted as shown on 4.7, and the performance parameters are determined. In total 60 configurations are evaluated, each with a unique combination of focus depth and F#.

Lateral resolution
The lateral resolution is investigated using simulations of the point target phantom. From each of the 14 points targets, data are extracted, and the lateral beam profile is determined. From the beam profiles, the lateral resolution is quantized at -6 dB, at -20 dB, and at -40 dB. Fig. 4.8 illustrates the average lateral resolution as function of focus depth and F#.

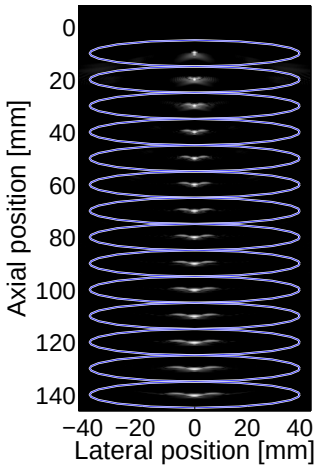

Figure 4.7: Simulated SASB second stage generated B-mode image of a point target phantom containing 14 point scatterers. The blue lines indicate the areas where the data is extracted and used to determine the performance parameters.

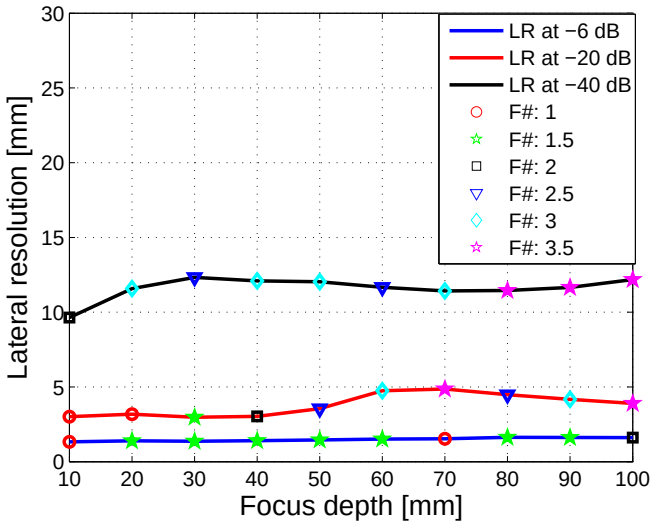

Figure 4.8: Simulated avg. lateral resolution as function of focus depth, and F#. The avg. lateral resolution for each configuration is calculated as an avg. from 14 point targets ranging from 10 to 140 mm. For each focus depth the configuration with the best lateral resolution is shown. The markers indicate which F# that is used in the respective configurations. The blue line indicate the FWHM, the red line the lateral resolution at -20 dB, and the black line the lateral resolution at -40 dB.

Note from Fig. 4.8 that there is no unique configuration that is best at all three levels (-6 dB, -20 dB, -40 dB). A trend is observed that a small F# is best to obtain a good FWHM, and a large F# is best if a good resolution is desired at -40 dB. This observation fits nicely with the theory of a Fourier relation [41] between the aperture and the beam profile, where a small aperture (due to the large F#) creates a wide main-lobe, but has low side-lobes, and a large aperture (due to a small F#) creates a narrow main-lobe, but has high side-lobes.

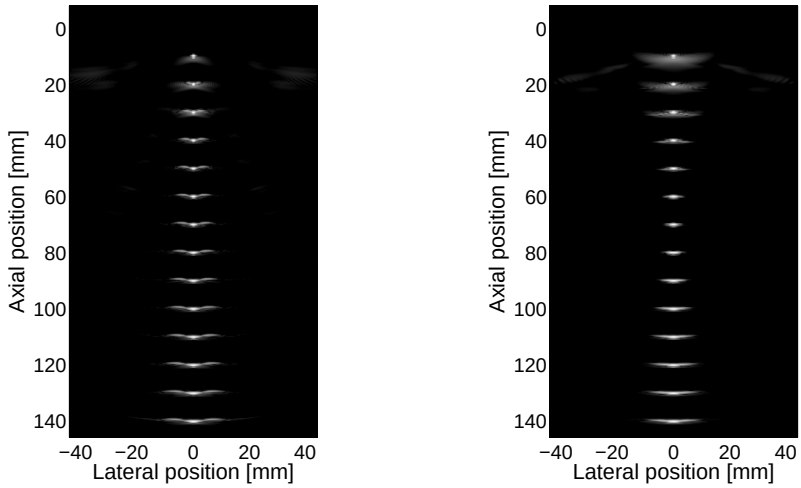

(a) VS: 10mm - F#: 1

(b) VS 70mm - F#: 3

Figure 4.9: Simulated B-mode images created using SASB and in (a) focus depth in 10 mm and a F# of 1, and in (b) focus depth in 70 mm and F# 3.

Fig. 4.10 shows the lateral resolution as function of depth for the two configurations shown in Fig. 4.9. Interpreting the figure, it is seen that the configuration using a focus depth of 10 mm is best at -6 dB and -20 dB, but is worse at -40 dB.

Clutter energy to total energy ratio

The clutter energy to total energy ratio is investigated using simulations of the point target phantom. For each of the 14 point targets the clutter energy to total energy is found using (2.13) and two cysts with a diameter of 4 and 7 mm. The 14 resulting ratios are averaged to obtain the average ratio for each configuration. For an easier interpretation of the results, the best configuration for each focus depth and cyst size is found and shown in Fig. 4.11.

Interpreting Fig. 4.11 it is seen that positioning the virtual source at 30 mm and using a F# of 1.5 results in the best ratio for a 4 mm cyst. For a 7 mm cyst

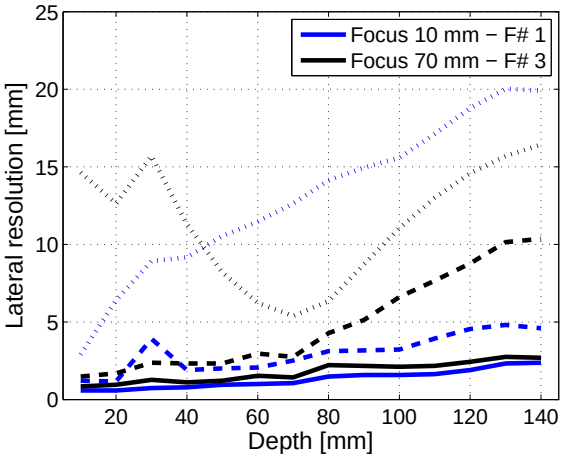

Figure 4.10: Simulated lateral resolution as function of depth for two configurations of SASB. The blue lines indicate a configuration using a focus depth of 10 mm and a F# of 1, and the black line a focus depth of 70 mm and a F# of 3. The solid line is the lateral resolution at -6 dB, the dashed line at -20 dB, and the dotted line at -40 dB.

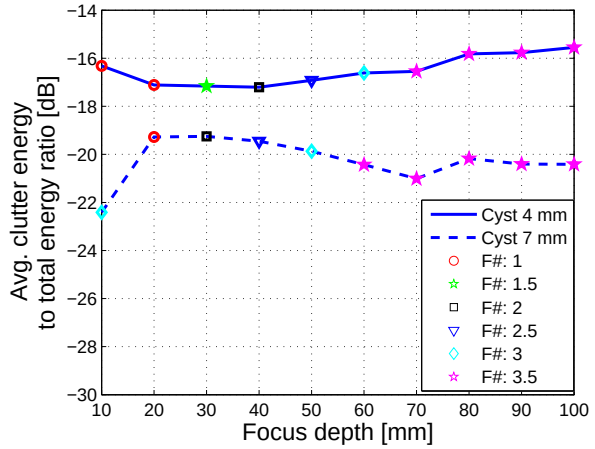

Figure 4.11: Simulated avg. clutter energy to total energy ratio of SASB as function of focus depth, cyst size, and F#. The avg. clutter energy to total energy ratio for each configuration is calculated as an avg. of 14 cysts with center ranging from 10 to 140 mm. For each focus depth the configuration with the best clutter energy to total energy ratio is shown. The markers indicate which F# that is used in the respective configurations. The blue line indicate the clutter energy to total energy ratio for a 4 mm cyst and the dashed line for a 7 mm cyst.

the best ratio is obtained using a virtual source position at 10 mm and a F # of 3. Further it can be generalized that as the depth of the virtual source is increased the best result is obtained using an increasing F#.

Cystic resolution
The cystic resolution is investigated using simulations of the point target phantom. For each of the 14 point targets the cyst size for a desired contrast of 20 dB is found using (2.13). The 14 resulting cyst sizes are averaged to obtain the average cyst size for each configuration. For an easier interpretation of the results, the best configuration for each focus depth is found and shown in Fig. 4.12.

Interpreting Fig. 4.12 it is seen that positioning the virtual source at 70 mm and using a F# of 3.5 results in the best cystic resolution.

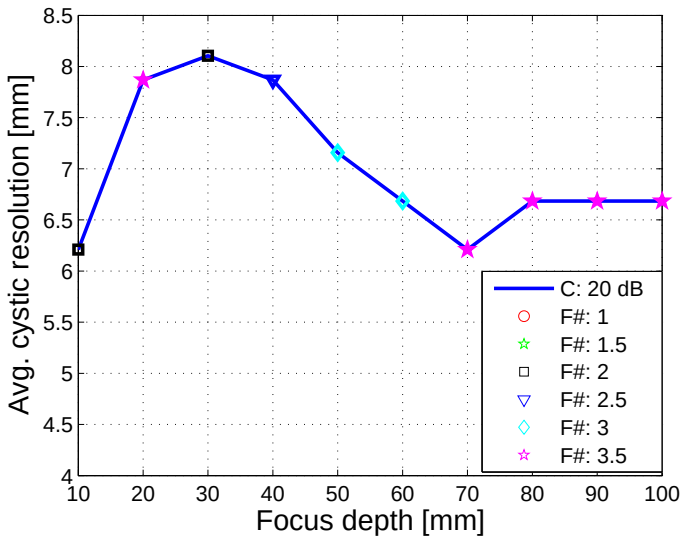

Figure 4.12: Simulated avg. cystic resolution of SASB as function of focus depth, and F#. The avg. cystic resolution for each configuration is calculated as a mean of 14 cysts with center ranging from 10 to 140 mm. For each focus depth the configuration with the best cystic resolution is shown. The markers indicate which F# that is used in the respective configurations. The blue line indicate the cystic resolution for a desired contrast of 20dB.

4.3.3 Discussion of the simulation results

A comprehensive simulation study of 60 different configurations of SASB were evaluated using the technical performance indicators introduced in Chapter 2.1. The results show that for all positions of the virtual source a good lateral resolution must be compromised to achieve a good contrast. Based on the evaluation of the cystic resolution and clutter energy to total energy ratio, it seems that a good configuration in relation to contrast, is one that uses a virtual source in 70 mm and a F# of 3.5. Based on the results from the lateral resolution and the contrast study two configurations were closer evaluated. The first configuration uses a virtual source in 10 mm and F# of 1, and the other a virtual source in 70 mm and a F# of 3. The comparison showed that the lateral resolution at -6 dB is approximately the same, but the resolution at -40 dB is improved noticeably using the second configuration.

4.4 Measured system performance evaluation

In this section SASB is investigated using a ProFocus scanner and the data acquisition system presented in chapter 3. The data acquisition system is used to acquire beamformed first stage scan line data, and BFT3 is used to second stage beamform the data. The purpose of the section is to confirm the simulation results and to determine which configurations to compare against conventional imaging. Each of the technical performance indicators evaluated in the simulation study will be evaluated using the same 60 configurations as in the simulation study. The evaluation of the lateral resolution, cystic resolution, and clutter energy to total energy ratio is investigated using a phantom containing 5 metal wires with a diameter of 0.07 mm, evenly distributed from 20 to 120 mm.

Lateral resolution
The lateral resolution is investigated using measurements of the wire phantom. From each of the 5 wires, data are extracted, and the lateral beam profile is determined. From the beam profiles, the lateral resolution is quantized at -6 dB, at -20 dB, and at -40 dB, and averaged to obtain the average lateral resolution for each configuration. For an easier interpretation of the results, the best configuration for each focus depth and F# is found and shown in Fig. 4.13.

Note from Fig. 4.13 that the measured results fits nicely with the simulated results shown on Fig. 4.8. As with the simulated results there is no unique

configuration that is best at all three levels (-6 dB, -20 dB, -40 dB). There seem however to be a trend that a deeper position of the virtual source increases the lateral resolution at -40 dB.

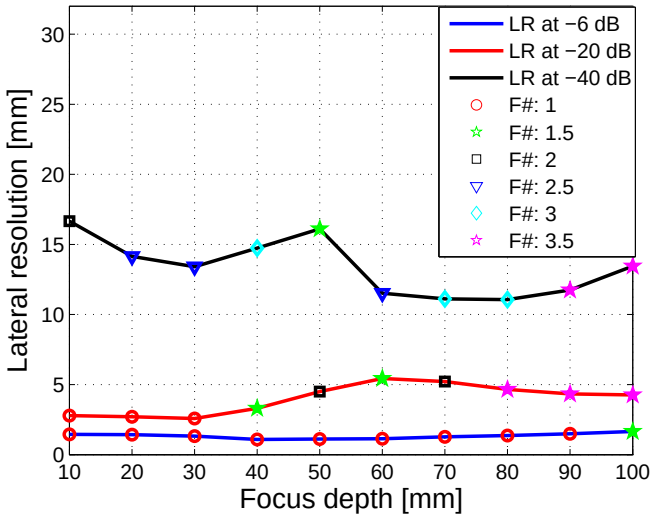

Figure 4.13: Measured avg. lateral resolution as function of focus depth, and F#. The avg. lateral resolution for each configuration is calculated as an avg. from 5 wires ranging from 20 to 120 mm. For each focus depth the configuration with the best lateral resolution is shown. The markers indicate which F# that is used in the respective configurations. The blue line indicate the FWHM, the red line the lateral resolution at -20 dB, and the black line the lateral resolution at -40 dB.

Fig. 4.14 shows two measured B-mode images created using the same two configurations as used in Fig. 4.9. Comparing the two figures with a virtual source at 10 mm, note the grating lobes in the measured B-mode image. Also note the clutter that spreads from each wire and reduces the lateral resolution. The B-mode images created using a virtual source at 70 mm seem to create less clutter and the grating lobes are suppressed.

Fig. 4.15 shows the lateral resolution as function of depth for the two configurations shown in Fig. 4.9. Comparing the results with the simulated results it is seen that the measured results fits nicely with the simulated. There is however a significant difference at the -40 dB resolution from a depth of 20 to 60 mm, where SASB is performing better in measurements than in simulations, and the conventional method is performing worse.

Clutter energy to total energy ratio

The clutter energy to total energy ratio is investigated using measurements

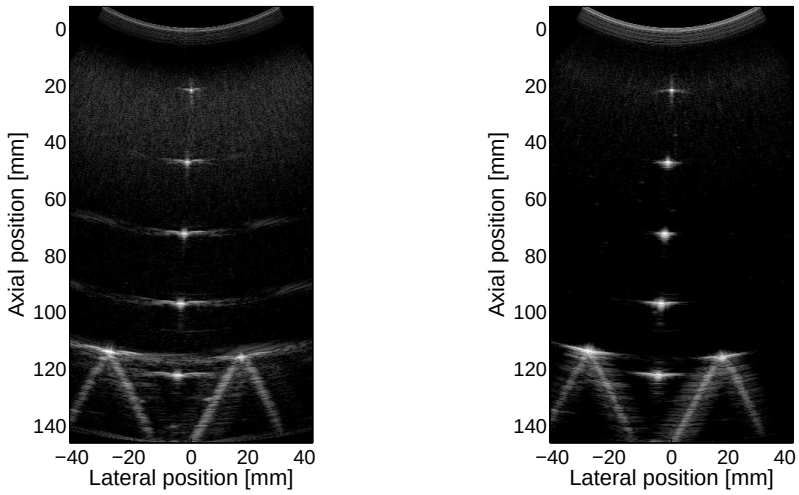

(a) VS: 10mm - F#: 1

(b) VS 70mm - F#: 3

Figure 4.14: Measured B-mode images created using SASB and in (a) focus depth in 10 mm and a F# of 1, and in (b) focus depth in 70 mm and F# 3.

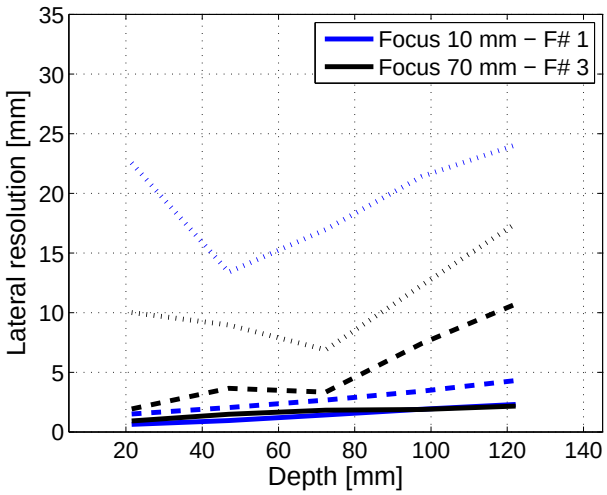

Figure 4.15: Measured lateral resolution as function of depth for two configurations of SASB. The blue lines indicate a configuration using a focus depth of 10 mm and a F# of 1, and the black line a focus depth of 70 mm and a F# of 3. The solid line is the lateral resolution at -6 dB, the dashed line at -20 dB, and the dotted line at -40 dB.

of the wire phantom, but only data from the first 4 wires are used. The last wire is too close to the damping material which compromises the results.

The clutter energy to total energy ratio is found using (2.13) and two cysts with a diameter of 4 and 7 mm. The 4 resulting ratios are averaged to obtain the average ratio for each configuration. For an easier interpretation of the results, the best configuration for each focus depth and cyst size is found and shown in Fig. 4.16.

Interpreting Fig. 4.16 it is seen that positioning the virtual source at 80 mm and using a F# of 3.5 results in the best ratio for both the 4 and 7 mm cyst.

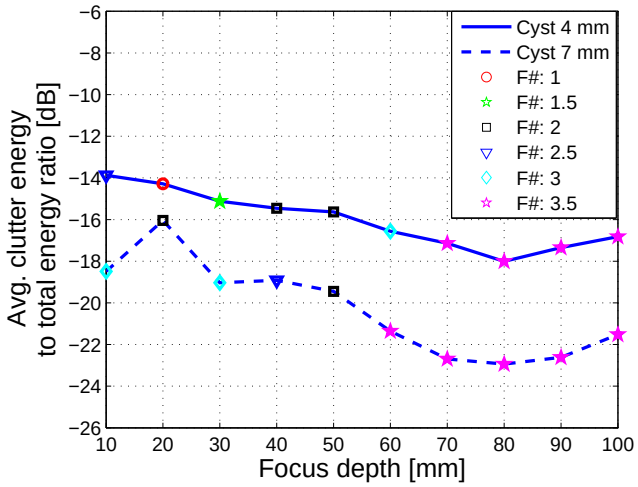

Figure 4.16: Measured avg. clutter energy to total energy ratio of SASB as function of focus depth, cyst size, and F#. The avg. clutter energy to total energy ratio for each configuration is calculated as an avg. of 4 cysts with center ranging from 20 to 120 mm. For each focus depth the configuration with the best clutter energy to total energy ratio is shown. The markers indicate which F# that is used in the respective configurations. The blue line indicate the clutter energy to total energy ratio for a 4 mm cyst and the dashed line for a 7 mm cyst.

Cystic resolution

The cystic resolution is investigated using measurements of the wire phantom. For each of the 4 point targets the cyst size for a desired contrast of 20 dB is found using (2.13). The 4 resulting cyst sizes are averaged to obtain the average cyst size for each configuration. For an easier interpretation of the results, the best configuration for each focus depth is found and shown in Fig. 4.17.

Interpreting Fig. 4.17 it is seen that positioning the virtual source at 80 mm and using a F# of 3.5 results in the best cystic resolution.

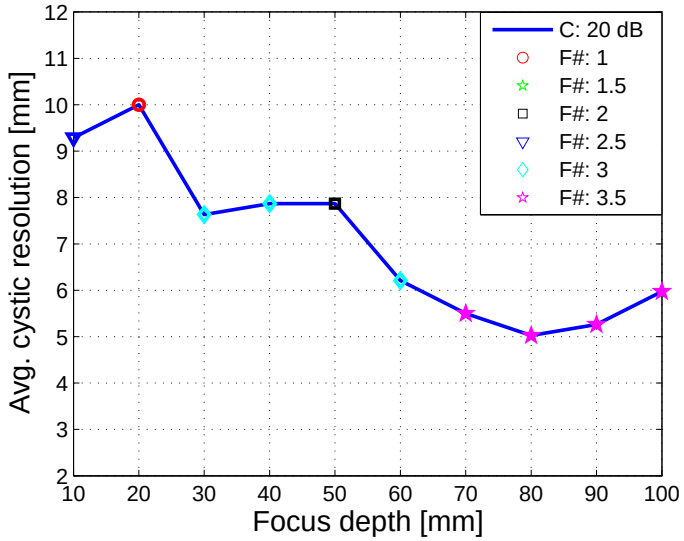

Figure 4.17: Measured avg. cystic resolution of SASB as function of focus depth, and F#. The avg. cystic resolution for each configuration is calculated as a mean of 4 cysts with center ranging from 20 to 120 mm. For each focus depth the configuration with the best cystic resolution is shown. The markers indicate which F# that is used in the respective configurations. The blue line indicate the cystic resolution for a desired contrast of 20dB.

4.4.1 Discussion of the measurement results

A comprehensive study using the same 60 configurations of SASB, as evaluated in the simulation study, is evaluated. The study of the lateral resolution showed as in the simulation study that for all positions of the virtual source, a good lateral resolution must be compromised to achieve a good contrast. There where however observed a tendency that positioning the virtual source at lower depths resulted in less clutter and therefore also better lateral resolution at -40 dB. For the configurations using a low F# grating lobes where observed, this favors using a high F#. Based on the evaluation of the cystic resolution and clutter energy to total energy ratio, it seems that a good configuration in relation to contrast, is one that uses a virtual source in 80 mm and a F# of 3.5. Evaluating the same two configurations, as evaluated closer in the simulation study, approximately the same beam profiles where observed. There were however some deviation, in favor of the measurement, at the -40 dB resolution level. The comparison of the two configurations showed that the lateral resolution at -6 dB is approximately the same, but the resolution at -40 dB is improved noticeably using the second configuration.

4.5 Comparison to conventional imaging

SASB imaging has been compared to conventional imaging using a BK8820e abdominal transducer, and a STI 3ML3.5CLA192 abdominal transducer. Paper VI presents the comparison study for the setup using the BK8820e transducer, a field of view of 12 cm, and a 5 MHz excitation pulse. The results show that SASB is able to maintain a more isotropic point spread function through depth and has a better lateral resolution. The lateral resolution is in average improved by 17.9% at FWHM and 6.1% at -20 dB using SASB. The standard deviation on the lateral resolution at FWHM is improved by 0.61 mm at FWHM using SASB compared to DRF.

This section will continue the comparison of SASB imaging to conventional imaging using the 3ML3.5CLA192 transducer from STI. The chosen configuration of the conventional imaging setup is a default configuration of the ProFocus scanner for abdominal imaging using a field of view of 14.6 cm and a 5 MHz excitation pulse. The configuration of SASB is based on the simulated and measured system performance evaluation studies, and the comparison study presented in appendix A. Table 4.3 lists the parameters of the two configurations.

Table 4.3: Imaging parameters

Imaging parameters	Conventional	SASB	Unit
Transmit Focus	105.5	70	mm
Transmit F#	5.0	2.0	
Transmit Apodization	Boxcar	Boxcar	
Receive Focus	dynamic	70	mm
Receive F#	0.8	2.0	
Receive Apodization	$\text{Gauss}_{\alpha:0.4}$	$\text{Gauss}_{\alpha:0.4}$	
$\text{Apodization}_{\text{2nd stage SASB}}$		$\text{Gauss}_{\alpha:0.4}$	

Lateral resolution

The lateral resolution is compared using a wire and contrast phantom, Model 525 (Danish Phantom Service, Frederikssund, Denmark). This phantom allows for a comparison of the speckle appearance, and investigation of the lateral resolution at -6 dB, and at -20 dB. For a more detailed comparison of the lateral resolution see appendix A.

Fig. 4.18 shows the generated B-mode images of the wire and contrast phan-

tom. From each of the 14 wires in the center of the images, the lateral resolution is determined and shown in Fig. 4.19. Note from Fig. 4.18 that the speckle appear more uniform as function of depth. Further note that the wires are easier resolved due to the improved lateral resolution and lower side-lobes. This is quantized in Fig. 4.19.

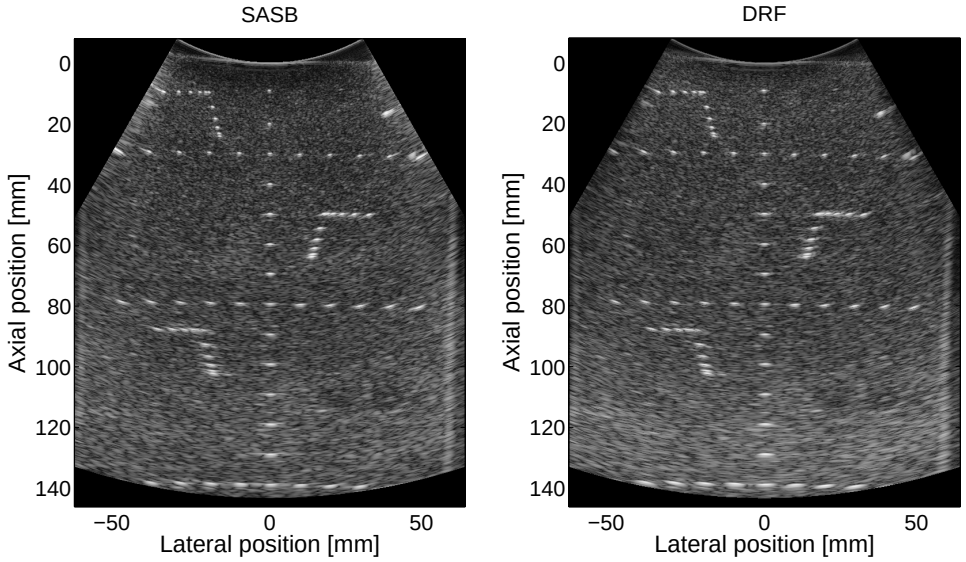

Figure 4.18: B-mode images of the wire and contrast phantom, Model 525, using SASB and DRF. Dynamic range is 60 dB. A digital TGC is applied on both images for a uniform speckle level through depth. The median speckle level of each image is normalized to each other. Figure taken from Paper I.

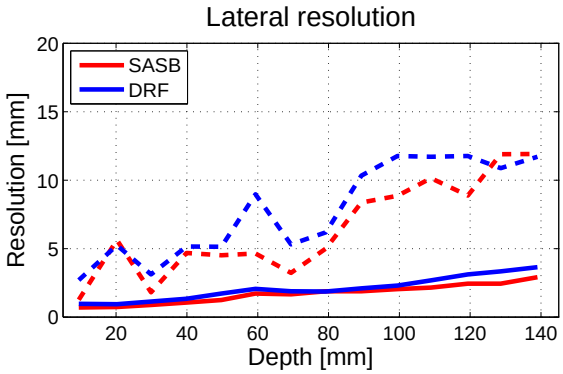

Figure 4.19: Measured lateral resolution for the B-mode images shown in Fig. 4.18. Figure taken from Paper I.

Contrast

The contrast to noise ratio is investigated using 2.14 and a speckle and contrast phantom, Model 571 (Danish Phantom Service, Frederikssund, Denmark). Fig. 4.20 shows the generated B-mode images. From each of the 6 large anechoic cysts data is extracted and paired with data from a region of the same size at the same depth and the CNR is determined. The resulting CNR as function of depth is shown in Fig. 4.21. Note from the figure that the CNR is marginally different between the two imaging methods, where SASB has a higher CNR until 70 mm and DRF has a better CNR from 85 mm.

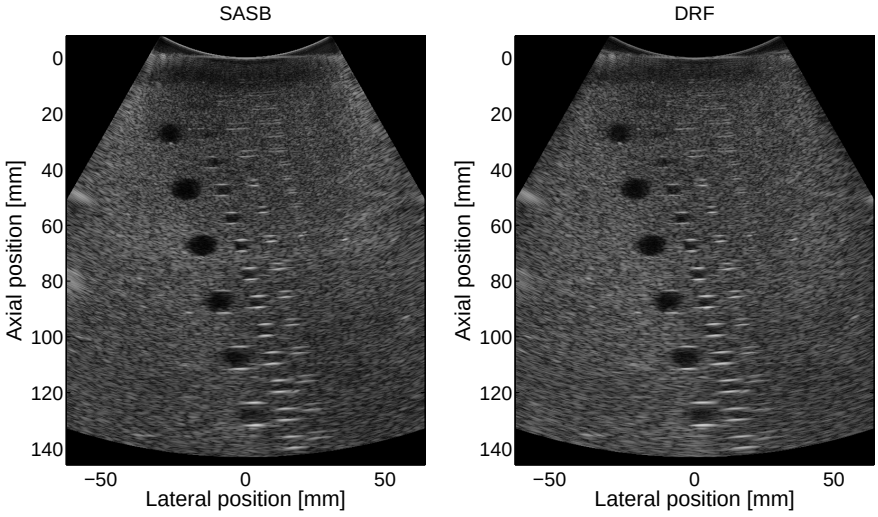

Figure 4.20: B-mode images of the contrast phantom, Model 571, using SASB and DRF. Dynamic range is 60 dB. A digital TGC is applied on both images for a uniform speckle level through depth. The median speckle level of each image is normalized to each other.

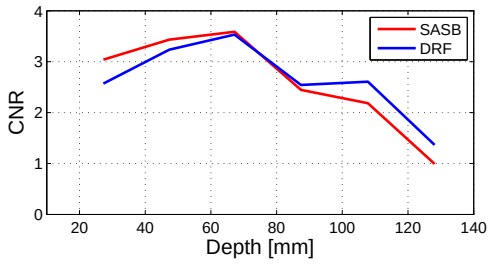

Figure 4.21: Measured CNR for the B-mode images shown in Fig. 4.20.

Signal to Noise Ratio

The signal-to-noise ratio defined by 2.4 is investigated using the speckle and contrast phantom, Model 571, and is based on 20 frames and 384 scan lines. The frames were acquired such that none of the contrast objects interfered with the measurement.

Fig. 4.22 shows the measured SNR as function of depth. Note from the figure that SASB has a marginally better SNR from 40 mm to 90 mm, which is around the transmit focus point. The penetration depth defined by a SNR of 0 dB is not reached with the given setups.

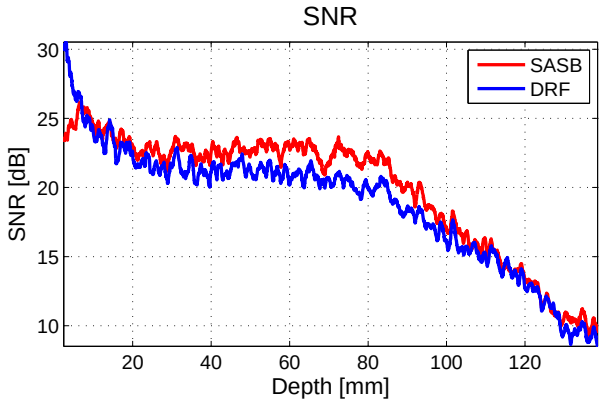

Figure 4.22: Visualization of the SNR using SASB and DRF. Figure taken from Paper I.

4.5.1 In vivo comparison

In the final part of the comparison study an *in vivo* scan of the Morison's Pouch from a 30 year old male volunteer was scanned. The B-mode images are shown in Fig. 4.23. Each of the images are shown with a dynamic range of 60 dB and are post-processed using a digital TGC for a uniform speckle level through depth. The median speckle level of each image is normalized to each other.

Note from Fig. 4.23 that the details in the image is better visualized using SASB. Small vessels are easier to detect and boundaries are sharper.

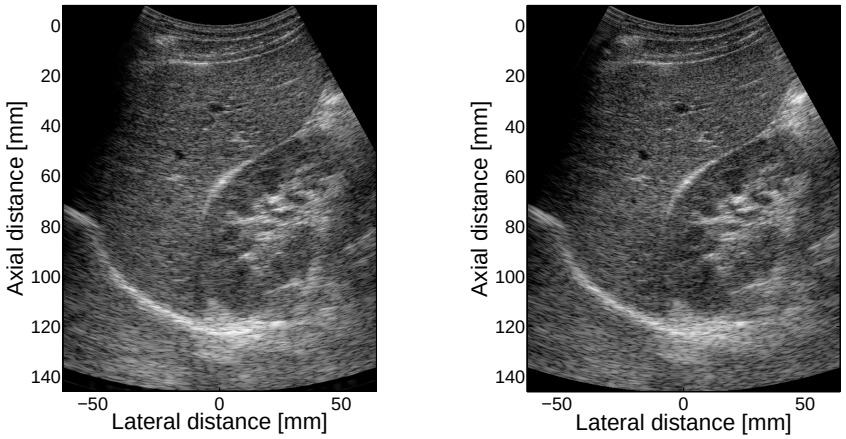

(a) DRF (b) SASB

Figure 4.23: Measured *in vivo* B-mode image of the Morison's pouch, using (a) DRF and (b) SASB. Figure taken from Paper I.

4.5.2 Discussion of the comparison results

Several configurations of SASB were compared to a conventional imaging setup for abdominal imaging. The configuration of SASB positioning the virtual source at 70 mm and using a F# of 2 is a good setup, and was compared to a default manufacturer specified conventional setup. The two methods were compared in terms of lateral resolution, contrast to noise ratio, signal to noise ratio, and in *in vivo* measurements.

The results of the lateral resolution evaluation showed that at -6 dB and -20 dB the lateral resolutions are on average improved by 18.4% at -6 dB and 17.4% at -20 dB using SASB. The standard deviation on the lateral resolution at -6 dB were improved from 0.9 mm using DRF to 0.7 mm using SASB. At -20 dB the standard deviation were 3.5 for both modalities. A lower standard deviation of the lateral resolution can be interpreted as a more uniform apearance of the images.

The result from the contrast to noise ratio evaluation showed that the CNR using SASB and conventional imaging is on average equally good. A tendency that SASB had a better CNR at lower depths, and conventional imaging at deeper positions were observed.

The result from the signal to noise ratio evaluation showed that the SNR using SASB is on average 6.2% or 1.18 dB better than the SNR using DRF.

The technical performance evaluation was further supported by *in vivo* scans of the right kidney and the adjacent liver. The results presented prove the viability of SASB for 2D ultrasound imaging.

4.6 Conclusion

This chapter has presented the theory behind SASB imaging, an implementation and beamforming strategy, a comprehensive simulation and measurement study, and a comparison study evaluating SASB in comparison to conventional imaging.

The theory of 2 dimensional SASB imaging is implemented in a novel implementation using the beamformation toolbox BFT3, and has been used to generate both simulated and measured B-mode images. The implementation is based on a sequential processing of each first stage scan line, producing a set of low resolution images, that is summed to generate the final high resolution image. Furthermore, an implementation based on parallel processing of multiple first stage scan lines were presented, and the hardware requirements were discussed for a real time implementation.

Based on the comprehensive simulation and measurement study evaluating each of the technical performance indicators presented in Chapter 2, configurations of SASB were compared to conventional imaging. A good configuration of SASB showed to be using a virtual source depth of 70 mm and a F# of 2. The lateral resolution, contrast to noise ratio, signal to noise ratio, and *in vivo* measurements were evaluated and showed that SASB imaging is viable for 2D ultrasound imaging. Further evaluation of the clinical efficacy will determine if the image quality of SASB imaging is better than using conventional imaging, and will be the topic of Chapter 5.

CHAPTER

FIVE

Clinical evaluation of Synthetic Aperture Sequential Beamforming

This chapter describes the evaluation of a novel implementation of 2-dimensional SASB imaging in comparison to conventional dynamic receive focusing imaging. The evaluation is performed as a three phased clinical study as proposed in Paper III, and discussed in Chapter 2 section 2.2.

The basic concept of SASB imaging is introduced in Chapter 4, where the theory behind the method is explained in detail, followed by a simulation and measurement parameter study. The parameter study evaluated each of the technical indicators presented in Chapter 2 and good configurations was determined and presented as a prototype in Paper VI and Chapter 4. In the following of this chapter the results from the pre-clinical trial, presented in Paper V, and the result from the clinical trial, presented in Paper II, will be introduced and discussed. Special focus is on describing the data processing, determination of the acoustic output, and presentation of the data material.

5.1 Hypothesis

The two null hypotheses tested in the clinical trials are:

- SASB imaging has no effect on penetration depth.
- SASB imaging has no effect on image quality.

5.2 Methods and Materials

The evaluation of the hypotheses are performed in two clinical trials using healthy volunteers, and evaluated by ultrasound specialists (medical doctors). The pre-clinical trial is used to determine the relevance of a clinical trial, and the clinical trial is used to determine the clinical efficacy. Both trials are conducted for abdominal imaging using a multi element convex array transducer, and is compared to conventional dynamic receive focusing imaging using dynamic apodization.

5.2.1 Equipment and imaging configuration

The *in-vivo* measurements were performed using the data acquisition system described in Chapter 3 and presented in Paper I and III. In both trials the same convex array, STI 3ML 3.5CLA192, transducer is used as in the prototype phase. The shoot sequence is configured such that one frame from one method followed directly after the other. Hereby, images from exactly the same field-of-view were obtained, enabling direct comparison of the methods. The depth of each scan was set to 14.6 cm and the interleaved frame rate was set to 10 frames per second, i.e., 5 conventional and 5 SASB frames per second. The chosen excitation waveform and transmit voltage is a preset standardized setting from the manufacturer and is the same for both the conventional and SASB imaging ($\pm$ 75 V).

The applied imaging configuration of SASB is determined based on the prototype study described in Chapter 4 and the configuration of DRF is chosen based on the standard manufacturer settings for abdominal imaging with a field-of-view of 14.6 cm using a center frequency of 5 MHz and a BK8820e transducer. The BK8820 and the used transducer has identical geometrical parameters.

The excitation pulse and imaging configuration of SASB and DRF is characterized by the parameters given in Table 5.1. Note that the frame rate used in the intensity measurements is 10 frames per second using a single configuration at a time. This result in a conservative measure of the intensity, and the actual intensity in the interleaved configuration will be lower.

Table 5.1: Imaging configurations

Imaging parameters	Conventional	SASB	Unit
Transmit Focus	105.5	70	mm
Transmit F#	5.0	2.0	
Transmit Apodization	Boxcar	Boxcar	
Receive Focus	dynamic	70	mm
Receive F#	0.8	2.0	
Receive Apodization	$\text{Gauss}_{\alpha:0.4}$	$\text{Gauss}_{\alpha:0.4}$	
$\text{Apodization}_{\text{2nd stage SASB}}$		$\text{Gauss}_{\alpha:0.4}$	
System and pulse parameters			
No. of emissions per image	384		
No. of scan lines per image	384		
No. of frames per sec.	10		
Max. no. of active elem.	64		
Center frequency	5		MHz
Transmit voltage	75		V

5.2.2 Data processing

The data acquired by the ProFocus scanner is beamformed baseband data. Each acquired frame is split into conventional image frames and SASB image frames. The image frames are subsequently converted to RF data, and the SASB image frames are processed using the beamformation toolbox BFT3 [10] to generate SASB second stage RF data. The second stage scan lines are defined with the same location and direction as the first stage scan lines. Note, however, that any number of scan lines or image points could have been beamformed for SASB imaging, from the acquired data.

The processing steps performed to generate B-mode images for display are shown in Fig. 5.1. First the RF data is scaled to compensate for edge effects. The compensation factor is simply one over the number of contributing channels. The data is subsequently envelope detected and automatic TGC corrected. After TGC correction, image sequence pairs are normalized to an overall median envelope level, matching a gray tone of 70 (27% of the gray tone scale) after compression. Subsequently data is μ-law compressed, scan converted, and saved in an palindromatic order, to avoid annoying temporal discontinuities at the ends during visualization.

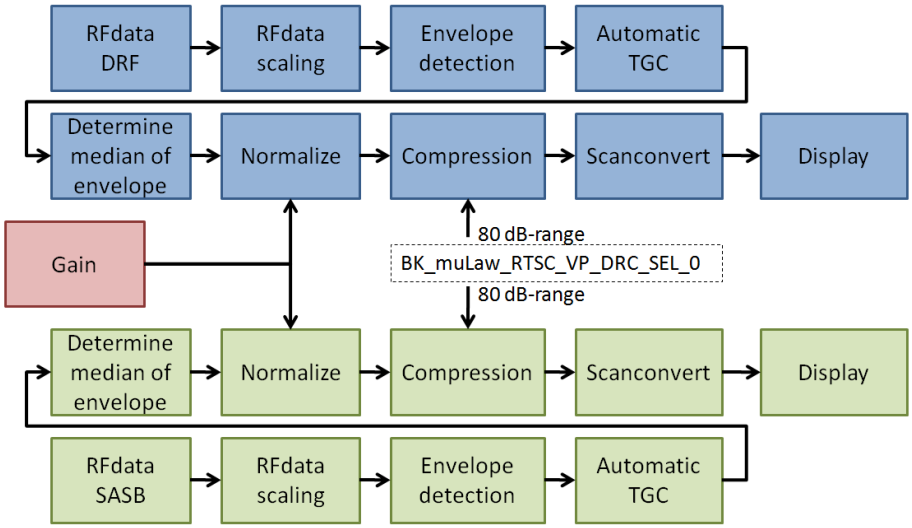

Figure 5.1: Block diagram of the data path for generating the individual B-mode images. The blue color indicate the data path for the DRF method, the green color the data path for the SASB method, and the red color the overall gain setting which the speckle level of the resulting images are normalized to.

Automatic TGC correction

The automatic TGC correction is applied to obtain a homogeneous speckle level through depth. The automatic TGC correction simulates the TGC adjustments performed by a physician, eliminating the possible bias from human intervention.

The TGC correction is performed by calculating a mask to filter out strong and weak specular regions. The mask is then applied to the enveloped detected data and the median value of all lines for all depths in the first recorded frame is found. The resulting curve is normalized to a maximum of one, inverted, and used to normalize all lines in all frames. Fig. 5.2 shows a block diagram of the data path, and Fig. 5.3 shows an example of a B-mode image before and after post-processing.

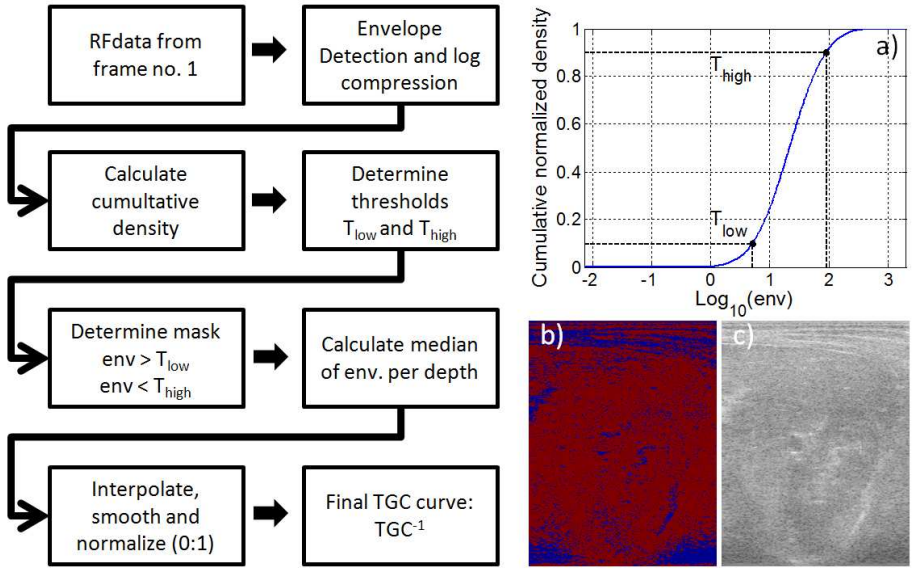

Figure 5.2: Block diagram of the data path for calculation of the digital TGC. (a) shows the calculated cumulative density and the threshold values T_{high} and T_{low}. (b) shows the mask with red color for determining the speckle level. (c) shows the corresponding B-mode image. Note how strong and weak regions are masked out.

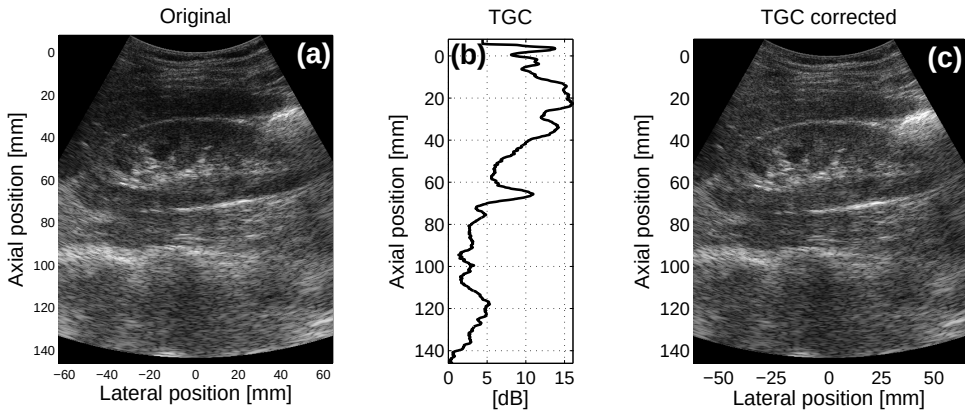

Figure 5.3: Automatic TGC post correction. (a) shows the B-mode image prior to TGC correction, (b) shows the TGC curve expressed in dB, and (c) shows the same image as in (a) after TGC correction. Figure taken from Paper II.

Compression

Compression is done by mapping the envelope detected data to a quantized 8-bit linear gray scale for display. Different types of mapping is investigated,

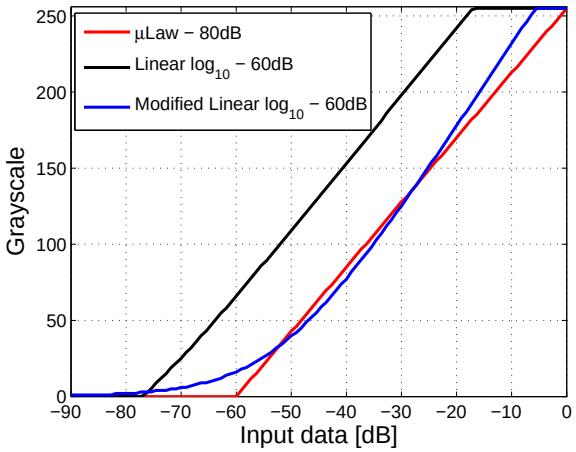

Figure 5.4: Illustration of three different compression schemes, μ-low using 80 dB dynamic range, linear mapping using $\log_{10}$ compression, and linear mapping using a modified $\log_{10}$ compression.

and some of the mappings are shown in Fig. 5.4.

As shown in Fig. 5.5 the mapping from envelope detected data to gray scale has a significant influence on performance perception. This mapping can be designed to emphasize or attenuate different features of the image data. The empirical evaluation performed in the prototype phase, showed that map-

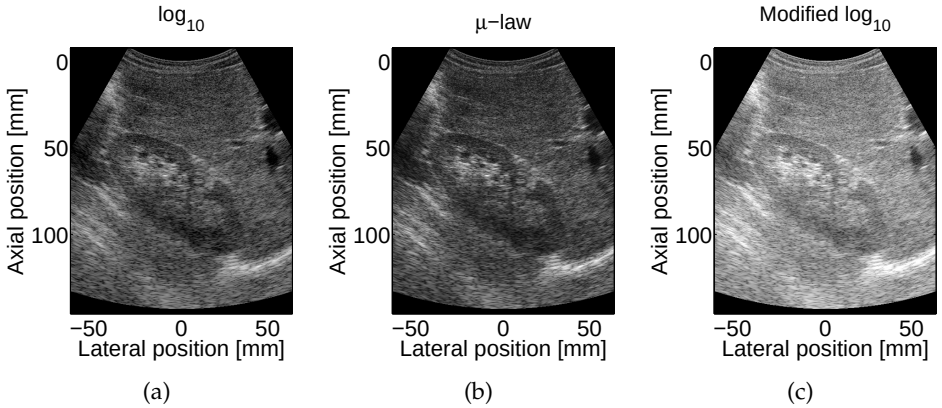

Figure 5.5: B-mode images using different types of compression. (a) Linear $\log_{10}$ compression using 60 dB dynamic range. (b) μ-law compression using 80 dB dynamic range. (c) Modified linear $\log_{10}$ compression using 60 dB dynamic range.

pings that discard the information in the highest envelope amplitudes, and attenuate the information at speckle level is best suited. From the mappings evaluated the μ-law compression scheme using a dynamic range of 80 dB is best and is used in the two clinical studies.

5.2.3 Data material

In both the pre-clinical and the clinical trial a data sequence of 3 seconds is obtained from each scan location. Due to the low frame rate and for an easier visual comparison of the two methods, the physician tried to hold the probe in the same view throughout the recording.

In the pre-clinical trial a data set comprising 32 image sequences were created from 2 volunteers. Fig. 5.6 presents the first frame from two of the image sequences. The full data set is presented in appendix B.

In the clinical trial a data set comprising 84 image sequences were created from 18 volunteers. During the data acquisition 6 image sequences were dropped due to patient specific issues.

Five different upper abdominal locations were scanned on each volunteer. The physician recorded two sequences of the right, middle and left hepatic veins and their entry in the inferior caval vein, one sequence of the liver alongside the right kidney, and one sequence of each kidney by itself. Fig. 5.7 illustrates the five scan locations and examples of B-mode images from each location using conventional imaging and SASB imaging. The full data set is presented in appendix C.

5.2.4 Data evaluation

In both the pre-clinical and the clinical trial, five medical doctors, all used to working with ultrasound, evaluated the image sequences. None of the ten doctors had knowledge about synthetic aperture imaging, and none had seen any of the recorded sequences before. Evaluation were done using the developed image quality assessment program (IQap) described in Chapter 2.

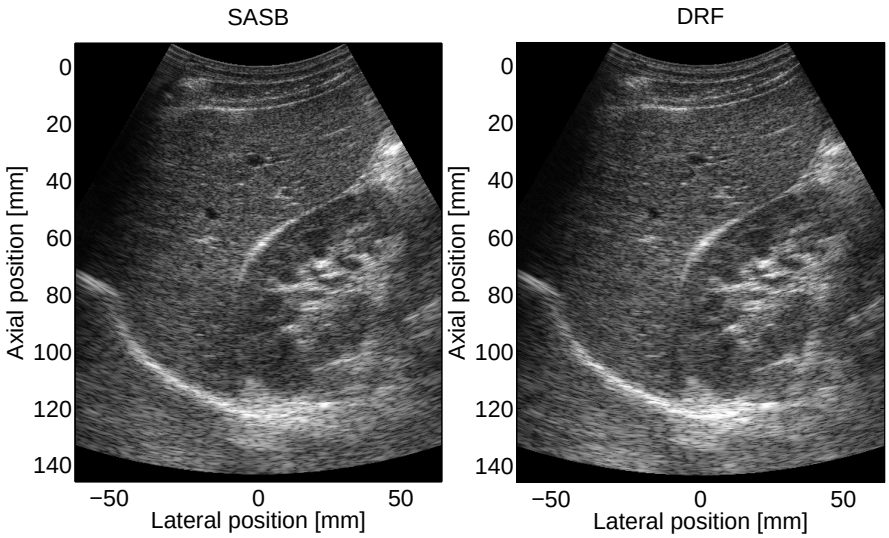

(a)

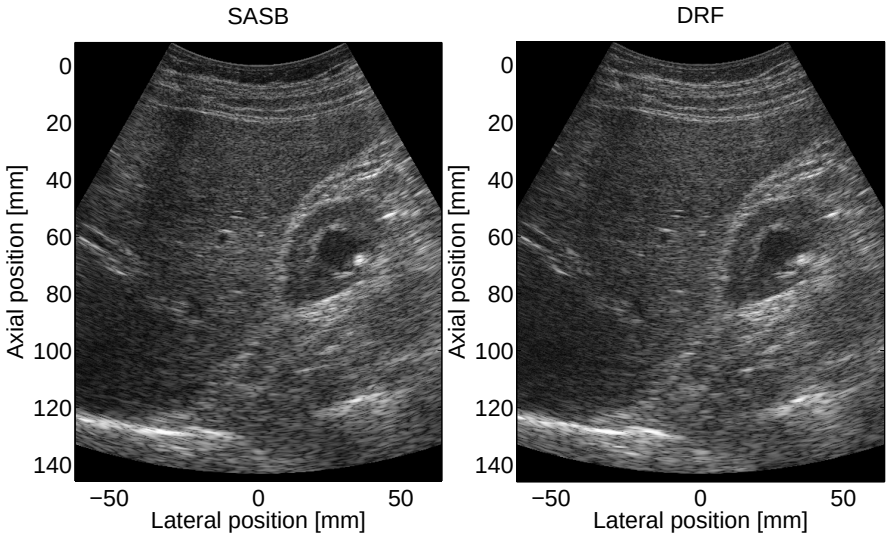

(b)

Figure 5.6: B-mode images created using SASB on the left and conventional imaging on the right. (a) Longitudinal section of right liver lobe, the kidney and diaphragm at the bottom, (b) Liver and top of right kidney. Figure taken from Paper V.

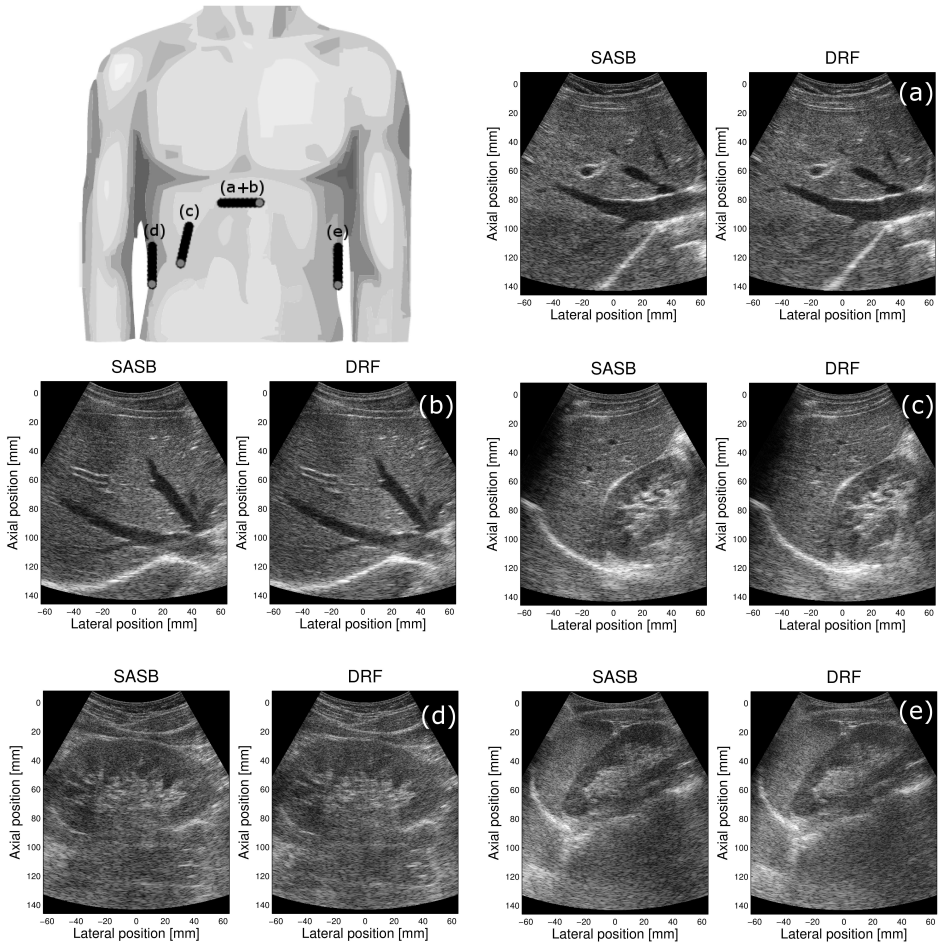

Figure 5.7: The images, next to the torso illustrating the scan locations, shows in (a) Transverse scanning of liver, (b) Transverse scanning of liver using different angulation of the transducer, (c) Longitudinal scanning of the right kidney with adjacent liver, (d) Longitudinal scanning of right kidney, and in (e) Longitudinal scanning of left kidney with adjacent spleen. Figure taken from Paper II.

5.2.5 Data analysis

The statistical data analysis of the VAS score and the penetration depth is performed using the statistical data analysis program R version 2.12.2 (http://www.r-project.org/), and a mixed effect linear model [42]. The mixed effect linear model is well suited for this type of data analysis because of the clustered and therefore dependent data. The data is clustered because a single image pair is evaluated by all evaluators, and further, the total data

set of image pairs are recorded from a smaller group of volunteers.

The mixed effect linear model is a statistical model that incorporate both fixed-effects parameters and random effects. The model describes a relationship between a response variable and some of the covariates that have been measured or observed along with the response. The response are thought to be the linear sum of the fixed and random effects, and can be expressed in matrix form as:

$$y = \mu + X\beta + Z\gamma + \epsilon, \tag{5.1}$$

where y is a vector of responses, μ is the intercept or average score for the entire data set. $X\beta$ models the fixed effects, and X is the fixed-effects design matrix, and β is a vector of fixed-effects parameters. $Z\gamma$ models the random effects, and Z is the design matrix of random effects and γ is the vector of random effect parameters. ϵ is a vector of residual errors.

The covariates that have been measured along with the response are divided into fixed effects and random effects. The covariate is a fixed effect if it affects the evaluators population mean, and is a random effect if it is associated with a sampling procedure (e.g., evaluator or image pair). Random effects contribute only to the covariance structure of the data, not the mean effect.

The only fixed parameter in the developed model is a descriptor of the displayed image order (left right placement of the SASB image). The random effect is modeled for each image pair and each doctor, thereby accounting for the dependence induced by repeatedly scoring the same image pair and collecting multiple scores from the same doctor.

Evaluating the model, the parameter of interest is the intercept, which captures the average score and will be negative if SASB is preferred to conventional imaging.

As a robustness check the analysis was repeated with a transformed score (the square root and negative square root of positive and negative scores, respectively). In addition Wilcoxon [43] tests were performed for each doctor and side (SASB on left or right) separately. Within these stratums the observations are independent and p-values for the hypothesis that the two methods are equally good (i.e. probability of a positive score equal the probability of a negative score) are therefore readily available.

The depth scores given to SASB and conventional imaging were initially subtracted from each other and the resulting differences were analyzed as described above.

5.3 Acoustic Output

This section documents that the configuration of the transmitted field using SASB and the conventional method is within the limits proposed by the United States Food and Drug Administration (FDA) [33]. This is done by measuring the 3-D pressure field from a single pulse in the center of the transducers scan plane and by calculating the corresponding intensity values and the mechanical index.

5.3.1 The measurement system

The acoustic outputs were measured in a water tank using a high precision 3-dimensional position system (AIMS III using Soniq Software) and a HGL0400 hydrophone (Onda, Sunnyvale, CA, USA) by following the guidelines given by the American Institute of Ultrasound in Medicine (AIUM) [44] and the International Electrotechnical Commission (IEC) [45].

It should be noted that the effective size of the hydrophone radius, a, apply to the current written standards from AIUM [44] and IEC [45]. The standards address the limits on the maximum effective hydrophone radius, a_{max}, and the IEC criterion is given by:

$$a_{max} = \frac{\lambda}{4}\left[\left(\frac{l}{2r}\right)^2 + 0.25\right], \tag{5.2}$$

where λ is the ultrasonic wavelength, $l/2r$ is the normalized distance of the hydrophone from the transducer, where l is the distance and r is the transducer radius [46]. The effective hydrophone radius, is given approximately by:

$$a = \left(a_g^2 + \frac{1}{4f_0^2}\right)^{1/2}, \tag{5.3}$$

where f_0 is the center frequency in MHz, a_g is the geometrical radius of the hydrophone. Another way of determining the required size of the hydrophone is to use a hydrophone with a diameter less than one third of the FWHM of the beam-profile [47]. In this case then the error in the measurement of the peak pressure should normally be less than 3%. In both methods the used hydrophone apply to the recommendations.

5.3.2 Data acquisition

Using the AIMS III system and the Soniq software a 3D scan sequence was defined to measure the acoustic output in a $8_x \times 8_y \times 90_z$ mm volume, with a resolution of 0.38 mm in x and y and 1 mm in z. For each of the scan positions the received waveform is averaged over two emissions, stored, and subsequently converted to pressure using:

$$p = V/M, \tag{5.4}$$

where p is the acoustic pressure, V is the measured voltage, and M is the system sensitivity (0.421 V/MPa at 5 MHz). A sampling frequency of 50 MHz is used by the AIMS III system, and a total of 1000 samples are acquired at each scan position.

5.3.3 Concept of in-situ or derated levels

The measured intensities need to satisfy upper limits regulated by the FDA [33], which have been introduced as safety guides to avoid damage to the tissue and pain to the patient. These limits concern the mechanical index, MI ≤ 1.9, the spatial-peak-pulse-average intensity, $\mathrm{I_{sppa}} \leq 240\ \mathrm{W/cm^2}$, the spatial-peak-temporal-average intensity $\mathrm{I_{spta}} \leq 1500\ \mathrm{mW/cm^2}$, and the spatial-peak-half-cycle-maximum intensity $\mathrm{I_m} \leq 600\ \mathrm{W/cm^2}$ [33] for diagnostic ultrasound imaging.

Acoustical output measurements of medical ultrasonic equipment are made with the field propagating in water. The measurements are made in water because of its availability and well-known characteristics. A factor is applied to acoustic output parameters intended to account for ultrasonic attenuation of tissue between the source and a particular location in the tissue. The average ultrasonic attenuation is assumed to be a 0.3 dB/cm/MHz along the beam axis in the body [44]. This coefficient accounts for the lose of energy from propagating the ultrasound beam either by conversion to other forms of energy or from reflection from small inhomogeneities in the medium. The effect on a plane wave of initial pressure amplitude $p(0)$ will, after traveling a distance z, have a pressure amplitude $p(z)$ given by:

$$p(z) = p(0) \exp\left(-\mu z\right), \tag{5.5}$$

where $p(z)$ is the pressure amplitude at a distance z from the initial position with a pressure amplitude of $p(0)$, and μ is the attenuation coefficient

expressed in units of Nepers per meter (Np/m). The difference between a Neper and dB is a fixed ratio, and is given as:

$$dB/Np = 20 * \frac{\log\left(\frac{a}{b}\right)}{\ln\left(\frac{a}{b}\right)} = \frac{20}{\ln(10)} = 8.68588 \tag{5.6}$$

Using an attenuation of 0.3dB/cm/MHz the attenuation coefficient for pressure is 0.0345 and the derated pressure, denoted with a subscript .3, is expressed as:

$$p(t)_{.3} = p(t)\exp(-0.0345t), \tag{5.7}$$

where t is time. The derated instantaneous intensity is expressed as:

$$I(t)_{.3} = I(t)\exp(-0.069t). \tag{5.8}$$

Pulse Intensity Integral

The propagating acoustic wave carries energy, and the amount of energy per unit area is called the pulse intensity integral,(PII). PII is the basis for the calculation of the intensity output profiles, and is given as the integral of the instantaneous intensity over the time interval, T, where the received pulse at the hydrophone is nonzero [44]. The instantaneous intensity, I, is found from:

$$I(t) = \frac{p(t)^2}{\rho c}, \tag{5.9}$$

where $p(t)$ is the time domain ultrasonic pressure waveform, ρ is the density of the propagating medium (997.0479 kg/m^3), and c is the speed of sound (1499 m/s). The unit for the intensity is watts per square meter (W/m^2). The PII is given as:

$$PII = \int_0^T I(t)dt \tag{5.10}$$

The units for the PII are joules per square meter (J/m^2), but it is more common in biomedical ultrasound to use centimeters (J/cm^2).

Fig. 5.8 illustrates the PII for the SASB and DRF configuration. The peak PII is determined for each 2D scan (x,y) and plotted as a function of the distance from the transducer.

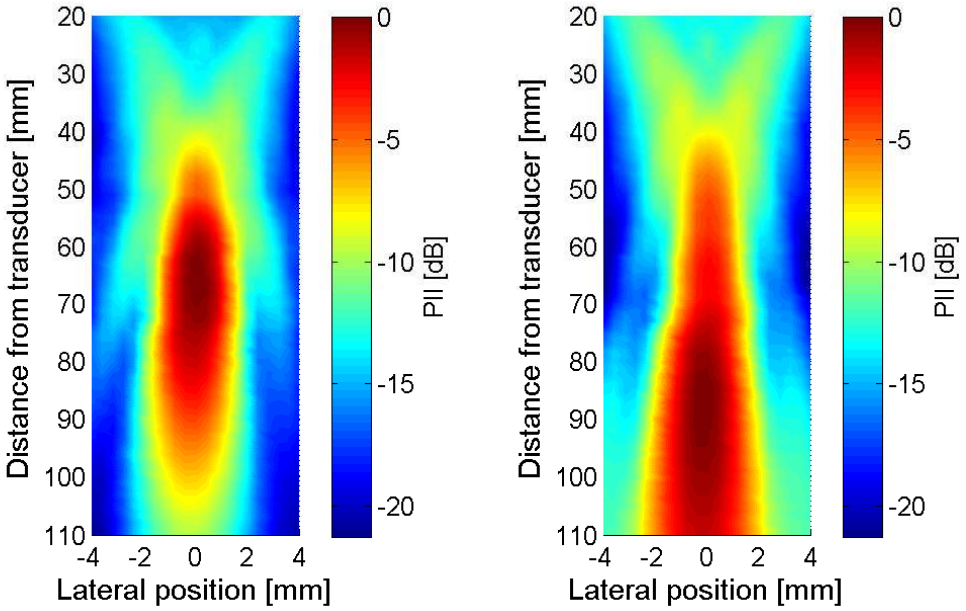

Figure 5.8: Measured pulse intensity integral as function of distance from the transducer and lateral position. (a) for the SASB configuration and (b) for the DRF configuration. The shown PII have been normalized to the peak PII for each configuration.

Peak pressure

Each pressure waveform collected during the measurement process has a peak positive pressure, or compressional pressure P_c, and a peak negative pressure, or rarefractional pressure P_r, associated with it. The unit for the peak pressures are mega pascal (MPa). Typical acoustical power outputs for diagnostic B-mode scans generate a peak compressional pressure of 2-5 MPa, and a peak rarefractional pressure of 1-3 MPa [47, 48]. Fig. 5.9 illustrates the measured peak pressures for the configuration of SASB and DRF. The peak pressures are determined for each 2D scan (x,y) and plotted as a function of the distance from the transducer.

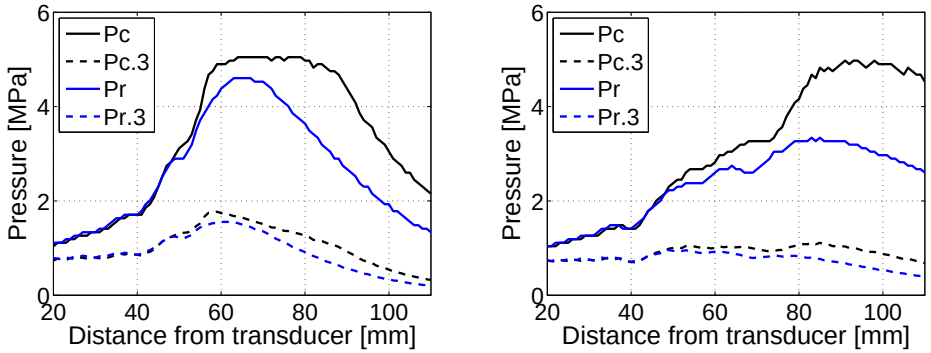

Figure 5.9: Measured peak compressional and rarefractional pressure as function of distance from the transducer. (a) for the SASB configuration and (b) for the DRF configuration. The profiles are shown for both the water measurement and derated using an attenuation coefficient of 0.3dB/cm/MHz.

Pulse duration

The pulse duration, t_d is equal to 1.25 times the interval between the time when the time integral of the instantaneous acoustic pressure squared reaches 10% and 90% of its final value. The final value being the pulse pressure squared integral, p_i. Once p_i has been determined, t_d can be calculated from:

$$t_d = 1.25(t_2 - t_1), \tag{5.11}$$

where t_1 and t_2 are given by:

$$\int_0^{t_1} p(t)^2 dt = 0.1 p_i \qquad \int_0^{t_2} p(t)^2 dt = 0.9 p_i \tag{5.12}$$

A typical t_d for a diagnostic B-mode scan is 0.2-1 μsec [47]. Fig. 5.10 illustrates the pulse duration for the SASB and DRF configuration. The peak pulse duration is determined for each 2D scan (x,y) and plotted as a function of the distance from the transducer.

Intensity pulse average

The pulse average of the instantaneous intensity, I_{pa}, is found by taking the average over one pulse duration, and can be directly derived from the PII

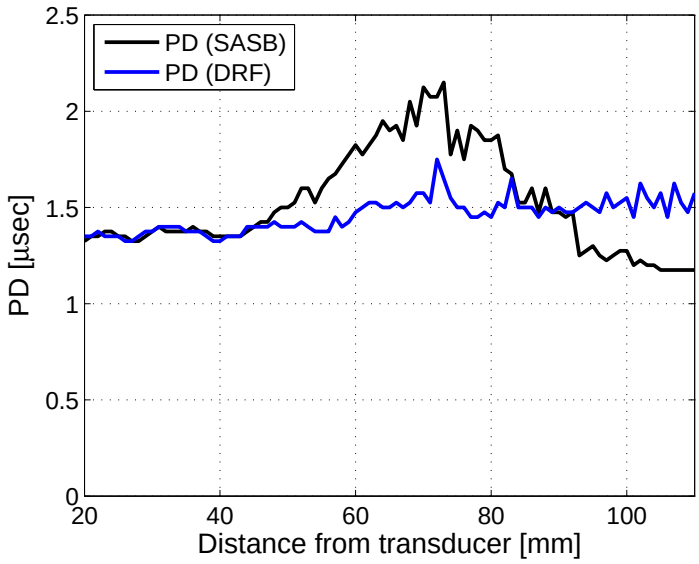

Figure 5.10: Measured pulse duration as function of distance from the transducer. The pulse duration is shown for the configuration of SASB and DRF.

and t_d by.

$$Ipa = \frac{PII}{t_d}. \tag{5.13}$$

The units for the I_{pa} are watts per square centimeter (W/m^2), but again it is more common to use centimeters (W/cm^2).

A typical I_{sppa} for a diagnostic B-mode scan is 50-200 W/cm^2 [47, 48]. Fig. 5.11 illustrates the measured I_{pa} for the SASB and DRF configuration. The spatial peak intensity, I_{sppa}, is determined for each 2D scan (x,y) and plotted as a function of the distance from the transducer.

Intensity temporal average

The time average of the instantaneous intensity, I_{ta}, is found by taking the average over one acoustic repetition period and is given as:

$$I_{ta} = PII * fprf \tag{5.14}$$

where $fprf$ is the rate of identical acoustic pulses per second. The units for the I_{ta} are watts per square meter (W/m^2), but it is more common to use centimeters and milliwatts (mW/cm^2).

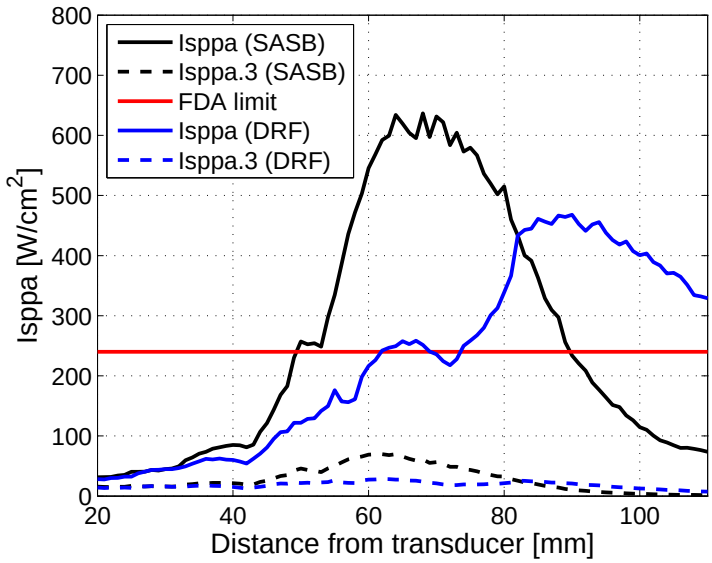

Figure 5.11: Measured spatial peak pulse average intensity as function of distance from the transducer. The intensity is shown for the configuration of SASB and DRF. The profiles are shown for both the water measurement and derated using an attenuation coefficient of 0.3dB/cm/MHz.

The regulatory limit set by the FDA is an I_{spta} of 1500 mW/cm^2 [33]. A typical I_{spta} for a diagnostic B-mode scan is 1-30 $\mathrm{mW/cm^2}$ [47, 48]. Fig. 5.12 illustrates the measured I_{ta} for the SASB and DRF configuration. The spatial peak intensity, I_{spta}, is determined for each 2D scan (x,y) and plotted as a function of the distance from the transducer.

Eqn. 5.14 does not take the possible contribution from other scan lines into account. This can be important because the beams from adjacent scan lines might overlap each other. The determination of the temporal average intensity considering overlapping beams can be determined from:

$$I_{ta} = \sum_{n=1}^{N} I_{ta}(n), \tag{5.15}$$

where $I_{ta}(n)$ is the temporal average intensity for the nth contributing scan line and N is the total number of contributing scan lines at a given spatial location [47]. This number has not been evaluated because the measured I_{ta} from a single beam is well below the FDA limit, and even an overlap factor of 384, will be below the FDA limit.

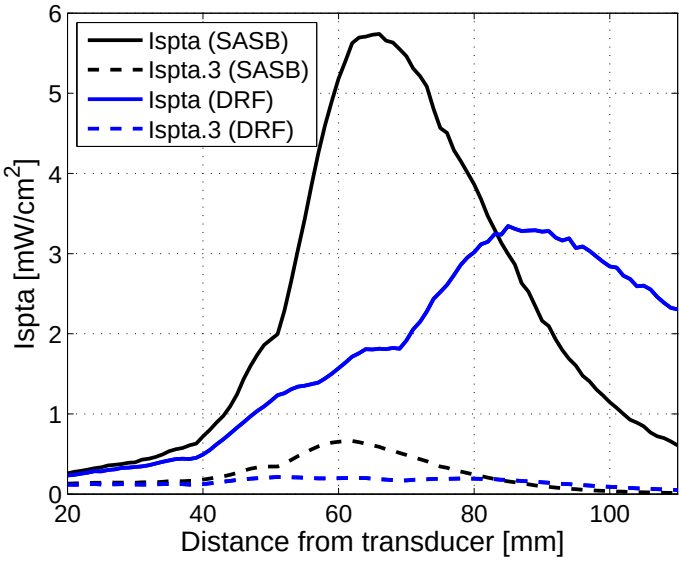

Figure 5.12: Measured spatial peak temporal average intensity as function of distance from the transducer. The intensity is shown for the configuration of SASB and DRF. The profiles are shown for both the water measurement and derated using an attenuation coefficient of 0.3dB/cm/MHz.

Intensity half-cycle maximum

Average intensity over the pulse half-cycle having the greatest temporal-peak intensity, and is determined by:

$$I_m = \frac{t_d}{2} \int_{t_1}^{t_1+t_d/2} I(t)dt, \tag{5.16}$$

where t_1 is the time where the integration over half the time period t_d is the maximum. The regulatory limit set by the FDA is an I_m of 600 W/cm^2 [33]. Fig. 5.13 illustrates the measured I_m for the SASB and DRF configuration. The spatial peak intensity, I_m, is determined for each 2D scan (x,y) and plotted as a function of the distance from the transducer.

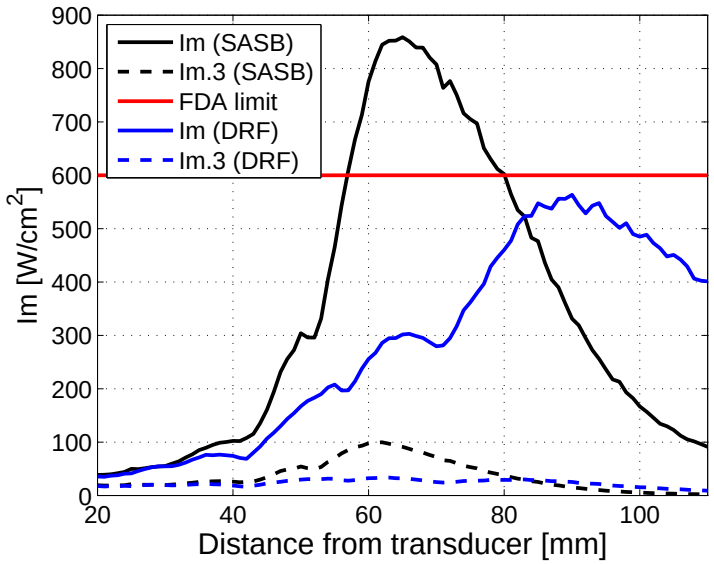

Figure 5.13: Measured maximum intensity over one half pulse cycle as function of distance from the transducer. The intensity is shown for the configuration of SASB and DRF. The profiles are shown for both the water measurement and derated using an attenuation coefficient of 0.3dB/cm/MHz.

Mechanical Index

The mechanical index (MI) is a value that estimates the likelihood of cavitation by the ultrasound beam. The MI is directly proportional to the peak rarefactional (negative) pressure, and inversely proportional to the square root of the ultrasound frequency. The definition of MI used by the FDA is given as:

$$MI = \frac{P_r}{\sqrt{f_0}} \tag{5.17}$$

evaluated at the position of peak pulse intensity integral, PII. P_r is the peak rarefaction pressure in MPa, and f_0 is the center frequency (acoustic working frequency) in MHz. The regulatory limit set by the FDA is an MI of 1.9 [33]. Fig. 5.14 illustrates the measured MI for the SASB and DRF configuration. The spatial peak mechanical index, MI, is determined for each 2D scan (x,y) and plotted as a function of the distance from the transducer.

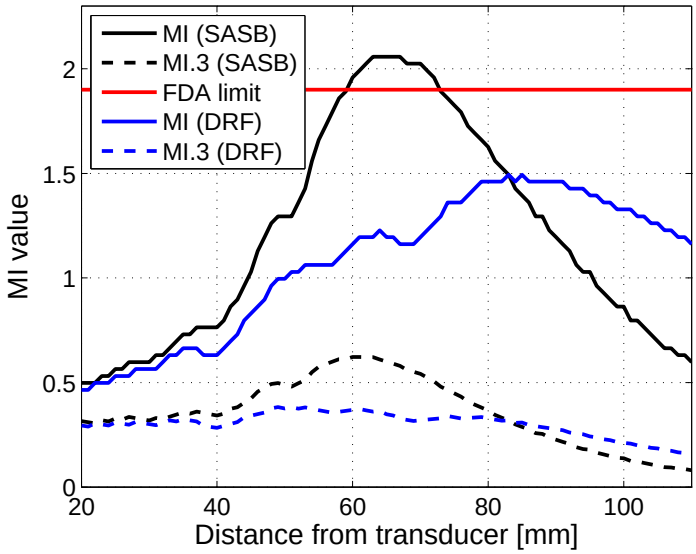

Figure 5.14: Measured mechanical index for the configuration of SASB and DRF. The MI is shown for both the water measurement and derated using an attenuation coefficient of 0.3dB/cm/MHz.

5.3.4 Results from the acoustic output measurements

The intensity and mechanical index was obtained for both imaging methods, and are listed in Table 5.2. These values are considerably lower than the FDA limits, and *in-vivo* scanning is therefore safe using the present imaging configurations.

Table 5.2: Measured intensities and mechanical index for the configuration of SASB and conventional imaging.

Parameter	FDA limit	Value in Water		Value in-situ	
		(SASB)	(DRF)	(SASB)	(DRF)
I_{spta} [mW/cm^2]	< 1500	5.74	3.34	0.66	0.21
I_{sppa} [W/cm^2]	< 240	636.70	467.77	69.74	28.49
I_m [W/cm^2]	< 600	858.63	563.33	99.48	33.65
MI	< 1.9	1.73	2.38	0.80	0.51

5.4 Data evaluation results

5.4.1 Pre-clinical trial

From the 320 ($32_{image\ pairs} \times 5_{evaluators} \times 2_{presentations}$) image quality ratings, 75 (24%) favored conventional imaging, 197 (61%) favored SASB and 48 (15%) were rated equally good. The distribution of ratings from the individual doctors are shown in Fig. 5.15.

The statistical analysis showed that the average VAS score is significantly negative (p-value: 0.0005) and estimated to be -2.9 (95% CI: -4.54; -1.26). The analysis of the transformed score yields qualitatively the same result and the 10 Wilcoxon tests performed in each stratum defined by doctor id and side, 7 found a significant difference in favor of SASB and none in favor of the conventional method. Thus, the data clearly show that SASB is preferred compared to conventional imaging. Table 5.3 documents the results from the Wilcoxon tests.

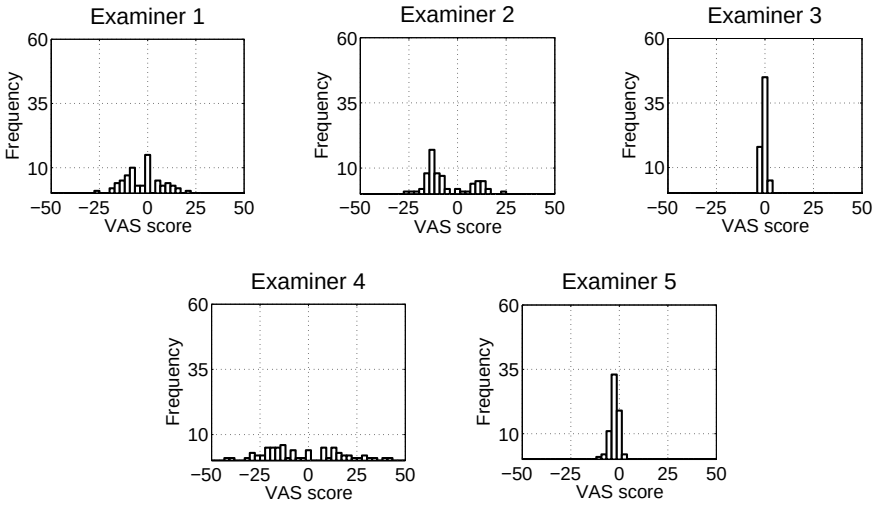

Figure 5.15: Distribution of pooled answers from assessment of overall image quality in the pre-clinical trial. Negative values favor SASB. Figure taken from Paper V.

The differences in penetration depths between the two techniques are shown in Fig. 5.16. The analysis of the depth scores showed that the average difference is insignificant (p-value: 0.98).

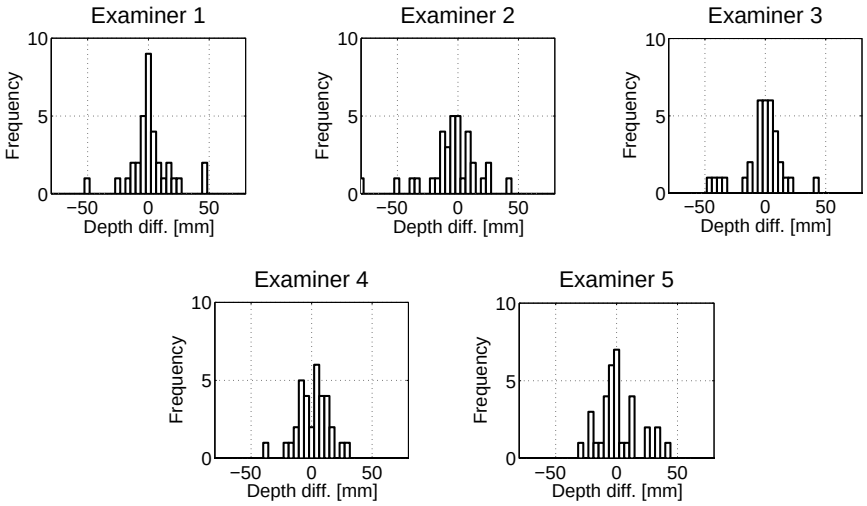

Figure 5.16: Distribution of pooled answers from assessment of penetration in the pre-clinical trial. Negative values favor SASB. Figure taken from Paper V.

Table 5.3: Results from the pre-clinical evaluation

Evaluator	VAS: p-value: SASB left DRF right	VAS: p-value: DRF left SASB right	Depth: p-value
1	0.39981	0.02525	0.63824
2	0.04056	< 0.01	0.30097
3	0.03308	< 0.01	0.85752
4	0.18103	0.47144	0.54958
5	< 0.01	< 0.01	0.97539

5.4.2 Clinical trial

From the 840 ($84_{image\ pairs} \times 5_{evaluators} \times 2_{presentations}$) image quality ratings, 117 (14%) favored conventional imaging, 614 (73%) favored SASB and 109 (13%) image pairs were rated equally good. The distribution of ratings from the individual doctors are shown in Fig. 5.17.

The statistical analysis showed that the average VAS score is significantly negative (p-value: 0.0005) and estimated to be -3.5 (95% CI: -5.5; -1.5). The analysis of the transformed score yields qualitatively the same result and the 10 Wilcoxon tests performed in each stratum defined by doctor id and side are all significant (p-values ranging from 10^{-14} to 0.025). Thus, the data clearly show that SASB is preferred compared to conventional imaging. However, there is a substantial variance on the individual scores. Table 5.4 documents

the results from the Wilcoxon tests.

The linear mixed effect model predicts that for a new image pair, rated by a new doctor, there is 70% probability that the doctor will prefer the SASB image and 30% probability of prefering the conventional image.

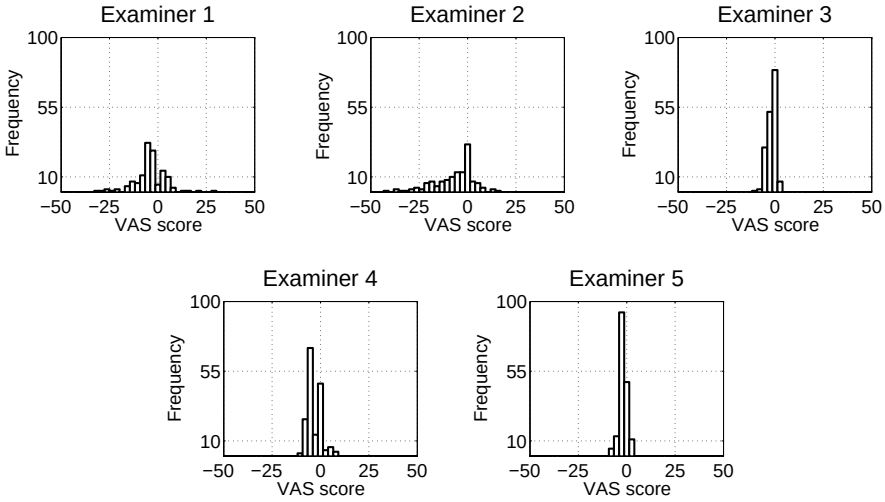

Figure 5.17: Distribution of pooled answers from assessment of overall image quality in the clinical trial. Negative values favor SASB. Figure taken from Paper II.

The differences in penetration depths between the two techniques are shown in Fig. 5.18. The analysis of the depth scores showed that the average difference is insignificant (p-value: 0.55) and estimated to be 0.37 mm (95% CI: -0.83; 1.6 mm).

Table 5.4: Results from the clinical evaluation

Evaluator	VAS: p-value: SASB left DRF right	VAS: p-value: DRF left SASB right	Depth: p-value
1	0.02558	< 0.01	0.82925
2	< 0.01	< 0.01	0.80715
3	< 0.01	< 0.01	0.51618
4	< 0.01	< 0.01	0.03481
5	< 0.01	< 0.01	0.69093

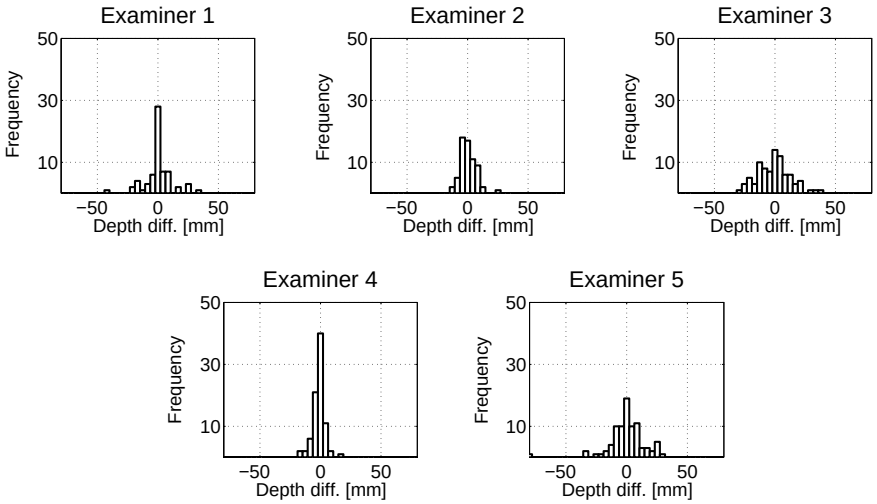

Figure 5.18: Distribution of pooled answers from assessment of penetration in the clinical trial. Negative values favor SASB. Figure taken from Paper II.

5.5 Discussion and conclusion

The three phased setup for clinical studies presented in Paper III, proved to be good methodology for the evaluation of clinical efficacy. The methodology has ensured that the obtained results are valid and reliable, as the investigator was separated from the evaluation procedure. Furthermore, were the physician that recorded the images not included in the evaluation procedure.

The image quality methodology and software presented in Paper III, proved to be well suitable for the evaluation of the clinical efficacy. The methodology ensures that the evaluator is blinded from the method labels and that the data is evaluated without bias from left/right placement of the images. An important aspect of the evaluation is that it is performed on image sequences and not on still images. The evaluation of live image sequences ensures that the evaluation is as close as possible to the clinical setup.

The VAS scale is inherently interpreted differently by the evaluators, and the evaluators inherently have different image quality preferences. The interpretation of the VAS scale can be sought normalized by performing an introduction to the data material. In this study five image sequence pairs were shown prior to the evaluation. This number could have been increased for improved normality.

In the evaluation of the pre-clinical trial the evaluators used 24 seconds in

average on each of the VAS scores and 5 seconds in average on each of the depth scores. In the clinical trial the evaluators used 17 seconds in average on the VAS scores and 5 seconds in average on the depth scores. This means that for an average evaluator the time needed to evaluate a sufficient data set is one hour. This amount of time, is small enough to conduct these clinical studies for new configurations, and new processing methods.

The results from the two clinical trials, showed that the image quality using SASB imaging is statistically significant improved compared to conventional imaging. Furthermore, the result from the penetration study showed that SASB imaging can produce images with satisfying penetration.

The images were produced with an acoustic output profile that is within the current limits set by the FDA. The acoustic output of the SASB configuration is higher than the one used for the conventional setup. This opens for the question if the comparison is performed fair? The answer to the question is simple. Given the ProFocus system where the configurations are optimized for, the comparison is performed fair and the results show the best possible outcome for both modalities.

CHAPTER

SIX

Simulation of acoustic fields

Ultrasound imaging is an active field of research and each year new imaging schemes are proposed. The performance of these new methods is often documented in an idealized framework, ignoring the complications of real and non-ideal transducers. The work by Mårtensson [49] showed that transducers are deteriorating over time, and it is therefore relevant to investigate how imaging methods perform in non-idealized systems. Furthermore with the increasing system complexity and image quality, the requirements for an accurate and realistic prediction of the acoustic field is increasing.

Simulation of acoustic fields using linear acoustics is extensively used, and is a standard tool in ultrasound research and development. In ultrasound imaging, a pulse is emitted into the body and is scattered and reflected by density and propagation velocity perturbations. The received field can be found by solving an appropriate wave equation. Gore and Leeman [50] considered a wave equation where the scattering term was a function of the adiabatic compressibility and the density. Jensen [51] used an equivalent wave equation as the one used by Gore and Leeman [50], but changed the scattering term for the wave equation to a function of density and propagation velocity perturbations. The derived model has no restrictions enforced on the transducer geometry or its excitation and its implementation, Field II, has become a widely used tool for simulations in ultrasound research and development.

This chapter will in combination with Paper IV and VII investigate if a detailed and realistic prediction of the acoustic field of a high quality imaging system, can be obtained by combining experimental determination of the individual element pulse echo wavelets and numerical modeling using Field II. The investigation is performed as a series of simulations and measurements using a BK8804 192-element linear array transducer.

6.1 The Field II simulation model

This section gives a short introduction to the theory behind the simulation software Field II and is a composition of Paper VII and [51].

Field II is a linear acoustics simulation software that can be used to calculate the received signal from a collection of point scatterers using:

$$V_r(t) = V_{pe}(t) \underset{t}{\star} f_m(\vec{r}_1) \underset{r}{\star} h_{pe}(\vec{r}_1, t), \tag{6.1}$$

where $\underset{r}{\star}$ denotes spatial convolution, $\underset{t}{\star}$ temporal convolution, and $\vec{r}_1$ the position of the point scatterer. $V_{pe}(t)$ is the transducer element pulse-echo wavelet, which includes both the transducer excitation and the electro-mechanical impulse response during emission and reception of the pulse. $f_m(t)$ accounts for the inhomogeneities in the tissue due to density and speed of sound perturbations that generates the scattering, and $h_{pe}(\vec{r}_1, t)$ is the pulse-echo spatial impulse response that relates the transducer geometry to the spatial extent of the scattered field. Explicitly written out the latter term is:

$$h_{pe}(\vec{r}_1, t) = h_t(\vec{r}_1, t) \underset{t}{\star} h_r(\vec{r}_1, t), \tag{6.2}$$

where $h_t(\vec{r}_1, t)$ is the spatial impulse response for the transmitting aperture and $h_r(\vec{r}_1, t)$ is the spatial impulse response for the receiving aperture. Both impulse responses are a superposition of the spatial impulse responses from the individual elements of a multi-element aperture properly delayed and apodized. Each impulse response is:

$$h(\vec{r}, t) = \sum_{i=1}^{N_e} a_i(t) h_i(\vec{r}_1, t - \Delta_i(t)), \tag{6.3}$$

where $a_i(t)$ denotes the apodization and $\Delta_i(t)$ focusing delay, which both are a function of position in space and thereby time. N_e is the number of transducer elements. The received signal from each scatterer must be calculated for each new focusing scheme corresponding to the different lines in an image. The resulting *rf* signal is then found by summing the responses from the individual scatterers using (6.1).

The model expressed in (6.1) can be extended with individual element pulse-echo wavelets by rearranging (6.1), (6.2), and (6.3) such that the time convolution between the element pulse-echo wavelet, the receive spatial impulse response, and the transmit spatial impulse response is convolved individu-

ally per element as:

$$V_r(t) = f_m(\vec{r}_1) \underset{r}{\star} \sum_{i=1}^{N_e} V_{pe,i}(t) \underset{t}{\star} h_{pe,i}(\vec{r}_1, t), \tag{6.4}$$

where $V_{pe,i}(t)$ is the element pulse-echo wavelet for the i'th element, and $h_{pe,i}(\vec{r}_1, t)$ is the element pulse-echo spatial impulse response and can be calculated using (6.2) and (6.3) on individual element basis.

6.2 Determination of the pulse-echo wavelets

To perform the calculations in (6.1) and (6.4), V_{pe} must be determined, as h ca be calculated from the physical dimensions of the transducer. V_{pe} can either be constructed from knowledge of the electromechanical properties of the transducer [52] or it can be measured. Here the second approach is chosen, and the measurements are performed using the data acquisition system presented in chapter 3.

The measurement setup described in [53] measures the element pulse echo by mounting the transducer in a water tank on a device permitting independent angular adjustment in two orthogonal planes and translation in the third plane. The target is a stainless steel plate, which dimensions are much larger than the transducer beam being measured. This is to avoid multiple reflections from the back surface and sides. The plane reflector is placed at the elevation focal point of the transducer and parallel to the acoustic surface of the transducer. This ensures that the equiphase surfaces of the return pulse match the curvature of the generating element and the spatial impulse response is a Dirac impulse. The transducer is then adjusted in angle until the echo amplitude is simultaneously peaked in both orthogonal planes. The author of [53] notes that a source of error of the method is a misaligned transducer.

The parallel alignment of the transducer and the reflector can be difficult to obtain, especially because it is unknown if the transducer elements are perfectly aligned or there exist some round trip time-of-flight phase error. In the following the round trip time-of-flight phase error is referred to as the phase error. To help the alignment, it is proposed to estimate a phase error profile using a point source. The transducer can then be aligned to the plane reflector, such that the phase error profile using the plane reflector match the profile estimated using the point source. The benefit of using a point source for the estimation of the phase error profile, is because it is angle independent.

It has earlier been proposed to use cross correlation measurements on signals emanating from a point source to determine phase errors for different types of sampled aperture, coherent imaging systems [54, 55]. Here the method is adapted for estimation of the phase error. The method is based on a metal wire submerged in a water tank, and a sliding single element sub-aperture with the same element transmitting and receiving.

The method can be described as: When the transmitted wave impinges on the wire, a spherical wave is expected to emanate since the wire thickness is small with respect to the wavelength. This means that the field is uniform on the plane where it is sampled and as a consequence all the array elements receive the same signal except for a delay. This delay is a function of the position of the wire and must be compensated for to determine the phase errors using cross-correlation.

A simple way to compensate for the delay is to beamform the individual received signals with transmit reference position at the transmitting and receiving element, and receive reference position at the wire projected onto the aperture. The received signals before and after compensation, are respectively shown in Fig. 6.1(a) and 6.1(b) for a wire positioned at a depth of 80 mm. The figure uses a display format introduced by Flax and O'Donnell [55], where the rf signals are displayed as they are received by the array elements. Negative signal values are in black, while positive signal values are in white. The time axis is scaled to only show the relevant part of the received signals.

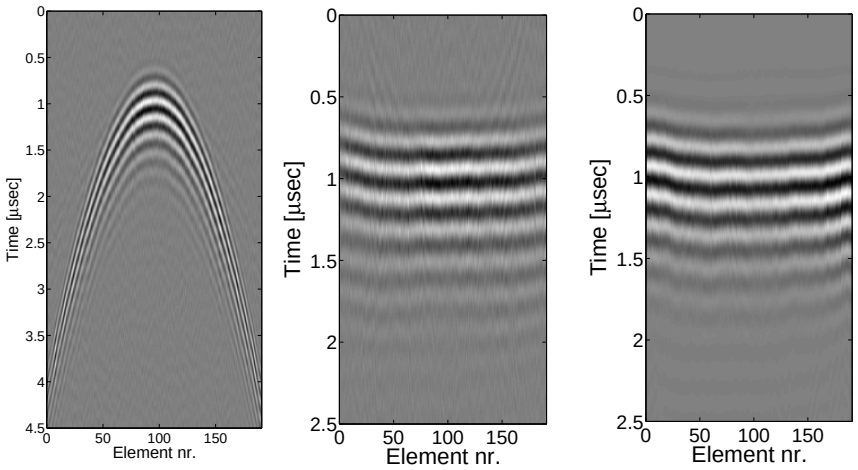

Figure 6.1: Measured pulse echo response using (a) wire target, (b) wire target compensated for phase error, and (c) a plate reflector. Figure taken from Paper VII.

The round trip phase profile is found by upsampling the individual element pulse echo wavelets from Fig. 6.1(c) to 800 MHz for subsample accuracy and then calculating the cross-correlation between the wavelets of the individual elements and the center element. The phase profile is then found from the lags that gives the highest correlations.

Using the estimated phase profile the transducer can now be positioned such that the plate reflector is placed at the elevation focal point of the transducer and the phase phase profile match the one estimated from the wire target. Fig. 6.2 shows the estimated phase phase profile using the wire target and the plate reflector. From the figure, notice the very good agreement between the two estimates of the phase profile. Calculating the maximum phase error based on the profile from the wire target, the error is 0.0813 μsec or 0.61 λ, found between element 2 and 60. In the following two sections, it will be shown that the phase error is significantly influencing the image quality, and investigations will be performed to try and compensate for the error.

Fig. 6.1(c) shows the measured element pulse echo wavelets using the plate reflector and the same transducer position as used in Fig. 6.2. The center wavelet will be used in the reminder of this chapter as the pulse echo, V_{pe}, from (6.1), and the entire set of wavelets will be used as the individual element pulse echo, $V_{pe,i}$, from (6.4) and will be referred to as Model 2.

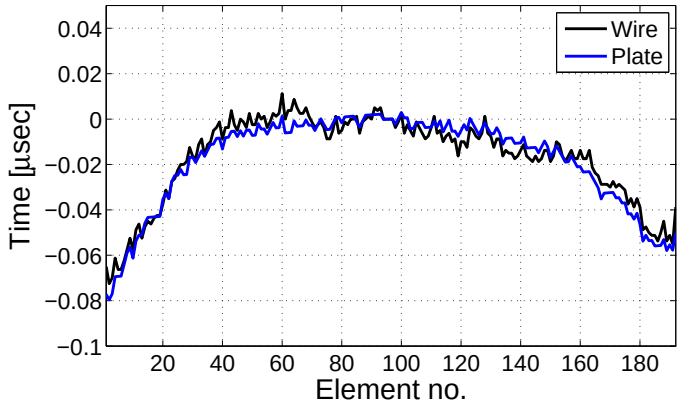

Figure 6.2: Measured phase profile using the wire target and the plate reflector. Figure taken from Paper VII.

The measurement of the element pulse echo wavelets also enables the estimation of the two-way sensitivity profile, which can be found by calculating

the energy, E, of the individual wavelets as

$$E_i = \sum_{n=1}^{N} V_i(n)^2 \tag{6.5}$$

where i is the i'th element and $V(n)$ is the pulse echo wavelet at sample n. N is the number of samples in the wavelet. Fig. 6.3 shows the sensitivity profile. The maximum sensitivity deviation is 1.9 dB between channel 42 and 86.

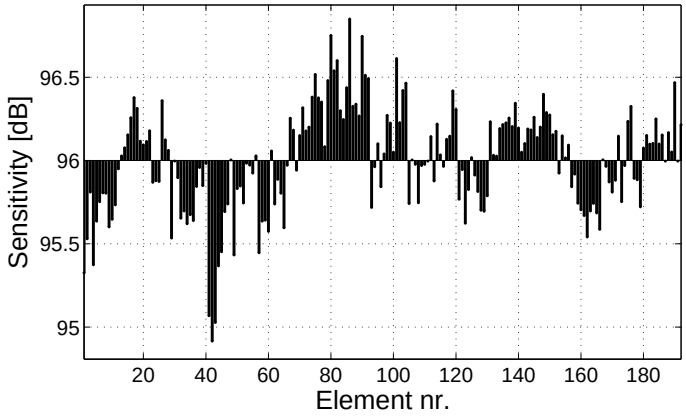

Figure 6.3: Measured two-way element sensitivity profile. Figure taken from Paper VII.

6.3 Wave propagation experiment

This section investigates the accuracy of the predicted SASB beamformed received pressure field, from three point scatterers embedded in a homogeneous medium, with a measurement of three thin metal wires in a water tank. The measurement describes how a point is imaged by the system, by scanning the wire orthogonal to the image plane. The metal wires have a diameter of 0.07 mm and are fixated at three depths, 29.8 mm, 54.7 mm, and 79.4 mm. Specification of the measurement and simulation parameters can be found in Table 6.1.

In the following, each measured first stage scan line is the average of 15 measurements to reduce measurement noise. The simulations are based on the solutions from (6.1) referred to as Model 1, and (6.4) referred to as Model 2. In Model 1 the measured center element pulse echo wavelet is used as V_{pe}, and in Model 2 the entire set of wavelets will be used as the individual element pulse echo, $V_{pe,i}$.

Table 6.1: Measurement parameters

Transducer Parameters (BK8804)	
Pitch (mm)	0.208
Elevation focus (mm)	20
Number of elements (mm)	192
Imaging parameters	
Focus Tx / Rx (mm)	10 / 10
F# Tx / Rx	2 / 2
Apodization Tx / Rx	Boxcar / Gauss
Scanner setting	
Waveform	7.5 MHz 2 cycle sinusoid
No. of emissions / scan lines	190 / 190

The simulated center responses are compared to the measured response and are visualized in Fig. 6.4(a) to 6.4(c). Note how well both models accurately predicts the measured response. The accuracy is quantitatively determined using the relative sum-of-squared error defined in (6.6) for I equal to the center scan line. The error for the two models are shown in Table 6.2.

Fig. 6.4(d) to Fig. 6.4(l) shows contour plots of the logarithm compressed envelope detected responses for all scan lines. Comparing the contour plots for the measured responses and the simulated responses, one sees that the main differences between the contours is the width of the point spread functions.

Including the individual element pulse echo wavelets into the simulation model, improves the accuracy and gives a more reliable realization of the pressure. There are however still differences between the simulated response and the measured response and this might be due to the finite size of the wire, and inaccurate prediction of the true transducer characteristic or effective geometry. These deviations are, however, small compared to the overall capability of the model to predict the actual response and improved capabilities to estimate the performance of SASB imaging. The models are compared quantitatively to the measured data by calculating the relative sum of squared error as:

$$E = \frac{\sum_{n=1}^{N} \sum_{i}^{I} (V_s(n,i) - V_m(n,i))^2}{\sum_{n=1}^{N} \sum_{i}^{I} V_m(n,i)^2} * 100 \tag{6.6}$$

where $V_s(n,i)$ and $V_m(n,i)$ is the simulated and measured received response at sample n for scan line i. The error for the two models are shown in Table 6.2.

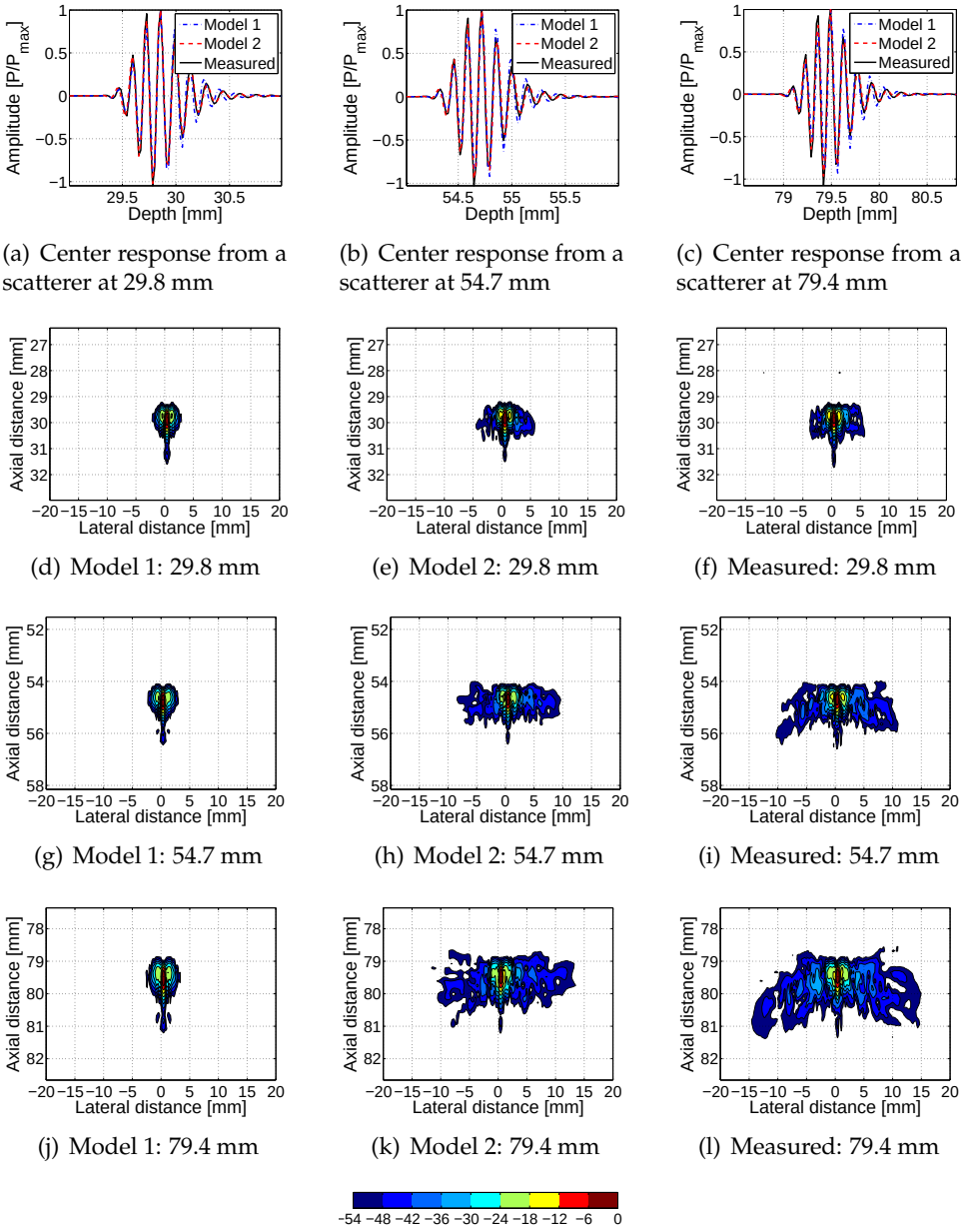

(a) Center response from a scatterer at 29.8 mm

(b) Center response from a scatterer at 54.7 mm

(c) Center response from a scatterer at 79.4 mm

(d) Model 1: 29.8 mm

(e) Model 2: 29.8 mm

(f) Measured: 29.8 mm

(g) Model 1: 54.7 mm

(h) Model 2: 54.7 mm

(i) Measured: 54.7 mm

(j) Model 1: 79.4 mm

(k) Model 2: 79.4 mm

(l) Measured: 79.4 mm

Figure 6.4: Fig. (a) to (c) illustrates the measured and simulated second stage SASB responses from the center scan line from three scatterers at (a) 29.8 mm, (b) 54.7 mm, and (c) 79.4 mm from the transducer surface. Fig. (d) to (l) illustrates contour plots with 6 dB contour coloring for the three scatters using Model 1 in (d,g,j), Model 2 in (e,h,k), and measured response in (f,i,l). Figure taken from Paper VII.

Table 6.2: Simulation accuracy

		Scatter depth:		
Center scan line	Unit	29.8 mm	54.7 mm	79.4 mm
$E_{Model\ 1}$	%	6.7	8.6	14.3
$E_{Model\ 2}$	%	1.7	3.7	3.4
All scan lines				
$E_{Model\ 1}$	%	8.5	10.5	15.6
$E_{Model\ 2}$	%	4.1	6.5	11.6

To investigate the level of agreement between the measured and simulated responses, the covered area of the point spread function at different amplitude levels can by considered, as shown in Fig. 6.5. Note how the covered area is approximately the same for Model 1, Model 2, and the measured data until -35 dB. From -35 dB, Model 1 fails to predict the received response, and Model 2 is able to predict the covered area with a small underestimation. This shows that by including individual element pulse echo wavelets into the simulation model, the model is able to predict not only the energy in the main-lobe, but also in a the side-lobe.

Paper IV investigates the influence on image quality using real and non-ideal transducers characteristics in a comparative simulation study between SASB and conventional DRF imaging. The study shows that SASB imaging is more sensitive to delay errors, and as such including individual element pulse echo into the models of future high quality imaging systems will improve the reliability of the modeling.

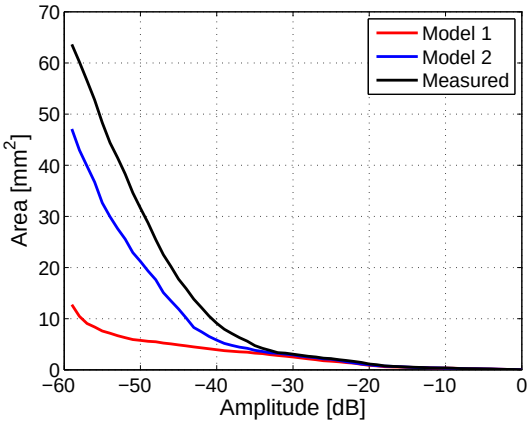

Figure 6.5: Area covered by the point spread function from the scatter at 79.4 mm.

6.4 Beamforming optimization

The measured phase error is on the order of what can be expected from phase fluctuations in arrival time due to the presence of a fat human abdominal wall [56]. Several studies report significant image quality degradation from phase aberration [57, 58], and several techniques are developed for compensation [55, 59–61]. The main difference between the fluctuations in arrival time due to the human tissue and the measured phase error due to the transducer characteristics is that the human tissue results in a non-structural error. The measured phase error is structural and can be compensated for by modification of the receive and transmit delay profiles.

Ideally, the estimated phase and amplitude profile should be applied in both transmit and receive, as the phase error affects wave propagation on both transmit and receive. Unfortunately it is only possible, with the used data acquisition system, to modify the receive delay and apodization profiles. Fig. 6.6 shows B-mode images pre and post phase and sensitivity compensation. Note from the figure that the energy in the side-lobes has been reduced.

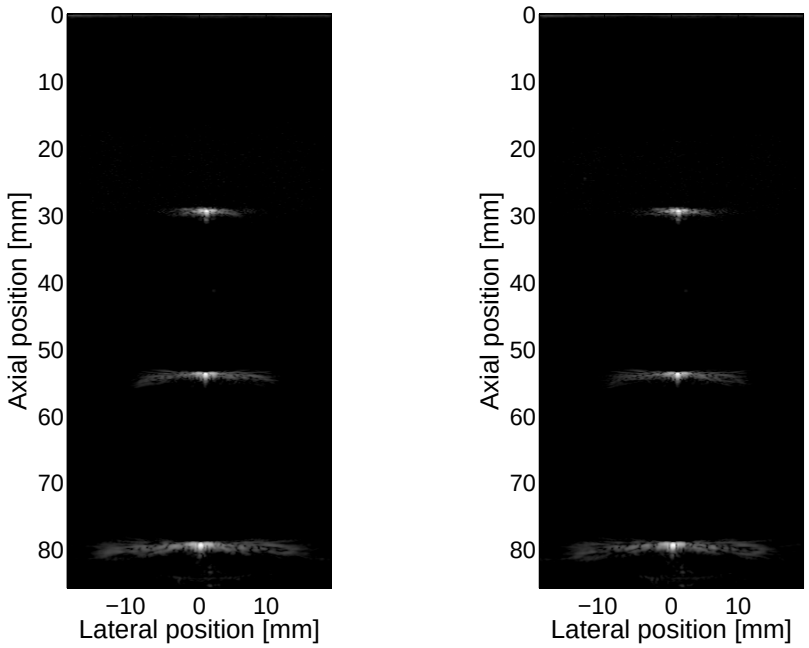

(a) Original (b) Compensated

Figure 6.6: B-mode images of a wire phantom (a) pre and (b) post phase and sensitivity compensated.

Fig. 6.7 shows the area covered by the point spread function from the scatterer at 79.4 mm. Note from the figure that the covered area below -30 dB until -55 dB is decreased. The compensation, however, fails to decrease the total covered area, and the expected improvement based on simulations presented in Paper VII is not achieved.

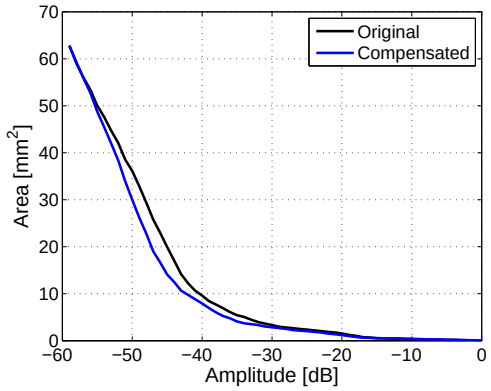

Figure 6.7: Area covered by the point spread function from the scatter at 79.4 mm, pre and post compensation for the phase error.

Fig. 6.8 shows B-mode images of a wire and contrast phantom, Model 525 (Danish Phantom Service, Frederikssund, Denmark) pre and post phase and sensitivity compensation. Note the improvement at the bottom of the image of Fig. 6.8(b) compared to Fig. 6.8(a).

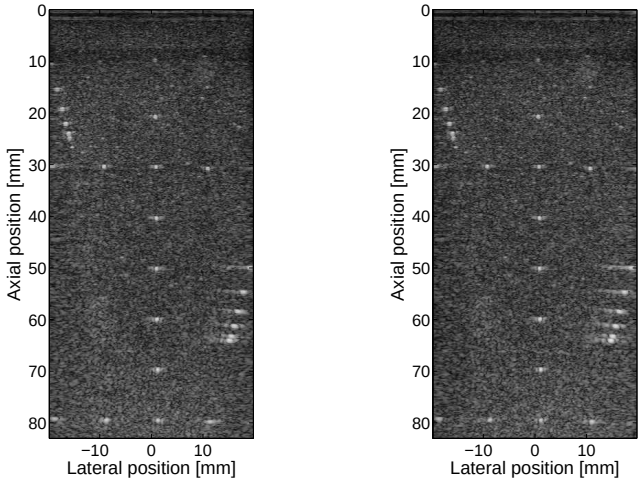

(a) Original (b) Compensated

Figure 6.8: B-mode images of a speckle and wire phantom (a) pre and (b) post phase and sensitivity compensated.

6.5 Discussion and conclusion

As noted by many authors, both phase and amplitude variations across the transducer array can result in severely degraded beam profiles, and hence degraded images. This chapter showed that the influence on image quality using real and non-ideal transducers can be simulated with an sufficient accuracy, to reveal system performance. The simulation model combines experimentally determined element pulse echo measurements and the solution to the wave equation implemented by Field II.

An angle independent method was proposed to accurately measure the phase error profile of a linear array transducer. The method is well suited for alignment of the transducer for an accurate measurement of the element pulse echo wavelets.

Furthermore it was shown that SASB imaging is more sensitive to errors than conventional imaging, and as such including individual element pulse echo into the models of future high quality imaging systems will improve the reliability of the modeling.

CHAPTER

SEVEN

Project conclusion

This project was divided into three main topics. 1) Development and implementation of a versatile research data acquisition system. 2) Clinical evaluation of SASB using a convex array transducer. 3) Simulation of acoustic fields for high quality ultrasound imaging.

1) The developed highly versatile research data acquisition system consists of a standard PC equipped with a X64-CL Express camera link (Dalsa, Waterloo, Ontario, Canada) and a 2202 ProFocus equipped with a UA2227 research interface (BK-Medical, Herlev, Denmark). The system uses an open architecture that allows acquisition of data for experimental research, such as developing new image processing algorithms. With the system, users can tailor the data acquisition to fit their working environment, while still maintain the clinical integrity of using a robust medical device. This allows researchers and clinicians to rapidly develop applications and move them relatively easy to the clinic for evaluation. The system is well suited for clinical trials and investigational purposes, because data can be captured interleaved with different configurations. Furthermore, the system is able to acquire and store data fast enough for multiple acquisitions in the same scanning session. Due to the advantages of speed of acquisition and clinical benefit, multiple research projects have successfully used the system to test and implement their customized solutions for different applications.

2) The clinical evaluation of SASB was performed as a three phased study in collaboration between medical doctors at Rigshospitalet, a statistician from Copenhagen University, and technical personal from Technical University of Denmark. The clinical evaluation was performed as a double blinded side-by-side comparison study between SASB and conventional imaging, evaluating the penetration depth and image quality. In the phase two pre-clinical

study five medical doctors evaluated 34 image sequence pairs. The statistical analysis showed no significantly ($p = 0.98$) increase nor decrease in penetration using SASB. Overall image quality was highly significantly increased ($p < 0.001$). In the phase three clinical study five medical doctors evaluated 84 image sequence pairs. The statistical analysis showed no significantly ($p = 0.55$) increase nor decrease in penetration using SASB. Overall image quality was highly significantly increased ($p < 0.001$).

The results of the clinical evaluation significantly show that SASB can be used in medical ultrasound imaging. The worry, that tissue motion would make coherent summation of samples and, thereby, image formation, impossible, can be discarded for the abdominal images generated in this study. Based on the clinical evaluation it can be concluded that SASB imaging can obtain satisfying penetration within the current intensity limits. Image quality evaluation showed highly significant improvement in SASB images compared with conventional images. The statistical model predicts that for a new image pair, rated by a new doctor, there is a 70% probability that the doctor will prefer the SASB image compared to the conventional image.

3) The work on combining the Field II program with experimentally determined element pulse echo wavelets, studies if the influence on the acoustic field using physical transducers can be modeled with a sufficient accuracy to reveal system performance of a high quality imaging system. The study revealed that the prediction of the acoustic pressure field can be improved using an individual pulse-echo wavelet for each element compared to using a common pulse echo wavelet for all elements. By including individual pulse echo wavelets in the simulation model, the model is able to include important transducer characteristics such as delay errors, sensitivity, and deviating transfer functions between elements. Measurements of the element pulse echo of a BK8804 transducer showed a significant delay error and sensitivity deviation between elements. By utilizing the element pulse echo in the simulations the accuracy and reliability of the predicted acoustic field is improved. The detailed predictions can be used as an early performance indicator of new imaging methods, and help gain insight into how physical transducer characteristics influence image quality.

Paper I

Implementation of a versatile research data acquisition system using a commercially available medical ultrasound scanner

Martin Christian Hemmsen, Svetoslav Ivanov Nikolov, Mads Møller Pedersen, Michael Johannes Pihl, Marie Sand Enevoldsen, Jens Munk Hansen, and Jørgen Arendt Jensen

IEEE Transactions on Ultrasonics, Ferroelectrics, and Frequency Control

In review 2011

Implementation of a versatile research data acquisition system using a commercially available medical ultrasound scanner

Martin Christian Hemmsen, Svetoslav Ivanov Nikolov, Mads Møller Pedersen, Michael Johannes Pihl, Marie Sand Enevoldsen, Jens Munk Hansen, and Jørgen Arendt Jensen

Abstract

This paper describes the design and implementation of a versatile and open architecture research data acquisition system using a commercially available medical ultrasound scanner. The open architecture will allow researchers and clinicians to rapidly develop applications and move them relatively easy to the clinic. The system consists of a standard PC equipped with a X64-CL Express camera link (Dalsa, Waterloo, Ontario, Canada) and a 2202 ProFocus equipped with a UA2227 research interface (BK-Medical, Herlev, Denmark). The 2202 ProFocus ultrasound scanner is an easy to use imaging device that is capable of generating high quality images. In addition to supporting the acquisition of multiple data types such as B-mode, M-mode, pulsed Doppler and color flow imaging, the machine provides users with full control over imaging parameters such as transmit level, excitation waveform, beam angle, and focal depth. Beamformed radio frequency data can be acquired from regions of interest throughout the image plane and stored to a file with a simple button press. For clinical trials and investigational purposes, where an identical image plane is wanted on both an experimental and a reference dataset, data can be captured interleaved. This form of data acquisition, allows switching between multiple setups, maintaining identical transducer, scanner, region of interest, and recording time. Essential in any reliable clinical trial. The data acquisition is controlled through a GUI running on the PC. This program implements an interface for third-party software, such as Matlab, to interact with the application. A software development toolkit (SDK) is developed to give researchers and clinicians the ability to utilize Matlab for data analysis and flexible manipulation of control parameters. Due to the advantages of speed of acquisition and clinical benefit, research projects have successfully used the system to test and implement their customized solutions for different applications. Three examples of system use are presented in this paper: Evaluation of Synthetic Aperture Sequential Beamformation (SASB), Transverse Oscillation (TO) for blood velocity estimation, and Acquisition of spectral velocity data for evaluating aortic aneurysms.

Martin Christian Hemmsen is with BK Medical, Denmark, and the Department of Electrical Engineering, Center for Fast Ultrasound, Technical University of Denmark. e-mail: mah@elektro.dtu.dk.

Svetoslav Ivanov Nikolov is with BK Medical, Denmark.

Mads Møller Pedersen is with the Department of Radiology, Rigshospitalet.

Michael Johannes Pihl is with the Department of Electrical Engineering, Center for Fast Ultrasound, Technical University of Denmark.

Marie Sand Enevoldsen is with the Department of Electrical Engineering, Center for Fast Ultrasound, Technical University of Denmark.

Jens Munk Hansen is with the Department of Electrical Engineering, Center for Fast Ultrasound, Technical University of Denmark.

Jørgen Arendt Jensen is with the Department of Electrical Engineering, Center for Fast Ultrasound, Technical University of Denmark.

I. Introduction

Difficulties accessing ultrasound data in the laboratory and clinic has not only limited the basic research, but also hindered the clinical testing of new ultrasound applications. In order to access raw ultrasound data, researchers have worked with ultrasound manufacturers to build custom ultrasound systems such as RASMUS [1], [2] and SARUS [3], but due to the size of these scanners they are inaccessible in the clinic. Recently, a number of research interface platforms for clinical ultrasound scanners have been developed for systems such as Hitachi HiVision 5500 [4], Siemens Antares [5] and the Ultrasonix 500 [6]. With the introduction of research interface platforms on clinically available scanners it is now possible to acquire and store data. However, for a system to be suitable for acquisition of data for clinical evaluations, the system has to keep factors, such as identical transducer, region of interest, and recording time constant on both the reference and the experimental image. Another system requirement is the ability to get sufficient number of scans under realistic operating conditions. Thus, the data acquisition should be capable of acquiring and storing data fast enough to conduct an ultrasound examination with multiple image sequences. The objective of this work is to develop and implement a versatile research data acquisition system using a commercially available medical ultrasound scanner. This will allow researchers and clinicians to rapidly develop applications and ease the transition to the clinic for evaluation.

The ProFocus research package was developed by BK Medical ApS to ease experimental ultrasound data acquisition and control of scanner operation. The package includes a UA2227 research interface for real-time data acquisition and remote control of basic scanner operation, and a software toolbox for easy access of the complete control parameter set. The research package offers access to beamformed radio frequency data and provides flexible manipulation of control parameters such as filtering, compression, transmit level, excitation waveform, beam angle, and focal depth *etc*.

The developed research data acquisition system consists of a standard PC and a ProFocus ultrasound scanner. The system uses an open architecture that allows acquisition of data for experimental research, such as developing new image processing algorithms. With the system, users can tailor the data acquisition to fit their working environment, while still maintain the clinical integrity of using a robust medical device. This will allow researchers and clinicians to rapidly develop applications and move them relatively easy to the clinic for evaluation. A central part of developing new applications and methods is determination of both technical and diagnostic efficacy. With the system, users can acquire interleaved data sequences switching between an experimental setup and a reference setup. This, in combination with the ability to acquire and store multiple data sets during the same examination, makes the system adequate for clinical trials.

This paper describes the capabilities of the research data acquisition system, and demonstrates how it is used to test and implement customized solutions for different research applications. Three examples of system use are presented: Evaluation of Synthetic Aperture Sequential Beamformation (SASB), Transverse Oscillation (TO) for blood velocity estimation, and Acquisition of spectral velocity data for evaluating aortic aneurysms.

The rest of this manuscript is organized as follows. Section II and III describes the system and developed Matlab

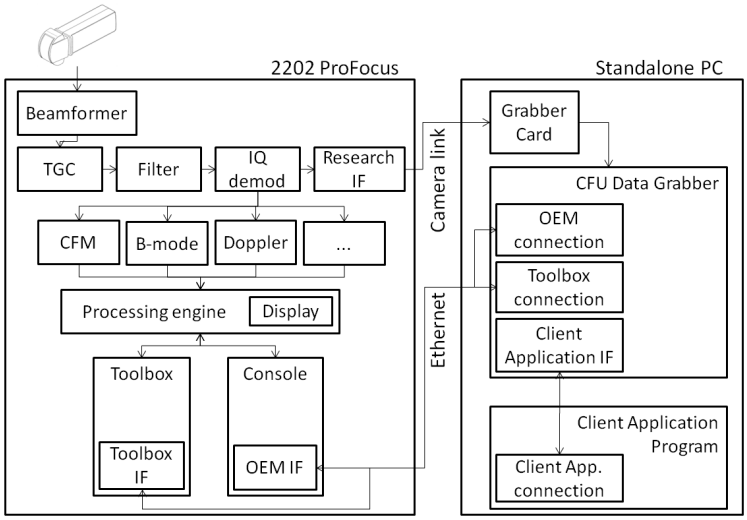

Fig. 1. Data flow and structure of the software and hardware of the system.

Tools, and Section IV presents three examples of system use, followed by conclusions in Section V.

II. System Description

The developed ultrasound research system consists of a commercially available ultrasound scanner (2202 ProFocus equipped with a UA2227 Research Interface, BK-Medical, Herlev, Denmark) and a standard PC. The research interface implements a camera link protocol and allows the acquisition of digital beamformed radio frequency (RF) echo data. The acquired data can be received by any video grabber card that supports camera link. In our configuration a X64-CL Express camera link (Dalsa, Waterloo, Ontario, Canada) is used. The developed software running on the PC is based on libraries by Sapera, now a part of Dalsa. The PC is also connected to the scanner through an Ethernet link which provides access to system parameters. The research and OEM interfaces on the 2202 ProFocus architecture allows external devices to control and access data on the scanner. The OEM interface makes it possible to set and read system parameters and can be used to stream processed images. It is basically a substitute of the normal interface: keyboard, track ball, and screen, and enables embedding in 3rd party products as a self-sufficient component. The research interface on the other hand, streams data prior to envelope detection. Unlike some other research interfaces all data is sent out of the scanner. It is however, possible to filter out undesired modes and e.g. only to receive CFM or B-mode data.

Fig. 1 illustrates the data flow and the structure of the software and hardware in the system. Raw channel data from the individual transducer elements are sampled and sent to the beamformer. The beamformed data is minimally processed because, aside from an optional time-variant band-pass filter, the only other processing is application of the time gain compensation (TGC) and transformation to baseband I/Q data and down sampling by a factor of 2. The beamformed data stream is processed and sent to the research interface.

The I/Q data is further processed to generate B-mode, CFM, Doppler, and M-mode images. The results of this

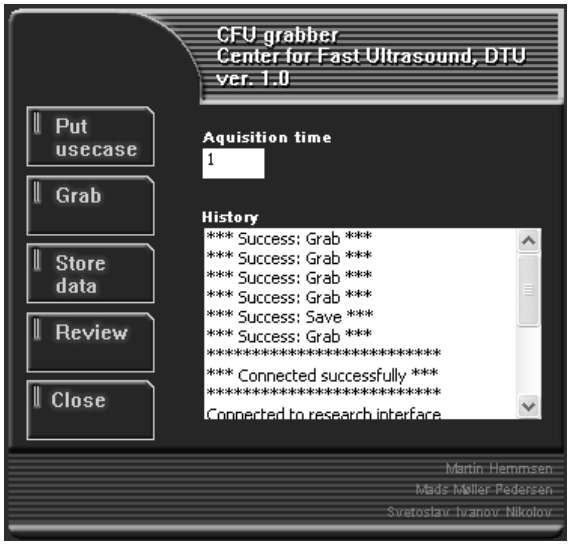

Fig. 2. CFU Data Grabber GUI that is available on the PC for uploading a Usecase to the scanner, acquisition of data, review, and download of data to hard drive.

processing are transferred to the processing engine for subsequent post-processing and display. The user interface and the calculation of control parameters are handled by the main application called Console. The system architecture of the 2202 ProFocus makes it possible for several standalone applications to coexist and to interact with the control parameters. One such application is the Toolbox, and it is used for debugging of the system, for prototyping of new algorithms, and for image optimization. An example of image optimization is the design of pulses, definition of receive F-number, specification of center frequency and bandwidth for the sliding filter. One can view the Toolbox as a form of parameter control unit. Furthermore, it implements an interface that allows remote reading and writing of a complete control parameter set called a Usecase. The OEM interface is implemented by a module in the Console. As such it has access to the control parameters, and has knowledge of the user input. Using the OEM interface, one can, for example, query which transducer is used, get information about image geometry and imaging mode, set focus depth, manipulate settings, and start/freeze the scanner. One can view the OEM interface as a form of remote control. Furthermore, it can stream processed images as they were displayed on the scanner screen. The Research Interface is implemented as a separate hardware module. One can stream raw beamformed data to external devices using the Research Interface. Each scan line in the data stream is tagged with a header containing information to what kind of acquisition the line belongs - B-mode, CFM, Doppler. It also contains information about the length of a line, if the line is last-in-frame, and if the line is last-in-block, where block refers to the block of data needed to estimate flow. The remote control of acquisition and parameters is handled by the application called CFU Data Grabber. The application implements a communication module to the OEM interface and the Toolbox interface. Furthermore, it implements an interface that makes it possible for 3rd party programs, such as Matlab (Mathworks, Natick, MA, USA), to interact with the application.

A. Data Acquisition

The acquisition of data is controlled via the CFU Data Grabber software and can be performed with a single button click. Alternatively, the acquisition can be issued from a 3th party program using messaging. In both cases, data are acquired and temporarily stored in memory for either review or download to a hard drive for storage. The maximum length of acquisition stored in memory varies depending on the depth of acquisition, the number of scan lines or ultrasound beams used to create a single frame, and the frame rate. Typical simultaneous dual screen B-mode acquisitions each using 384 scan lines and 15 cm of depth with a frame rate of 7 Hz, allows acquisition of a 22 second sequence. Fig. 2 shows the CFU Data Grabber GUI that allows uploading a Usecase to the scanner, acquisition, review, and download of data to hard drive. The user can use the review function to display the acquired B-mode image of the first frame, and once the user is satisfied with their scan, they can save the data to hard drive. The data files stored to disk, can later be opened on any computer for analysis and processing. The data storage time is approximately 15.1 seconds for a 3 sec interleaved B-mode sequence including complete scanner settings and patient information.

The scan sequence of the ProFocus is defined as a set of one or multiple basic modes. The basic modes available on the ProFocus is B-mode, M-mode, CFM-mode, and spectral Doppler mode. The scan sequence can be split into two independent views; view A and view B. Each view can be a composition of one or more basic modes and both view A and B can be updated simultaneous. This feature allows data to be acquired interleaved, switching between multiple basic modes, maintaining identical transducer, scanner, region of interest, and recording time on both views. This allows for acquisition of an experimental and standardized data set for evaluation of new processing methods.

The available data for acquisition in all basic modes are beamformed complex baseband data. In the rest of this paper, this type of data will be referred to as RF data.

To complement the RF data, acquisition of the complete control parameter set including the individual basic mode setups and the scanner user interface setup is available. The control parameter set is called a Usecase and the scanner user interface setup is called OEM parameters.

B. Parameter Control

The system allows manipulation of the control parameters in two ways, either through the Console or using standalone applications such as the Toolbox. The Console is the standard user interface and the main application. Modifications made through the Console are limited to standard clinical use and a set of precalculated and validated control parameter setups. The Toolbox allows manipulation of the full control parameter set. A subset of the parameters available, is described in Table I. These parameters are not available on the normal clinical interface or other typical scanners. The manipulation of the control parameters allows a wide degree of experimentation with the receive and transmit aperture control, color flow control, and Doppler control. We describe each below, and the examples included in Section IV demonstrate their use. Modifications made through the Toolbox can result in non-validated setups and measurements must be performed to ensure FDA regulation is not compromised.

TABLE I
DESCRIPTION OF A SUBSET OF THE PARAMETER CONTROLS.

Parameter	Description
Dynamic focusing and dynamic apodization	Receive aperture dynamic focusing and aperture growth can be disabled individually. When disabled, receive aperture size and focal position are fixed.
F#	Receive and transmit aperture size can be adjusted individually.
Receive apodization	Receive apodization can be chosen from a fixed list of standard curves such as Hamming, Gaussian, or rectangular apodization or optionally to upload a custom made apodization matrix. If defined as a matrix the apodization can vary between individual beam lines.
Receive time delay profile	Receive time delay profile can be specified individually for each image line when dynamic focusing is disabled.
Line density	The image line density can be chosen from a range of half an element pitch to two element pitch.
Speed of sound	Speed of sound can be specified to match the imaging application.
Excitation waveform	A bipolar excitation waveform can be specified with a time resolution of 8.3 nsec.
Region of interest	The region of interest can be adjusted in all imaging modes.
Ensemble size and Pulse repetition frequency	The ensemble size and pulse repetition frequency can be adjusted in both CFM imaging and Doppler imaging. A change in the ensemble size or pulse repetition frequency will trigger an automatically recalculation of the shot macro.

1) Receive and Transmit Aperture Control: The Receive and transmit aperture control give the user the ability to control the fundamental parameters related to the formation of an echo line. The available parameters span from adjusting the size and growth of the aperture to controlling the weighting of the individual elements. A subset of the parameters are described in the following:

- Aperture growth and dynamic focusing. By default, the system dynamically moves the receive focal point outward and grows the aperture to optimize echoes received from increasing depths. With the Toolbox, the user is given the control to override this dynamic updating and define a static size and focal position of the receive aperture. Hereafter, the default state is referred to as a dynamic aperture, and the opposite, a static aperture. Of course, once the aperture is made static, the user has to choose a focal position and a size for the aperture.
- Aperture focal position. When the receive aperture is static, the user can adjust the focal position to any depth. The transmit focal position is adjusted independently.
- Aperture size. The user can adjust the aperture size in dimensionless units of F-number.

- Aperture apodization. The user is given the ability to select between a set of predefined receive aperture weight functions, such as Hamming, Gaussian, or rectangular apodization or optionally to upload a custom made apodization matrix. If defined as a matrix, the apodization can vary between individual beam lines.

2) Color Flow Control: The Color flow Control gives the user the ability to control the fundamental parameters related to the formation of the echo lines for CFM. The available parameters span from adjusting the size of the color box to adjusting the time between individual beam lines. A subset of the parameters are described in the following:

- Region of interest. By default, the region of interest is selected as a square in the center of the imaging plane. The user is given the control to move and change the region of interest, either through the Console or the Toolbox.
- Ensemble size. The ensemble size is the number of color firings that are used in the velocity estimate along each beam line. The user is given the ability to experiment with the number of acquisitions to fit a specific application.
- Pulse repetition frequency. The pulse repetition frequency determines the time between to successive echo lines. The user is given the ability to change this frequency to fit a specific application. A change in the pulse repetition frequency, region of interest or ensemble size will trigger an automatically recalculation of the basic mode acquisition sequence.

3) Doppler Control: The Doppler control give the user the ability to control the fundamental parameters related to the formation of the echo lines for Doppler imaging. The available parameters span from adjusting the length of the echo lines to adjusting the time between each acquisition. A subset of the parameters are described in the following:

- Range gate. The parameters related to the range gate determines the angle of the beam line relative to the center of the aperture and the length of the echo line. The user is given the control to move and expand the range gate, either through the Console or the Toolbox.
- Pulse repetition frequency. As with the Color Flow Control, the pulse repetition frequency can be specified.

C. Data Management

Data management of the OEM parameters, Usecase, and RF data is split into three different file types and formats. Each type has a different file extension, and this information along with a summary of their use is contained in Table II.

The file format used for handling RF data is a custom made file format. The file handling is developed in C++, and it is described in Table III. The file format enables the user to load specified frames from a long data sequence, without loading the entire data set first. Data are stored as 16 bit signed integers.

For handling the OEM interface data characteristic, a C++ class called oemArray is implemented. The design of oemArray, resembles to a great extend the design of mexArray by Matlab. One of the design ideas was that

TABLE II
FILE TYPES.

Extension	Description
.dat	The usecase is a complete description of the control parameters used by the scanner and includes information such as excitation waveform, receive F-number, center frequency and bandwidth for the sliding filter.
.oem	The oem parameter file is a complete description of the scanner User Interface setup and includes information such as zoom, overall gain, persistence, and various other visualization settings. The scanner parameters aids the user to redo experiments and to visualize images offline as they were shown on the scanner.
.cfu	The file format used for handling RF data is a custom made file format. The file format enables the user to load specified frames from a long data sequence, without loading the entire data set first. RF data are stored as a number of volumes each consisting of a number of planes. This allows handling of 3D data sets. Each plane consist of a number of lines and each line of a number of samples, where each sample is represented by a number of bits. The file can be divided into two logical parts: (a) header, (b) data. The header contains data in ASCII format. Allowing the user to open the file with a normal text editor and to see a description of the data. Data are stored immediately after the header.

TABLE III
C++ FUNCTIONS FOR FILE HANDLING OF .CFU FILE TYPES.

Function name	Description
Create File	This function creates a new file. If a file with the same name exist, it is replaced.
Close File	This function closes an open file. As the file is being closed the information in the file header is updated.
Append Plane	This function appends a whole plane at the end of the a file.
Read Plane	This function reads a whole plane from a file into memory.

oemArray can create its own queries to the OEM interface, as well as parse the data contained in a data string received by the OEM interface. The full parameter set describing the characteristic of the user interface on the scanner is saved in a XML format. The resulting OEM parameter file is a complete description of the scanner user interface setup and includes information such as zoom, overall gain, persistence, and various other visualization settings. The scanner parameters aids the user in redoing experiments by setting up the Console in the exact same mode as it was when the parameters were saved. A library is provided to read and write the parameters in Matlab.

The Usecase is a complete description of the control parameters used by the scanner and includes information such as excitation waveform, receive F-number, center frequency and bandwidth for the sliding filter. The control parameters aids the user to redo experiments, as well as create simulations using tools such as Field II [7], [8] with

TABLE IV
DESCRIPTION OF A SUBSET OF THE FUNCTIONS AVAILABLE IN THE SDK.

Function name	Description	Matlab call
Connect	Opens a connection to the CFU Data Grabber application. Optionaly an IP address can be specified as a char array.	`.Connect`
Disconnect	Disconnects any open connections to the CFU Data Grabber application.	`.Disconnect`
Grab	Grabs N seconds or N frames of data to application memory.	`.Grab('Nsec') or .Grab(N)`
Review	Displays the first B-mode data frame envelope detected and log-compressed to 60 dB dynamic range.	`.Review`

Save	The function allows storing of the usecase, OEM parameters and acquired RFdata, to a specified filename. The procedure for saving the usecase and OEM parameters includes fetching the active parameters on the scanner and transfering to local hard drive. RFdata must have been acquired to application memory prior to the function call.	`.Save('C:test','usecase')`
		`.Save('C:test','oem')`
		`.Save('C:test','frame')`
		`.Save('C:test','all')`

Load	The function allows uploading of a specified usecase or OEM parameter file to the scanner.	`.Load('C:test','usecase')` `.Load('C:test','oem')`
Send_msg	Transfers a message to the OEM interface (oem) or to the research interface (ri) on the scanner.	`.Send_msg('oem','msg')` `.Send_msg('ri','msg')`
Read_Usecase	Reads the specified file, parses the data and returns a Matlab structure.	`Read_Usecase('c:test.dat')`
cff_file_open	Opens a user specified cfu file type and returns a file identifier.	`cff_file_open('c:test.cfu')`
cff_file_close	Closes the file specified.	`cff_file_close(fid)`
cff_file_plane_read	Returns the data from the specified file and plane nr.	`cff_file_plane_read(fid,plane_nr)`

identical setup as used in measurements. The parameter set is saved in ASCII format. This allows the user to open the file with a normal text editor to read or write application specific initialization of control parameters.

III. MATLAB TOOLS

The CFU Data Grabber application implements an interface that makes it possible for 3rd party products, such as Matlab, to interact with the application via messaging. The interface provides the user to access the service

interface layer in the application, giving access to system functions. Since many researchers utilize Matlab for data analysis, a SDK for Matlab is developed. The SDK implements a CFU_Data_Grabber class that allows a flexible manipulation of the control parameters and data acquisition. Further, the SDK implements a set of functions for basic file handling of the files collected with the system. A description of CFU_Data_Grabber member functions and functions available for file handling are listed in Table IV.

IV. Results

The developed ultrasound data acquisition system has extensively been used to acquire *in vivo* data from volunteers in the clinic as well as phantom measurements in the lab. Three research studies, that have benefited from the system, are presented here.

A. Preliminary evaluation of Synthetic Aperture Sequential Beamformation

1) Background: In multi-element Synthetic Aperture (SA) imaging the basic idea is to create a pressure wave from multiple elements with a focused transmission. The concept of using the transmit focal point as a virtual source was introduced by Passmann and Ermert [9]. Virtual sources in Synthetic Aperture Focusing (SAF) was further investigated by Frazier and O'Brien [10], Nikolov and Jensen [11], [12], and Bae and Jeong [13]. It was shown that the virtual source coincides with the focal point of the transducer, and that a depth independent resolution can be achieved. Kortbek et al. introduced in [14] the concept of Sequential Beamforming to SA imaging to reduce system requirements for real time implementation. It was shown that for a multi element linear array transducer the lateral resolution could be made more range independent and improved significantly compared to conventional Dynamic Receive Focusing (DRF). Hemmsen et al. applied in [15] SASB to medical ultrasound imaging using convex array transducers. It was shown that the method is applicable for medical imaging and improves the lateral resolution compared to DRF.

The basic idea in Synthetic Aperture Sequential Beamforming (SASB) is to create a dual-stage procedure using two separate beamformers. In the initial stage a beamformer using a single focal point in both transmit and receive, creates a set of focused image lines. A second stage beamformer creates a set of high resolution image points by combining information from multiple first stage focused image lines. The effect is a dynamically expanding array as the image depth increases and a more range independent lateral resolution is obtained.

In the following example, the developed system is used to acquire RF signals in order to create B-mode images using Dynamic Receive Focus (DRF) and Synthetic Aperture Sequential Beamformation (SASB). In this experiment the lateral resolution and signal-to-noise ratio of SASB will be calculated and compared to DRF. Furthermore, *in vivo* data are acquired, and B-mode images are generated for a visual comparison and evaluation of the image quality of the two image modalities.

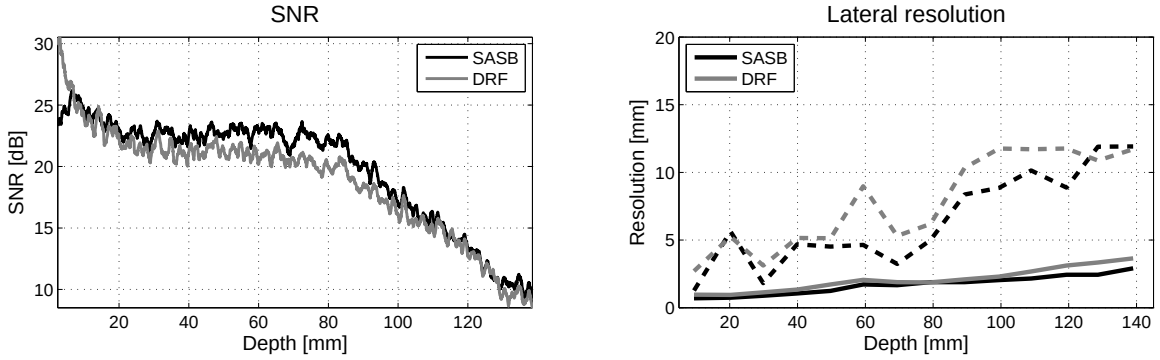

(a) (b)

Fig. 3. (a) Visualization of the SNR using SASB (solid gray line) and DRF (solid black line) (b) Visualization of the lateral resolutions at FWHM (solid line) and -20 dB (dashed line) using DRF (gray line) and SASB (black line).

2) Method: In the following experiment an abdominal 3.5 MHz probe with a room-temperature vulcanization (RTV) lens, 3ML35CLA192 (Sound Technology Inc., 1363 South Atherton St., State College, PA 16801, USA) transducer was used. In the first part of the experiment the transducer was clamped to immobilize the transducer over a speckle phantom, Model 571 (Danish Phantom Service, Frederikssund, Denmark). A water bath at the top of the phantom provided a coupling medium between the transducer and the phantom. The transmit frequency of the transducer was set to 5 MHz, and the transducer was fixed such that the transducer surface was orthogonal to the phantom. Using the Console application both view A and B was set to simultaneous B-mode imaging with a field of view of 14.6 cm and neutral TGC. Using the Toolbox, dynamic receive focusing and dynamic apodization were disabled on view A. Subsequently the F-number were fixed to 2 in both transmit and receive and the transmit and receive focus were set to 70 mm. The transmit focus point for view B was set to 105.5 mm with a transmit F-number of 5 and receive F-number of 0.8. Using the Matlab SDK, 20 frames of beamformed RF data from view A and B were acquired interleaved with identical excitation waveforms, TGC, and overall gain in both setups. The scan sequence was specified to a line density of 2 lines pr. element, resulting in 384 lines for each image. The acquired RF data from view A was subsequently processed using the Beamformation Toolbox III [16] to generate SASB second stage RF data. The method used to compute the SNR of the second stage RF data and the acquired RF data from view B is described as

$$SNR(z) = \frac{1}{L}\sum_{l=1}^{L}\frac{S(z,l)^2}{N(z,l)}. \tag{1}$$

Where L is the number of acquired beam lines and $S(z,l)$ and $N(z,l)$ is the mean power of the signal and noise at depth z for the $l'th$ beam line and is expressed as

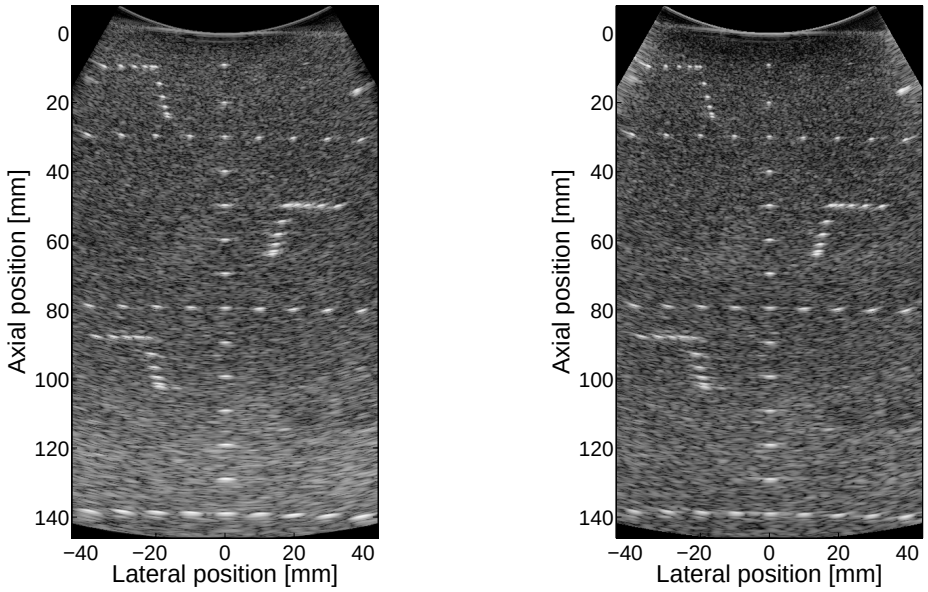

(a) DRF (b) SASB

Fig. 4. Visualization of wire and contrast phantom measurement, using (a) DRF beamforming (b) SASB beamforming.

$$S(z,l) = \frac{1}{N}\sum_{n=1}^{N} x(z,l,n).$$

$$N(z,l) = \frac{1}{N}\sum_{n=1}^{N} (x(z,l,n) - S(z,l))^2.$$

Where $x(z,n)$ is the rf sample at depth z for the $n'th$ frame and N is the total number of acquired frames.

In the second part of the experiment the transducer was clamped to immobilize the transducer over a wire and contrast phantom, Model 525 (Danish Phantom Service, Frederikssund, Denmark). A water bath at the top of the phantom provided a conducting medium between the transducer and the phantom. The transmit frequency was set to 5 MHz, and the transducer was fixed such that the vertical wires were placed along the vertical center of the field of view. The Usecase from the first experiment was uploaded to the scanner and 20 frames were acquired. The acquired RF data from view A was subsequently processed to generate SASB second stage RF data. The second stage RF data and the acquired RF data from view B was envelope detected, log-compressed, and scan converted to create B-mode images. Using the B-mode images the lateral resolutions at full-width-at-half-max (FWHM) and -20 dB were extracted.

In the final part of the experiment an *in vivo* scan of the Morison's Pouch from a 30 year old male volunteer was scanned. The scanner setup, control parameters, and scan sequence were identical to the one used in the first

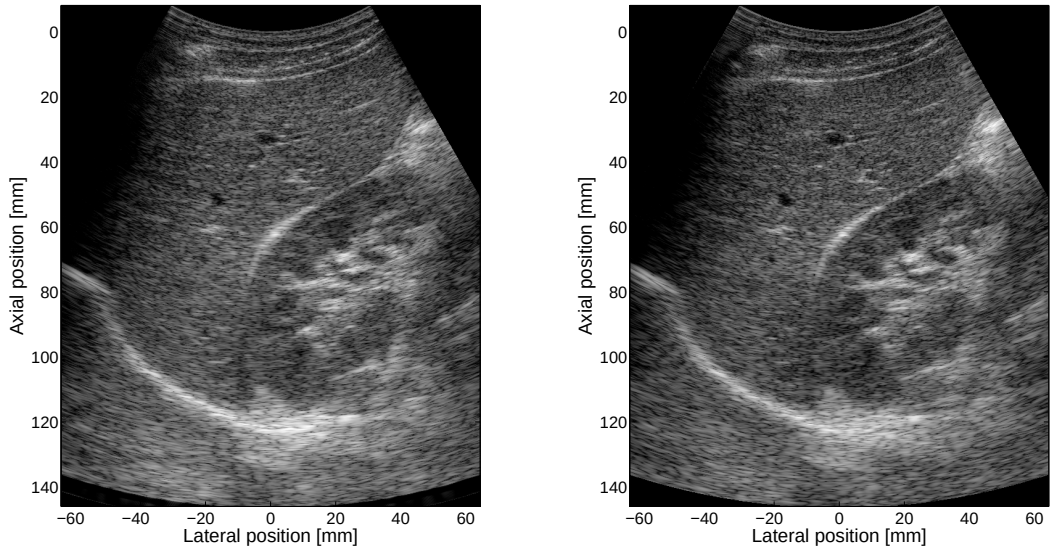

(a) DRF (b) SASB

Fig. 5. Visualization of *in vivo* measurement of the liver (left side of the image) and right kidney (right side of the image) and Morison's pouch, not containing fluid, using (a) DRF and (b) SASB.

and second part of the experiment.

3) Results: Fig. 3(a) presents the SNR calculated as the ratio between the mean power of the signal divided by the power of the noise. The gray line represents the SNR using DRF and the black line using SASB. The SNR using SASB is on average 6.2 % or 1.18 dB better than the SNR using DRF.

Fig. 3(b) presents the lateral resolution calculated from the B-mode images of the measurement on the wire and contrast phantom. The lateral resolutions are calculated at FWHM (solid line) and -20 (dashed line) using DRF (gray line) and SASB (black line) in the range 10 to 140 mm. At FWHM and -20 dB the lateral resolutions are on average improved by 18.4% at FWHM and 17.4% at -20 dB using SASB. The standard deviation on the lateral resolution at FWHM were improved from 0.9 mm using DRF to 0.7 mm using SASB. At -20 dB the standard deviation were 3.5 for both modalities.

For visual inspection, Fig. 4 displays the B-mode images created from the measurement on the wire and contrast phantom, using (a) DRF and (b) SASB. Note how SASB is able to maintain a more isotropic point spread function through depth and has a better lateral resolution. Fig. 5 displays the B-mode images from the *in vivo* measurement of the Morison's Pouch, the right kidney, and the adjacent part of the liver from a 30 year old male, using (a) DRF and (b) SASB.

4) Summary: Three experiments were performed. The first two experiments were performed to measure the performance of SASB compared to DRF. The SNR and the lateral resolution were used as quantitative measures. The third experiment was performed as a preliminary *in-vivo* evaluation of the method. The evaluation using the

quantitative measures showed the ability of SASB to decrease the standard deviation of the lateral resolutions at FWHM, the ability to obtain a more isotropic point spread function compared to DRF, and to improve the SNR. The performance gain using SASB compared to DRF was further supported by *in-vivo* scan of the right kidney and the adjacent liver. The results presented prove the viability of SASB for 2D ultrasound imaging using commercially available equipment.

B. Transverse Oscillation for blood velocity estimation

1) Background: Medical ultrasound is widely used to study blood flow dynamics in the human circulatory system. For instance, the estimation of blood flow velocities plays a key role in diagnosing major diseases in the carotid arteries [17]. However, blood velocity estimates using conventional color flow imaging or Doppler techniques are angle dependent. That is a major limitation, and poses a huge challenge for quantitatively estimating the magnitude of the blood velocity.

Several techniques [18]–[22] have been proposed to compensate for the inherent angle dependency problem. In this case, the Transverse Oscillation (TO) method suggested by Jensen and Munk [23] is used. Anderson [24] suggested a similar approach. The TO method has demonstrated promising *in vivo* results [25], [26]. However, the previously reported results have been obtained using the experimental scanner RASMUS [1], [2].

The basic idea in the TO method is to create a double oscillating field by using special apodization profiles in receive. Two lines with a lateral displacement of a quarter spatial wavelength, corresponding to a 90° phase shift, are beamformed simultaneously in receive. A center line is also beamformed for traditional axial velocity estimation. For a description and derivation of the estimator, the reader is referred to Jensen [27]. The lateral wavelength, λ_x, can be found by

$$\lambda_x = 2\lambda_z \frac{z}{D}, \tag{2}$$

where λ_z is the axial wavelength, z is the depth, and D is the distance between the two peaks in the receive apodization.

In the following example, the initial work on investigating the feasibility of a commercial implementation of the TO method for clinical use is presented. The developed research data acquisition system is used to acquire RF data from a flow rig for a statistical evaluation of the TO implementation.

2) Method: In the following experiment a linear array transducer BK8812 (BK-Medical, Herlev, Denmark) was used. Velocity measurements were performed using a custom made circulating flow rig to evaluate the TO method. The setup consists of a long rigid metal tube replaced by a rubber tube (radius 5.7 mm) inside a water filled container as illustrated in Fig. 6. The tube is filled with a blood mimicking fluid [25]. A Cole-Parmer (Vernon Hills, IL) 75211-60 centrifugal pump controls the fluid flow, and a Danfoss (Sønderborg, Denmark) MAG 3000 magnetic volume flow meter is used to measure the actual volume flow. The centrifugal pump is only able to keep the flow constant at sufficiently low flow rates ($Q < 60$ L/h). Therefore, the peak velocity of the flow, v_0 was set

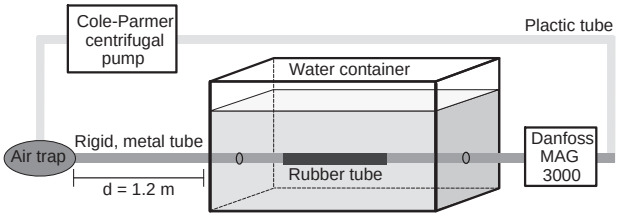

Fig. 6. The flow rig setup with a Cole-Parmer centrifugal pump, an air entrapment device, a water container with a rubber tube, and a Danfoss MAG 3000 magnetic flow meter. Notice that this figure is not to scale, and that the entrance length of the tube is more than 1.2 m, enough to ensure fully developed laminar flow. A fixture can be placed in the water container to keep the transducer fixed at a known beam-to-flow angle.

TABLE V
PARAMETERS FOR THE EXPERIMENTAL FLOW RIG MEASUREMENTS.

Scanner Parameters	Value
Pulse repetition frequency	1.3 kHz
Speed of sound	1480 m/s
Number of transmit cycles	6
Ensemble size	16
Transmit focus depth	15 mm
Center frequency of the CFM pulse	5 MHz
Transmit F-number	4
Line density	1 per element
Multibeam (parallel beamforming)	3

to 0.215 m/s. The entrance length of the tube is more than 1.2 m, and, under the given settings, sufficient in length to ensure fully developed flow. The transducer was fixated with a distance of 16 mm to the center of the rubber tube and the beam-to-flow angle was set to $90°$.

Using the Console application view A was set to B-mode and CFM imaging. A number of parameters were set manually in either the Console or the Toolbox. They are listed in Table V. Multibeam of 3 means that three lines are beamformed simultaneously in receive: Two are TO lines, one is a center line for conventional axial velocity estimation.

Subsequently, the CFM receive delays and apodizations were downloaded from the scanner, modified according to the principles of the TO method, and then uploaded to the scanner again. With a focal point at 15 mm, a line density of 1 line per element, and beamforming the two TO lines next to each other ($i.e.$ $\lambda_x/4$ is equal to the pitch), the spacing between the two aperture peaks has to be 6.6 mm. The transmit and receive aperture functions are illustrated in Fig. 7.

Using the Matlab SDK, beamformed RF data from view A were acquired. Although data for whole CFM frames were acquired, only the central CFM line was extracted from each frame for further offline processing using Matlab. 75 flow profiles were generated for the purpose of investigating the performance of the TO estimator.

The performance of the method is investigated by comparing the true profile with the measured velocity profiles. The measured velocity is estimated from a number of emissions. The average, $\bar{v}(z_k)$, of N estimates and the

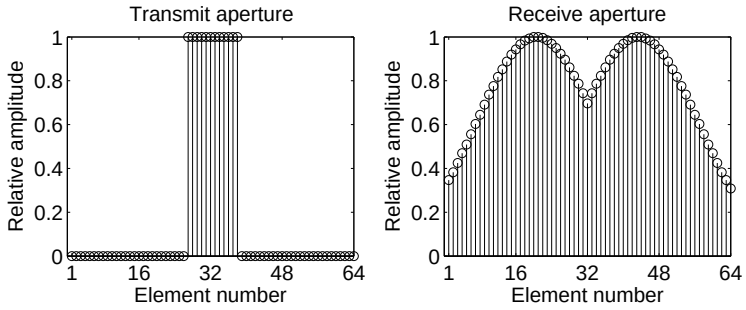

Fig. 7. The transmit and receive aperture for the TO estimator with a transmit focal depth at 15 mm. The transmit aperture is rectangular, and the F-number is 4. The receive aperture is the TO apodization.

estimated standard deviation, $\sigma(z_k)$, is calculated at each discrete depth as

$$\bar{v}(z_k) = \frac{1}{N}\sum_{i=1}^{N} v_i(z_k) \tag{3}$$

$$\sigma(z_k) = \sqrt{\frac{1}{N-1}\sum_{i=1}^{N}\left(v_i(z_k)-\bar{v}(z_k)\right)^2}, \tag{4}$$

where $v_i(z_k)$ is the ith velocity estimate at the discrete depth z_k.

3) Results: Fig. 8 shows the estimated lateral velocity component of the flow profiles for 75 measurements at a beam-to-flow angle of 90°. It also indicates the mean estimate $\pm$ one standard deviation and the expected true velocity. The TO method is clearly able to estimate the lateral velocity component, which is not possible with conventional estimators. As expected, the estimated lateral velocity profile has a parabolic shape.

Due to a mismatch between the theoretical λ_x from Eq. 2 and the simulated mean $\bar{\lambda}_x$ in the generated TO field, the velocities are underestimated. Using Field II, the mean lateral wavelength can be estimated based on the 2D spatio-temporal frequency domain of the combined pulse-echo TO field. At 15 mm, the theoretical λ_x is 1.35 mm and the simulated mean $\bar{\lambda}_x$ is 2.66 mm. Calculating the relative bias between the simulated mean value and the theoretical value one obtains (2.66-1.35)/2.66 = 0.494. The bias correction factor is therefore 1.494, and this value is multiplied to the estimated velocity. The mean $\bar{\lambda}_x$ is simulated for each 1/2 mm from 10 to 22 mm and interpolated before bias compensation is applied to the 75 velocity profiles. With this bias compensation, the mean of the estimated velocities closely follow the theoretical profile.

4) Summary: By using the research data acquisition system, beamformed data for the TO method were obtained. Based on these data the transverse (lateral) velocity component perpendicular to the ultrasound beam could be measured. The results demonstrate that the TO method is suitable for a commercial implementation.

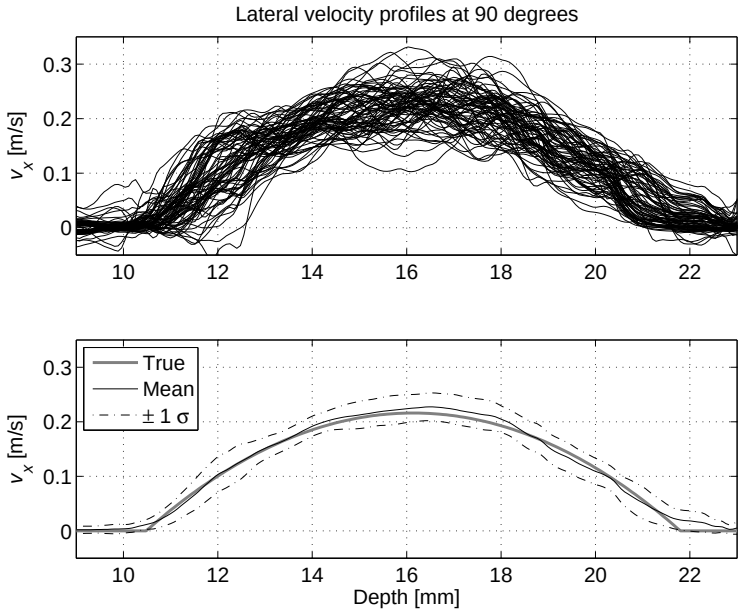

Fig. 8. TO estimated lateral velocities for 75 flow profiles with a beam-to-flow angle of 90° (top). Mean estimate ± one standard deviation and expected theoretical velocity profile (bottom).

C. Acquisition of spectral velocity data for evaluating aortic aneurysms

1) Background: Medical ultrasound is commonly used to study and diagnose cardiovascular disease because it provides a non-invasive, real time imaging technique to visualize pathology in both the solid arterial wall and abnormal flow patterns in the blood. One of the first attempts to quantify blood velocities was performed by Satomura [28] using a continuous wave Doppler system and estimating the flow pattern from the Doppler spectrum. This system was then further developed into a pulsed wave system able to probe at a certain depth and thereby the possibly to investigate individual blood vessels, mapping the velocity and time evolution of the velocity [29]. Blood consists of many scatterers, and it is the reflective scattering from these that constitutes the flow signal from the blood. The basic principle in spectral recordings using the pulsed wave system is that a number of pulses are emitted into the tissue from the same position. The received backscattered signal is then sampled at the time relative to the emission, yielding a frequency that is proportional to the blood velocity [30].

In the following application, the developed system is used to acquire RF signals in order to obtain patient-specific spectral measurements to calculate velocity profiles in the human abdominal aorta. These velocity profiles are intended to be applied as inlet condition for the pulsating blood in a patient-specific fluid-structure interaction model which can be used as part of the diagnostic process of cardiovascular disease.

The finite element (FE) analysis of the combination of solid arteries (structure) and flowing blood (fluid) has developed over the years with different purposes and spectral measurements has been used as a tool to construct realistic numerical models of the fluid-structure interaction [31]. For example in the clinical quantification of coronary plaque progression, ultrasound simulation of velocity fields based on computational fluid dynamics [32], and rupture risk assessment of abdominal aortic aneurysms [33]. The spectral measurements are rarely used for other

purposes than determination of inlet conditions in these simulation models. With the versatile data acquisition system the large amount of data can be used for further analysis of modeling results. For example the wall displacement during the heart cycle can be measured and compared to simulated results providing a method to evaluate the performance of different structural material models.

2) Method: Data for the presented application of the research interface origins from a study on the biomechanical properties of the human abdominal aorta. The total data set was collected from a group of 11 healthy volunteers and consists of a magnetic resonance angiography and an ultrasound scan using the Spectral Doppler method to obtain measurements of the blood flow in the abdominal aorta. To demonstrate the use of the research data acquisition system the collection and processing of Spectral Doppler measurements from a 53 year old healthy male is presented.

The data acquisition was performed using a convex array transducer, BK8803 (BK-Medical, Herlev, Denmark) with a center frequency of 5 MHz. Using the Console a scan sequence containing B-mode and Doppler mode was specified. The pulse repetition frequency of the Spectral Doppler mode was set to 2 kHz, interleaving the acquisition of the individual scan lines from the two basic modes.

The same clinician performed all ultrasound scans to avoid differences in scanning technique from subject to subject. During the scans the clinician was asked only to adjust the size of the range gate, angling of the flow direction relative to the beam direction without allowing beam steering, and the overall gain using the only the Console. The reason for this was to standardize the scanning sequence, and only allow changes in the scanner setup that would not affect the data acquisition method. This limitation of manipulation with control parameters was decided with the intention of providing clinicians with a simple method to collect flow data for investigation of pathological flow patterns. Fig. 9 illustrates the Console interface and the different control parameters available for the clinician to adjust are listed to right of the duplex image display. Four data sequences of Spectral Doppler spectrum data and B-mode image data were obtained from the volunteer, and using the Matlab SDK RF data for each sequence was acquired and stored subsequently.

The acquisition time for each blood flow measurement was set to five seconds in the CFU Data Grabber corresponding to approximately five cardiac cycles. The volunteer was asked to stop breathing during each of the acquisitions to ensure as little artifacts from movement of the surrounding abdominal structures as possible. Each of the collected RF data sets for velocity estimation of the blood flow is a matrix with 10.240 lines and 1062 samples in each line. Subsequently, data was processed offline to inspect the quality of the RF data and to calculate the Spectral density spectrogram of the received flow signals. Each Spectral density spectrum was calculated from 16 emissions each having an overlap of 50%. Each Spectral density spectrum had a length of 128 samples and the time between spectra was five milliseconds resulting in 1011 spectra.

3) Results: Fig. 10 shows the computed Spectral density spectrum from the acquired RF data sequence corresponding to the setup displayed in Fig. 9. Comparing the two Spectral density spectra a high similarity is seen. In both spectra the peak velocity is approximately 68 m/s in the forward flow direction (from proximal to distal

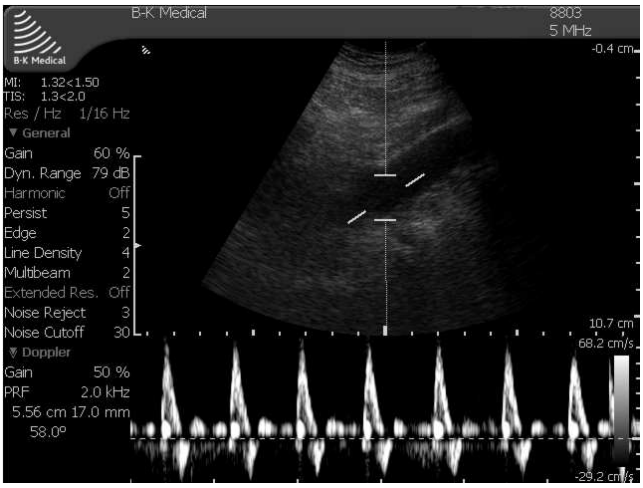

Fig. 9. Duplex interface on the Profocus scanner during the data acquisition. All parameters listed to the left are also registered in the usecase produced at each data acquisition sequence.

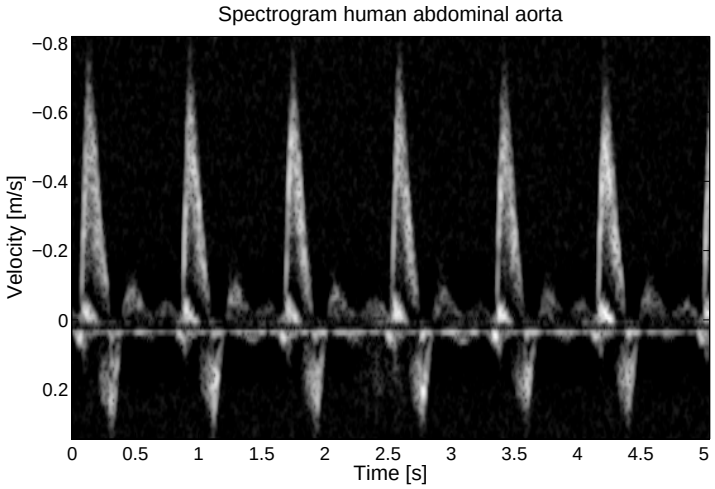

Fig. 10. Spectral density spectrum of the blood velocity in the abdominal aorta using the extracted research data set from the scanning sequence corresponding to the interface shown in Fig. 9.

relative to the heart) and a peak velocity in the backward flow direction of approximately 29 m/s. In general the peak forward velocity in the abdominal aorta is around 0.5-0.6 m/s with a mean velocity of 0.08-0.2 m/s [34]. So, this volunteer show a slightly increased velocity in the abdominal aorta compared to the general case.

The velocity change can be used to establish a patient-specific inlet condition for each patient-specific abdominal aortic geometry constructing a realistic simulation model for diagnostic purposes. This is done by assuming that the inlet cross-section is rotational symmetric, the flow is fully-developed, and that the blood is a Newtonian fluid in which case Womersleys theorem can be used to determine the flow pattern during the cardiac cycle.

4) Summary: The research data acquisition system facilitates access to raw flow data from Spectral Doppler spectral measurements which can be directly applied in a finite element model for simulation of patient-specific

flow and biomechanical properties of the arterial wall. This is an important step towards a realistic patient-specific simulation model to support diagnosis of various cardiovascular diseases which can be introduced to and used directly in the clinic.

V. Conclusions

A versatile and open architecture research data acquisition system using a commercially available medical ultrasound scanner has been implemented. The system consists of standard PC and a BK Medical ProFocus ultrasound scanner. The system uses an open architecture that allows acquisition of data for experimental research, such as developing new imaging processing algorithms. With the system users can tailor the data acquisition to fit their working environment while still maintain the clinical integrity of using a robust medical device. This will allow researchers and clinicians to rapidly develop applications and move them relatively easy to the clinic.

The clinical usability of the scanner, including the frame rate, is unaffected by data acquisition. Furthermore the system allows remote control of basic scanner operation, and software for easy access of the complete control parameter set. The system allows access to beamformed radio frequency data and provides flexible manipulation of control parameters such as filtering, compression, transmit level, excitation waveform, beam angle, and focal depth etc. The system offers high speed data acquisition, beneficial for clinical scanning and system evaluation.

Data acquisition can be controlled through a GUI running on the PC or using third party products, such as Matlab. The developed software development toolkit (SDK) will give researchers and clinicians the ability to utilize Matlab for data analysis and flexible manipulation of control parameters. Due to these advantages, research projects have successfully used the system to test and implement their customized solutions for different applications. We believe that the system can contribute to accelerated advancements in ultrasound imaging by allowing more ultrasound researchers to test and clinically evaluate promising new applications.

Acknowledgment

This work is supported by grant 08-036099 from the Danish Science Foundation and by BK Medical Aps, Herlev, Denmark.

References

[1] J. A. Jensen, O. Holm, L. J. Jensen, H. Bendsen, H. M. Pedersen, K. Salomonsen, J. Hansen, and S. Nikolov, “Experimental ultrasound system for real-time synthetic imaging,” in *Proc. IEEE Ultrason. Symp.*, vol. 2, 1999, pp. 1595–1599.

[2] J. A. Jensen, O. Holm, L. J. Jensen, H. Bendsen, S. I. Nikolov, B. G. Tomov, P. Munk, M. Hansen, K. Salomonsen, J. Hansen, K. Gormsen, H. M. Pedersen, and K. L. Gammelmark, “Ultrasound Research Scanner for Real-time Synthetic Aperture Image Acquisition,” *IEEE Trans. Ultrason., Ferroelec., Freq. Contr.*, vol. 52 (5), pp. 881–891, May 2005.

[3] J. A. Jensen, H. Holten-Lund, R. T. Nielson, B. G. Tomov, M. B. Stuart, S. I. Nikolov, M. Hansen, and U. D. Larsen, “Performance of SARUS: A Synthetic Aperture Real-time Ultrasound System,” in *Proc. IEEE Ultrason. Symp.*, Oct. 2010, p. published.

[4] V. Shamdasani, U. Bae, S. Sikdar, Y. M. Yoo, K. Karadayi, R. Managuli, and Y. Kim, “Research interface on a programmable ultrasound scanner,” *Ultrasonics*, vol. 48, no. 3, pp. 159–168, 2008.

[5] S. Brunke, M. Insana, J. Dahl, C. Hansen, M. Ashfaq, and H. Ermert, “Errata - an ultrasound research interface for a clinical system,” *Ultrasonics, Ferroelectrics and Frequency Control, IEEE Transactions on*, vol. 54, no. 1, pp. 198–210, January 2007.

[6] T. Wilson, J. Zagzebski, T. Varghese, Q. Chen, and M. Rao, "The ultrasonix 500rp: A commercial ultrasound research interface," *Ultrasonics, Ferroelectrics and Frequency Control, IEEE Transactions on*, vol. 53, no. 10, pp. 1772–1782, October 2006.

[7] J. A. Jensen and N. B. Svendsen, "Calculation of Pressure Fields from Arbitrarily Shaped, Apodized, and Excited Ultrasound Transducers," *IEEE Trans. Ultrason., Ferroelec., Freq. Contr.*, vol. 39, pp. 262–267, 1992.

[8] J. A. Jensen, "Field: A Program for Simulating Ultrasound Systems," *Med. Biol. Eng. Comp.*, vol. 10th Nordic-Baltic Conference on Biomedical Imaging, Vol. 4, Supplement 1, Part 1, pp. 351–353, 1996.

[9] C. Passmann and H. Ermert, "A 100-MHz ultrasound imaging system for dermatologic and ophthalmologic diagnostics," *IEEE Trans. Ultrason., Ferroelec., Freq. Contr.*, vol. 43, pp. 545–552, 1996.

[10] C. H. Frazier and W. D. O'Brien, "Synthetic aperture techniques with a virtual source element," *IEEE Trans. Ultrason., Ferroelec., Freq. Contr.*, vol. 45, pp. 196–207, 1998.

[11] S. I. Nikolov and J. A. Jensen, "Virtual ultrasound sources in high-resolution ultrasound imaging," in *Proc. SPIE - Progress in biomedical optics and imaging*, vol. 3, 2002, pp. 395–405.

[12] ——, "3D synthetic aperture imaging using a virtual source element in the elevation plane," in *Proc. IEEE Ultrason. Symp.*, vol. 2, 2000, pp. 1743–1747.

[13] M. H. Bae and M. K. Jeong, "A study of synthetic-aperture imaging with virtual source elements in B-mode ultrasound imaging systems," in *IEEE Trans. Ultrason., Ferroelec., Freq. Contr.*, vol. 47, 2000, pp. 1510–1519.

[14] J. Kortbek, J. A. Jensen, and K. L. Gammelmark, "Synthetic aperture sequential beamforming," *J. Acoust. Soc. Am.*, p. Submitted, 2009.

[15] M. C. Hemmsen, J. M. Hansen, and J. A. Jensen, "Synthetic aperture sequential beamformation applied to medical imaging using a multi element convex array transducer," "October" "2011", "Submitted to IEEE Ultrason. Symp, 16 - 18 October 2011, Kobe, Japan".

[16] J. M. Hansen and J. A. Jensen, "An object-oriented multi-threaded software beamformation toolbox," Feb. 2011, submitted to SPIE Medical Imaging, 12 -17 February 2011, Lake Buena Vista (Orlando), Florida, USA.

[17] E. G. Grant, C. B. Benson, G. L. Moneta, A. V. Alexandrov, J. D. Baker, E. I. Bluth, B. A. Carroll, M. Eliasziw, J. Gocke, B. S. Hertzberg, S. Katanick, L. Needleman, J. Pellerito, J. F. Polak, K. S. Rholl, D. L. Wooster, and R. E. Zierler, "Carotid Artery Stenosis: Gray-Scale and Doppler US Diagnosis - Society of Radiologists in Ultrasound Consensus Conference," *Radiology*, vol. 229, no. 2, pp. 340–346, 2003.

[18] M. D. Fox, "Multiple crossed-beam ultrasound Doppler velocimetry," *IEEE Trans. Son. Ultrason.*, vol. SU-25, pp. 281–286, 1978.

[19] G. E. Trahey, J. W. Allison, and O. T. von Ramm, "Angle independent ultrasonic detection of blood flow," *IEEE Trans. Biomed. Eng.*, vol. BME-34, pp. 965–967, 1987.

[20] V. L. Newhouse, D. Censor, T. Vontz, J. A. Cisneros, and B. B. Goldberg, "Ultrasound Doppler probing of flows transverse with respect to beam axis," *IEEE Trans. Biomed. Eng.*, vol. BME-34, pp. 779–788, 1987.

[21] O. Bonnefous, "Measurement of the complete (3D) velocity vector of blood flows," in *Proc. IEEE Ultrason. Symp.*, 1988, pp. 795–799.

[22] J. A. Jensen, "Directional velocity estimation using focusing along the flow direction: I: Theory and simulation," *IEEE Trans. Ultrason., Ferroelec., Freq. Contr.*, vol. 50, pp. 857–872, 2003.

[23] J. A. Jensen and P. Munk, "A New Method for Estimation of Velocity Vectors," *IEEE Trans. Ultrason., Ferroelec., Freq. Contr.*, vol. 45, pp. 837–851, 1998.

[24] M. E. Anderson, "Multi-dimensional velocity estimation with ultrasound using spatial quadrature," *IEEE Trans. Ultrason., Ferroelec., Freq. Contr.*, vol. 45, pp. 852–861, 1998.

[25] J. Udesen and J. A. Jensen, "Investigation of Transverse Oscillation Method," *IEEE Trans. Ultrason., Ferroelec., Freq. Contr.*, vol. 53, pp. 959–971, 2006.

[26] J. Udesen, M. B. Nielsen, K. R. Nielsen, and J. A. Jensen, "Examples of *In Vivo* blood vector velocity estimation," *Ultrasound in Med. & Biol.*, vol. 33, no. 4, pp. 541–548, 2007.

[27] J. A. Jensen, "A New Estimator for Vector Velocity Estimation," *IEEE Trans. Ultrason., Ferroelec., Freq. Contr.*, vol. 48, no. 4, pp. 886–894, 2001.

[28] S. Satomura, "Ultrasonic Doppler method for the inspection of cardiac functions," *J. Acoust. Soc. Am.*, vol. 29, pp. 1181–1185, 1957.

[29] D. W. Baker, "Pulsed ultrasonic Doppler blood-flow sensing," *IEEE Trans. Son. Ultrason.*, vol. SU-17, pp. 170–185, 1970.

[30] J. A. Jensen, *Estimation of Blood Velocities Using Ultrasound: A Signal Processing Approach*. New York: Cambridge University Press, 1996.

[31] M. S. Olufsen, C. S. Peskin, W. Y. Kim, E. M. Pedersen, A. Nadim, and J. Larsen, "Numerical simulation and experimental validation of blood flow in arteries with structured-tree outflow conditions." *Ann Biomed Eng*, vol. 28, no. 11, pp. 1281–1299, 2000.

[32] A. Swillens, L. Lovstakken, J. Kips, H. Torp, and P. Segers, "Ultrasound simulation of complex flow velocity fields based on computational fluid dynamics," *Ultrasonics, Ferroelectrics and Frequency Control, IEEE Transactions on*, vol. 56, no. 3, pp. 546–556, 2009.

[33] E. Di Martino, G. Guadagni, A. Fumero, G. Ballerini, R. Spirito, P. Biglioli, and A. Redaelli, "Fluid-structure interaction within realistic three-dimensional models of the aneurysmatic aorta as a guidance to assess the risk of rupture of the aneurysm," *Medical engineering & physics*, vol. 23, no. 9, pp. 647–655, 2001.

[34] C. G. Caro, T. J. Pedley, R. C. Schroter, and W. A. Seed, "Mechanics of the circulation," in *Cardiovascular Physiology*, A. Guyton, Ed. Medical and Technical Publishers, 1974.

Paper II

In Vivo Evaluation of Synthetic Aperture Sequential Beamforming

Martin Christian Hemmsen, Peter Møller Hansen, Theis Lange, Jens Munk Hansen, Ye Li, Michael Bachmann Nielsen, and Jørgen Arendt Jensen

Ultrasound in Medicine and Biology

In review 2011

In Vivo Evaluation of Synthetic Aperture Sequential Beamforming

Martin Christian Hemmsen[a,b,*], Peter Møller Hansen[c], Theis Lange[d], Jens Munk Hansen[b], Michael Bachmann Nielsen[c], Jørgen Arendt Jensen[b]

[a]*Department of Electrical Engineering, Center for Fast Ultrasound Imaging, Technical University of Denmark, Kgs. Lyngby, Denmark.*
[b]*BK Medical, Herlev, Denmark*
[c]*Department of Radiology, Rigshospitalet, Copenhagen, Denmark.*
[d]*Department of Biostatistics, University of Copenhagen, Copenhagen, Denmark.*

Abstract

Ultrasound *in-vivo* imaging using Synthetic Aperture Sequential Beamformation (SASB) is compared to conventional imaging in a double blinded study using side-by-side comparisons. The objective is to evaluate if the image quality in terms of penetration depth, spatial resolution, contrast, and unwanted artifacts is comparable to conventional imaging. *In-vivo* data was acquired using a ProFocus ultrasound scanner (BK Medical, Herlev, Denmark) and a 192 element 3.5 MHz convex array transducer (Sound Technology Inc., PA 16801, USA). Data were acquired interleaved, ensuring that the exact same anatomical locations were scanned. Eighteen volunteers were scanned abdominally resulting in 84 image sequence pairs. Evaluation of image quality was performed by 5 medical doctors. Results show that image quality using SASB was significantly better than conventional imaging (p-value: < 0.01).

*Corresponding Author: Martin Christian Hemmsen, Ørsteds Plads, Bldg. 349, Technical University of Denmark, Kgs. Lyngby, Denmark; Email, mah@elektro.dtu.dk; Phone, +45 45255738

There was not a significant difference in penetration depth (p-value: 0.55). The study supports that *in-vivo* ultrasound imaging using SASB is feasible for abdominal imaging.

Keywords: Ultrasound imaging, Synthetic aperture sequential beamforming, In-vivo evaluation

---

Introduction

Conventional ultrasound imaging is technically intuitive and an easily implementable solution. The method creates an image by emitting a focused beam in one direction at a time, and sequentially acquires an image from consecutive scan lines. In receive mode, dynamic focus is used by adjusting the delays and number of active elements of the transducer as a function of the depth, to yield an optimal receive focus and a constant receive F-number. In transmit, usually the focus point is set in the middle of the region being imaged. The lateral beamwidth is the smallest at the focus point (and the best lateral resolution is obtained), while away from the focus point the lateral beamwidth increases. The spatial resolution of the ultrasound image can be improved by using several transmit beams (composite imaging) during the acquisition of a single scan line, each with a different transmit focus depth. It is employed in modern ultrasound imaging systems at the cost of a decrease in frame rate, proportionally to the number of transmit foci (Holm and Yao, 1997). An alternative way to obtain an appropriate spatial resolution, without the decrease in frame rate, is to use synthetic aperture techniques.

The basic idea in synthetic aperture techniques is to synthesize a large aperture by moving, or multiplexing, a small active aperture over a larger array (Sherwin et al., 1962). There are several variants of the technique for ultrasonic imaging, that all make it possible to generate images with dynamic focusing during both transmit and receive. The synthetic aperture focusing technique (SAFT) (Thomson, 1984) is the simplest synthetic aperture method, where each time only a single element is used for trans-

mission and reception. Simple transmit and receive electronics is needed, but it requires data memory for all N data recordings. The main disadvantage of SAFT is the low signal-to-noise ratio (SNR) and as a result, a poor contrast resolution. In multi-element synthetic aperture focusing (MSAF) a group of elements transmits and receives signals simultaneously for each emission, which increases acoustic power and signal-to-noise ratio (Karaman et al., 1995). Synthetic transmit aperture (STA) and Multi-element synthetic transmit aperture are methods where respectively one or a group of array elements transmit a pulse, and all aperture elements receive the echo signals(Gammelmark and Jensen, 2002, 2003). The advantage of this approach is that full dynamic focusing can be applied to transmit and receive, achieving the highest quality of image. The shortcoming is that N^2 echo recordings are required to synthesize an image. This disadvantage can be overcome to some extent, at the cost of image quality, if a sparse configuration is applied (Behar and Adam, 2005). Significant tissue motion can affect synthetic aperture images, as shown by Nock and Trahey (1992); Karaman et al. (1998) and Gammelmark and Jensen (2003). However, *in vivo* studies of STA imaging have been published with good results (Pedersen et al., 2007).

Recently Kortbek et al. (2009) introduced the concept of Synthetic Aperture Sequential Beamforming (SASB) to overcome the high system requirements of STA imaging. It was shown that for a multi element linear array transducer the lateral resolution could be made more range independent and improved significantly compared to conventional imaging. Hemmsen et al. (2011b) applied SASB to medical ultrasound imaging using convex array transducers. To investigate the viability of the technique *in vivo*, the pro-

cedure described by Hemmsen et al. (2010) for a small preliminary study were followed and the results show that the image quality is improved statistically significant using SASB compared to conventional imaging $p < 0.01$ (Hemmsen et al., 2011c).

In this paper a novel implementation of 2-dimensional SASB imaging is evaluated in a more comprehensive clinical trial using eighteen healthy volunteers and evaluated by ultrasound specialists (medical doctors). The method is investigated for abdominal imaging using a multi element convex array transducer, and it is compared to conventional convex array imaging. The investigation is based on a double blinded clinical evaluation using paired image sequences. A data acquisition system (Hemmsen et al., 2011a) capable of producing simultaneous recordings of the exact same locations using both techniques is used.

The manuscript is organized as follows. Section II presents the basic idea behind synthetic transmit aperture and synthetic aperture sequential beamforming, with focus on comparison of the system requirements for a real-time implementation. Section III presents the methods used for data acquisition and processing, followed by a description of the image assessment and statistical analysis. The results are presented in section IV and discussed in section V, followed by conclusions in section VI.

Theory

In multi-element synthetic aperture imaging the basic idea is to create a pressure wave from multiple elements with a focused transmission. The focal point is introduced as a virtual source, from which a spherical wave

emanates within a limited angular region (Passmann and Ermert 1996; Frazier and O'Brien 1998; Bae and Jeong 2000; Nikolov and Jensen 2000,2002) . In synthetic aperture sequential beamforming the concept of virtual sources is combined with a dual-stage procedure using two separate beamformers. In the initial stage a simple beamformer using a single focal point in both transmit and receive, creates a set of focused scan lines. Each sample in the focused scan lines contains information from image points within the focused beam. A single image point is therefore potentially represented in multiple first stage scan lines obtained from multiple emissions. The process of combining the information from multiple scan lines is done in the second stage beamformer. The second stage beamformer creates a set of high resolution image points by combining information from multiple first stage focused scan lines, which results in a dynamically expanding array as the image depth increases and a more range independent lateral resolution is obtained (Kortbek et al., 2009). Fig. 1 exemplifies the beamforming method for a three emission setup and a single image point. More details on this processing can be found in Kortbek et al. (2009) and Hemmsen et al. (2011b) . Fig. 2 illustrates a schematic diagram of the process for a sequential implementation that is used in this study.

Material and Methods

Eighteen healthy volunteers (fifteen males and three females, age range 23-34 years, all with normal Body Mass Index) entered the study after informed consent. They were scanned in supine position by an experienced physician.

Equipment and imaging set-up

The measurements were performed using a data acquisition system consisting of a 2202 ProFocus ultrasound scanner (BK Medical, Herlev, Denmark) equipped with a research interface connected to a standard PC (Hemmsen et al., 2010, 2011a). The system enables acquisition of several seconds of real-time beamformed radio frequency data, and it is remotely controlled through a developed Matlab Software Development Kit (MathWorks Inc., Natick, Mass., USA). Data can be acquired interleaved with identical excitation waveforms, TGC, and field-of-view on both an experimental and reference setup. In the following experiment the shoot sequence were configured such that one frame from one mode followed directly after the other. Hereby, images from exactly the same *in-vivo* view were obtained, enabling direct comparison of the methods. The depth of each scan was set to 14.6 cm and the interleaved frame rate was set to 5 frames/s, i.e., 5 conventional and 5 SASB frames/s. The chosen excitation waveform and transmit voltage is a preset standardized setting from the manufacturer and is the same for both the conventional and SASB imaging ($\pm$ 75 V).

In the following experiment an abdominal 3.5 MHz probe with a room-temperature vulcanization (RTV) lens, 3.5CL192-3ML (Sound Technology Inc., 1363 South Atherton St., State College, PA 16801, USA) transducer was used. Specification of the transducer and imaging setup can be found in Table 1.

Acoustic Output

Prior to conducting the *in-vivo* experiments, the acoustic outputs of the ultrasound scanner were measured for the imaging modes under investiga-

tion. The measured intensities need to satisfy preamendments upper limits regulated by the United States Food and Drug Administration (FDA, 1997), which have been introduced as safety guides to avoid damage to the tissue and pain to the patient. These limits concern the mechanical index, MI$\leq$ 1.9, the derated spatial-peak-pulse-average intensity, $I_{sppa} \leq 190\,W/cm^2$, and the derated spatial-peak-temporal-average intensity $I_{spta} \leq 720\,mW/cm^2$ (FDA, 1997).

The acoustic outputs were measured in a water tank using a high precision 3-dimensional position system and a HGL0400 hydrophone (Onda, Sunnyvale, CA, USA) by following the guidelines given by the American Institute of Ultrasound in Medicine (AIUM, 1998). The levels obtained for both imaging methods are listed in Table 2. These values are considerably lower than the FDA limits and *in-vivo* scanning is therefore safe using the present imaging modes.

Data Acquisition

Five different upper abdominal locations were scanned on each volunteer. The physician recorded two sequences of the right, middle and left hepatic veins and their entry in the inferior caval vein, one sequence of the liver alongside the right kidney, and one sequence of each kidney by itself. Fig. 3 illustrates the five scan locations and examples of B-mode images from each location using conventional imaging and SASB imaging. From each location a data sequence of 3 seconds was obtained. Due to the low frame rate and for an easier visual comparison of the two methods, the physician tried to hold the probe in the same view throughout the recording. A total of 85 recordings were acquired from the 18 volunteers.

Data Processing

The conventional data were beamformed by the ProFocus scanner using dynamic receive focusing. The RF signals were filtered using a manufacturer specified sliding filter and dynamic apodization using a modified Gaussian ($\alpha = 0.5$) window with raised edge levels was applied, which kept the receive F-number fixed until the receive aperture was fully opened. The first stage SASB data were beamformed by the ProFocus scanner using a fixed receive focus and a fixed modified Gaussian ($\alpha = 0.5$) apodization window with raised edge levels. The RF signals were filtered using the same manufacturer specified sliding filter as used for conventional imaging. The acquired RF data were subsequently extracted in Matlab and the SASB second stage RF data were generated using the acquired first stage RF data and the beamformation toolbox BFT3 (Hansen and Jensen, 2011). The second stage scan lines were defined with same location and direction as the first stage scan lines. Dynamic apodization was applied in the second stage using a Gaussian window ($\alpha = 0.5$). Note, however, that any number of scan lines or image points could have been beamformed for SASB imaging, from the acquired data.

Automatic TGC post correction

Before scan line conversion, the TGC was corrected according to depth to obtain homogeneous images. The automatic TGC correction simulates the TGC adjustments performed by a physician, eliminating the possible bias from human intervention. The correction was performed by calculating a mask to filter out strong and weak specular regions. The mask were then applied to the enveloped detected data and the median value of all lines for

all depths in the first recorded frame was found. The resulting curve was normalized to a maximum of one, inverted, and used to normalize all lines in all frames. Fig. 4, shows an example of a B-mode image before and after correction and the TGC curve.

Movie Generation

After TGC correction, image sequence pairs were normalized to an overall median envelope level, matching a gray tone of 70 (27% of the gray tone scale) after compression. Subsequently data was μ-law compressed, scan converted, and saved in an palindromatic order, to avoid annoying temporal discontinuities at the ends during visualization.

Image Assessment

Five medical doctors, all used to working with ultrasound, evaluated the image sequences. None of the five doctors had knowledge about synthetic aperture imaging, and none had seen any of the recorded sequences before. Evaluations were done blinded and each doctor sat isolated during the assessment, and was not allowed to discuss the sequences with the others, until all had finished. The assessment consisted of two parts - an assessment of image quality regarding spatial resolution, contrast, noise, formation of unwanted artifacts, and an assessment of penetration depth. Visualization and assessment were handled using the program IQap Hemmsen et al. (2010) .

Assessment of image quality was performed as a blinded comparison between matching sequence pairs, displayed side-by-side in random order. Each presentation consists of an image sequence generated using the conventional

and the new method. Each sequence pair was displayed two times with opposite left-right placement. This gave 170 presentations of the 85 sequence pairs. The doctors were asked to assess which of the two paired sequences was the best on a visual analog scale (VAS) (Altman, 1997), see Fig. 5a. Before the assessment the doctors were introduced to the program and the VAS scale was explained using Fig. 6. The figure instructs the doctor on how to interpret the scale when performing the assessments, but was hidden during the actual evaluation to avoid categorized data and get a smoother distribution. Before the actual assessment, five trial examples was shown to get the doctors acquainted with the task at hand and which types of images to expect.

Assessment of penetration depth was performed by presenting the 85 sequence pairs as single movies one after the other in random order. Hereby the doctors assessed 170 sequences without information about the technique used to generate each sequence. The doctors were asked: "To what depth is the visualization of the anatomic structures reliable for clinical use?" The penetration depth in cm was assessed as shown in Fig. 5b.

Statistical Analysis

The VAS scores were analyzed by a mixed effect linear model with a random effect (Laird and Ware 1982) for each image pair and each doctor, thereby accounting for the dependence induced by repeatedly scoring the same image pair and collecting multiple scores from the same doctor. Since all image pairs were shown both with the SASB image on the left and on the right it is not necessary to further control for any left/right differences. The parameter of interest is the intercept, which captures the average score

and will be negative if SASB is preferred to conventional imaging. Note that the use of the mixed effect model solely was to account for dependencies induced by image pair and doctor and thereby providing a valid confidence interval for the intercept. The model fit was assessed by Q-Q plots (Wilk and Gnanadesikan, 1968) to check for normality of the data. As a further robustness check the analysis was repeated with a transformed score (the square root and negative square root of positive and negative scores, respectively). In addition Wilcoxon tests were performed for each doctor and side (SASB on left or right) separately. Within these stratums the observations are independent and p-values for the hypothesis that the two methods are equally good (i.e. probability of a positive score equal the probability of a negative score) are therefore readily available. The depth scores given to SASB and conventional imaging were initially subtracted from each other and the resulting differences were analyzed as described above. The statistical data analysis language R version 2.12.2 (http://www.r-project.org/) was used for statistical computations.

Results

Both the conventional and SASB images were generally of good quality and undoubtedly applicable for clinical imaging.

Image quality

Of the 425 image quality ratings, 81 favored conventional imaging, 232 favored SASB and 112 images were rated equally good. The distribution of ratings from the individual doctors are shown in Fig. 7. The statistical analysis show that the average VAS score is significantly negative (p-value:

0.0005) and estimated to be -3.5 (95% CI: -5.5; -1.5). The analysis of the transformed score yields qualitatively the same result and the 10 Wilcoxon tests performed in each stratum defined by doctor id and side are all significant (p-values ranging from 10^{-14} to 0.025). Thus, the data clearly show that SASB is preferred compared to conventional imaging. However, there is a substantial variance on the individual scores. The model predicts that for a new image pair, rated by a new doctor, there is 70% probability that the doctor will prefer the SASB image and 30% probability of prefering the conventional image.

Penetration

The differences in penetration depths between the two techniques are shown in Fig. 8. The analysis of the depth scores showed that the average difference is insignificant (p-value: 0.55) and estimated to be 0.37 mm (95% CI: -0.83; 1.6 mm).

Discussion

The major benefit with SASB compared to STA imaging is a reduced system requirement obtained through a massive data reduction by the sequential beamforming. SASB can be implemented using an analog beamformer with a fixed delay and apodization profile and a single A/D converter. After A/D conversion the data is sent to the second stage beamformer and a high resolution image is sequentially build up over several transmissions. The system requirements for the digital part of the beamforming, is limited to a single receive channel, and requires a dynamical beamformer with just one time-of-flight (TOF), calculation for each image point and emission. In contrary

to STA that needs N TOF calculations per image point and emission. Further, SASB only needs one channel of data in memory, where STA needs N channels.

In this study SASB were compared to conventional imaging to determine if the image quality using SASB is at least as good as using conventional imaging. In the study medical doctors evaluated sequences generated with SASB imaging to be significantly better than sequences generated with conventional imaging. The results significantly show that SASB can be used in medical ultrasound imaging. The worry, that tissue motion would make coherent summation of samples and, thereby, image formation, impossible, can be discarded for the abdominal images generated in this study. The clinical evaluation performed by the medical doctors showed no difference in penetration depth.

Conclusions

Ultrasound imaging using synthetic aperture sequential beamforming has been demonstrated and evaluated in an *in vivo* double blinded clinical trial compared to conventional ultrasound imaging. The result of the statistical evaluation showed that SASB imaging can obtain satisfying penetration within the current intensity limits. Furthermore, the image quality evaluation showed highly significant improvement in SASB images compared with conventional images. One should be careful about interpreting the absolute VAS values, since the interobserver variation in VAS scale interpretation is always large. The statistical model predicts that for a new image pair, rated by a new doctor, there is a 70% probability that the doctor will prefer the

SASB image compared to the conventional image.

Acknowledgements

Thanks are due to M.D. Dr. Med. Flemming Jensen, M.D. Sonia Branci, M.D. Rikke Norling, and M.D. Martin Lundsgaard Hansen for evaluating the ultrasound images and to the volunteers for participating. This work is sponsored by grant 08-036099 from the Danish Ministry of Science and Technology and by BK Medical ApS, Herlev, Denmark.

References

AIUM. Acoustic output measurement standard for diagnostic ultrasound equipment. Tech. rep., American Institute of Ultrasound in Medicine & National Electrical Manufacturers Association, 1998.

Altman DG. Practical Statistics for Medical Research. Vol. 14. Chapman and Hall / CRC, London, 1997.

Bae MH, Jeong MK. A study of synthetic-aperture imaging with virtual source elements in B-mode ultrasound imaging systems. In: IEEE Trans. Ultrason., Ferroelec., Freq. Contr. Vol. 47, 2000. pp. 1510–1519.

Behar V, Adam D. Optimization of sparse synthetic transmit aperture imaging with coded excitation and frequency division. Ultrasonics, 2005;4310:777–788.

FDA. Information for manufacturers seeking marketing clearance of diagnostic ultrasound systems and transducers. Tech. rep., Center for Devices and Radiological Health, United States Food and Drug Administration, 1997.

Frazier CH, O'Brien WD. Synthetic aperture techniques with a virtual source element. IEEE Trans. Ultrason., Ferroelec., Freq. Contr., 1998;45:196–207.

Gammelmark KL, Jensen JA. Multi-element synthetic transmit aperture imaging using temporal encoding. In: Proc. SPIE: Progress in biomedical optics and imaging. Vol. 3, 2002. pp. 25–36.

Gammelmark KL, Jensen JA. Multielement synthetic transmit aperture

imaging using temporal encoding. IEEE Trans. Med. Imag., 2003;224:552–563.

Hansen JM, Jensen JA. An object-oriented multi-threaded software beamformation toolbox, 2011. Submitted to SPIE Medical Imaging, 12 -17 February 2011, Lake Buena Vista (Orlando), Florida, USA.

Hemmsen MC, , Nikolov SI, Pedersen MM, Pihl MJ, Enevoldsen MS, Hansen JM, Jensen JA. Implementation of a versatile research data acquisition system using a commercially available medical ultrasound scanner. IEEE Trans. Ultrason., Ferroelec., Freq. Contr., 2011a:Submitted.

Hemmsen MC, Hansen JM, Jensen JA. Synthetic Aperture Sequential Beamformation applied to medical imaging using a multi element convex array transducer. In: Proc. IEEE Ultrason. Symp., 2011b. p. Submitted.

Hemmsen MC, Hansen PM, Lange T, Hansen JM, Nielsen MB, , Jensen JA. Preliminary In-Vivo evaluation of Synthetic Aperture Sequential Beamformation using a multielement convex array. In: Proc. IEEE Ultrason. Symp., 2011c. p. Submitted.

Hemmsen MC, Petersen MM, Nikolov SI, B. M, Nielsen, Jensen JA. Ultrasound image quality assessment: A framework for evaluation of clinical image quality. In: Proceedings of SPIE–the international society for optical engineering. Vol. 76291. Medical Imaging 2010: Ultrasonic Imaging, Tomography, and Therapy, 2010. pp. 76290C–12.

Holm S, Yao H. Improved framerate with synthetic transmit aperture imaging

using prefocused subapertures. In: Proc. IEEE Ultrason. Symp., 1997. pp. 1535–1538.

Karaman M, Li PC, O'Donnell M. Synthetic aperture imaging for small scale systems. IEEE Trans. Ultrason., Ferroelec., Freq. Contr., 1995;42:429–442.

Karaman M, Ş. Bilge H, O'Donnell M. Adaptive multi-element synthetic aperture imaging with motion and phase aberation correction. IEEE Trans. Ultrason., Ferroelec., Freq. Contr., 1998;42:1077–1087.

Kortbek J, Jensen JA, Gammelmark KL. Synthetic aperture sequential beamforming. Ultrasonics, 2009:Submitted.

Laird NM, Ware JH. Random-Effects Models for Longitudinal Data. Biometrics., 1982;384:963–974.

Nikolov SI, Jensen JA. 3D synthetic aperture imaging using a virtual source element in the elevation plane. In: Proc. IEEE Ultrason. Symp. Vol. 2, 2000. pp. 1743–1747.

Nikolov SI, Jensen JA. Virtual ultrasound sources in high-resolution ultrasound imaging. In: Proc. SPIE - Progress in biomedical optics and imaging. Vol. 3, 2002. pp. 395–405.

Nock LF, Trahey GE. Synthetic receive aperture imaging with phase correction for motion and for tissue inhomogenities - part I: basic principles. IEEE Trans. Ultrason., Ferroelec., Freq. Contr., 1992;39:489–495.

Passmann C, Ermert H. A 100-MHz ultrasound imaging system for derma-

365 tologic and ophthalmologic diagnostics. IEEE Trans. Ultrason., Ferroelec.,
366 Freq. Contr., 1996;43:545–552.

367 Pedersen MH, Gammelmark KL, Jensen JA. In-vivo evaluation of convex
368 array synthetic aperture imaging. Ultrasound Med. Biol., 2007;33:37–47.

369 Sherwin CW, Ruina JP, Rawcliffe D. Some early developements in synthetic
370 aperture radar systems. IRE Trans. Mil. Elect., 1962;MIL-62:111–115.

371 Thomson R. Transverse and longitudinal resolution of the synthetic aperture
372 focusing technique. Ultrasonics, 1984;22:9–15.

373 Wilk MB, Gnanadesikan R. Probability plotting methods for the analysis of
374 data. Biometrika, 1968;551:1–17.

Figure Captions

Figure 1: Illustration of SASB beamforming for a three emission setup. The elements contributing to the three emissions are shown in shades of gray. From each of the three emissions a scan line is created by the first stage beamformer, with reference position in $\vec{r}_\theta$, and a fixed transmit and receive focus in $\vec{r}_{vs}$. This creates a set of focused scan lines, where each point in a focused scan line contains information from a set of spatial positions, shown by the dotted lines. The single image point, $\vec{r}_{ip}$, is therefore represented in both the black and dark gray scan line. The second stage beamformer determines which first stage scan lines that contain information about a given image point, and by summing these contributions a high resolution image point is obtained.

Figure 2: Schematic illustration of a sequential implementation of SASB imaging. At each emission event, a wave is transmitted from a group of elements, and the echoes are recorded by the same group of elements. The echoes from each emission are beamformed along the scan line direction with the same fixed delay profile as used in transmit, creating a virtual source. The resulting data is subsequently again beamformed with focus at each pixel in the image, producing the low resolution images, and these images are finally summed coherently to form the displayed high resolution image.

Figure 3: The images, next to the torso illustrating the scan locations, shows in (a) Transverse scanning of liver, (b) Transverse scanning of liver using different angulation of the transducer, (c) Longitudinal scan-

ning of the right kidney with adjacent liver, (d) Longitudinal scanning of right kidney, and in (e) Longitudinal scanning of left kidney with adjacent spleen.

Figure 4: Automatic TGC post correction. (a) shows the B-mode image prior to TGC correction, (b) shows the TGC curve expressed in dB, and (c) shows the same image as in (a) after TGC correction.

Figure 5: Screen shots from IQap. (a) Visualization of an image pair for overall image quality evaluation. The scale used for scoring is shown in the bottom and the control panel for navigating the sequences are shown in the lower right corner. (b) Visualization of an image for penetration evaluation. The bar used for scoring is shown across the image and the control panel for navigating the sequences are shown in the lower right corner.

Figure 6: Visual Analog Scale used for assessment of image quality.

Figure 7: Distribution of pooled answers from assessment of overall image quality. Negative values favor SASB.

Figure 8: Distribution of pooled answers from assessment of penetration. Negative values favor SASB.

Tables

Table 1: Measurement parameters.

Transducer Parameters (STI - 3ML 3.5CLA192)		
Pitch	0.33	mm
Elevation focus	65	mm
Number of elements	192	
Radius of curvature	60	mm
Field of view (FOV)	60.5	^{o}
Bandwidth at -6 dB	85	%

Imaging Set-up	Conventional	SASB
Focus Tx / Rx (mm)	105.5 / dynamic	70 / 70
F# Tx / Rx	5.0 / 0.8	2 / 2
Apodization Tx	Boxcar	Boxcar
Apodization Rx (dynamic)	Gauss, $\alpha = 0.5$	Gauss, $\alpha = 0.5$
$\text{Apodization}_{\text{2nd stage SASB}}$		Gauss, $\alpha = 0.5$

Scanner setting	
No. of emissions	384
No. of scan lines	384
Max. no. of active elem.	64

Table 2: Ultrasound intensities and mechanical index (MI).

	Conventional	SASB	Unit
$I_{sppa.3}$	28.49	69.74	W/cm^2
$I_{spta.3}$	0.21	0.66	mW/cm^2
MI	0.51	0.80	-

Figure

Click here to download Figure: Theory_SASB_illustrated.pdf

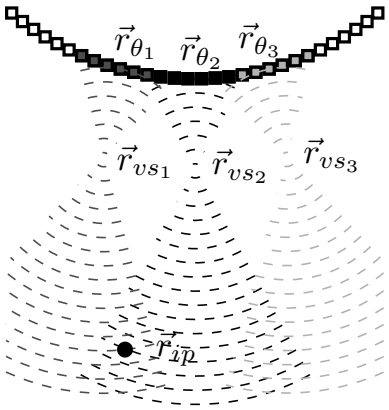

Figure

Click here to download Figure: Theory_Schematic.pdf

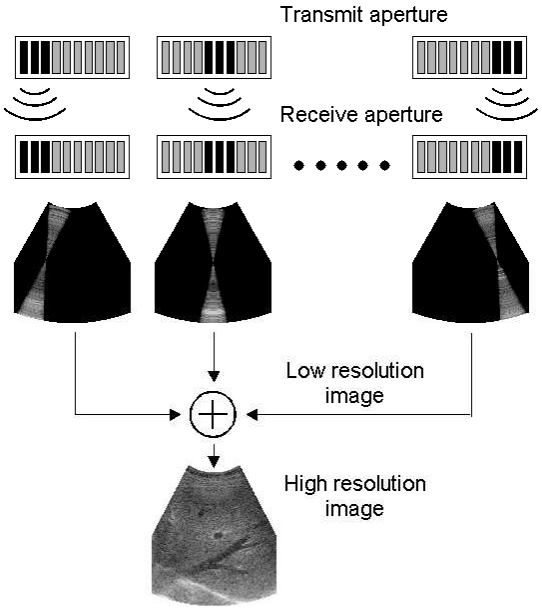

Figure

Click here to download Figure: Method_scan_locations.pdf

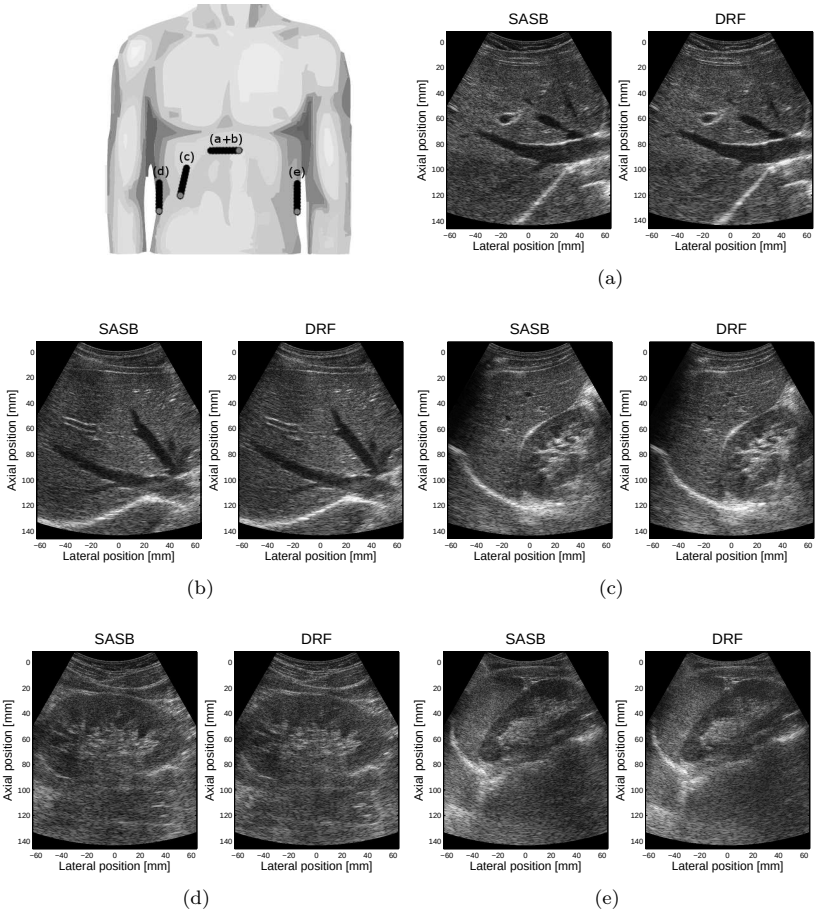

Figure
Click here to download Figure: Method_TGC.pdf

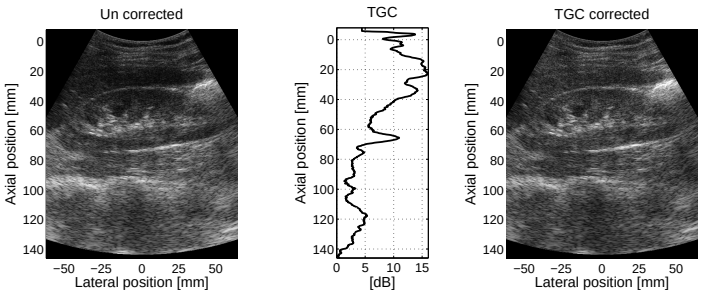

(a) (b) (c)

Figure

Click here to download Figure: Method_IQap.pdf

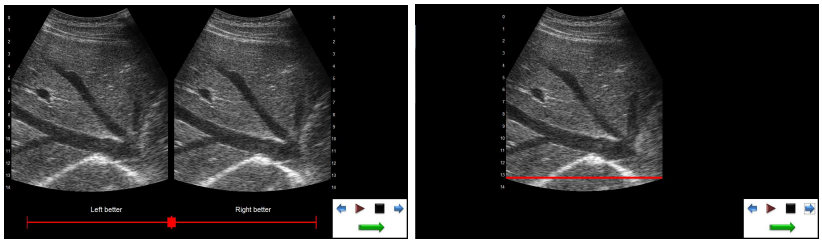

(a) (b)

Figure

Click here to download Figure: Method_IQap_VAS_slider.pdf

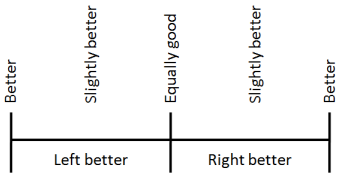

Figure

Click here to download Figure: Result_VAS.pdf

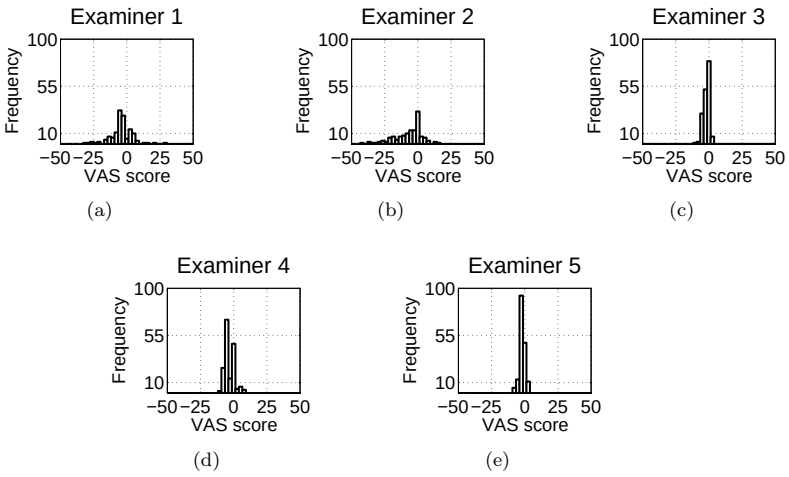

Figure
Click here to download Figure: Result_depth.pdf

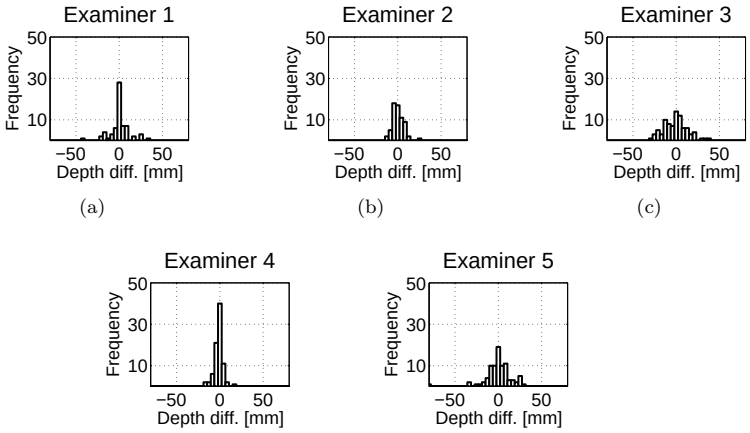

Paper III

Ultrasound Image Quality Assessment: A framework for evaluation of clinical image quality

Martin Christian Hemmsen, Mads Møller Pedersen, Svetoslav Ivanov Nikolov, Michael Bachmann Nielsen, and Jørgen Arendt Jensen

Proceedings of the SPIE Medical Imaging

Presented in San Diago, USA, 2009

Ultrasound Image Quality Assessment: A framework for evaluation of clinical image quality

Martin Christian Hemmsen[a,b], Mads Møller Pedersen[c], Svetoslav Ivanov Nikolov[b], Michael Backmann Nielsen[c], Jørgen Arendt Jensen[a]

[a]Center for Fast Ultrasound Imaging, Technical University of Denmark, 2800 Lyngby, Denmark
[b]B-K Medical A/S, Mileparken 34, 2730 Herlev, Denmark
[c]Department of Radiology, Rigshospitalet, 2100 Copenhagen, Denmark

ABSTRACT

Improvement of ultrasound images should be guided by their diagnostic value. Evaluation of clinical image quality is generally performed subjectively, because objective criteria have not yet been fully developed and accepted for the evaluation of clinical image quality. Based on recommendation 500 from the International Telecommunication Union - Radiocommunication (ITU-R) for such subjective quality assessment, this work presents equipment and a methodology for clinical image quality evaluation for guiding the development of new and improved imaging. The system is based on a BK-Medical 2202 ProFocus scanner equipped with a UA2227 research interface, connected to a PC through X64-CL Express camera link. Data acquisition features subject data recording, loading/saving of exact scanner settings (for later experiment reproducibility), free access to all system parameters for beamformation and is applicable for clinical use. The free access to all system parameters enables the ability to capture standardized images as found in the clinic and experimental data from new processing or beamformation methods. The length of the data sequences is only restricted by the memory of the external PC. Data may be captured interleaved, switching between multiple setups, to maintain identical transducer, scanner, region of interest and recording time on both the experimental- and standardized images. Data storage is approximately 15.1 seconds pr. 3 sec sequence including complete scanner settings and patient information, which is fast enough to get sufficient number of scans under realistic operating conditions, so that statistical evaluation is valid and reliable.

Keywords: Ultrasound imaging, Methodology for clinical quality assessment, Statistical analysis

1. INTRODUCTION

Researchers of new ultrasound imaging methods are interested in assessing the clinical quality of their method to increase the impact and attention it receives by manufacturers and other researchers. Such assessment of clinical quality is generally performed subjectively, because objective criteria have not yet been fully developed and accepted for the evaluation of clinical image quality. One major limitation with subjective assessment is, if the opinion is just based on an impression of quality, the usefulness of the assessment may be questionable (Vucich 1979, Barrett and Myers 2004, Månsson 2000). When judged by task-based critera - for example by the opinion of the radiologist relating to his/her ability to perceive certain anatomical details or features in the image and his/her confidence on the perception of these details, the assessment is more relevant.[1] Major difficulties accessing ultrasound data in the laboratory and clinic has not only limited the basic research, but also hindered the clinical testing of new ultrasound applications. In order to access raw ultrasound data, researchers have worked with ultrasound manufacturers to build custom ultrasound systems such as RASMUS,[2] but due to the size of the scanner it is inaccessible to the clinic. Recently a number of research interface platforms for

Further author information: (Send correspondence to Martin Christian Hemmsen)
Martin Christian Hemmsen: E-mail: mah@elektro.dtu.dk, Telephone: (+45) 45 25 57 38
Mads Møller Pedersen: E-mail: phd@medit.dk, Telephone: +45 35 45 18 23
Svetoslav Ivanov Nikolov: E-mail: sin@bkmed.dk, Telephone: +45 44 52 82 07
Michael Backmann Nielsen: E-mail: mbn@dadl.dk, Telephone: +45 35 45 35 45
Jørgen Arendt Jensen: E-mail: jaj@elektro.dtu.dk, Telephone: +45 45 25 39 24

clinical ultrasound scanners has been developed for systems such as Hitachi HiVision 5500,[?] Siemens Antares[3] and the Ultrasonix 500.[4] With the introduction of research interface platforms on clinicaly available scanners it is now possible to acquire and store data. However, for a system to be suitable for acquisition of data for clinical evaluations, the system has to keep factors, such as identical transducer, region of interest and recording time constant on both images. Another system requirement is the ability to get sufficient number of scans under realistic operating conditions, so that the statistical evaluation is reliable. Thus the data acquisition should, be capable of acquiring and storing sufficiently enough data, fast enough to conduct an ultrasound examination with multiple image sequences. The objective of this work is to develop a methodology and equipment for image quality evaluation for guiding the development of new and improved imaging methods.

2. EVALUATION METHODOLOGY

The main issue in performing a structured and fair comparison between images is to keep factors, such as transducer, scanner, region of interest and recording time constant. Other issues to consider is to get sufficient number of scans under realistic operating conditions and separating the developer and assessor in the evaluation process. To fullfill these demands we propose that evaluations of new methods is conducted in a three stage research, as illustrated on figure 1:

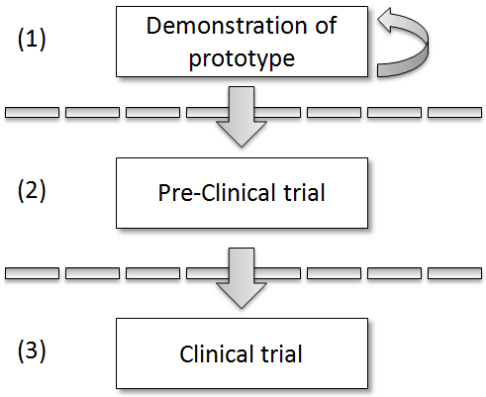

Figure 1: Diagram of the methodology

1. **Demonstration of prototype**, is the stage where developers demonstrate new imaging methods with measurements on phantoms and a few in-vivo images to demonstrate a workable prototype. In a collaboration between the developer and the ultrasound specialists, the new method's parameters are iteratively optimized to achieve the best possible setup. This stage ends and a pre-clinical study is started once all parameters are fixed.
2. **Pre-clinical trial**, is the stage where the relevance of a clinical investigation is tested. The necessary number of patients for the real clinical study is determined. This stage ends and the clinical trial begins when an exact clinical protocol is developed. It describes the method and its parameters in such a degree that the developer is and should be left out in the active part of the following research and should not have any influence on the outcome of the research in either data acquisition, any form of processing of it or evaluation.
3. **Clinical trial**, is the stage of research that determines the statistical significance of the new method. Assessment of the method is performed by a number of ultrasound specialists independent to the method. Furthermore, the assessors must be separeted from the specialists performing the ultrasound scanning, blinding them from the acquisition and any form of processing of it.

The evaluation methodology should ensure the validity of the assessment, as it separates the developer, investigator, and assessor once a research protocol has been established. This separation eliminates any confounding influence on the result from the developer and new processing schemes is not driven by the developers, but by the clinical value.

3. SYSTEM DESCRIPTION

3.1 Data Acquisition

The Ultrasound Research Interface (URI) consists of a commercially available ultrasound scanner (2202 ProFocus with a UA2227 research interface, BK-Medical, Herlev, Denmark) and a standard pc. The pc is connected to the scanner though a X64-CL Express camera link (Dalsa, Waterloo, Ontario, Canada) that allows the acquisition of digital beamformed RF echo data.

Figure 2 illustrates a simplified signal flow through the scanner to the research interface. A set of broadband pressure pulses centered at 2-10 MHz are transmitted into the tissue. As these pressure waves propagate, they are partially reflected at interfaces formed by two materials having different acoustic impedances. The transducer, in receive mode, detects the reflected echos as they impinge on the individual elements. Each of these signals arriving from the transducer elements are then processed by a beamformer to form one coherent signal. To e.g. form a 2-D image, this process is repeated for multiple angles or spatial positions. We refer to the echo data at the individual elements as "element RF data", element because it is the output of a single element, RF because the data spectrum is in the radio frequency band. The processed signal output from the beamformer is called "beamformed RF data" - this is the data that is accessible using the URI, and it will hereafter be referred to as RF data.

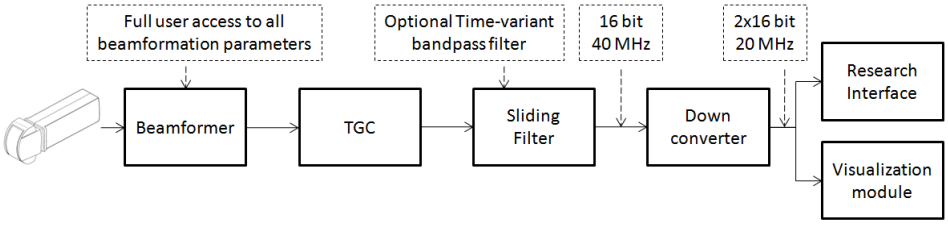

Figure 2: Simplified signal flow through the scanner

The RF data accessible through the URI is complex baseband signals stored as signed 16 bit integers, digitized at a rate of up to 40 samples/microsecond for all beam lines in a frame over a range of up to 22 cm. Users can also acquire pre-beamformed data by adjusting the receive aperture to a single element of interest. Acquired data is minimally processed because, aside from an optional time-variant bandpassfilter and beamforming, the only other processing is application of the time gain compensation (TGC) and transformation to I/Q data.

The acquisition of data is controlled via an in-house data grabber software module that features loading and saving of exact scanner settings for later experiment reproducibility. The data grabber module further enables the user to operate in two different modes:

1. **Standard mode**, in this mode the scanner is operating in factory default mode and standard scanner operation is available.
2. **Extended mode**, in this mode the user interface on the scanner is extented to enable control of various scanner settings, such as shoot sequence, receive- and transmit profiles, excitation waveforms and apodization functions.

Scanning in Standard mode the scanner is FDA approved and the grabber software captures standardized images as found in the clinic. Operating in Extended mode gives free access to all system parameters for beamformation, pulse shaping, and is applicable for clinical use. This enables researchers to capture experimental data that can be processed offline to evaluate new processing or beamformation methods. See Table 1 for a description of a subset of the parameter controls available for B-mode data acquisition in the extended scanner mode.

Data may be captured interleaved, switching between multiple basic mode setups, to maintain identical transducer, scanner, region of interest, and recording time on both the experimental- and standardized images. A basic mode setup is defined by the acquisition type, such as B-mode, M-mode, CFM-mode, power doppler

Table 1: Description of a subset of the parameter controls available in the extended scanner mode.

Parameter	Description
Dynamic focusing and dynamic apodization	Receive aperture dynamic focusing and aperture growth can be disabled individualy. When disabled, receive aperture size and focal position are fixed.
F#	Receive and transmit aperture size can be adjusted individualy. A maximum of 64 active elements is posible in standard mode and 128 elements in a synthetic aperture setting where rf data are acquired over two excitations.
Receive apodization	Receive apodization can be choosen from a fixed list of standard curves such as uniform or hamming weighting, or defined as a vector of element weights. If defined as a vector the curve can vary between individual image lines.
Receive time delay profile	Receive time delay profile can be specified individualy for each image line when dynamic focusing is disabled.
Line density	The image line density can be choosen from a range of one-half element pitch to two element pitch, in increments of one-half element pitch.
Speed of sound	Speed of sound can be defined in the interval from 1080 m/sec to 2500 m/sec.
Excitation waveform	Excitation waveform can be specified with a time resolution of 8.3 nsec and amplitude $\pm$ 1 or 0

mode or transverse oscillation. The ability to capture data interleaved enables processing on identical data in different ways, for assessment of different processing schemes.

The URI gives the researcher a high flexibility and enables multiple examinations to be performed in short time. The short time between examinations allows for a large database of processed images to be build; suitable for assessments where the specialists are off-site and where people who assess quality of the images must be independent of the aquisition. The length of the data sequences is only restricted by the memory on the external PC (one possible setup could be 20 seconds of interleave B-mode acquisition each with 192 image lines and depth of 11 cm). The data storage time is approximately 15.1 seconds for a 3 sec interleaved B-mode sequence including complete scanner settings and patient information. It is fast enough to obtain a sufficient number of scans under realistic operating conditions for valid and reliable statistical evaluations.

3.2 Data Management

Important aspects of data recording for clinical evaluations, is the ability to study under which conditions data were recorded (to be able to draw any conclusions from the data) and experiment reproducibility (to be able to reproduce the conclusions).

Data management is split into three new file formats

1. **RF data**, a file format with zero compression is developed to store the RF data from the scanner. The file format enables the user to load specified frames from a long data sequence without loading the entire data set first. RF data are stored as complex baseband signals as signed 16 bit integers.

2. **Scanner parameters**, are stored at recording time. The parameter set is a complete description of the scanner setup and includes information such as beam geometry, probe name, transmit frequency, and TGC settings. The scanner parameters aids the user to redo experiments, generate images from the RF data, as well as creating simulation comparisons using tool such as Field II.[5]

3. **User Interface setup**, are stored at recording time. The parameter set is a full description of the user specified scanner setup and includes information such as zoom, overall gain, persistence, and various other visualization settings.

As a separate part of the URI, an open source, Matlab toolbox for basic file handling of the files collected with the URI is developed and available at http://server.elektro.dtu.dk/www/mah/. The file handling uses an open format develped in C++, available as a library and source code.

3.3 Graphical User Interface

The URI provides a simple graphical user interface, which offers the capability to load a given predefined scanner parameter set on the scanner, grab data to memory, review acquired B-mode data, and save data to disk. Figure 3a illustrates the GUI interface. Figure 3b illustrates a review of a B-mode scan of the right kidney and part of the right liver lobe. The URI implements a process running in the background featuring a service for communication with Matlab. See section 3.4 for more details.

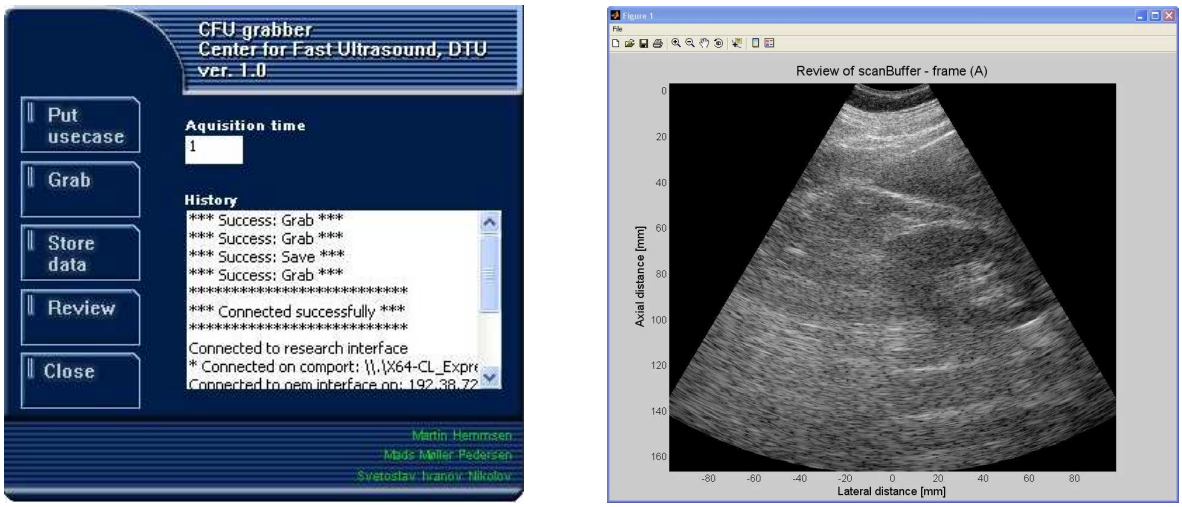

(a) (b)

Figure 3: (a) Illustrates the Graphical User Interface which offers the capability to load scanner settings, grab data, save data and review data. (b) illustrates a review image of a B-mode scan in a standard Matlab figure.

The GUI is implemented in C++ and source code is available at http://server.elektro.dtu.dk/www/mah/, enabling users who are familiar with the C++ programming language to immediately develop customized client applications.

3.4 Matlab Control

As a separate part of the URI, an open source Matlab-based toolbox for remote control of the scanner was developed. The tools are available at http://server.elektro.dtu.dk/www/mah/, and provide access to a communication library developed in C++, see Table 2 for a subset of communication commands.

Table 2: Description of a subset of the commands available in the communication library.

Command	Description
Grab	This command initiate the URI to grab data to memory. The duration in seconds is specified as argument two, e.g. `TCPClient('Grab',10)`.
Review	This command initiate the URI to scan convert the data stored in memory and display the first B-mode frame, e.g. `TCPClient('Review')`.
Save	This command initiate the URI to acquire the scanner settings and save them along with the data stored in memory to disk, e.g. `TCPClient('Save','C:test.cfu')`. The resulting files saved to disk is test.cfu, test.dat and test.oem.
Put Usecase	This command loads a complete scanner parameter set on the scanner, e.g. `TCPClient('Put_usecase','test.dat')`.
OEM message	This command queries a message to the scanner and waits for reply, e.g. `TCPClient('OEM Message','Query:Gain')`.

Because the files are open source, users can download the toolbox and make customized functions that e.g. sets the scanner in a certain mode or build scripts for automization of recording procedures with e.g. varying parameters between each data acquisition.

3.5 Data Analysis

Based on earlier publications of studies of clinical evaluation between pairs of sequences[6] and recommended testing procedurs according to recommendation 500 from ITU-R[7] for subjective quality assessment, we propose a methodology for the assessment of subjective image quality and penetration depth of medical ultrasound imaging.

3.5.1 Movie generation

Scan line conversion and movie generation are performed in Matlab. The movies are generated using Matlabs build-in functions `avifile` and `addframe`, using zero-compression, to generate Windows AVI files. Data from an acquisition with multiple parameter setup is split into two movies, one for each parameter setup. In this way it is possible to generate both single image movies and paired movies where images are shown side-by-side.

3.5.2 Image quality assessment

The presentation method for assessment of image quality combines elements of the simultaneous double stimulus for continuous evaluation (SDSCE) method (ITU BT.500-11, Section 6.4) and the double stimulus continuous quality scale (DSCQS) method (ITU BT.500-11, Section 5). For reference, it may be called the simultaneous stimulus relative quality scale (SSRQS) method.

As with the SDSCE method, each trial will involve a split-screen presentation of material from two movies. One of the movie sources will be the reference (i.e., source movie), while the other is the test movie. The reference could be a conventional setup or the setup to compare against, and the test movie is the method under investigation. For both methods the parameters are optimized according to the diagnostic performance of the recording medium. Unlike the SDSCE method, observers will be unaware of the scanner conditions represented by the two members of the movie pair and the left-right placement of the movies are randomized.

As with the DSCQS method, a test session comprises a number of presentations, each with a single observer. Unlike the DSCQS method where the assessor only observes the stimulus two times and rates each stimuli, the assessor is free to observe the stimuli until a mental measure of relative quality associated with the stimulus is obtained. Figure 4a shows a basic test cell illustrating the presentation structure of reference and test material. Reference and test movies are displayed as matching pairs side-by-side with random left-right placement. Stimuli are visualized in a palindromic (playback may be reversed in time) display fashion in order to minimize discontinuity at the joints.

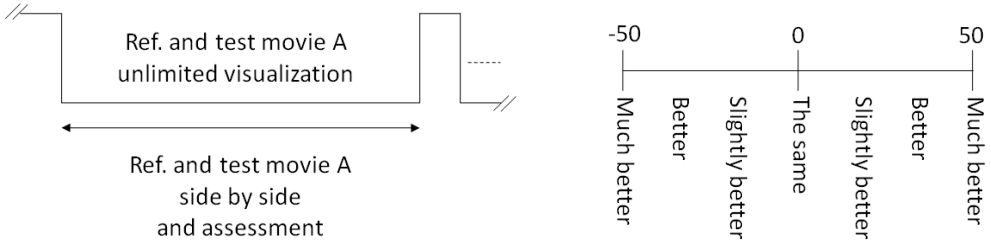

(a) (b)

Figure 4: Image quality assessment. (a) Basic test cell illustrating the presentation structure of reference and test material. Reference and test movies are displayed as matching pairs side-by-side with random left-right placement. Assessors are free to observe the stimuli until a mental measure of relative quality associated with the stimuli is obtained. (b) Visual analog scale (VAS) for image quality comparison between left and right stimuli.

The most often used criteria for manufacturers to implement new processing methods in their equipment is better diagnostic value compared to the existing method. Accordingly, a stimulus comparison scale, as described in ITU BT.500-11, Section 6.2, is recommended to be used. The specific judgement scale used is a non-categorical (continuous) scale, as described in ITU BT.500-11, Section 6.2.4.2, for reference it may be called Visual Analog Scale (VAS). During introduction of the assessors to the system and the rating methods, VAS is described

with the same number of labels as on the ITU-R categorical comparison scale but with slighty modified labels (much better, better, slightly better, the same, slightly better, better, much better) to report the existence of perceptible quality differences and allow the random left-right placement of the stimuli. After introduction and during assessment the labels are hidden to avoid categorized data and to get a smoother distribution. Figure 4b shows the associated VAS for image quality comparison between left and right stimuli.

Judgement sessions consists of a series of assessment trials. These should be presented randomized, blinded, and independently of each other and, preferably, in a different random sequence for each observer. As with the judgement method described in ITU-R TG6/9[8] Section 7.1.1.3, each session shall involve two types of trials: test trials and check trials. However, each trial involves the display of the full width of the stimuli. The purpose of the check trial is to assess a measure of judgement bias. For each method under investitation, the following test trials are required for each test sequence:

Table 3: Description of the required test trials for each test sequence under investigation.

Left stimuli	Right stimuli
Reference sequence	Test sequence
Test sequence	Reference sequence

Preferably, there would be at least 2 repetitions of each of the cases above. For each method under investigation, the following check trials are required for each test sequence:

Table 4: Description of the check trials for each test sequence under investigation.

Left stimuli	Right stimuli
Reference sequence	Reference sequence
Test sequence	Test sequence

Again, preferably there would be at least 2 repetitions of each of the cases above.

The judgement sessions should be divided into sittings not more than one hour in duration separated by 15-minute rest periods. Assessors are instructed to evaluate which of the two presented stimuli is better on a visual analog scale. Figure 5 illustrates the GUI assosiated with the rating process of image quality. The assessment of penetration depth follows the assessment of image quality.

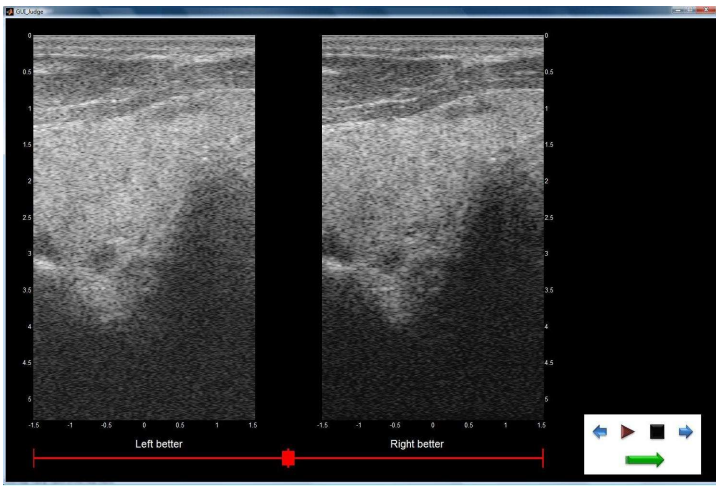

Figure 5: Illustration of the GUI assosiated with the rating process

3.5.3 Penetration assessment

The presentation method for assessment of penetration depth combines elements of the double stimulus continuous quality scale (DSCQS) method (ITU BT.500-11, Section 5) and the non-categorical judgement methods (ITU BT.500-11, Section 6.1.4.3). For reference, it may be called the sequential stimulus absolute scale (SSAS) method.

As with the DSCQS method, a test session comprises a number of presentations, each with a single observer. Unlike the DSCQS method where the assessor only observes the stimulus two times and rates each stimuli, the assessor is free to observe the stimuli until a mental measure of penetration depth associated with the stimuli is obtained. Figure 6a shows a basic test cell illustrating the presentation structure of reference and test material. Reference and test movies are displayed in a randomized sequential order. As with the SSRQS method stimuli are visualized in a palindromic display fashon. Observers will be unaware of the scanner conditions represented by the shown stimuli. Figure 6b shows the associated absolute penetration scale.

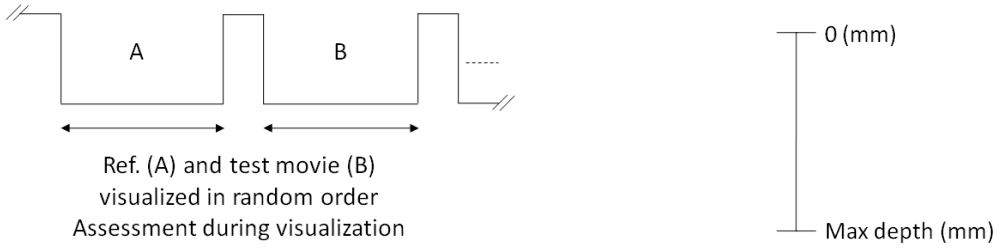

(a) (b)

Figure 6: Penetration depth assessment. (a) Basic test cell illustrating the presentation structure of reference and test material. Reference and test movies are displayed individualy in randomized order. Assessors are free to observe the stimuli until a mental measure of penetration depth associated with the stimuli is obtained. (b) Measure of penetration depth.

Besides the already described evaluation method in section 3.5.2 for comparison of image quality of new processing methods with conventional methods, it's interesting to investigate the penetration depth. Accordingly, a non-categorical judgement method as described in ITU BT.500-11, Section 6.1.4.2 is recommended to be used. The specific judgement scale used is a numerical scale, where assessors assign a value to each stimuli that reflect its penetration depth. The range of values are restricted to the same dimension as the dimension of the stimuli (e.g. 0 mm to 100 mm). During introduction of the assessors to the system and the rating methods, the assessors were asked: "After what depth is the image quality not usable for reliable diagnostic use?". After assessment the differences between depths in matching image pairs (reference and test stimuli) are used for the statistical analysis in order to avoid the bias from different assessors, who undoubtedly would have different opionions on how to answer the posed question.

Judgement sessions consists of a series of assessment trials. These should be presented randomized, blinded, and independently of each other and, preferably, in a different random sequence for each observer. For each method under investitation, the following test trials are required for each test sequence:

Table 5: Description of the required test trials for each test sequence under investigation.

Stimuli
Reference sequence
Test sequence

Preferably, there would be at least 2 repetitions of each of the cases above.

The judgement sessions followes the assessment of image quality and follows the quidelines described in section 3.5.2. Assessors are instructed to evaluate at what depth the image quality is no longer usable for reliable diagnostic use on a numerical scale, where they assess the sequence by placing a horizontal bar at the respective depth. Figure 7 illustrates the GUI assosiated with the rating process of penetration depth.

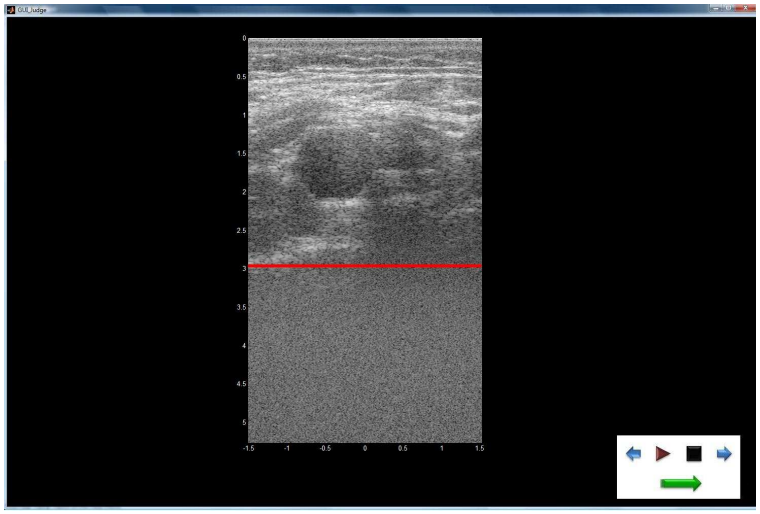

Figure 7: Illustration of the GUI assosiated with the assessment of penetration depth. The horizontal line (illustrated at 3 cm) is placed at the respective depth where the assessor evaluates the image quality no longer usable for reliable diagnostic use.

3.5.4 Statistical analysis

The following analysis is applicable to the results of SSRQS method and SSAS method for the assessment of image quality and penetration depth. In the first case, image quality is rated on a continuous scale indicating differences in image quality for the reference movie and test movie. The scale is defined as integer values between -50 and 50. In the second case penetration depth is rated on continuous scale indicating at what depth image quality is no longer usable for reliable diagnostic use. The readings from the scale is in millimeters between 0 and an arbitrary maximum equal to the size of the movies. Common for both methods is variations in the resulting distributions due to the differences in judgement between assessors and the effect of a variety of conditions associated with the experiment, for example, the use of several movies.

A test will consist of a number of judgement sessions, L, each with independent assessors. At each session, N independent sequence pairs will be presented, in some cases each pair will be presented a number of times, R.

Image quality

The statistical analysis of image quality is introduced, for each assessor, to test for any significant intraobserver variability with a Student's (one sample two-sided) t-test on the two cases from the test trials (Table 3). Secondly, judgement bias confined as a left-right bias for each assessor with a Student's (one sample two-sided) t-test on the two cases from the check trials (Table 4) is tested. Any assessors with a significant bias or significant variability shall be excluded in further investigations.

Since each assessor most likely has his own interpretation of the visual analog scale and shows different degrees of attraction to the center point in side-by-side image quality comparisons, no assumptions of normal distributed data can be made. Consequently, Wilcoxon signed-rank test with continuity correction could be used. The p-values of the pooled data should be corrected for multiple comparison using the Bonferroni method (Pedersen et al, 2006).

For a further detailed analysis of the distribution of ratings we propose to examine the median, 5% and 95% fractiles, with their associated confidence intervals. For each judgement session the standard error derived from N independent values with spread SD can traditionally be calculated as:

$$\sigma_i = \frac{Z * SD}{\sqrt{N}} \tag{1}$$

Where Z is 1.253 for the median and 2.108 for the 5% and 95% fractiles assuming a symmetrical (not skewed) distribution.

The standard deviation is the best measure of spread of an approximately normal distribution. This is not the case when there are extreme values in a distribution or when the distribution is skewed, in these situations interquartile range or semi-interquartile are preferred measures of spread. Interquartile range is the difference between the 25th and 75th centiles. Semi-interquartile range is half of the difference between the 25th and 75th centiles (StatsDirect).

For all assessors, the average of the median, 5% and 95% fractiles are then calculated. The standard error for each average is given as:

$$\sigma = \frac{\sqrt{\sum \sigma_i^2}}{L} \tag{2}$$

The confidence interval for the average of the median, $\bar{\mu}$, and each fractile can then be expressed as:

$$[\bar{\mu} - \delta, \bar{\mu} + \delta] \tag{3}$$

where:

$$\delta = t_{0.95}\sigma \tag{4}$$

The values of $t_{0.95}$ to be used in a confidence interval can be looked up in a table of the t distribution.

Penetration depth

The statistical analysis of penetration depth is performed with a student's (one sample two-sided) t-test on the resulting differences between sequence pairs, assuming normal distribution. In case of a significant difference it is relevant to examine the distribution of ratings and calculate the median, the 5% and 95% fractile together with their respective standard errors to be able to associate a confidence interval.

It is proposed to use the 95% confidence interval which is given by:

$$[\bar{\mu} - \delta, \bar{\mu} + \delta] \tag{5}$$

where:

$$\delta = t_{0.95}\sigma_m \tag{6}$$

The values of $t_{0.95}$ to be used in a confidence interval can be looked up in a table of the t distribution. The standard error σ_m can be derived from $M = N * R * J$ independent values with standard deviation σ and can traditionally assuming normal distribution be calculated as:

$$\sigma_m = \frac{Z * \sigma}{\sqrt{M}} \tag{7}$$

Where Z is 1.253 for the median and 2.108 for the 5% and 95% fractiles assuming a symmetrical (not skewed) distribution.

4. RESULTS

A system for acquisition and statistical evaluation of image sequences has been developed, based on a commercial available ultrasound scanner connected to a standard pc. Data acquisition features subject data recording, loading / saving of exact scanner settings for later experiment reproducibility, free access to all system parameters for beamformation and is certified for clinical use. The free access to all system parameters enables the ability to switch between standard mode and extended mode to capture standardized images as found in the clinic and experimental data from new processing or beamformation methods. Data may be captured interleaved, switching between multiple setups, to maintain identical transducer, scanner, region of interest and recording time on both the experimental- and standardized images. Data storage time is approximately 15.1 seconds pr. 3 sec sequence including complete scanner settings and patient information, which is fast enough to get sufficient number of scans under realistic operating conditions, so statistical evaluation is valid and reliable.

5. CONCLUSION

This work presents a methodology for clinical evaluation of image quality, which addresses the main problems in assessing clinical ultrasound image quality. The evaluation methodology should ensure the validity of the assessment, as it separates the developer, investigator, and assessor once a research protocol has been established. This separation eliminates any confounding influence on the result from the developer and new processing schemes is not driven by the developers, but by the clinical value.

We further present a research platform with free access to all system parameters for beamforming and with certification for clinical use. The clinical usability of the scanner, including the frame rate, is unaffected by activating the research interface.

The capabilities of the research interface module are fourfold; it allows one to:

- Acquire beamformed RF data to a file or memory on a remote pc running Matlab for offline processing. RF data are stored as complex baseband signals as signed 16 bit integers with a sampling rate of up to 40 MHz.
- Free access to all system parameters for beamforming and with certification for clinical use.
- Save and Load complete scanner parameters for experiment reproducibility.
- Remote control of scanner setup and acquisition from Matlab, enabeling automation of parameter studies.

As the core capabilities (saving and loading of complete scanner settings and interleaved RF data acquisition between multiple scanner setups) are available through a simple user interface on a standard pc, the research interface is well suited to obtaining data for clinical trials.

We believe that the research interface platform and the methodology for performing clinical evaluation of image quality can contribute to accelerated advancements in the diagnostic value of ultrasound imaging by allowing more ultrasound researchers to test and clinically evaluate promissing new methods in a standardized way.

ACKNOWLEDGMENTS

This work is sponsored by grant from the Danish Science foundation and BK Medical. Special thanks to Theis Lange for discussion and valuable input.

REFERENCES

[1] Tapiovaara, M., "Review of relationships between physical measurements and user evaluation of image quality," *Radiat Prot Dosimetry* **129 (1-3)**, 244–248 (2008).

[2] Jensen, J. A., Holm, O., Jensen, L. J., Bendsen, H., Pedersen, H. M., Salomonsen, K., Hansen, J., and Nikolov, S., "Experimental ultrasound system for real-time synthetic imaging," *IEEE Ultrason. Symp.* , 1595–1599 (October 1999).

[3] Brunke, S., Insana, M., Dahl, J., Hansen, C., Ashfaq, M., and Ermert, H., "Errata - an ultrasound research interface for a clinical system," *Ultrasonics, Ferroelectrics and Frequency Control, IEEE Transactions on* **54**, 198–210 (January 2007).

[4] Wilson, T., Zagzebski, J., Varghese, T., Chen, Q., and Rao, M., "The ultrasonix 500rp: A commercial ultrasound research interface," *Ultrasonics, Ferroelectrics and Frequency Control, IEEE Transactions on* **53**, 1772–1782 (October 2006).

[5] Jensen, J. A., "Field: A program for simulating ultrasound systems," **10th Nordic-Baltic Conference on Biomedical Imaging, Vol. 4, Supplement 1, Part 1**, 351–353 (1996b).

[6] Pedersen, M. H., Gammelmark, K. L., and Jensen, J. A., "In-vivo evaluation of convex array synthetic aperture imaging," *UMB* **33**, 37–47 (2007).

[7] "Recommendation 500-11: Methodology for the subjective assessment of the quality of television pictures," *ITU-R* (1974-2002).

[8] "Expert viewing to assess the quality of systems for the digital display of motion pictures in theatres," *ITU-R TG6/9 (Digital Cinema)* (2002).

Paper IV

Simulation of High Quality Ultrasound Imaging

Martin Christian Hemmsen, Jacob Kortbek, Svetoslav Ivanov Nikolov, and Jørgen Arendt Jensen

Proceedings of the IEEE International Ultrasonics Symposium

Presented in San Diego, USA, 2010

Simulation of High Quality Ultrasound Imaging

Martin Christian Hemmsen[1,2], Jacob Kortbek[2], Svetoslav Ivanov Nikolov[2] and Jørgen Arendt Jensen[1]

[1]Center for Fast Ultrasound Imaging, Department of Electrical Engineering,
Technical University of Denmark, DK-2800 Kgs. Lyngby, Denmark

[2]BK Medical, Mileparken 34, DK-2730 Herlev, Denmark

***Abstract*— This paper investigates if the influence on image quality using physical transducers can be simulated with an sufficient accuracy to reveal system performance. The influence is investigated in a comparative study between Synthetic Aperture Sequential Beamformation (SASB) and Dynamic Receive Focus (DRF). The study is performed as a series of simulations and validated by measurements. The influence from individual element impulse response, phase, and amplitude deviations are quantized by the lateral resolution (LR) at Full Width at Half Maximum (FWHM), Full Width at One-Tenth Maximum (FWOTM), and at Full Width at One-Hundredth Maximum (FWOHM) of 9 points spread functions resulting from evenly distributed point targets at depths ranging from 10 mm to 90 mm. The results are documented for a 64 channel system, using a 192 element linear array transducer model. A physical BK Medical 8804 transducer is modeled by incorporating measured element pulse echo responses into the simulation software. Validation is performed through measurements on a water phantom with three metal wires, each with a diameter of 0.07 mm. Results show that when comparing measurement and simulation, the lateral beam profile using SASB can be estimated with a correlation coefficient of 0.97. Further, it is shown that SASB successfully maintains a constant LR though depth at FWHM, and is a factor of 2.3 better than DRF at 80 mm. However, when using SASB the LR at FWOHM is affected by non-ideal element responses. Introducing amplitude and phase compensation, the LR at FWOHM improves from 6.3 mm to 4.7 mm and is a factor of 2.2 better than DRF. This study has shown that individual element impulse response, phase, and amplitude deviations are important to include in simulated system performance evaluations. Furthermore, it is shown that SASB provides a constant LR through depth and has improved resolution and contrast compared to DRF.**

I. Introduction

Ultrasound imaging is an active field of research and each year new imaging schemes are proposed. The performance of these new methods is often documented in an idealized framework, ignoring the complications of real and non-ideal transducers. The consequence of this might lead to a rejection of the new scheme when tested *in-vivo*.

To gain an insight into how physical transducer characteristics influence the image quality, this paper investigates if they can be simulated to reveal system performance with side-lobe levels down to -60 dB. The investigation is performed as a comparative study between Synthetic Aperture Sequential Beamforming (SASB) [1] and DRF beamformation.

The study is performed as a series of simulations validated by measurements. The simulations are performed using the Field II [2], [3] simulation software to acquire data and the Beamformation Toolbox III [4] to beamform data.

This paper shows that individual element impulse response, phase, and amplitude deviations are important to include in simulated system performance evaluations. The paper suggests to incorporate measured element pulse echo responses into the simulation sofware as a transducer model that combines excitation waveform and the two-way element impulse response. To emulate a physical 8804 BK Medical 192-element linear array transducer, measured element pulse echo responses are acquired using a BK Medical ProFocus ultrasound scanner.

The rest of this manuscript is organized as follows. Section II presents the measurement system and how the *in silico* model is created. A brief explanation of the theory behind Synthetic Aperture Sequential Beamforming is also discussed. The results using the *in silico* model to accurately predict the received echo signal from a multielement focused aperture, is presented and discussed in Section III. This section is followed by conclusions in Section IV.

II. Methods

A. Synthetic Aperture Sequential Beamforming

The basic idea in multi-element synthetic aperture imaging is to create a pressure wave from multiple elements with a focused transmission. The focal point is introduced as a virtual source, from which a spherical wave emanates within a limited angular region. With SASB a first stage beamformer with a fixed receive time-delay profile and apodization values creates a set of N focused image lines from M emissions. Each point in the focused image line contains information from a set of spatial positions limited by the arc of a circle and the opening angle of the virtual source. A single image point is therefore represented in multiple 1st stage focused image lines obtained from multiple emissions. A second stage beamformer creates a set of high resolution image points by combining information from multiple first stage focused image lines that contain information from the spatial position of the image point.

B. Measurements

The measurement setup consist of a 2202 ProFocus ultrasound scanner (BK-Medical, Herlev, Denmark) connected to a standard pc through a X64-CL Express camera link (Dalsa, Waterloo, Ontario, Canada) and has previously been described in [5].

The measurement of the individual element pulse echo responses from a BK Medical 8804 linear array transducer is performed as described in [6], where a transducer is mounted in a water tank on a device permitting independent angular adjustment in two orthogonal planes. The target is a stainless steel plate, which dimensions are much larger than the

transducer beam being measured. This is to avoid multiple reflections from the back surface and sides. The excitation waveform is a bipolar 7.5 MHz 2 cycle sinusoid.

The individual element pulse echo time responses are measured by aligning the acoustic surface of the transducer so that the distance from the surface to the steel block is approximately a^2/λ, a being half the length of the largest dimension of the transducer element and λ the wavelength of sound in water at the center frequency.

C. Simulation

Simulated data of 9 point targets has been obtained. The points are evenly distributed at depths ranging from 10 mm to 90 mm. The sampling frequency was set to 120 MHz. Specification of simulation parameters can be found in table I. Data was obtained using 3 different simulation setups:

- Idealized: In this setup the transducer element impulse responses are the same across the array. The used element impulse response is aproximated with a measured unit step response from a single element. The excitation waveform is hamming windowed 7.5 MHz 2 cycle sinusoid.
- Realistic: In this setup measured element pulse echo responses are used in the simulation software as element excitation that combines excitation waveform and the two-way element impulse response.
- Compensated: This setup is based on the realistic setup, but the measured element pulse echo responses are compensated for amplitude and phase deviations.

Transducer Parameters (8804)	
Pitch	0.208 mm
Elevation focus	20 mm
Number of elements	192
Radius of curvature	linear
Element impulse response	delta function
Dynamic Receive Focus (SASB)	
Focus (Tx / Rx)	60 mm / - (10 / 10 mm)
F# (Tx / Rx)	4.51 / 0.5 (2 / 2)
Apodization (Tx / Rx)	Boxcar / Gauss
$\text{Apodization}_{\text{2nd stage}}$	Hamming
Fixed scanner setting	
Waveform (idealized)	7.5 MHz 2 cycle sinusoid
Waveform (realistic)	element pulse echo
Number of emissions / RF lines	190 / 190
Maximum no. of active elements	64

TABLE I
SIMULATION PARAMETERS

D. Visualization

The simulated and measured B-mode images were generated by envelope detection using a Hilbert transform, log-compressed to a dynamic range of 60 dB, scan converted and visualized. The images were normalized prior to visualization by calculating the maximum reflection for each of the 9 points targets to determine a normalization curve, so that the maximum reflection for each of the point targets was equal to 0 dB. dB values were mapped linearly to gray scale with 256 shades of gray.

III. RESULTS

To address the feasibility of SASB, improved resolution and contrast, the method is first compared in an idealized setup with DRF. Fig. 1 illustrates the simulated B-mode images of 9 point targets using the idealized transducer model (a) DRF and (b) SASB. From Fig. 1(a) it is clearly identified that when using DRF, the lateral resolution and contrast is a function of depth. However, when using SASB the lateral resolution and contrast is much less dependent on depth and a significant improvement compared to DRF is obtained.

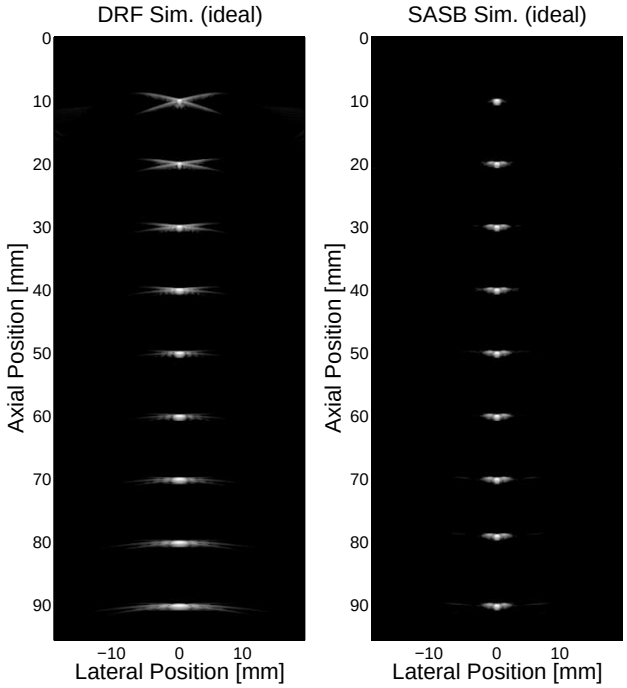

(a) DRF (b) SASB

Fig. 1. Visualization of 9 point spread functions, using (a) DRF beamforming (b) SASB beamforming (idealized transducer model).

System performance can be significantly influenced by the real and non-ideal physical transducer characteristics. To show that simulations can reveal system performance by incorporating element pulse echo responses into the simulation model, the element pulse echo responses are measured and used as a realistic transducer model. The measurement of the array revealed a deviation in the amplitude and a phase error between the elements. Fig. 2 shows the measured amplitude and phase error profile.

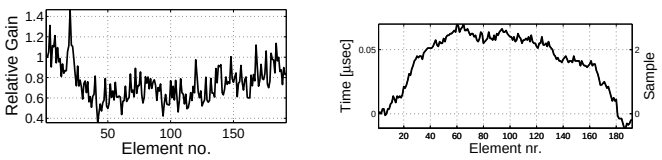

(a) (b)

Fig. 2. (a) Relative amplitude gain and (b) relative phase error

The amplitude has a Coefficient of Variation of 0.24 and the maximum phase error is 0.08μsec or 0.43λ, determined by finding the largest relative lag though cross-correlation.

Fig. 3 illustrates the measured element pulse echo responses. In (a) the pulse echo responses for all 192 elements are visualized, black colors indicate negative amplitude and white positive amplitude. Note how the waveform at the edges of the array is offset relative to the center of the array. In (b) the waveform for element no. 10, 96 and 182 are shown. Note how the waveforms at the edges of the array are almost

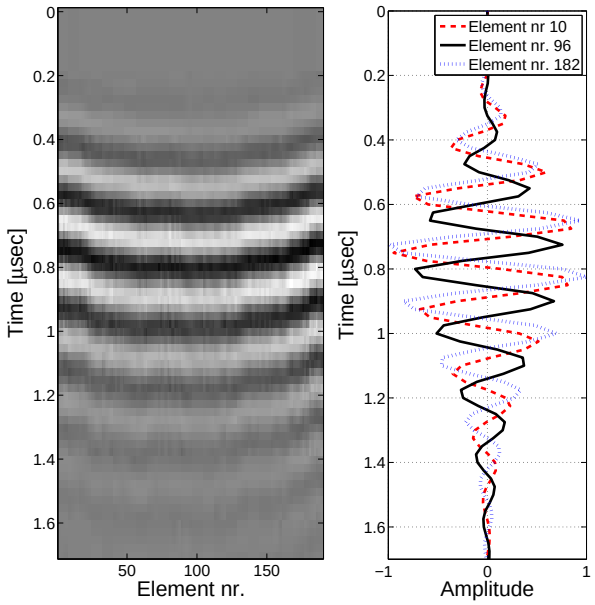

(a) (b)

Fig. 3. Element pulse echo visualized (a) for all 192 elements seen from the top (negative amplitude is black and positive amplitude white) and (b) for element no. 10, 96 and 182.

in phase and have a 154° phase shift relative to the center element. Fig. 4(a) illustrates the B-mode image generated using measured data beamformed with SASB. Comparing Fig. 4(a) and 1(b) it is clearly seen that using the idealized transducer model the point spread functions does not compare well with measured data. To investigate if the influence on image quality using physical transducers can be simulated with sufficient accuracy, to reveal system performance measured element pulse echo responses are incorporated into the simulation software as a transducer model that combines excitation waveform and the two-way element impulse response. Fig. 4(b) illustrates the simulated B-mode image using SASB for the realistic transducer model. Note how the introduction of inter element deviations in amplitude, phase, and impulse response affect the image quality and how the image compares well with the measured data in Fig. 4(a).

Fig. 4(c) and 4(d) illustrate the simulated B-mode images of the 9 point targets using the realistic transducer model and an amplitude and phase compensated element pulse echo beamformed with (c) SASB and (d) DRF. The amplitude of the waveforms are compensated by normalizing the energy of the 20 dB most significant part of the waveforms to the energy of element no. 1, after phase alignment. The phase deviation between the waveforms is compensated by upsampling to 800 MHz and then using cross-correlation to find the lag with the highest correlation, relative to the waveform of element no. 1.

Comparing Fig. 1(a) and 4(d), it is clear that use of the compensated transducer model does not noticeably influence the image quality when using DRF. Comparing Fig. 1(b) and 4(c) it is observed that the constant resolution as a function of depth is achievable and unaffected by amplitude and phase errors. However, the contrast is seen to be influenced, but much less than when using the uncompensated model.

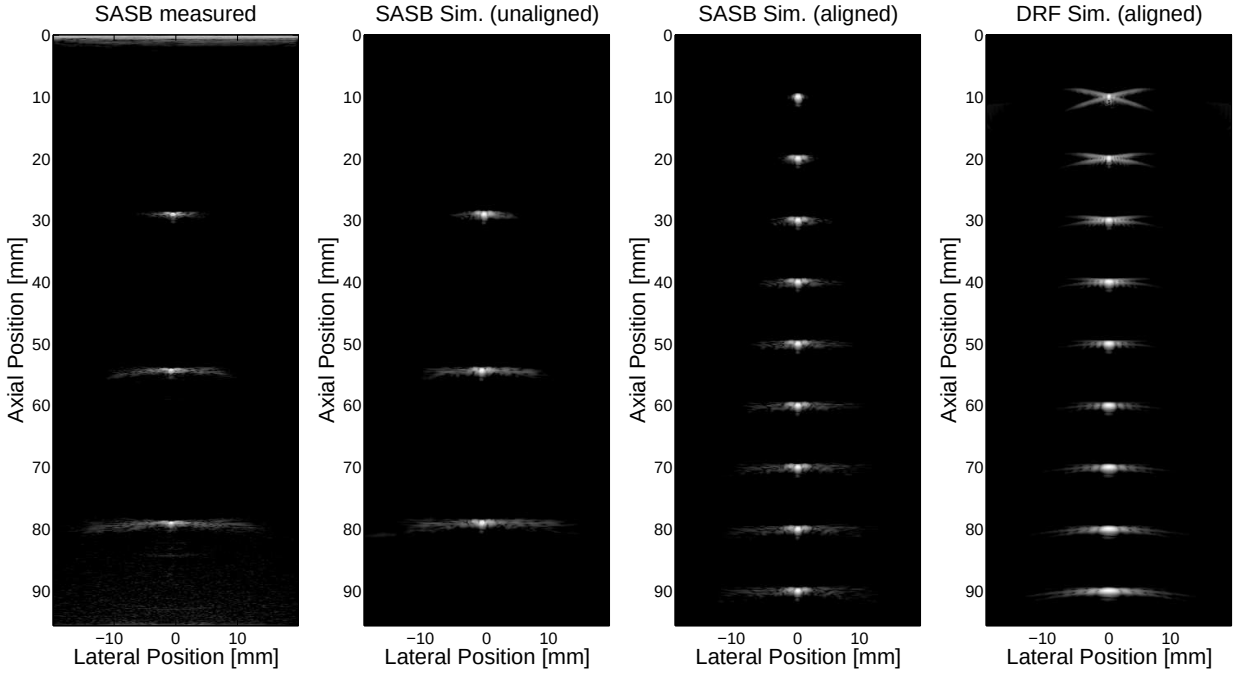

(a) (b) (c) (d)

Fig. 4. Visualization of point spread functions using SASB beamformation (a) measured (b) simulated (realistic transducer model) (c) SASB beamforming (compensated transducer model) and (d) DRF beamforming (compensated transducer model).

Fig. 5 illustrates the lateral beam profile of the point spread function at 80 mm, beamformed using SASB and measured data, the idealized transducer model, the realistic transducer model, and the compensated transducer model. Note how the 3 models fit with the measured data until -30 dB. Beyond this level the influence from the transducer model is significant. Clearly having an amplitude and phase aligned transducer is important to achieve good contrast.

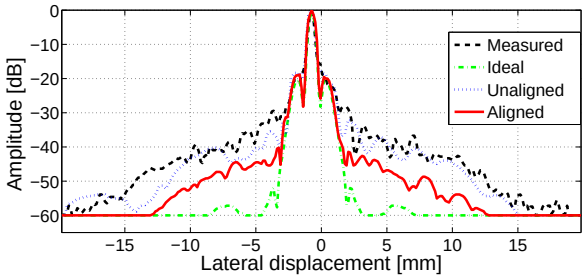

Fig. 5. Lateral cut of the point spread function at 80mm, using SASB beamforming and measured data, idealized transducer model, realistic transducer model and compensated transducer model

Fig. 6 illustrates the lateral resolution at FWHM, FWOTM and FWOHM using DRF and SASB beamforming using the compensated transducer model. Note how the lateral resolution using DRF expands through depth. Using SASB a constant lateral resolution at FWHM and FWOTM is maintained down to 90 mm. The lateral resolution at FWHM at a depth of 80 mm using SASB is a factor of 2.3 better compared to DRF. At FWOHM the lateral resolution is a factor of 2.2 better then DRF.

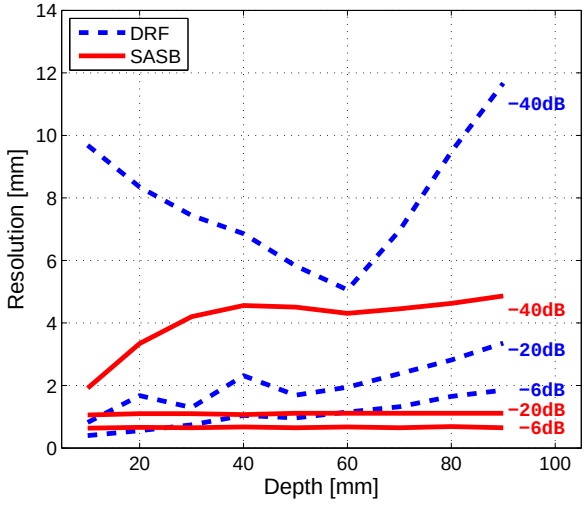

Fig. 6. Lateral resolution at FWHM, FWOTM and FWOHM using DRF (dashed line) and SASB (solid line) beamforming (compensated transducer).

Table II summarizes the lateral resolution using the three different model types and measurements for DRF and SASB beamforming. Values in the table denote the lateral resolution in mm, at FWHM and at FWOHM in parenthesis.

	Depth		
Method	30 mm	55 mm	80 mm
$\text{DRF}_{\text{measured}}$	0.6(7.1)	0.9(6.1)	1.5(9.3)
$\text{DRF}_{\text{unaligned}}$	0.7(7.1)	1.0(5.3)	1.6(9.8)
$\text{DRF}_{\text{ideal}}$	0.7(7.2)	1.0(5.4)	1.6(9.2)
$\text{DRF}_{\text{aligned}}$	0.8(7.5)	1.0(4.6)	1.7(9.7)
$\text{SASB}_{\text{measured}}$	0.5(4.4)	0.6(6.8)	0.5(8.8)
$\text{SASB}_{\text{unaligned}}$	0.6(4.7)	0.6(7.3)	0.6(6.3)
$\text{SASB}_{\text{ideal}}$	0.6(3.6)	0.6(4.2)	0.6(4.3)
$\text{SASB}_{\text{aligned}}$	0.7(3.7)	0.7(4.4)	0.7(4.7)

TABLE II

SUMMARY OF LATERAL RESOLUTION PERFORMANCE.

IV. CONCLUSIONS

This paper has shown that the influence on image quality using real and non-ideal transducers can be simulated with an sufficient accuracy, to reveal system performance. Furthermore it is shown that inter element impulse response, phase, and amplitude deviations are important to include in simulated system performance evaluations. The influence on image quality using real and non-ideal transducers characteristics has been investigated in a comparative study between Synthetic Aperture Sequential Beamformation and Dynamic Receive Focus. The study documents the importance of validating high quality imaging systems using realistic simulations, as they reveal the system's performance. Simulations using three different transducer models (idealized, realistic and compensated) show that SASB is more sensitive to element variation than DRF. However, compensating for element phase and amplitude variation, the lateral resolution at FWHM and a depth of 80 mm using SASB is a factor of 2.3 better compared to DRF. At -40 dB the lateral resolution is a factor of 2.2 better than DRF. Furthermore when using SASB the lateral resolution can be kept constant though depth.

ACKNOWLEDGMENT

This work was supported by the Danish Science Foundation and by BK Medical ApS, Denmark.

REFERENCES

[1] J. Kortbek, J. A. Jensen, and K. L. Gammelmark, "Sequential beamforming - an efficient synthetic aperture technique," *IEEE Transactions on Ultrasonics, Ferroelectrics and Frequency Control*, Submitted 2010.

[2] J. A. Jensen and N. B. Svendsen, "Calculation of Pressure Fields from Arbitrarily Shaped, Apodized, and Excited Ultrasound Transducers," *IEEE Trans. Ultrason., Ferroelec., Freq. Contr.*, vol. 39, pp. 262–267, 1992.

[3] J. A. Jensen, "Field: A Program for Simulating Ultrasound Systems," *Med. Biol. Eng. Comp.*, vol. 10th Nordic-Baltic Conference on Biomedical Imaging, Vol. 4, Supplement 1, Part 1, pp. 351–353, 1996.

[4] J. M. Hansen and J. A. Jensen, "An object-oriented multi-threaded software beamformation toolbox," Feb. 2011, submitted to SPIE Medical Imaging, 12 -17 February 2011, Lake Buena Vista (Orlando), Florida, USA.

[5] M. C. Hemmsen, M. M. Petersen, S. I. Nikolov, M. B., Nielsen, and J. A. Jensen, "Ultrasound image quality assessment: A framework for evaluation of clinical image quality," in *Proceedings of SPIE–the international society for optical engineering*, vol. 76291. Medical Imaging 2010: Ultrasonic Imaging, Tomography, and Therapy, 2010, pp. 76 290C–12.

[6] K. Erikson, "Tone-burst testing of pulse-echo transducers," *IEEE Transactions on Sonics and Ultrasonics*, vol. 26, no. 1, pp. 7–13, 1979.

Paper V

Preliminary In-Vivo evaluation of Synthetic Aperture Sequential Beamformation using a multielement convex array

Martin Christian Hemmsen, Peter Møller Hansen, Jens Munk Hansen, Michael Bachmann Nielsen, and Jørgen Arendt Jensen

Proceedings of the IEEE International Ultrasonics Symposium

Accepted for conference in Orlando, USA, 2011

Preliminary In-Vivo evaluation of Synthetic Aperture Sequential Beamformation using a multielement convex array

Martin Christian Hemmsen[1,2], Peter Møller Hansen[3], Theis Lange[4], Jens Munk Hansen[1], Svetoslav Ivanov Nikolov[2], Michael Bachmann Nielsen[3] and Jørgen Arendt Jensen[1]

[1]Center for Fast Ultrasound Imaging, Department of Electrical Engineering, Technical University of Denmark, 2800 Lyngby, Denmark

[2]BK Medical, Mileparken 34, 2730 Herlev, Denmark

[3]Department of Radiology, Rigshospitalet, 2100 Copenhagen, Denmark

[4]Department of Biostatistics, University of Copenhagen, 1014 Copenhagen, Denmark

***Abstract*— This paper presents a preliminary *in-vivo* study of synthetic aperture sequential beamforming (SASB) in comparison with conventional imaging. The advantage of SASB compared to conventional imaging, is the ability to obtain a more range independent point spread function, without any loss in lateral resolution or frame rate. The objective of this study is to evaluate whether SASB imaging is feasible *in-vivo* and whether the image quality obtained is comparable with traditional scanned imaging in terms of penetration depth, spatial resolution, contrast, and unwanted artifacts. Acquisition was performed using a ProFocus ultrasound scanner and a 3.5 MHz convex array transducer. First stage beamformed SASB radio frequency (RF) data were acquired using a transmit and receive focal depth of 70 mm and 63-element subapertures. Subsequently the data were off-line processed to generate second stage SASB RF data. For conventional imaging, beamformed RF data was acquired using 63-element sub-apertures in transmit with a focal depth of 105 mm, in receive an expanding aperture using dynamic focusing with a F-number of 0.8 was used. Both modalities used the same standard manufacturer specified pulse. Conventional and SASB RF data were acquired interleaved, ensuring that the exact same anatomical location was scanned. RF data were recorded in real time and processed off-line to generate image sequences. Two male volunteers were scanned abdominally resulting in 34 image sequence pairs. Evaluation of image quality and penetration was performed by five medical doctors. Results showed no significantly ($p = 0.98$) increase nor decrease in penetration using SASB. Overall image quality was highly significantly ($p < 0.001$) increased. Results show that *in-vivo* ultrasound imaging using SASB is feasible for abdominal imaging without severe motion artifacts.**

I. Introduction

Conventional ultrasound imaging is technically intuitive and an easily implementable solution. The method creates an image by emitting a focused beam in one direction at a time, and sequentially building up an image of consecutive scan lines. Using array element transducers dynamic receive focusing and dynamic apodization can be adapted to yield an optimal receive focus and constant receive F-number at all depths in the image. The fixed transmit focus affects the image quality, which is only optimal at the transmit focus.

Synthetic transmit aperture (STA) imaging [1], [2], offers the same optimal resolution at all depths in transmit as well as receive, with the potential of increasing the overall spatial and contrast resolution. STA imaging, thus, offers both a high frame rate at the same time as a high image quality is obtained. *In-vivo* studies of STA imaging have been published with good results [3]. A drawback of STA is, however, an increase in computational demand. To reduce the computational demand Kortbek et al. introduced in [4] the concept of synthetic aperture sequential beamforming (SASB). It was shown that for a multi element linear array transducer the lateral resolution could be made more range independent and improved significantly compared to conventional imaging. The viability of the technique *in-vivo* is, however, yet to be proven and doubts have been uttered, stating that tissue motion will probably make the coherent summation of temporally separated signals break down.

In this paper an implementation of 2-dimensional SASB imaging will be tested in a clinical setting on healthy volunteers and evaluated by ultrasound specialists (medical doctors). The method is investigated for abdominal imaging using a multi element convex array transducer, and it is compared to conventional imaging. The investigation is based on a blinded clinical evaluation using paired *in-vivo* image sequences as in [3]. A data acquisition system [5], [6] capable of simultaneous recordings of the exact same locations using both techniques is used. The following two null hypotheses are tested:

1) SASB imaging has no effect on penetration depth.
2) SASB imaging has no effect on image quality (spatial resolution, image contrast, noise, and unwanted artifacts).

The paper is organized as follows. Section II presents the methods used for data acquisition and processing followed by a description of the image assessment and statistical analysis. The results is presented and discussed in Section III followed by conclusions in Section IV.

II. Methods

A. Data acquisition

Prior to conducting the *in-vivo* experiments, the acoustic outputs of the ultrasound scanner were measured for the imaging modes under investigation and written consense was obtained from the volunteers. The measured intensities satisfy upper limits regulated by the United States Food and Drug Administration [7].

The measurements were performed using a data acquisition system consisting of a BK Medical 2202 ProFocus ultrasound scanner (BK Medical, Herlev, Denmark) equipped with a research interface connected to a standard PC. The system can acquire beamformed radio frequency data interleaved with identical excitation waveforms, TGC, and field-of-view on both an experimental and reference setup. The chosen excitation waveform and transmit voltage used in this study is a preset standardized setting from the manufacturer. The two imaging setups were interleaved such that one frame from one setup followed directly after the other. Hereby, data from exactly the same *in-vivo* view were obtained, enabling direct comparison of the methods. The depth of each scan was 15 cm, and the interleaved frame rate was 5 frames/sec, i.e. 5 conventional and 5 synthetic frames per second. From each examination a data sequence of 3 seconds was obtained. Due to the low frame rate and for an easier visual comparison of the two methods, the sonographer tried to hold the probe in the same view throughout the recording.

Data were acquired from two healthy male volunteers, scanned in supine position by an experienced sonographer. Specification of the measurement parameters can be found in Table I.

TABLE I
Measurement parameters

Transducer Parameters (STI - 3ML 3.5CLA192)		
Pitch	0.33	mm
Elevation focus	65	mm
Number of elements	192	
Radius of curvature	60	mm
Field of view (FOV)	60.5	^{o}
Bandwidth at -6 dB	85	%

	Conventional	SASB
Focus Tx / Rx (mm)	105.5 / dynamic	70 / 70
F# Tx / Rx	5.0 / 0.8	2 / 2
Apodization Tx / Rx	Boxcar / Gauss	Boxcar / Gauss
$\text{Apodization}_{\text{2nd stage SASB}}$		Gauss

Scanner setting	
No. of emissions	384
No. of scan lines	384
Max. no. of active elem.	64

B. Data processing

The acquired RF data were subsequent extracted in MATLAB (MathWorks Inc., Natick, Mass., USA) and the SASB second stage RF data were generated using the acquired first stage RF data and the beamformation toolbox BFT3 [8]. Data were after envelope detection, automatically TGC corrected according to the depth to obtain homegenous images suitable for comparison, normalized, μ-law compressed, and scan converted. The automated TGC correction was performed by calculating a mask to filter out strong and weak specular regions. The mask were then applied to the enveloped detected data and the median value of all lines for all depths in the first recorded frame was found. The resulting curve was normalized to a maximum of one, inverted, and used to normalize all lines in all frames. The two image sequences were normalized such that the median envelope value of the images matched 27% of the gray tone scale after compression. Subsequently palindromatic image sequences consisting of 3 sec recordings were created to avoid annoying temporal discontinuities.

C. Image Assessment

Five medical doctors (ultrasound specialists) evaluated the image sequences. None of the five were involved in the project, nor had they any prior knowledge about the details of SASB imaging, or seen any of the images beforehand. Evaluations were done blinded and independently of each other using the program IQap [5]. IQap is used for determination of technical efficacy using paired image sequences and allows assessment of image quality regarding spatial resolution, contrast, noise, formation of unwanted artifacts, and an assessment of penetration depth.

Assessment of image quality was performed as a blinded comparison between matching sequence pairs, displayed side-by-side in random order. Each presentation consists of an image sequence generated using the conventional and SASB imaging. Each sequence pair was displayed two times with opposite left-right placement. This gave 68 presentations of the 34 sequence pairs. The evaluators were asked to assess which of the two paired sequences was the best on a visual analog scale (VAS), see Fig. 1. Before the assessment the evaluators were introduced to the program and the VAS scale was explained using Fig. 2. The figure instructs them on how to interpret the scale when performing the assessments, but was hidden during the actual evaluation to avoid categorized data and get a smoother distribution. Before the actual assessment, five trial examples was shown to get the evaluators acquainted with the task at hand and which types of images to expect.

Fig. 1. Visualization of an image pair for overall image quality evaluation. The scale used for scoring is shown in the bottom and the control panel for navigating the sequences are shown in the lower right corner.

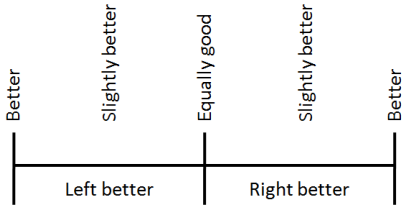

Fig. 2. The figure instructs the doctor on how to interpret the scale when performing the evaluation. To avoid categorized data and get a smoother distribution, this explanatory scale is not shown during the actual evaluation.

Assessment of penetration depth was performed by presenting the 34 sequence pairs as single movies one after the other in random order. Hereby the doctors assessed 68 sequences without information about the technique used to generate each sequence. The doctors were asked: To what depth is the visualization of the anatomic structures reliable for clinical use? The penetration depth in cm was assessed as shown in Fig. 3.

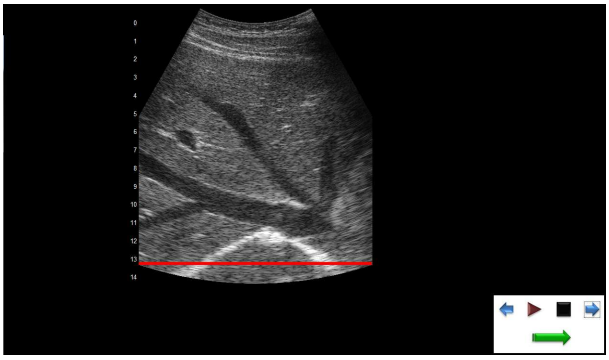

Fig. 3. Visualization of an image for penetration evaluation. The bar used for scoring is shown across the image and the control panel for navigating the sequences is shown in the lower right corner.

D. Statistical Analysis

The VAS scores were analyzed by a mixed effect linear model [9] with a random effect for each image pair and each evaluator, thereby accounting for the dependence induced by repeatedly scoring the same image pair and collecting multiple scores from the same evaluator. Since all image pairs were shown both with the SASB image on the left and on the right it is not necessary to further control for any left/right bias. The parameter of interest is the intercept, which captures the average score and will be negative if SASB is preferred to conventional imaging. Note that the use of the mixed effect model solely was to account for dependencies induced by image pair and evaluator and thereby providing a valid confidence interval for the intercept. The model fit was assessed by Q-Q plots to check for normality of the data. As a further robustness check the analysis was repeated with a transformed score (the square root and negative square root of positive and negative scores, respectively). In addition Wilcoxon tests were performed for each evaluator and side (SASB on left or right) separately. Within these stratums the observations are independent and p-values for the hypothesis that the two methods are equally

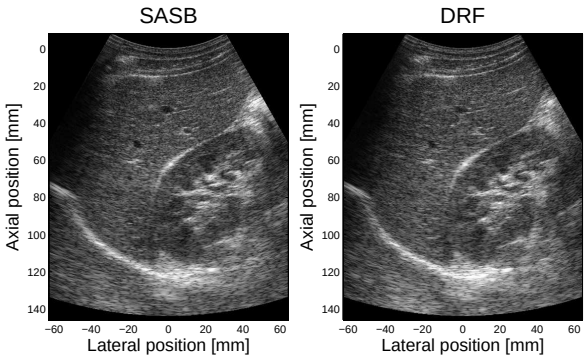

(a) Morisons Pounch

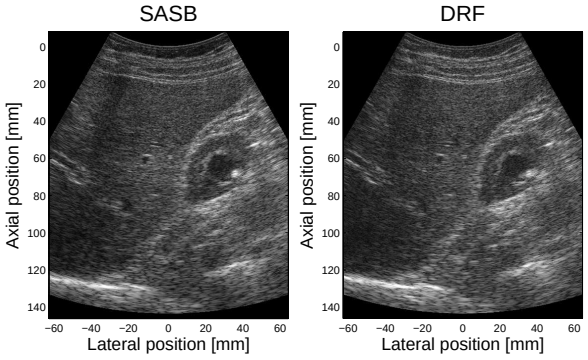

(b) Liver and tip of right kidney

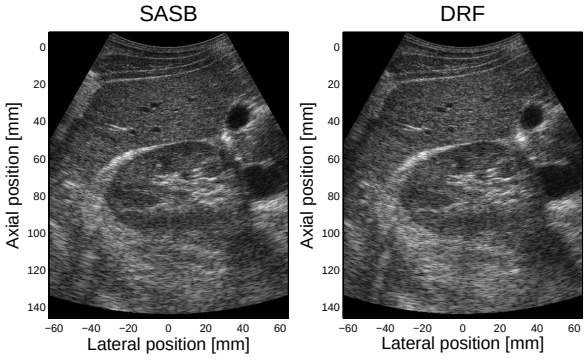

(c) Right kidney transversal cut

Fig. 4. Some examples of the produces In-vivo images. Left part is the conventional and right is the SASB image. (a) Longitudinal section of right liver lobe, the kidney and diaphragm at the bottom. (b) Liver and tip of right kidney. (c) Right kidney transversal.

good (i.e. probability of a positive score equal the probability of a negative score) are therefore readily available. The depth scores given to SASB and conventional imaging were initially subtracted from each other and the resulting differences were analyzed as described above. The statistical data analysis language R version 2.12.2 (http://www.r-project.org/) was used for statistical computations.

III. Results

The SASB images were generally good and undoubtedly applicable in clinical imaging. Examples are shown in Fig. 1, 3, and 4.

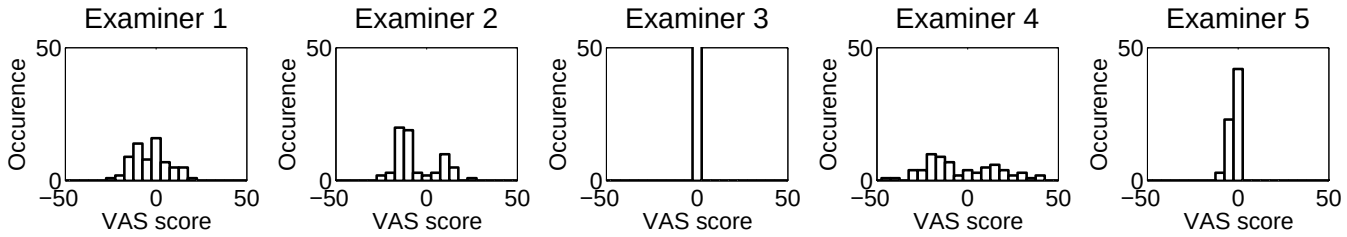

Fig. 5. Distribution of pooled answers from assessment of overall image quality. Negative values mean that the SASB method is rated better than the conventional method.

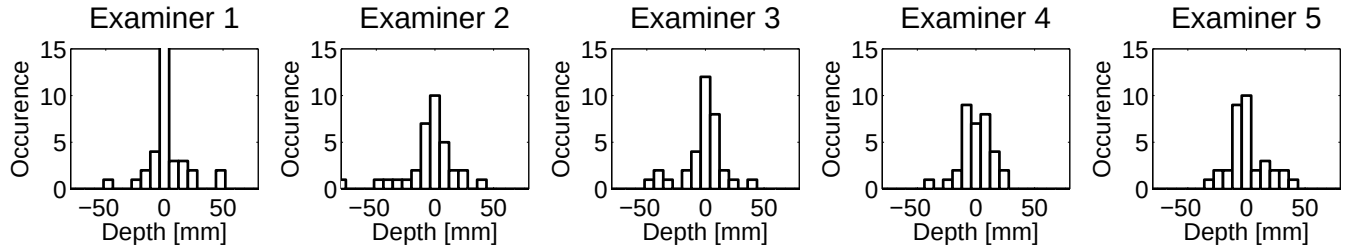

Fig. 6. Distribution of pooled answers from assessment of penetration. Negative values mean that the SASB method is rated better than the conventional method.

Of the 340 image quality ratings, 80 favored conventional imaging, 209 favored SASB and 51 were rated equally good. The distribution of ratings from the individual evaluators are shown in Fig. 5. The statistical analysis show that the average VAS score is significantly negative (p-value: 0.0005) and estimated to be -2.9 (95% CI: -4.54; -1.26). The analysis of the transformed score yields qualitatively the same result, and from the 10 Wilcoxon tests, performed in each stratum defined by evaluator id and side, seven tests found a significant difference in favor of SASB and none in favor of the conventional method. Thus, the data clearly show that SASB is preferred compared to conventional imaging. However, there is a substantial variance on the individual scores.

The differences in penetration depths between the two techniques are shown in Fig. 6. The analysis of the depth scores showed that the average difference is insignificant (p-value: 0.98).

IV. Conclusions

This paper has demonstrated and evaluated *in-vivo* imaging using synthetic aperture sequential beamforming in a side-by-side comparison to conventional ultrasound imaging. The result of the statistical evaluation showed that SASB imaging can obtain satisfying penetration within the current intensity limits. Furthermore, the image quality evaluation showed highly significant improvement in SASB images compared with conventional images. One should be careful about interpreting the absolute VAS values, since the interobserver variation in VAS scale interpretation is large. The conclusion is important for future development of ultrasound imaging. Especially for a future towards cheaper devices with more processing done by standard PC's.

Acknowledgment

Thanks to M.D. Mads Møller Pedersen, M.D. Esther Balmaati, and M.D. Kristoffer Lindskov Hansen for evaluating the ultrasound images, and to the volunteers for participating.

This work is supported by grant 08-036099 from the Danish Science Foundation and by BK Medical Aps, Herlev, Denmark.

References

[1] K. L. Gammelmark and J. A. Jensen, "Multi-element synthetic transmit aperture imaging using temporal encoding," in *Proc. SPIE: Progress in biomedical optics and imaging*, vol. 3, 2002, pp. 25–36.

[2] ——, "Multielement synthetic transmit aperture imaging using temporal encoding," *IEEE Trans. Med. Imag.*, vol. 22, no. 4, pp. 552–563, April 2003.

[3] M. H. Pedersen, K. L. Gammelmark, and J. A. Jensen, "In-vivo evaluation of convex array synthetic aperture imaging," *Ultrasound Med. Biol.*, vol. 33, pp. 37–47, 2007.

[4] J. Kortbek, J. A. Jensen, and K. L. Gammelmark, "Synthetic aperture sequential beamforming," *Ultrasonics*, p. Submitted, 2009.

[5] M. C. Hemmsen, M. M. Petersen, S. I. Nikolov, M. B., Nielsen, and J. A. Jensen, "Ultrasound image quality assessment: A framework for evaluation of clinical image quality," in *Proceedings of SPIE–the international society for optical engineering*, vol. 76291. Medical Imaging 2010: Ultrasonic Imaging, Tomography, and Therapy, 2010, pp. 76 290C–12.

[6] M. C. Hemmsen, , S. I. Nikolov, M. M. Pedersen, M. J. Pihl, M. S. Enevoldsen, J. M. Hansen, and J. A. Jensen, "Implementation of a versatile research data acquisition system using a commercially available medical ultrasound scanner," *IEEE Trans. Ultrason., Ferroelec., Freq. Contr.*, p. Submitted, 2011.

[7] FDA, "Information for manufacturers seeking marketing clearance of diagnostic ultrasound systems and transducers," Center for Devices and Radiological Health, United States Food and Drug Administration, Tech. Rep., 1997.

[8] J. M. Hansen and J. A. Jensen, "An object-oriented multi-threaded software beamformation toolbox," Feb. 2011, submitted to SPIE Medical Imaging, 12 -17 February 2011, Lake Buena Vista (Orlando), Florida, USA.

[9] N. M. Laird and J. H. Ware, "Random-Effects Models for Longitudinal Data," *Biometrics.*, vol. 38, no. 4, pp. 963–974, December 1982.

Paper VI

Synthetic Aperture Sequential Beamformation applied to medical imaging using a multi element convex array transducer

Martin Christian Hemmsen, Jens Munk Hansen, and Jørgen Arendt Jensen

Proceedings of the EUSAR 2012

Submitted for conference in Nürnberg, Germany 2012

Synthetic Aperture Sequential Beamformation applied to medical imaging using a multi element convex array transducer

Martin Christian Hemmsen[1,2], Jens Munk Hansen[1]and Jørgen Arendt Jensen[1]

[1]Center for Fast Ultrasound Imaging, Department of Electrical Engineering,
Technical University of Denmark, DK-2800 Kgs. Lyngby, Denmark

[2]BK Medical, Mileparken 34, DK-2730 Herlev, Denmark

***Abstract*— This paper evaluates the feasibility of applying Synthetic Aperture Sequential Beamforming (SASB) to 2-dimensional medical imaging using a multi element convex array transducer. The main motivation for SASB is to apply synthetic aperture techniques without the need for storing RF-data for a number of elements and hereby devise a system with a reduced system complexity. The objective is to obtain a more isotropic point spread function compared with conventional ultrasound imaging, without any loss in lateral resolution or frame rate. The method is evaluated using simulations from Field II and by measurements using a BK Medical ProFocus scanner and a BK8820e 192 element 5 MHz convex array (BK Medical, Herlev, Denmark). B-mode images are created and the lateral resolutions at full-width-at-half-max (FWHM), at -20 dB and -40 dB are extracted and used as quantitative measures. The lateral resolution for simulated scatterers placed at depths ranging from 10 to 120 mm was on average improved by 17.2% at FWHM and 25.4% at -20 dB using SASB compared to DRF. At -40 dB the lateral resolution was on average 0.8% better using DRF. The standard deviation on the lateral resolution at FWHM was improved improved by 0.46 mm at FWHM using SASB compared to DRF. SASB has shown the ability to increase the image range of a uniform lateral resolution and to obtain a more isotropic point spread function using a convex array. This was shown for simulations and for phantom measurements using commercially available equipment.**

I. Introduction

In multi-element Synthetic Aperture (SA) imaging the basic idea is to create a pressure wave from multiple elements with a focused transmission. The concept of using the transmit focal point as a virtual source was introduced by Passmann and Ermert [1]. Virtual sources in Synthetic Aperture Focusing (SAF) was further investigated by Frazier and O'Brien [2], Nikolov and Jensen [3], [4], and Bae and Jeong [5]. It was shown that the virtual source coincides with the focal point of the transducer, and that a depth independent resolution can be achieved. Kortbek et al. introduced [6] the concept of Sequential Beamforming to SA imaging to reduce system requirements for real time implementation. It was shown that for a multi element linear array transducer the lateral resolution could be made more range independent and improved significantly compared to conventional Dynamic Receive Focusing (DRF).

The basic idea in Synthetic Aperture Sequential Beamforming (SASB) is to create a dual-stage procedure using two separate beamformers. In the initial stage a beamformer using a single focal point in both transmit and receive, creates a set of focused image lines. A second stage beamformer creates a set of high resolution image points by combining information from multiple first stage focused image lines, which results in a dynamically expanding array as the image depth increases and a more range independent lateral resolution is obtained.

This paper evaluates the feasibility of applying SASB to 2-dimensional imaging using a multi element convex array transducer. The method is evaluated using simulations and validated with measurements. In simulations as well as measurements, B-mode images are created and the lateral resolution is extracted and used as quantitative measures.

The rest of this manuscript is organized as follows. Section II describes the SASB method applied to convex array transducers and Section III presents the results, followed by conclusions in Section IV.

II. Method

In ordinary dynamic receive beamforming (DRF) a new set of delay values is calculated for each focusing point (FP) and applied to the responses of the individual transducer elements which are then summed coherently. The delays are found from the round trip time-of-flight (TOF), which is the propagation time of the emitted wave in its path from the transmit origin, $\vec{r}_e$ to the receive focusing point, $\vec{r}_{fp}$ through the transmit focusing point $\vec{r}_{tfp}$ and return to one of the elements of the receive aperture, $\vec{r}_r$. Fig. 1(a) illustrates the time-of-flight calculation for DRF. Assuming the speed of sound c is known, the delay value, t_d for the receiving element with position $\vec{r}_r$ is calculated as

$$t_d(\vec{r}_r) = \frac{1}{c}\Big(|\vec{r}_{tfp} - \vec{r}_e| \pm |\vec{r}_{fp} - \vec{r}_{tfp}| + |\vec{r}_r - \vec{r}_{fp}|\Big). \quad (1)$$

With SASB a first stage beamformer with a fixed receive time-delay profile creates a set of N focused image lines from M emissions. The delay profile is found from the round trip time-of-flight (TOF), which is the propagation time of the emitted wave in its path from the transmit origin, to the focusing point through the virtual source (VS), and return to

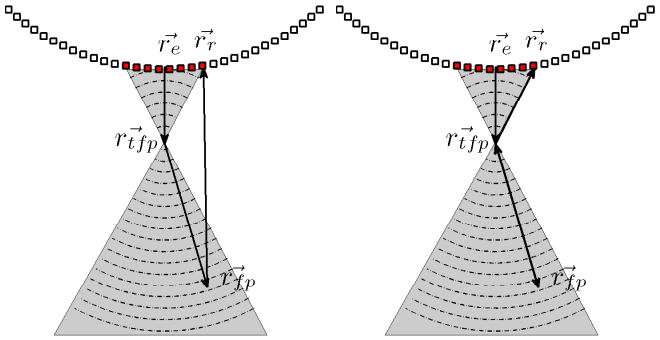

(a) Dynamic receive focus (b) Fixed receive focus

Fig. 1. Wave propagation path (solid line) for calculating the receive focusing time delays for a focused transmission (a) using dynamic receive focusing and (b) fixed receive focusing.

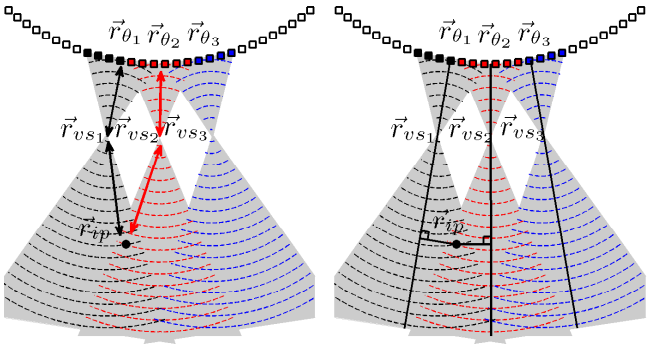

(a) Time-of-flight calculation (b) Apodization weight calculation

Fig. 2. In (a) and (b) the dashed lines indicate the propagating waves for three multi element emissions. The squares indicate the individual transducer elements. The black dot indicate a specific image point. In (a) the time-of-flight path for the individual emissions from the scan line reference point to the image point and back is illustrated by the arrows. In (b) the calculation of apodization weight is illustrated. Note that the apodization weights are determined based on the shortest distance from the image point to the respective scan lines. In both (a) and (b) note that the third emission shown in blue does not contribute to the image point as it contains no information about the spatial position of the image point due to the limited opening angle.

one of the elements of the receive aperture, again through the virtual source (VS). Fig. 1(b) illustrates the time-of-flight calculation for the SASB first stage beamformer. The delay value for the individual receive elements are calculated as

$$t_d(\vec{r}_r) = \frac{1}{c}\Big(|\vec{r}_{tfp} - \vec{r}_e| \pm 2|\vec{r}_{fp} - \vec{r}_{tfp}| + |\vec{r}_r - \vec{r}_{tfp}|\Big). \quad (2)$$

The $\pm$ in (1) and (2) refer to whether the image point is above or below the transmit focal point.

Each point in the focused image line contains information from a set of spatial positions limited by the opening angle of the virtual source. The opening angle is defined as

$$\alpha = 2\arctan\frac{1}{2F\#} \quad (3)$$

A single image point is therefore potentially represented in multiple first stage focused image lines. A second stage beamformer creates a set of high resolution image points by combining information from multiple first stage focused image lines that contain information from the spatial position of the image point. A single sample, h, representing the image point at the location $\vec{r}_{ip}$ can be expressed as

$$h(\vec{r}_{ip}) = \sum_{k=1}^{K(\vec{r}_{ip})} \mathcal{W}(k, \vec{r}_{ip}) \cdot l_k(t_{d_k}(\vec{r}_{ip})), \quad (4)$$

where $l_k(t_{d_k}(\vec{r}_{ip}))$ is the sample at time t_{d_k} from the scan line with propagation direction θ_k. The variable $\mathcal{W}$ is an apodization function with $K(\vec{r}_{ip})$ values, which controls the weighting of the contribution from each of the first stage scan lines.

The time delay, t_{d_k} for the individual scan lines are found from the round trip time-of-flight (TOF), which is the propagation time of the emitted wave in its path from the scan line reference position, $\vec{r}_{\theta_k}$ to the image point $\vec{r}_{ip}$ through the virtual source (VS), $\vec{r}_{VS}$ and return via the same path. Fig. 2(a) illustrates the time-of-flight calculation for the SASB second stage beamformer. The delay value for the scan line with reference position $\vec{r}_{\theta_k}$ and VS in $\vec{r}_{VS}$ is calculated as

$$t_{d_k}(\vec{r}_{ip}) = \frac{2}{c}\Big(|\vec{r}_{VS} - \vec{r}_{\theta_k}| \pm |\vec{r}_{ip} - \vec{r}_{VS}|\Big). \quad (5)$$

K is a function of the position of the image point, $\vec{r}_{ip}$ since the number of contributing emissions increases with distance from the VS. The synthesized aperture increases with range resulting in a less range dependent lateral resolution. To determine if a specific first stage scan line contains information about a given image point one has to evaluate if the image point is within the insonfied area from the VS. This can be done by evaluating the angle between the image point, $\vec{r}_{ip}$ and the VS, $\vec{r}_{VS_k}$ relative to the scan line direction and is calculated as

$$\Phi = \arccos\Big(\frac{\pm(\vec{r}_{ip} - \vec{r}_{VS_k})}{\|\vec{r}_{ip} - \vec{r}_{VS_k}\|} \cdot \frac{\vec{r}_{VS_k} - \vec{r}_{\theta}}{\|\vec{r}_{VS_k} - \vec{r}_{\theta_k}\|}\Big), \quad (6)$$

where $\vec{r}_{\theta_k}$ is the position of the scan line reference position.

The $\cdot$ in (6) is the dot product and $\pm$ refers to whether the image point is above or below the VS. The sign is positive if the image point is below the VS. Comparing Φ to half of the scan line opening angle, α, determines if the scan line contains information about the image point or not:

$$f(\vec{r}_{ip}, \vec{r}_{\theta_k}, \vec{r}_{VS_k}) = \begin{cases} 0, & \text{if } \Phi \text{ is } > \frac{\alpha}{2} \\ 1, & \text{if } \Phi \text{ is } \leq \frac{\alpha}{2} \end{cases} \quad (7)$$

In the case where $\Phi <= \frac{\alpha}{2}$ the first stage scan line contains information about the image point.

The total number of VS's that contribute to a specific image point can be determined from

$$K(\vec{r}_{ip}) = \sum_{k=1}^{N} f(\vec{r}_{ip}, \vec{r}_{\theta_k}, \vec{r}_{VS_k}), \quad (8)$$

where N is the total number of VS's in the scan sequence.

The variable $\mathcal{W}$ in (4) is an apodization function determining the weighting of the individual scan lines. The weight for the scan line, l_k contributing to image point $\vec{r}_{ip}$ can be

Dynamic Receive Focus			
Focus Tx (mm)	60		
F# Tx / Rx	4.51 / 0.5		
Apodization Tx / Rx	Boxcar / Gauss		
SASB	1	2	3
Virtual Source depth (mm)	20	20	40
Virtual Source F#	0.5	2	2
$\text{Apodization}_{\text{1nd stage}}$ Tx / Rx	Boxcar / Gauss		
$\text{Apodization}_{\text{2nd stage}}$	Hamming		

TABLE I
BEAMFORMATION PARAMETERS

calculated from (9)

$$\mathcal{W}(k,\vec{r}_{ip}) = \begin{cases} 0.54 - 0.46cos(2n\pi), & \text{if } n \text{ is } \leq 1 \\ 0, & \text{if } n \text{ is } > 0 \end{cases} \quad (9)$$

for the case of a desired Hamming apodization, where n can be calculated from

$$n = \frac{d(l_\theta, \vec{r}_{ip})}{\Delta} + 0.5, \quad (10)$$

and is given as the ratio between the shortest distance, $d(l_k, \vec{r}_{ip})$ from the image point, $\vec{r}_{ip}$ to the scan line, l_k and a desired aperture width, Δ. The distance $d(l_\theta, \vec{r}_{ip})$ can be expressed as

$$d(l_k, \vec{r}_{ip}) = \frac{|det(\vec{r}_{\theta_k} - \vec{r}_{VS_k}\ \vec{r}_{VS_k} - \vec{r}_{ip})|}{\|\vec{r}_{\theta_k} - \vec{r}_{VS_k}\|} \quad (11)$$

where $\vec{r}_{\theta_k}$ is the reference point of the scan line, $\vec{r}_{VS_k}$ is the position of the VS, and $\vec{r}_{ip}$ is the position of the image point all in Cartesian coordinates $(x, z)^T$. Fig. 2(b) illustrates the apodization weight calculation.

III. RESULTS

The method is investigated using simulations of point targets and validated with measurementes on a wire and contrast phantom, Model 525 (Danish Phantom Service, Frederikssund, Denmark). In both simulations and measurements, B-mode images are created and the lateral resolutions at full-width-at-half-max (FWHM), at -20 dB and -40 dB are extracted and used as quantitative measures. The method is evaluated using a BK Medical $8820e$ 192 element convex array transducer. The pitch is 0.33 mm, Radius of curvature is 60 mm and elevation focus 65 mm. All images are generated using 384 emissions, generating one RF line pr. emission and a maximum of 64 active elements. Table I specifies the beamformation setup for three different SASB setups and a standard DRF setup.

A. Simulation

The simulation software Field II [7], [8] is used to acquire RF data and beamforming is carried out using the Beamformation Toolbox III, BFT3. Simulated data is aquired using a point target phantom with 12 evenly distributed point targets in the range from 10 mm to 120 mm. A measured element pulse echo response from the center element is used as the combined excitation waveform and two-way element impulse response.

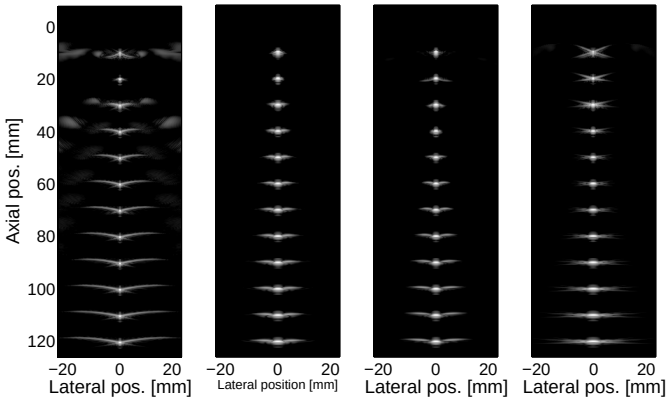

(a) SASB (1) (b) SASB (2) (c) SASB (3) (d) DRF

Fig. 3. Visualization of point target simulations, using (a) SASB (1) VS: 20 mm - F# 0.5 (b) SASB (2) VS: 20 mm - F# 2 (c) SASB (3) VS: 40 mm - F# 2 (d) DRF beamforming.

Figure 3 shows envelope detected and log-compressed B-mode images with a 60 dB dynamic range.

Note from Fig. 3(a) that at a low F# grating lobes become significant. Comparing Fig. 3(a) and 3(b) it is observed that as the F# is increased the side lobe level is decreasing at the cost of a decreasing lateral resolution at FWHM. From Fig. 3(b) and 3(c) it is observed that moving the focus point from 20 mm to 40 mm improves the range where the side lobes are insignificant, with no loss in lateral resolution at FWHM. From Fig. 3(c) and 3(d) it is clear that neither DRF og SASB can maintain a range independent lateral resolution, however SASB maintains a less range dependent lateral resolution. The performance differences between the images are quantified in Fig. 4 where the lateral beam widths at 40 mm and 120 mm are shown. Comparing the three SASB setups, SASB(3) clearly is the best overall setup due to the side lobe suppression and narrow main lobe. Note from (a) that DRF and SASB(3) have equally good lateral resolution at FWHM and at -20 dB, but at -40 dB the resolution is better using SASB(3). In (b) SASB(3)

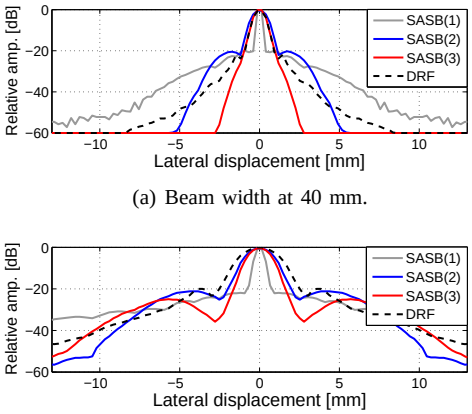

(a) Beam width at 40 mm.

(b) Beam width at 120 mm.

Fig. 4. Visualization of beam widths at (a) 40 mm (b) 120 mm. The three solid lines are the lateral beam width using SASB and the dashed line using DRF. SASB(1): VS 20 mm - F# 0.5, SASB(2): VS 20 mm - F# 2, SASB(3): VS 40 mm - F# 2, DRF: Tx focus 60 mm - F# 4.51.

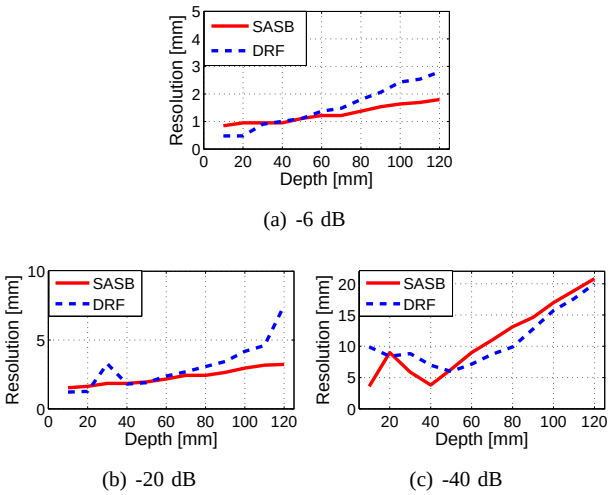

(a) -6 dB

(b) -20 dB (c) -40 dB

Fig. 5. Visualization of the lateral resolution at (a) FWHM, (b) -20, and (b) -40 dB using DRF (dashed blue line) and SASB(3): VS 40 mm - F# 2 (solid red line).

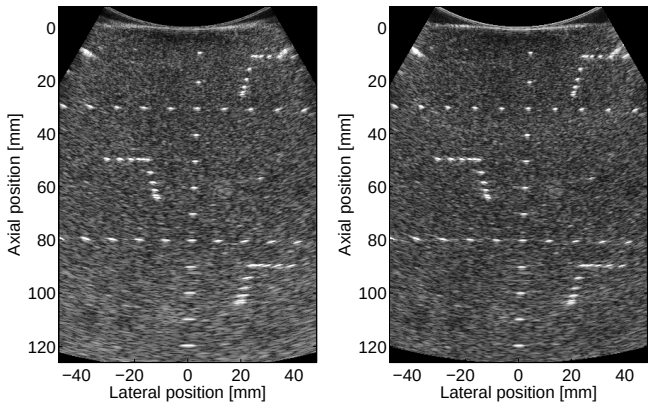

(a) DRF (b) SASB

Fig. 6. Visualization of wire and contrast phantom measurement, using (a) DRF beamforming (b) SASB beamforming.

improves the lateral resolution at both FWHM and -20 dB.

Fig. 5 presents the lateral resolution at FWHM, -20 and -40 dB using DRF (dashed blue line) and SASB(3) (solid red line) in the range 10 to 120 mm. Both DRF and SASB(3) clearly show the divergence of the beam away from the transmit focal point and the virtual source. The lateral resolution is in average improved by 17.2% at FWHM and 25.4% at -20 dB using SASB. At -40 dB the lateral resolution was on average 0.8% better using DRF. The ratio between the FWHM lateral resolution at 10 mm and 120 mm was improved from 5.9 using DRF to 2.1 using SASB.

B. Measurement

The measurement setup consist of a BK Medical 2202 Pro-Focus ultrasound scanner equipped with a research interface (BK Medical, Herlev, Denmark) and has previously been described in [9]. Data is acquired interleaved with identical excitation waveforms, TGC, and overall gain in both setups. The excitation waveform, transmit- and receive delay profile and apodization are preset standardized settings from the manufacturer. SASB second stage RF data is processed off-line using the acquired first stage RF data and the beamformation toolbox BFT3. The settings for SASB first and second stage beamformer are equal to SASB(3), specified in Table I.

Fig. 6 shows the B-mode images of the measurement on the wire and contrast phantom. Note how SASB is able to maintain a more isotropic point spread function through depth and has a better lateral resolution. The lateral resolution is in average improved by 17.9% at FWHM and 6.1% at -20 dB using SASB. The standard deviation on the lateral resolution at FWHM was improved by 0.61 mm at FWHM using SASB compared to DRF.

IV. Conclusions

SASB has been successfully implemented for a convex multi element array transducer. The method is not able to maintain a constant F# due to the curved shape of the transducer array, as the synthesized aperture only experiences a moderate expansion. However, the simulated results show an average improvement in the lateral resolution using SASB compared to DRF. Measurements confirmed the improvements on the lateral resolution. The method showed the ability to increase the image range of a uniform lateral resolution and to obtain a more isotropic point spread function. This was shown for simulations and for phantom measurements. The results presented in this paper proves the viability of the method for real-time 2D ultrasound imaging using commercially available equipment.

Acknowledgment

This work was supported by the Danish Science Foundation and by BK Medical ApS, Denmark.

References

[1] C. Passmann and H. Ermert, "A 100-MHz ultrasound imaging system for dermatologic and ophthalmologic diagnostics," *IEEE Trans. Ultrason., Ferroelec., Freq. Contr.*, vol. 43, pp. 545–552, 1996.

[2] C. H. Frazier and W. D. O'Brien, "Synthetic aperture techniques with a virtual source element," *IEEE Trans. Ultrason., Ferroelec., Freq. Contr.*, vol. 45, pp. 196–207, 1998.

[3] S. I. Nikolov and J. A. Jensen, "Virtual ultrasound sources in high-resolution ultrasound imaging," in *Proc. SPIE - Progress in biomedical optics and imaging*, vol. 3, 2002, pp. 395–405.

[4] ——, "3D synthetic aperture imaging using a virtual source element in the elevation plane," in *Proc. IEEE Ultrason. Symp.*, vol. 2, 2000, pp. 1743–1747.

[5] M. H. Bae and M. K. Jeong, "A study of synthetic-aperture imaging with virtual source elements in B-mode ultrasound imaging systems," in *IEEE Trans. Ultrason., Ferroelec., Freq. Contr.*, vol. 47, 2000, pp. 1510–1519.

[6] J. Kortbek, J. A. Jensen, and K. L. Gammelmark, "Synthetic aperture sequential beamforming," *J. Acoust. Soc. Am.*, p. Submitted, 2009.

[7] J. A. Jensen and N. B. Svendsen, "Calculation of Pressure Fields from Arbitrarily Shaped, Apodized, and Excited Ultrasound Transducers," *IEEE Trans. Ultrason., Ferroelec., Freq. Contr.*, vol. 39, pp. 262–267, 1992.

[8] J. A. Jensen, "Field: A Program for Simulating Ultrasound Systems," *Med. Biol. Eng. Comp.*, vol. 10th Nordic-Baltic Conference on Biomedical Imaging, Vol. 4, Supplement 1, Part 1, pp. 351–353, 1996.

[9] M. C. Hemmsen, M. M. Petersen, S. I. Nikolov, M. B. Nielsen, and J. A. Jensen, "Ultrasound image quality assessment: A framework for evaluation of clinical image quality," in *SPIE Med. Imag. V Symp.*, 2010, p. Accepted for publication.

Paper VII

Simulation of acoustic fields for high quality ultrasound imaging

Martin Christian Hemmsen, Jens Munk Hansen, and Jørgen Arendt Jensen

IEEE Transactions on Ultrasonics, Ferroelectrics, and Frequency Control

Draft

Simulation of acoustic fields for high quality ultrasound imaging

Martin Christian Hemmsen, Jens Munk Hansen, and Jørgen Arendt Jensen

Abstract

Ultrasound imaging is an active field of research and each year new imaging schemes are proposed. The performance of these new methods is often documented in an idealized framework, ignoring the complications of real and non-ideal transducers. Previous work has shown that transducers are deteriorating over time, significantly degrading image quality. It is therefore relevant to investigate how imaging methods perform in non-idealized systems. Furthermore with the increasing system complexity and image quality of new processing methods, the requirements for an accurate and realistic prediction of the acoustic field is increasing. This paper investigates if a detailed and realistic prediction of the acoustic field of a high quality imaging system, can be obtained by combining experimental determination of the individual element pulse echo wavelets and numerical modeling. The main motivation for the study is to investigate if the influence on the acoustic field using physical transducers can be modeled with an sufficient accuracy to reveal system performance. The investigation is performed as a series of simulations, compared to measured data. Measured data is acquired using a BK8804 192-element linear array transducer (BK Medical, Herlev, Denmark) and a BK Medical 2202 ProFocus ultrasound scanner. Synthetic Aperture Sequential Beamformation (SASB) is used to beamform the received pressure field, and is compared to measured data from three metal wires. Two simulation models are created, one with an identical element pulse echo wavelet for all elements and one with individual element pulse echo wavelets. The accuracy of the simulation models are quantized by calculating the sum-of-squared-error between the simulated and measured SASB second stage rf data. Results show that when comparing the sum-of-squared-error between the center scan line the accuracy increases from a relative error of 14.3% using an identical element pulse echo wavelet for all elements, to 3.4% using individual element pulse echo wavelets. Comparing the sum-of-squared-error between all scan lines the accuracy increases from a relative error of 15.6%, to 11.6%. This study shows that by including the individual element pulse echo wavelets into the simulation the accuracy and reliability of the simulated acoustic field is improved and allows for simulated system performance evaluation. The detailed predictions can be used as an early performance indicator of new imaging methods, and help gain insight into how physical transducer characteristics influence image quality.

I. Introduction

Simulation of acoustic fields for ultrasound imaging using linear acoustics is extensively used for optimization and evaluation of new imaging methods, and is a standard tool in ultrasound research and development. In medical

Martin Christian Hemmsen is with BK Medical, Denmark, and the Department of Electrical Engineering, Center for Fast Ultrasound, Technical University of Denmark. e-mail: mah@elektro.dtu.dk.

Jens Munk Hansen and Jørgen Arendt Jensen is with the Department of Electrical Engineering, Center for Fast Ultrasound, Technical University of Denmark.

ultrasound, a pulse is emitted into the body and is scattered and reflected by density and propagation velocity perturbations. The received field can be found by solving an appropriate wave equation. This has been done in a number of papers [1], [2]. Gore and Leeman considered a wave equation where the scattering term was a function of the adiabatic compressibility and the density. Jensen used an equivalent wave equation as the one used by Gore and Leeman, but changed the scattering term for the wave equation to a function of density and propagation velocity perturbations. The derived model has no restrictions enforced on the transducer geometry or its excitation and its implementation, Field II [3], [4], has become a widely used tool for simulations in ultrasound research and development.

With the emergence of new high quality imaging methods such as digital beamforming and synthetic aperture techniques, that have a side-lobe level well below -30dB and increased system complexity, it becomes important to include transducer characteristics into the simulation model for an accurate and reliable prediction of the acoustic field. This was shown by Hemmsen et al. in [5] that compared simulated and measured point spread functions using synthetic aperture sequential beamformation (SASB) [6].

This paper shows that a detailed prediction of the acoustic field of a diagnostic ultrasound scanner, can be obtained by combining experimental determination of the individual element pulse echo wavelets and numerical modeling. The predictions of the model is confirmed by comparison with measurements using a BK8804 192-element linear array transducer (BK Medical, Herlev, Denmark) and a BK Medical 2202 ProFocus ultrasound scanner. The investigation is performed as a series of simulations, performed using the Field II simulation software to generate data, and the Beamformation Toolbox III [7] to perform SASB beamforming on both measured and simulated data. Furthermore, it is investigated how the imperfectness of physical transducers, manifested as element phase error, element sensitivity deviations, and transfer characteristic influence SASB beamforming.

The rest of this manuscript is organized as follows. Section II briefly describes the theory behind the simulation software Field II. Section III describes the measurement setup and creation of the *in silico* transducer models. The results using the *in silico* models, to accurately predict the received echo signal from a multi element focused aperture, is presented and discussed in Section IV. Section V investigates how the imperfectness of physical transducers influence SASB imaging, followed by conclusions in Section VI.

II. THEORY

This section gives a short introduction to the theory behind the simulation software Field II to give the reader an understanding how the received voltage signal is generated and to show how the element pulse-echo wavelet is directly implemented into the model. Field II is a linear acoustics simulation software that can be used to calculate the received signal [2], [8] from a collection of point scatterers using:

$$V_r(t) = V_{pe}(t) \underset{t}{\star} f_m(\vec{r}_1) \underset{r}{\star} h_{pe}(\vec{r}_1, t), \tag{1}$$

for an identical element pulse-echo wavelet on all elements, where $\underset{r}{\star}$ denotes spatial convolution, $\underset{t}{\star}$ temporal convolution, and $\vec{r}_1$ the position of the point scatterer. $V_{pe}(t)$ is the pulse-echo wavelet, which includes both the

transducer excitation and the electro-mechanical impulse response during emission and reception of the pulse. $f_m(t)$ accounts for the inhomogeneities in the tissue due to density and speed of sound perturbations that generates the scattering, and $h_{pe}(\vec{r}_1, t)$ is the pulse-echo spatial impulse response that relates the transducer geometry to the spatial extent of the scattered field. Explicitly written out the latter term is:

$$h_{pe}(\vec{r}_1, t) = h_t(\vec{r}_1, t) \underset{t}{\star} h_r(\vec{r}_1, t), \tag{2}$$

where $h_t(\vec{r}_1, t)$ is the spatial impulse response for the transmitting aperture and $h_r(\vec{r}_1, t)$ is the spatial impulse response for the receiving aperture. Both impulse responses are a superposition of the spatial impulse responses from the individual elements of a multi-element aperture properly delayed and apodized. Each impulse response is:

$$h(\vec{r}, t) = \sum_{i=1}^{N_e} a_i(t) h_i(\vec{r}_1, t - \Delta_i(t)), \tag{3}$$

where $a_i(t)$ denotes the apodization and $\Delta_i(t)$ focusing delay, which both are a function of position in tissue and thereby time. N_e is the number of transducer elements. The received signal from each scatterer must be calculated for each new focusing scheme corresponding to the different lines in an image. The resulting *rf* signal is then found by summing the responses from the individual scatterers using (1).

The model expressed in (1) can be extended with individual element pulse-echo wavelets by rearranging (1), (2), and (3) such that the time convolution between the element pulse-echo wavelet, the receive spatial impulse response, and the transmit spatial impulse response is convolved individually pr. element as:

$$V_r(t) = f_m(\vec{r}_1) \underset{r}{\star} \sum_{i=1}^{N_e} V_{pe,i}(t) \underset{t}{\star} h_{pe,i}(\vec{r}_1, t), \tag{4}$$

where $V_{pe,i}(t)$ is the element pulse-echo wavelet for the i'th element, and $h_{pe,i}(\vec{r}_1, t)$ is the element pulse-echo spatial impulse response and can be calculated using (2) and (3) on individual element basis. In Section III the element pulse echo is determined for a BK8804 transducer. The characterization show that the element pulse echoes are not identical and it is easily understood that including individual element pulse-echo wavelets into the simulation model improves the transducer characterization. A more accurate characterization of the transducer will result in an improved accuracy and reliability of the simulation model.

III. Determination of pulse echo wavelets

A. Simulation model

To perform the calculations in (1) and (4), V_{pe} must be determined, as h ca be calculated from the physical dimensions of the transducer. V_{pe} can either be constructed from knowledge of the electromechanical properties of the transducer [9] or it can be measured. We choose the second approach here, as this gives the most accurate determination of V_{pe}. The model described using (1) is denoted Model 1 and the model described using (4) is denoted Model 2. Model 1 is the reference model implemented using a common pulse echo wavelet for all elements, and Model 2 is the extended model implemented using individual pulse echo wavelets for each element.

B. Measurement setup

The pulse echo wavelets are experimentally determined using a measurement system consisting of a BK Medical 2202 ProFocus ultrasound scanner (BK-Medical, Herlev, Denmark) equipped with a research interface and a standard PC. The scanner is connected to the PC through the Ethernet, and a X64-CL Express camera link (Dalsa, Waterloo, Ontario, Canada) and has previously been described in [10]. The transducer is a 192 element BK Medical 8804 linear array transducer with a nominal frequency of 7.5 MHz. The elevation focus is at 20 mm, pitch 0.208 mm, and height 4.5 mm.

The measurement of the individual element pulse echo responses from the transducer was performed as described in [11], where a transducer is mounted in a water tank on a device permitting independent angular adjustment in two orthogonal planes and translation in the third plane. The target is a stainless steel plate, which dimensions are much larger than the transducer beam being measured. This is to avoid multiple reflections from the back surface and sides. For a focused transducer the plane reflector is placed at the focal point and parallel to the acoustic surface of the transducer. This ensures that the equiphase surfaces of the return pulse match the curvature of the generating element and the spatial impulse response is a Dirac impulse. The transducer is then adjusted in angle until the echo amplitude is simultaneously peaked in both orthogonal planes. It must be emphasized that this is a critical part of the setup procedure, and the parallel alignment of the transducer and the reflector can be difficult to obtain, especially because it is unknown if the transducer elements are perfectly aligned or there exist some phase error. To help the alignment, it is proposed to estimate a time-of-flight phase error profile using a point source. The transducer can then be aligned to the plane reflector, such that the time-of-flight phase error profile using the plane reflector match the profile estimated using the point source. In the following of this paper the time-of-flight phase error will be referred to as the phase error. The benefit of using a point source for the estimation of the phase error profile, is because it is angle independent.

It has earlier been proposed to use cross correlation measurements on signals emanating from a point source to determine phase errors for different types of sampled aperture, coherent imaging systems [12], [13]. Here the method is adapted for estimation of the phase error based on a metal wire submerged in a water tank, using a sliding single element sub-aperture, with the same element transmitting and receiving.

The method can be described as: When the transmitted wave impinges on the wire, a spherical wave is expected to emanate since the wire thickness is small with respect to the wavelength. This means that the field is uniform on the plane where it is sampled and as a consequence all the array elements receive the same signal except for a delay. This delay is a function of the position of the wire and must be compensated for to determine the phase errors using cross-correlation.

The delay can be compensated for by beamforming the individual received signals with transmit reference position at the transmitting and receiving element, and receive reference position at the wire projected onto the aperture. The received signals before and after compensation, acquired using a bipolar 7.5 MHz 2 cycle sinusoid excitation waveform, are respectively shown in Fig. 1(a) and 1(b) for a wire positioned at a depth of 80 mm. The figures uses

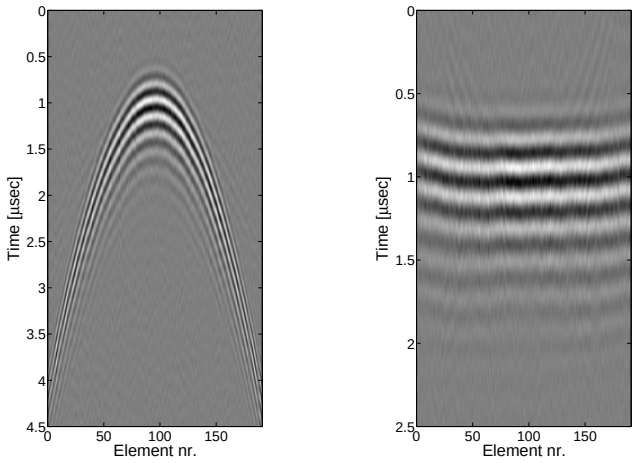

(a) (b)

Fig. 1. Received rf signals shown for (a) wire measurement and (b) wire measurement compensated for time-of-flight. The amplitude of the wavelets has been normalized relative to the peak value of all wavelets. Note that the time axis on (b) is identical with that of Fig. 3(a) so the responses can be qualitatively compared.

a display format introduced by Flax and O'Donnell [13], where the rf signals are displayed as they are received by the array elements. Negative signal values are in black, while positive signal values are in white. The time axis is scaled to only show the relevant part of the received signals.

The round trip phase error profile is found by upsampling the individual element pulse echo wavelets from Fig. 1(b) to 800 MHz for subsample accuracy and then calculating the cross-correlation between the wavelets of the individual elements and the center element. The phase profile is then found from the lags that gives the highest correlations.

Using the estimated phase error profile the transducer can now be positioned such that the plate reflector is placed at the elevation focal point of the transducer and the phase error profile match the one estimated from the wire target. Fig. 2 shows the estimated phase error profile using the wire target and the plate reflector. Note from the figure the very good agreement between the two estimates of the phase error profile. The maximum phase error is 0.0813 μsec or 0.61 λ, found between element 2 and 60 using the wire target.

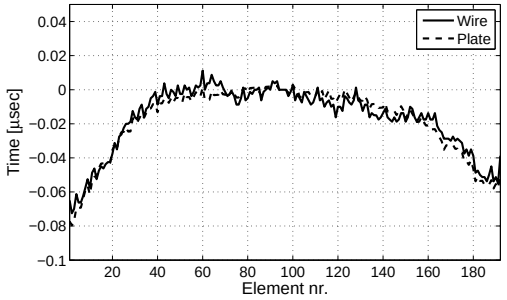

Fig. 2. Measured round trip phase error profile using the wire target and the plate reflector.

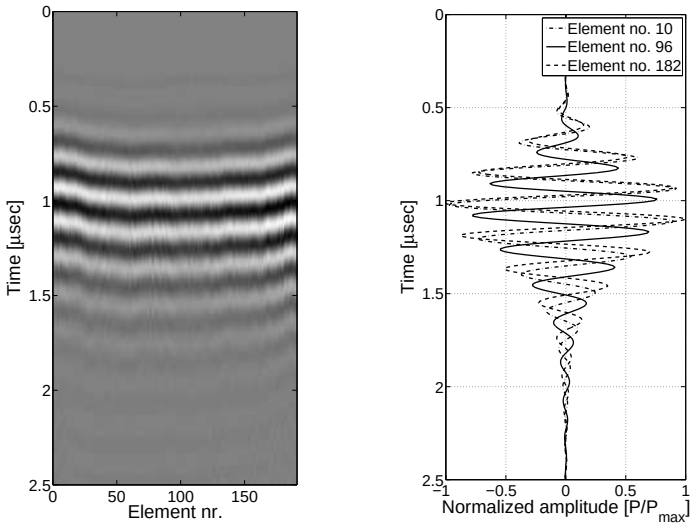

(a) (b)

Fig. 3. Measured pulse echo response for (a) all elements and (b) element 10, 96, and 182. The amplitude of the wavelets has been normalized relative to the peak value of all wavelets.

Fig. 3(a) shows the measured element pulse echo wavelets using the plate reflector and the same transducer position as used in Fig. 2. Fig. 3(b) shows the pulse echo wavelets for element no. 10, 98, and 182. Note how the waveforms at the edges of the array are almost in phase and have a significant phase shift relative to the center element. The resulting pulse echo response for the central element is shown in Fig. 4(a). To remove noise and ensure smooth transaction at the boundaries of the acquired responses, the element responses are averaged and windowed with a Tukey window ($\alpha = 0.2$). The resulting pulse echo wavelet for the central element is shown in Fig. 4(b) and will be used as V_{pe}, from (1), referred to as Model 1. The entire set of wavelets will be used as the individual element pulse echo, $V_{pe,i}$, from (4) and will be referred to as Model 2.

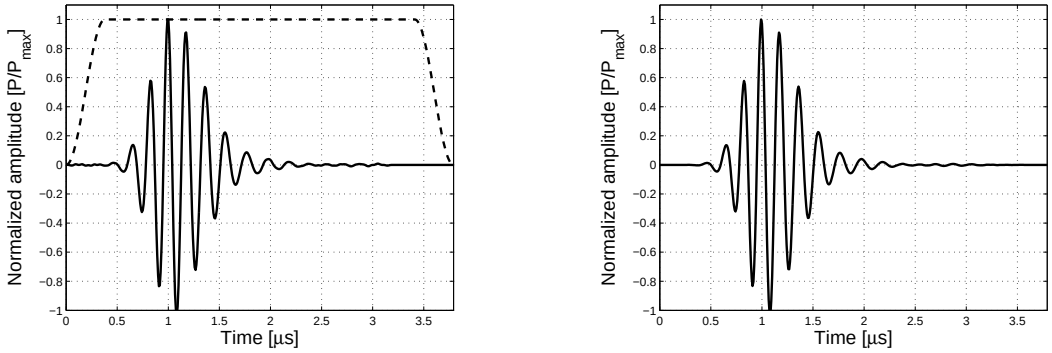

(a) Raw response (b) Processed response

Fig. 4. Measured pulse echo response for the center element. In (a) the solid line indicates the raw response and the dashed line the applied Tukey window, (b) shows the averaged and Tukey windowed response.

The measurement of the element pulse echo wavelets also enables the estimation of the two-way sensitivity profile, which can be found by calculating the energy, E, of the individual wavelets as

$$E_i = \sum_{n=1}^{N} V_i(n)^2 \tag{5}$$

where i is the i'th element and $V(n)$ is the pulse echo wavelet at sample n. N is the number of samples in the wavelet. Fig. 5 shows the sensitivity profile. The maximum sensitivity deviation is 1.9 dB between channel 42 and 86.

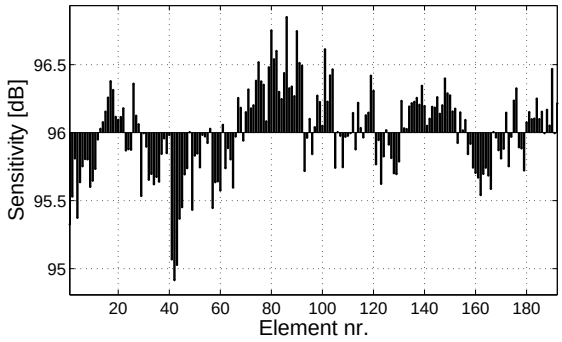

Fig. 5. Measured two-way element sensitivity profile.

IV. Wave Propagation experiment

This section investigates the accuracy of the predicted SASB beamformed received pressure field, from three point scatterers embedded in a homogeneous medium, with a measurement of three thin metal wires in a water tank. The measurement describes how a point is imaged by the system, by scanning the wire orthogonal to the image plane. The metal wires have a diameter of 0.07 mm and are fixated at three depths, 29.8 mm, 54.7 mm, and 79.4 mm. Specification of the measurement and simulation parameters can be found in Table I.

TABLE I
Measurement parameters

Transducer Parameters (BK8804)	
Pitch (mm)	0.208
Elevation focus (mm)	20
Number of elements (mm)	192
Imaging parameters	
Focus Tx / Rx (mm)	10 / 10
F# Tx / Rx	2 / 2
Apodization Tx / Rx	Boxcar / Gauss
Scanner setting	
Waveform	7.5 MHz 2 cycle sinusoid
No. of emissions / scan lines	190 / 190

TABLE II
SIMULATION ACCURACY

Center scan line	Unit	Scatter depth: 29.8 mm	54.7 mm	79.4 mm
$E_{Model\ 1}$	%	6.7	8.6	14.3
$E_{Model\ 2}$	%	1.7	3.7	3.4
All scan lines				
$E_{Model\ 1}$	%	8.5	10.5	15.6
$E_{Model\ 2}$	%	4.1	6.5	11.6

The simulated center responses are compared to the measured response and are visualized in Fig. 6(a) to 6(c). Note how well both models accurately predicts the measured response. The accuracy is quantitatively determined using the relative sum-of-squared error defined as:

$$E = \frac{\sum_{n=1}^{N} (V_s(n) - V_m(n))^2}{\sum_{n=1}^{N} V_m(n)^2} * 100 \tag{6}$$

where $V_s(n)$ and $V_m(n)$ is the simulated and measured received response from the center scan line at sample n. The error for the two models are shown in Table II.

Fig. 6(d) to Fig. 6(l) shows contour plots of the logarithm compressed envelope detected responses for all scan lines. Comparing the contour plots for the measured responses and the simulated responses, one sees that the main differences between the contours is the width of the point spread functions.

Including the individual element pulse echo wavelets into the simulation model, improves the accuracy and gives a more reliable realization of the pressure. There are however still differences between the simulated response and the measured response and this might be due to the finite size of the wire, and inaccurate prediction of the true transducer characteristic or effective geometry. These deviations are, however, small compared to the overall capability of the model to predict the actual response and improved capabilities to estimate the performance of SASB imaging. The models are compared quantitatively to the measured data by calculating the relative sum of squared error as:

$$E = \frac{\sum_{n=1}^{N} \sum_{i}^{I} (V_s(n,i) - V_m(n,i))^2}{\sum_{n=1}^{N} \sum_{i}^{I} V_m(n,i)^2} * 100 \tag{7}$$

where $V_s(n,i)$ and $V_m(n,i)$ is the simulated and measured received response at sample n for scan line i. The error for the two models are shown in Table II.

To further investigate the level of agreement between the measured and simulated responses, the covered area of the point spread function at different amplitude levels can by considered, as shown in Fig. 7. Note how the covered area is approximately the same for Model 1, Model 2, and the measured data until -35 dB. From -35 dB, Model 1 fails to predict the received response, and Model 2 is able to predict the covered area with a small underestimation. This shows that by including individual element pulse echo wavelets into the simulation model, the model is able to predict not only the energy in the main-lobe, but also in a the side-lobe.

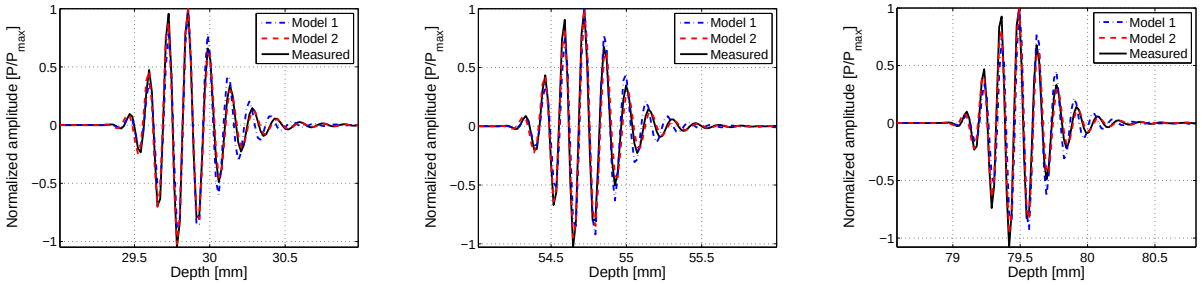

(a) Center response from a scatterer at 29.8 mm

(b) Center response from a scatterer at 54.7 mm

(c) Center response from a scatterer at 79.4 mm

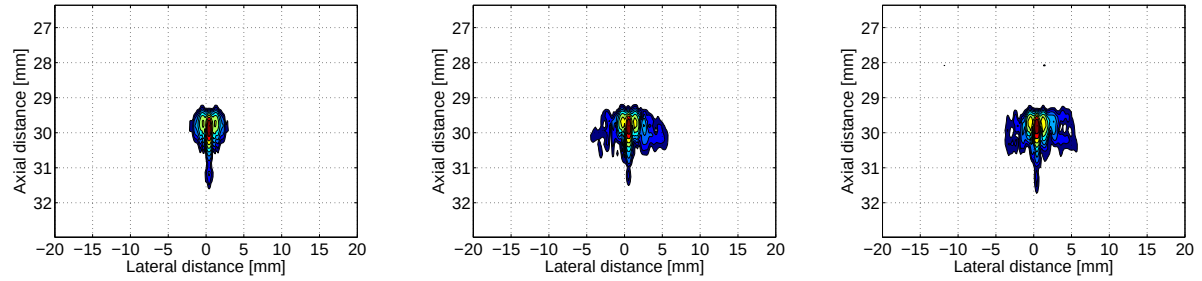

(d) Model 1: 29.8 mm

(e) Model 2: 29.8 mm

(f) Measured: 29.8 mm

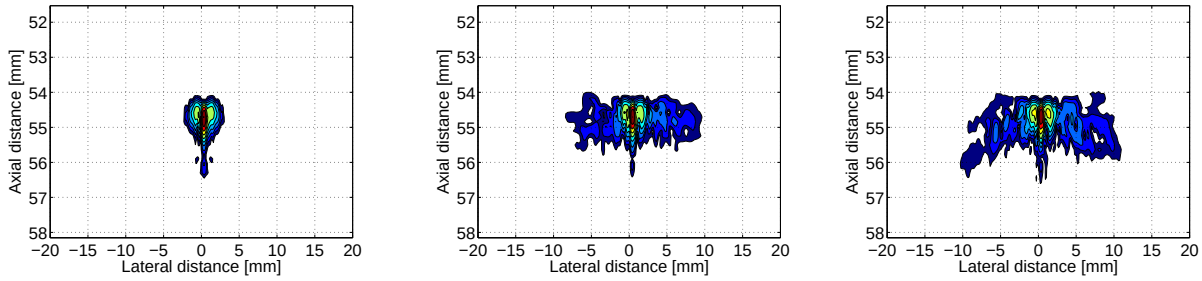

(g) Model 1: 54.7 mm

(h) Model 2: 54.7 mm

(i) Measured: 54.7 mm

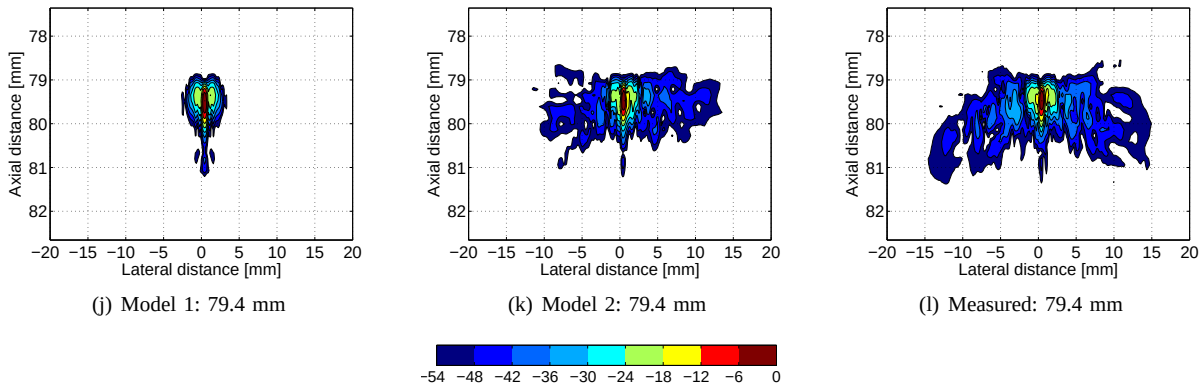

(j) Model 1: 79.4 mm

(k) Model 2: 79.4 mm

(l) Measured: 79.4 mm

Fig. 6. Fig. (a) to (c) illustrates the measured and simulated second stage SASB responses from the center scan line from three scatterers at (a) 29.8 mm, (b) 54.7 mm, and (c) 79.4 mm from the transducer surface. Fig. (d) to (l) illustrates contour plots with 6 dB contour coloring for the three scatters using Model 1 in (d,g,j), Model 2 in (e,h,k), and measured response in (f,i,l).

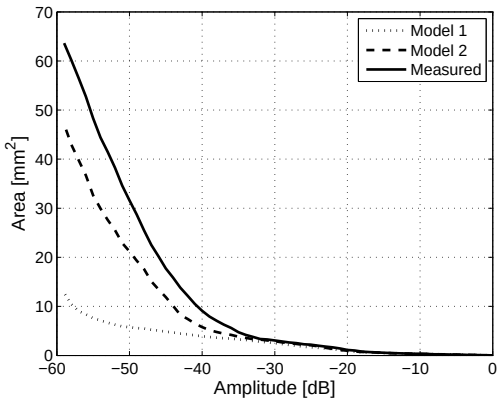

Fig. 7. Area covered by the point spread function from the scatter at 79.4 mm.

V. BEAMFORMING OPTIMIZATION

The measured phase error is on the order of what can be expected from phase fluctuations in arrival time due to the presence of a fat human abdominal wall [14]. Several studies report significant image quality degradation from phase aberration [15], [16], and several techniques are developed for compensation [13], [17]–[19]. The main difference between the fluctuations in arrival time due to the human tissue and the measured phase error due to the transducer characteristics, is that the human tissue results in a non-structural error. The measured phase error is structural and can easily be compensated for by modification of the receive and transmit delay profiles.

Ideally, half of the estimated phase and sensitivity profile should be applied in both transmit and receive, as they affects wave propagation on both transmit and receive. This section investigates how the phase error and the sensitivity deviation influence SASB imaging, and seeks to improve the image quality by compensating for the measured errors. The optimization of the beamforming is performed in three variations: sensitivity alignment, phase alignment, and the combination of sensitivity and phase alignment. The improvement is investigated in simulations and results are presented as contour and covered area plots for a single scatterer at 79.4 mm from the transducer surface and can be compared with Fig. 6(k) and Fig. 7.

The sensitivity of the individual elements is compensated for the relative sensitivity deviation, by adjusting the receive and transmit apodization profile to encompass the sensitivity profile. The resulting contour plot for the simulated point spread function is shown in Fig. 8(a). From the figure it is seen that the compensation for the sensitivity deviations alone is not enough to improve the point spread function. The summation of negative and positive pressures suppressing the side-lobes is not improved as the phase of the responses is not aligned correctly in the beamforming process.

Fig. 8(b) shows the simulated point spread function compensating for the phase error. The phase of the individual elements of the array is compensated for the relative phase deviation by adjusting the receive and transmit delay profile. From the figure it is seen that the compensation for the phase deviations improve the point spread function, by improving the ratio between the side-lobe and main-lobe levels. The phase correction ensures that the responses

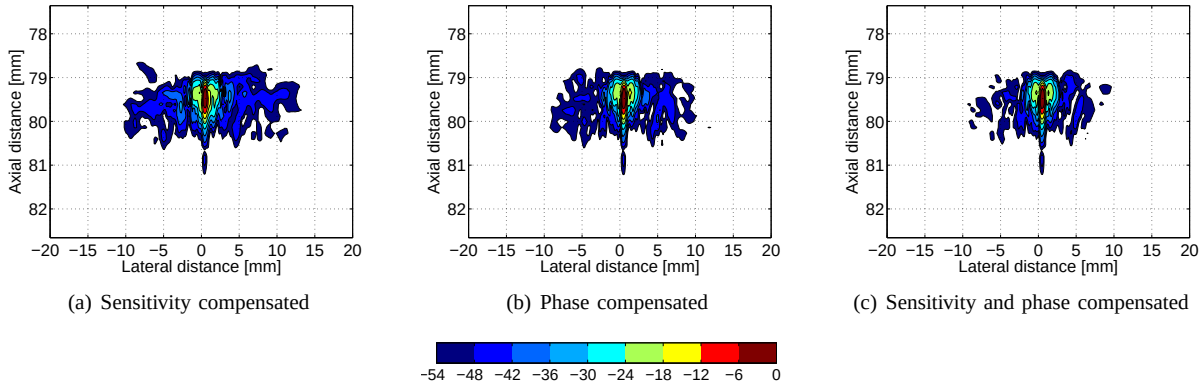

(a) Sensitivity compensated (b) Phase compensated (c) Sensitivity and phase compensated

Fig. 8. Simulated second stage SASB contour plots with 6 dB contour coloring down to -54 dB are shown using (a) sensitivity compensated, (b) phase compensated, and (c) sensitivity and phase compensated wavelets of a scatterer 79.4 mm from the transducer surface.

are aligned correctly in the beamforming process and a destructive summation of negative and positive pressures suppressing the side-lobes is obtained.

Fig. 8(c) shows the point spread function compensating for both the phase error and the sensitivity deviation. From the figure it is seen that the point spread function is much similar with that from Fig. 6(j) where an identical pulse echo wavelet is used for all elements. The remaining differences between the compensated model using individual element pulse echo measurements and Model 1, can be explained by the deviations in the individual elements transfer characteristics.

To further investigate the achieved improvements using the three compensated models, the covered area of the simulated point spread function at different amplitude levels can by considered, as shown in Fig. 9. Note how the covered area is approximately the same for all three models until -35 dB. From -35 dB, it is observed that compensating for phase is more important than compensating for sensitivity, and compensating for both sensitivity and phase is optimal.

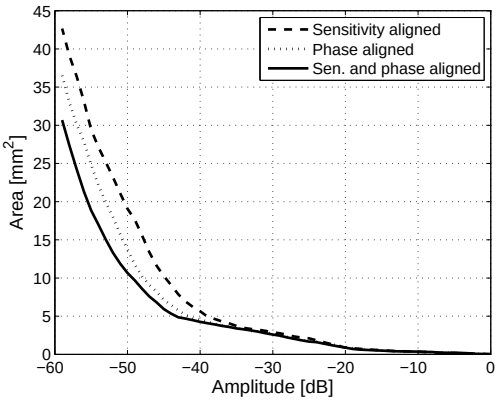

Fig. 9. Area covered by the point spread function from the scatter at 79.4 mm after compensation for phase error and sensitivity deviations.

VI. Conclusions

This paper has shown that the prediction of the receive pressure field can be improved by combining experimental determination of the individual element pulse echo wavelets into the simulation model. The investigation of the improved simulation model showed that the influence on the acoustic field using physical transducers can be modeled with an sufficient accuracy to reveal system performance for a high quality imaging method such as SASB.

Inspection of the measured pulse echo wavelets showed a significant deviation in sensitivity and phase profile. Using the proposed simulation model the influence from the deviations was investigated and revealed vital information how to optimize the beamformer by including the deviation profiles into the beamformers delay and apodization profiles.

Simulations has shown that systematic errors, that can easily be accounted and compensate for, is important to include into the beamforming process, for improved image quality using SASB.

Acknowledgment

This work was supported by the Danish Science Foundation and by BK Medical ApS, Denmark.

References

[1] J. Gore and S. Leeman, "Ultrasonic backscattering from human tissue: A realistic model," *Phys. Med. Biol.*, vol. 22, pp. 317–326, 1977.

[2] J. A. Jensen, "A model for the propagation and scattering of ultrasound in tissue," *J. Acoust. Soc. Am.*, vol. 89, pp. 182–191, 1991a.

[3] J. A. Jensen and N. B. Svendsen, "Calculation of Pressure Fields from Arbitrarily Shaped, Apodized, and Excited Ultrasound Transducers," *IEEE Trans. Ultrason., Ferroelec., Freq. Contr.*, vol. 39, pp. 262–267, 1992.

[4] J. A. Jensen, "Field: A Program for Simulating Ultrasound Systems," *Med. Biol. Eng. Comp.*, vol. 10th Nordic-Baltic Conference on Biomedical Imaging, Vol. 4, Supplement 1, Part 1, pp. 351–353, 1996.

[5] M. C. Hemmsen, J. Kortbek, S. I. Nikolov, and J. A. Jensen, "Simulation of high quality ultrasound imaging," in *Proc. IEEE Ultrason. Symp.*, Oct. 2010, p. Accepted for publication.

[6] J. Kortbek, J. A. Jensen, and K. L. Gammelmark, "Synthetic aperture sequential beamforming," *Ultrasonics*, p. Submitted, 2009.

[7] J. M. Hansen and J. A. Jensen, "An object-oriented multi-threaded software beamformation toolbox," Feb. 2011, submitted to SPIE Medical Imaging, 12 -17 February 2011, Lake Buena Vista (Orlando), Florida, USA.

[8] J. A. Jensen and S. Nikolov, "Fast simulation of ultrasound images," in *Proc. IEEE Ultrason. Symp.*, vol. 2, 2000, pp. 1721–1724.

[9] D. Bæk, J. A. Jensen, and M. Willatzen, "Multilayer piezoelectric transducer models combined with Field II," *J. Acoust. Soc. Am.*, p. Submitted, 2009.

[10] M. C. Hemmsen, , S. I. Nikolov, M. M. Pedersen, M. J. Pihl, M. S. Enevoldsen, J. M. Hansen, and J. A. Jensen, "Implementation of a versatile research data acquisition system using a commercially available medical ultrasound scanner," *IEEE Trans. Ultrason., Ferroelec., Freq. Contr.*, p. Submitted, 2011.

[11] K. Erikson, "Tone-burst testing of pulse-echo transducers," *IEEE Transactions on Sonics and Ultrasonics*, vol. 26, no. 1, pp. 7–13, 1979.

[12] C. N. Dorny, "A self-survey technique for self-cohering of antenna systems," *IEEE Trans. Antennas Propagat.*, vol. 26, pp. 877–881, 1978.

[13] S. W. Flax and M. O'Donnell, "Phase-aberration correction using signals from point reflectors and diffuse scatterers: basic principles," *IEEE Trans. Ultrason., Ferroelec., Freq. Contr.*, vol. 35, pp. 758–767, 1988.

[14] Y. Sumino and R. C. Waag, "Measurements of ultrasonic pulse arrival time differences produced by abdominal wall specimens," *J. Acoust. Soc. Am.*, vol. 90, no. 6, pp. 2924–2930, Dec. 1991.

[15] N. Oddershede and J. A. Jensen, "Phase aberration measurements in medical ultrasound: Human studies," *Ultrason. Imaging*, pp. 1–11, 1988.

[16] S. F. Tsai and T. W. H. Sheu, "Finite element analysis of three-dimensional vortical flow structure and topology inside a carotid bifurcation model," *Ultrason. Imaging*, vol. 10, no. 1, pp. 12–28, January 1988.

Bibliography

[1] K. E. Thomenius, "Evolution of ultrasound beamformers," in *Proc. IEEE Ultrason. Symp.*, vol. 2, 1996, pp. 1615–1621.

[2] M. H. Pedersen, K. L. Gammelmark, and J. A. Jensen, "In-vivo evaluation of convex array synthetic aperture imaging," *Ultrasound Med. Biol.*, vol. 33, pp. 37–47, 2007.

[3] S. Nikolov, J. Kortbek, and J. A. Jensen, "Practical applications of synthetic aperture imaging," in *Proc. IEEE Ultrason. Symp.*, 2010, p. submitted.

[4] V. Behar and D. Adam, "Optimization of sparse synthetic transmit aperture imaging with coded excitation and frequency division," *Ultrasonics*, vol. 43, no. 10, pp. 777–788, 2005.

[5] J. Kortbek, "Synthetic aperture sequential beamforming and other beamforming techniques in ultrasound imaging," Ph.D. dissertation, Ørsted•DTU, Technical University of Denmark, 2800, Lyngby, Denmark, 2007.

[6] J. Kortbek, J. A. Jensen, and K. L. Gammelmark, "Synthetic aperture sequential beamforming," *Ultrasonics*, p. Submitted, 2009.

[7] J. R. Thornbury, "Eugene w. caldwell lecture. clinical efficacy of diagnostic imaging: love it or leave it," *AJR*, vol. 162, no. 1, pp. 1–8, 1997.

[8] J. A. Jensen and N. B. Svendsen, "Calculation of Pressure Fields from Arbitrarily Shaped, Apodized, and Excited Ultrasound Transducers," *IEEE Trans. Ultrason., Ferroelec., Freq. Contr.*, vol. 39, pp. 262–267, 1992.

[9] J. A. Jensen, "Field: A Program for Simulating Ultrasound Systems," *Med. Biol. Eng. Comp.*, vol. 10th Nordic-Baltic Conference on Biomedical Imaging, Vol. 4, Supplement 1, Part 1, pp. 351–353, 1996.

[10] J. M. Hansen and J. A. Jensen, "An object-oriented multi-threaded software beamformation toolbox," Feb. 2011, submitted to SPIE Medical Imaging, 12 -17 February 2011, Lake Buena Vista (Orlando), Florida, USA.

[11] American Institute of Ultrasound in Medicine, *The AIUM 100 mm test object and recommended procedures for its use*. Rockville, MD: American Institute of Ultrasound in Medicine, 1974.

[12] P. L. Carson and J. A. Zagzebski, *Pulse echo ultrasound imaging systems: Performance tests and criteria*. American Institute of Physics, 1980.

[13] M. M. Goodsitt, P. L. Carson, S. Witt, D. L. Hykes, and J. M. Kofler, "Real-time B-mode ultrasound quality control test procedures," *Med. Phys.*, vol. 25, no. 8, pp. 1385–1405, 1998.

[14] K. Brendel, L. Filipczynski, R. Gerstner, C. Hill, G. Kossoff, G. Quentin, J. Reid, J. Saneyoshi, J. Somer, A. Tchevnenko, and P. Wells, "Methods of measuring the performance of ultrasonic pulse-echo diagnostic equipment," *Ultrasound Med. Biol.*, vol. 2, no. 4, pp. 343 – 350, 1977.

[15] D. Vilkomerson, J. Greenleaf, and V. Dutt, "Towards a Resolution Metric for Medical Ultrasound Imaging," in *Proc. IEEE Ultrason. Symp.*, 1995, pp. 1405–1410.

[16] J. A. Zagzebski, *Essentials of Ultrasound Physics*. Mosby, 1996.

[17] A. W. Rihaczek, *Principles of high-resolution radar*. New York: McGraw-Hill, 1969.

[18] D. H. Johnson and D. E. Dudgeon, *Array Signal Processing. Concepts and Techniques.* Englewood Cliffs, New Jersey: Prentice-Hall., 1993.

[19] S. W. Smith and H. Lopez, "A contrast-detail analysis of diagnostic ultrasound imaging," *Med. Phys.*, vol. 9, no. 1, pp. 4–12, Feb 1981.

[20] S. W. Smith, R. F. Wagner, J. M. Sandrik, and H. Lopez, "Low contrast detectability and contrast/detail analysis in medical ultrasound," *Ultrason. Imaging*, vol. 30, no. 3, pp. 164–173, May 1983.

[21] K. F. Ustuner and G. L. Holley, "Ultrasound imaging system performance assessment," *presented at 2003 AAPM Annual Meeting*, 2003.

[22] K. Ranganathan and W. F. Walker, "Cystic Resolution: A Performance Metric for Ultrasound Imaging Systems," *IEEE Trans. Ultrason., Ferroelec., Freq. Contr.*, vol. 54, no. 4, pp. 782–792, 2007.

[23] M. H. Pedersen, K. L. Gammelmark, and J. A. Jensen, "In-vivo evaluation of convex array synthetic aperture imaging," *Ultrasound Med. Biol.*, p. Submitted, 2006.

[24] "Recommendation 500-11: Methodology for the subjective assessment of the quality of television pictures," *ITU-R*, 1974-2002.

[25] D. G. Altman, *Practical Statistics for Medical Research*. London: Chapman and Hall / CRC, 1997, vol. 14.

[26] "Expert viewing to assess the quality of systems for the digital display of motion pictures in theatres," *ITU-R TG6/9 (Digital Cinema)*, 2002.

[27] J. A. Jensen, O. Holm, L. J. Jensen, H. Bendsen, H. M. Pedersen, K. Salomonsen, J. Hansen, and S. Nikolov, "Experimental ultrasound system for real-time synthetic imaging," in *Proc. IEEE Ultrason. Symp.*, vol. 2, 1999, pp. 1595–1599.

[28] J. A. Jensen, O. Holm, L. J. Jensen, H. Bendsen, S. I. Nikolov, B. G. Tomov, P. Munk, M. Hansen, K. Salomonsen, J. Hansen, K. Gormsen, H. M. Pedersen, and K. L. Gammelmark, "Ultrasound Research Scanner for Real-time Synthetic Aperture Image Acquisition," *IEEE Trans. Ultrason., Ferroelec., Freq. Contr.*, vol. 52 (5), pp. 881–891, May 2005.

[29] J. A. Jensen, H. Holten-Lund, R. T. Nielson, B. G. Tomov, M. B. Stuart, S. I. Nikolov, M. Hansen, and U. D. Larsen, "Performance of SARUS: A Synthetic Aperture Real-time Ultrasound System," in *Proc. IEEE Ultrason. Symp.*, Oct. 2010, p. published.

[30] V. Shamdasani, U. Bae, S. Sikdar, Y. M. Yoo, K. Karadayi, R. Managuli, and Y. Kim, "Research interface on a programmable ultrasound scanner," *Ultrasonics*, vol. 48, no. 3, pp. 159–168, 2008.

[31] S. S. Brunke, M. F. Insana, J. J. Dahl, C. Hansen, M. Ashfaq, and H. Ermert, "An ultrasound research interface for a clinical system," *Ultrasonics, Ferroelectrics and Frequency Control, IEEE Transactions on*, vol. 54, no. 1, pp. 198–210, January 2007.

[32] T. Wilson, J. Zagzebsk, T. Varghese, C. Quan, and R. Min, "The ultrasonix 500rp: A commercial ultrasound research interface," *Ultrasonics, Ferroelectrics and Frequency Control, IEEE Transactions on*, vol. 53, no. 10, pp. 1772–1782, October 2006.

[33] FDA, "Information for manufacturers seeking marketing clearance of diagnostic ultrasound systems and transducers," Center for Devices and Radiological Health, United States Food and Drug Administration, Tech. Rep., 1997.

[34] C. W. Sherwin, J. P. Ruina, and D. Rawcliffe, "Some early developements in synthetic aperture radar systems," *IRE Trans. Mil. Elect.*, vol. MIL-6, no. 2, pp. 111–115, 1962.

[35] R. Thomson, "Transverse and longitudinal resolution of the synthetic aperture focusing technique," *Ultrasonics*, vol. 22, pp. 9–15, 1984.

[36] M. Karaman, P. C. Li, and M. O'Donnell, "Synthetic aperture imaging for small scale systems," *IEEE Trans. Ultrason., Ferroelec., Freq. Contr.*, vol. 42, pp. 429–442, 1995.

[37] K. L. Gammelmark and J. A. Jensen, "Multi-element synthetic transmit aperture imaging using temporal encoding," in *Proc. SPIE: Progress in biomedical optics and imaging*, vol. 3, 2002, pp. 25–36.

[38] ——, "Multielement synthetic transmit aperture imaging using temporal encoding," *IEEE Trans. Med. Imag.*, vol. 22, no. 4, pp. 552–563, April 2003.

[39] L. F. Nock and G. E. Trahey, "Synthetic receive aperture imaging with phase correction for motion and for tissue inhomogenities - part I: basic principles," *IEEE Trans. Ultrason., Ferroelec., Freq. Contr.*, vol. 39, pp. 489–495, 1992.

[40] M. Karaman, H. Ş. Bilge, and M. O'Donnell, "Adaptive multi-element synthetic aperture imaging with motion and phase aberation correction," *IEEE Trans. Ultrason., Ferroelec., Freq. Contr.*, vol. 42, pp. 1077–1087, 1998.

[41] G. S. Kino, *Acoustic Waves, Devices, Imaging, & Analog Signal Processing*. Englewood Cliffs, N.J.: Prentice-Hall, 1987.

[42] N. M. Laird and J. H. Ware, "Random-Effects Models for Longitudinal Data," *Biometrics.*, vol. 38, no. 4, pp. 963–974, December 1982.

[43] F. Wilcoxon, "Individual comparison by ranking methods," *Biometrics Bulletin*, vol. 1, no. 6, pp. 80–83, 1945.

[44] AIUM, "Acoustic output measurement standard for diagnostic ultrasound equipment," American Institute of Ultrasound in Medicine & National Electrical Manufacturers Association, Tech. Rep., May 1998.

[45] IEC, "Measurement and characterisation of ultrasonic fields using hydrophones in the frequency range 0.5 mhz to 15 mhz," International Electrotechnical Commision, Tech. Rep., 1988.

[46] R. A. Smith, "Are hydrophones of diameter 0.5 mm small enough to characterize diagnostic ultrasound equipment," *Phys. Med. Biol.*, vol. 34, no. 11, pp. 1593–1607, May 1989.

[47] R. C. Preston, Ed., *Output Measurements for Medical Ultrasound*. London: Springer Verlag, 1991.

[48] J. T. Bushberg, J. A. Seibert, E. M. Leidholdt, and J. M. Boonel, *The Essential Physics of Medical Imaging*. Lippincott Williams & Wilkins, 2001.

[49] M. Mårtensson, "Evaluation of errors and limitations in ultrasound imaging systems," Ph.D. dissertation, School of Technology and Health, Stockholm,Sweden, 2011.

[50] J. Gore and S. Leeman, "Ultrasonic backscattering from human tissue: A realistic model," *Phys. Med. Biol.*, vol. 22, pp. 317–326, 1977.

[51] J. A. Jensen, "A model for the propagation and scattering of ultrasound in tissue," *J. Acoust. Soc. Am.*, vol. 89, pp. 182–191, 1991a.

[52] D. Bæk, J. A. Jensen, and M. Willatzen, "Multilayer piezoelectric transducer models combined with Field II," *J. Acoust. Soc. Am.*, p. Submitted, 2009.

[53] K. Erikson, "Tone-burst testing of pulse-echo transducers," *IEEE Transactions on Sonics and Ultrasonics*, vol. 26, no. 1, pp. 7–13, 1979.

[54] C. N. Dorny, "A self-survey technique for self-cohering of antenna systems," *IEEE Trans. Antennas Propagat.*, vol. 26, pp. 877–881, 1978.

[55] S. W. Flax and M. O'Donnell, "Phase-aberration correction using signals from point reflectors and diffuse scatterers: basic principles," *IEEE Trans. Ultrason., Ferroelec., Freq. Contr.*, vol. 35, pp. 758–767, 1988.

[56] Y. Sumino and R. C. Waag, "Measurements of ultrasonic pulse arrival time differences produced by abdominal wall specimens," *J. Acoust. Soc. Am.*, vol. 90, no. 6, pp. 2924–2930, Dec. 1991.

[57] N. Oddershede and J. A. Jensen, "Phase aberration measurements in medical ultrasound: Human studies," *Ultrason. Imaging*, pp. 1–11, 1988.

[58] S. F. Tsai and T. W. H. Sheu, "Finite element analysis of three-dimensional vortical flow structure and topology inside a carotid bifurcation model," *Ultrason. Imaging*, vol. 10, no. 1, pp. 12–28, January 1988.

[59] S. Måsøy, "Iteration of transmit-beam aberration correction in medical ultrasound imaging," *J. Acoust. Soc. Am.*, vol. 117, no. 1, pp. 450–461, 2005.

[60] G. C. Ng, S. S. Worrell, P. D. Freiburger, and G. E. Trahey, "A Comparative Evaluation of Several Algorithms for Phase Aberration Correction," *IEEE Trans. Ultrason., Ferroelec., Freq. Contr.*, vol. 41, no. 5, pp. 631–643, September 1994.

[61] L. Nock, G. E. Trahey, and S. W. Smith, "Phase aberration correction in medical ultrasound using speckle brightness as a quality factor," *J. Acoust. Soc. Am.*, vol. 85, no. 5, pp. 1819–1833, May 1989.

APPENDIX

A

SASB parameter study

The following figures presents additional data material used to select the configuration of SASB used for comparison with conventional imaging. The configuration of DRF is using a transmit focus in 105.5 mm, and a Gaussian dynamic receive apodization.

Fig. A.1 illustrates the B-mode images and lateral resolution investigating apodization.

Fig. A.2 illustrates the B-mode images and lateral resolution investigating virtual source position.

Fig. A.3 illustrates the B-mode images and lateral resolution investigating F#.

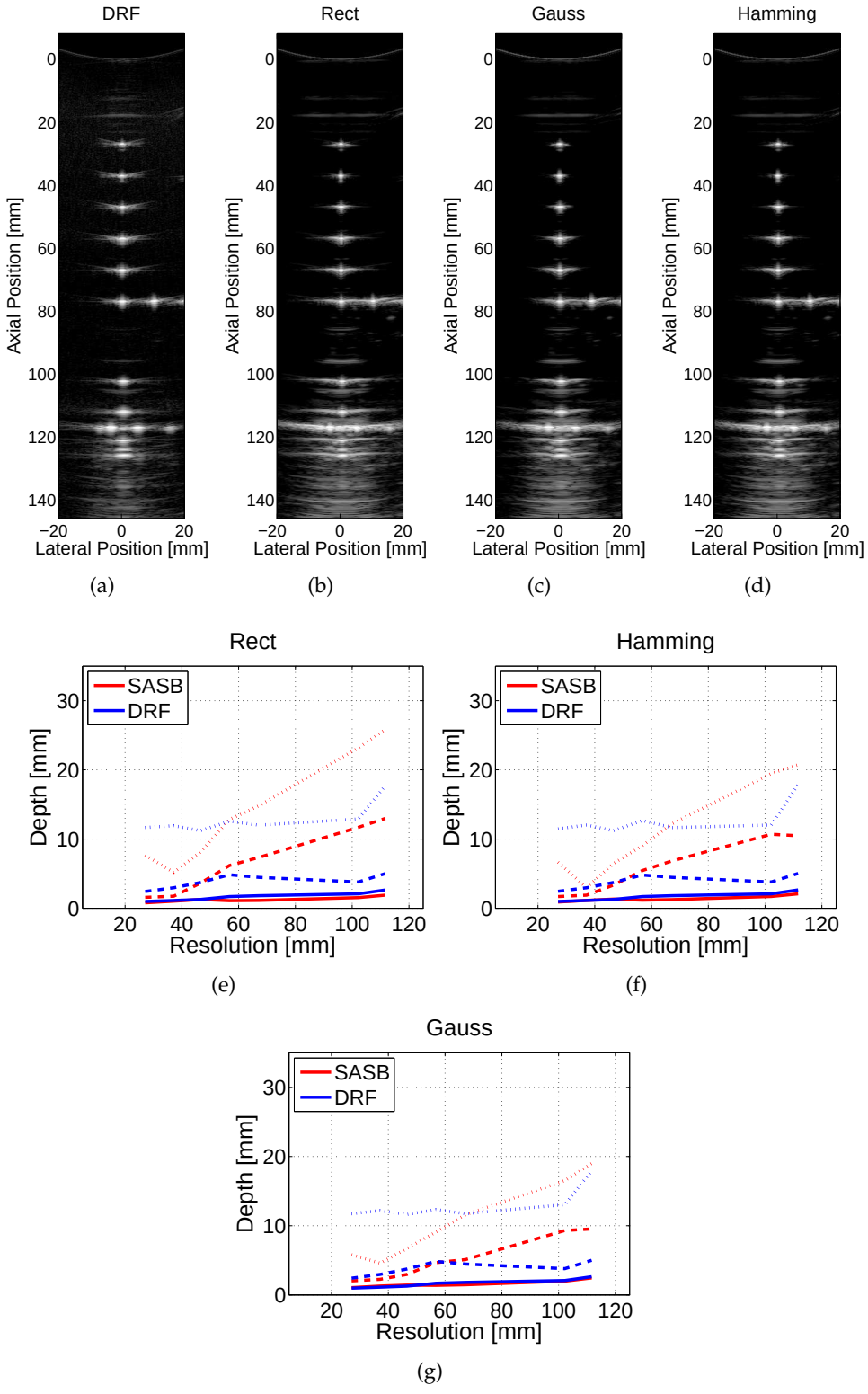

Figure A.1: Comparison of SASB vs. DRF. (a-d) B-mode images. (e-g) Lateral resolution at -6 dB (solid line), -20 dB (dashed line), and -40 dB (dotted line). SASB: VS: 40 mm - F# 2.5. Apodization Rect, Gauss, and Hamming.

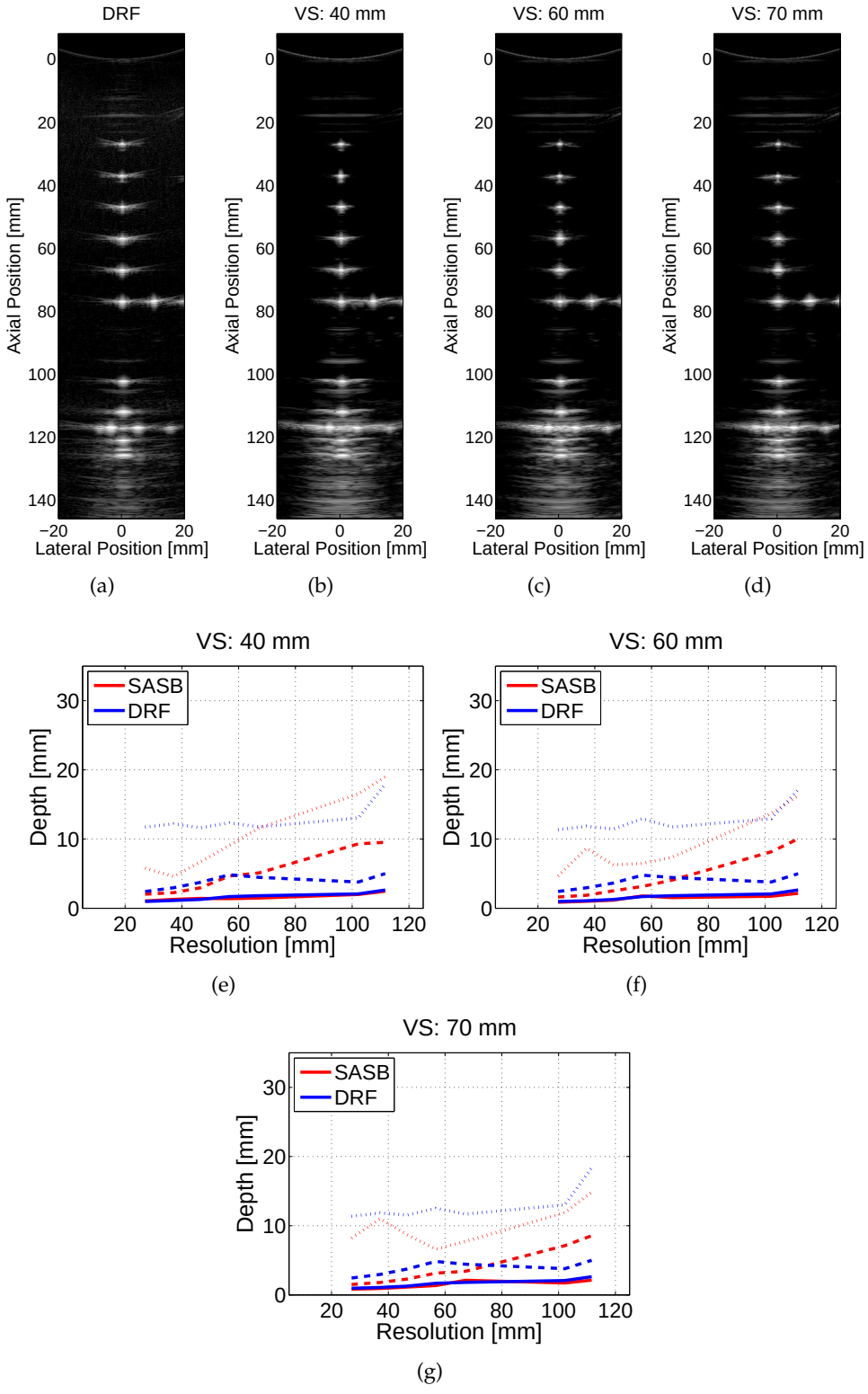

Figure A.2: Comparison of SASB vs. DRF. (a-d) B-mode images. (e-g) Lateral resolution at -6 dB (solid line), -20 dB (dashed line), and -40 dB (dotted line). SASB: VS: 40, 60, and 70 mm - F# 2.5. Apodization Gauss.

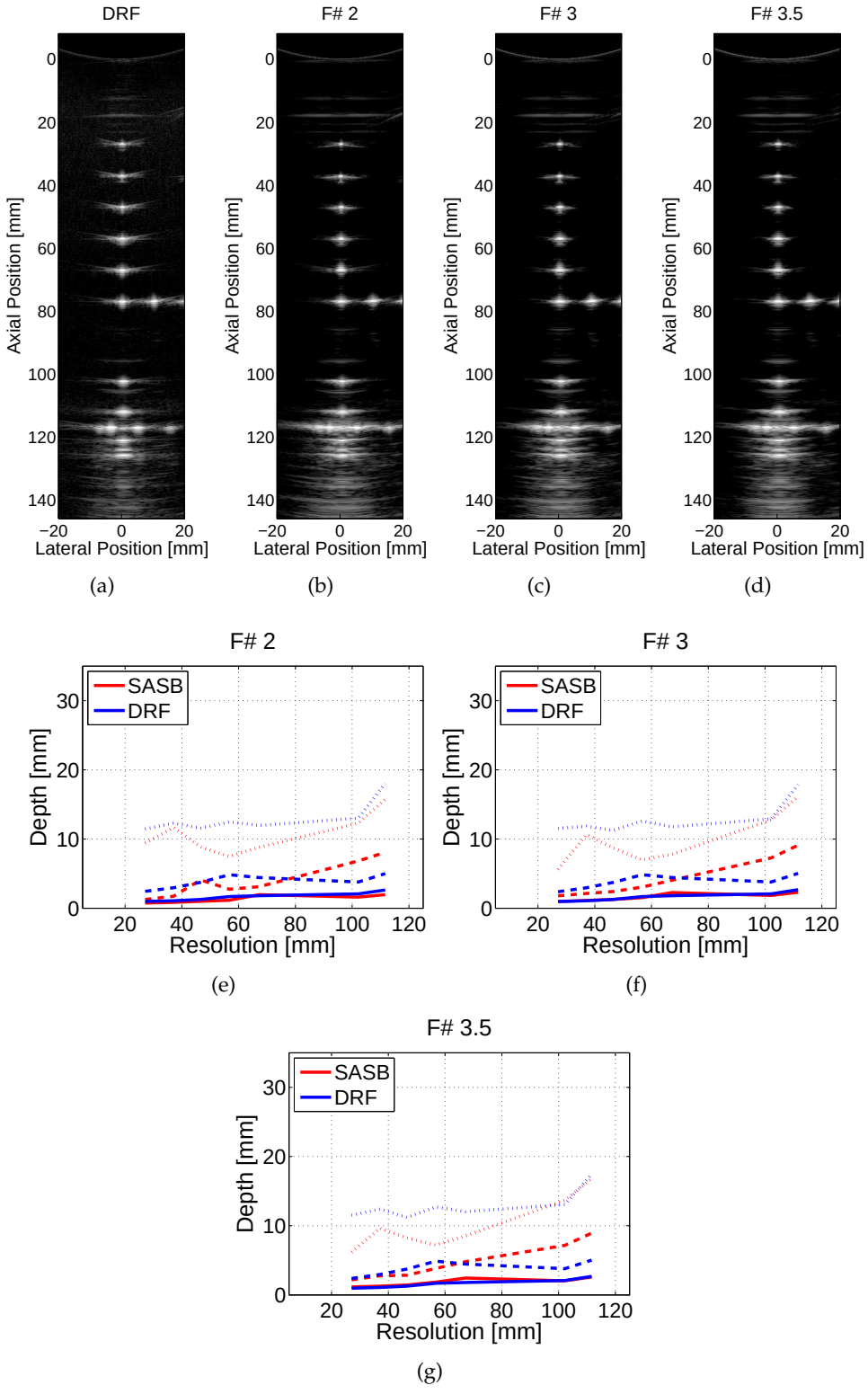

Figure A.3: Comparison of SASB vs. DRF. (a-d) B-mode images. (e-g) Lateral resolution at -6 dB (solid line), -20 dB (dashed line), and -40 dB (dotted line). SASB: VS: 70 mm - F# 2, 3, and 3.5. Apodization Gauss.

APPENDIX

B

Data material used in the pre-clinical trial.

The following figures presents the first B-mode image in each of the 32 image sequences presented to the evaluators in the pre-clinical trial.

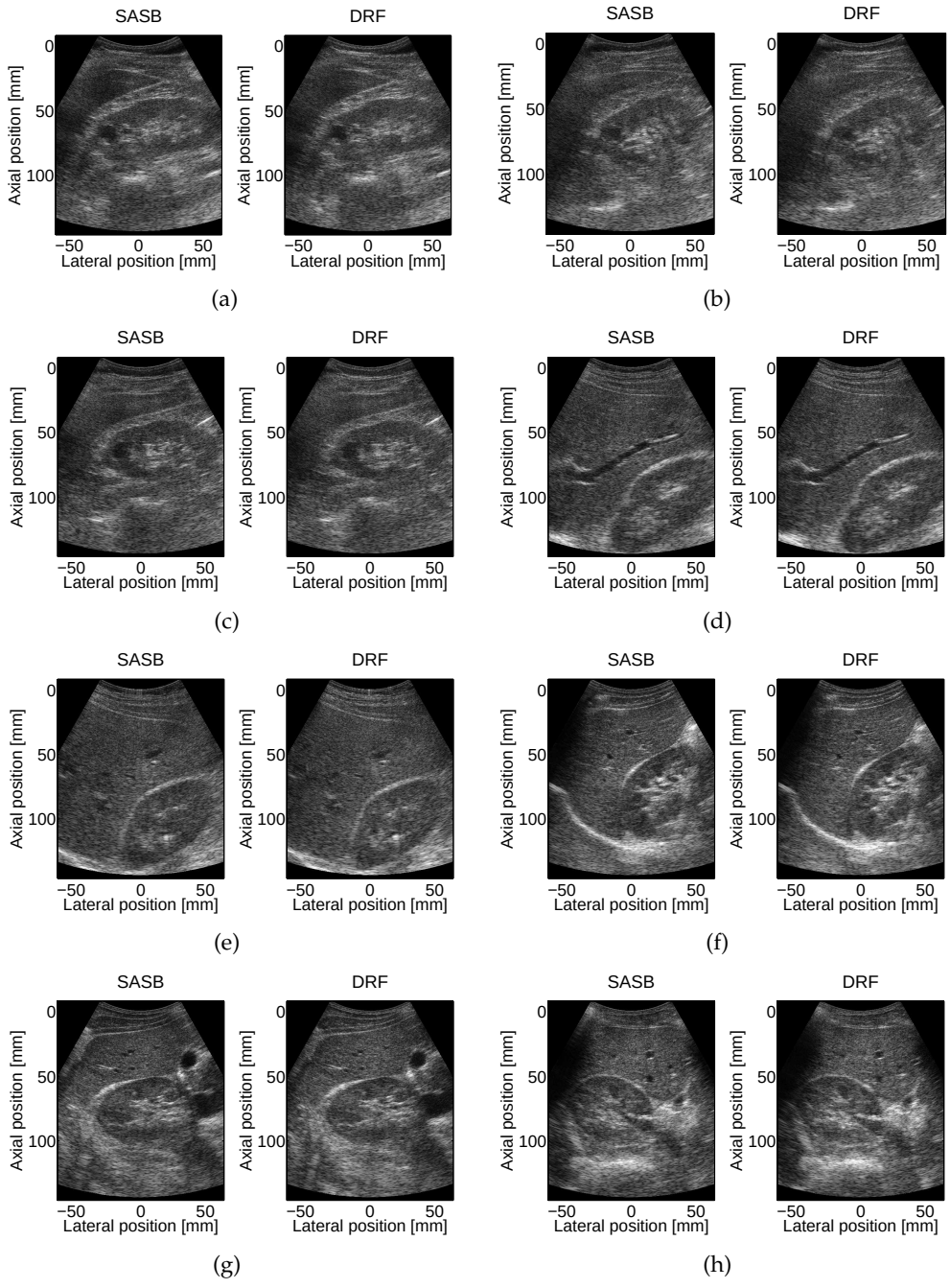
SASB
DRF
Axial position [mm]
Lateral position [mm]
0
50
100
−50
0
50
(a)
(b)
(c)
(d)
(e)
(f)
(g)
(h)

Figure B.1

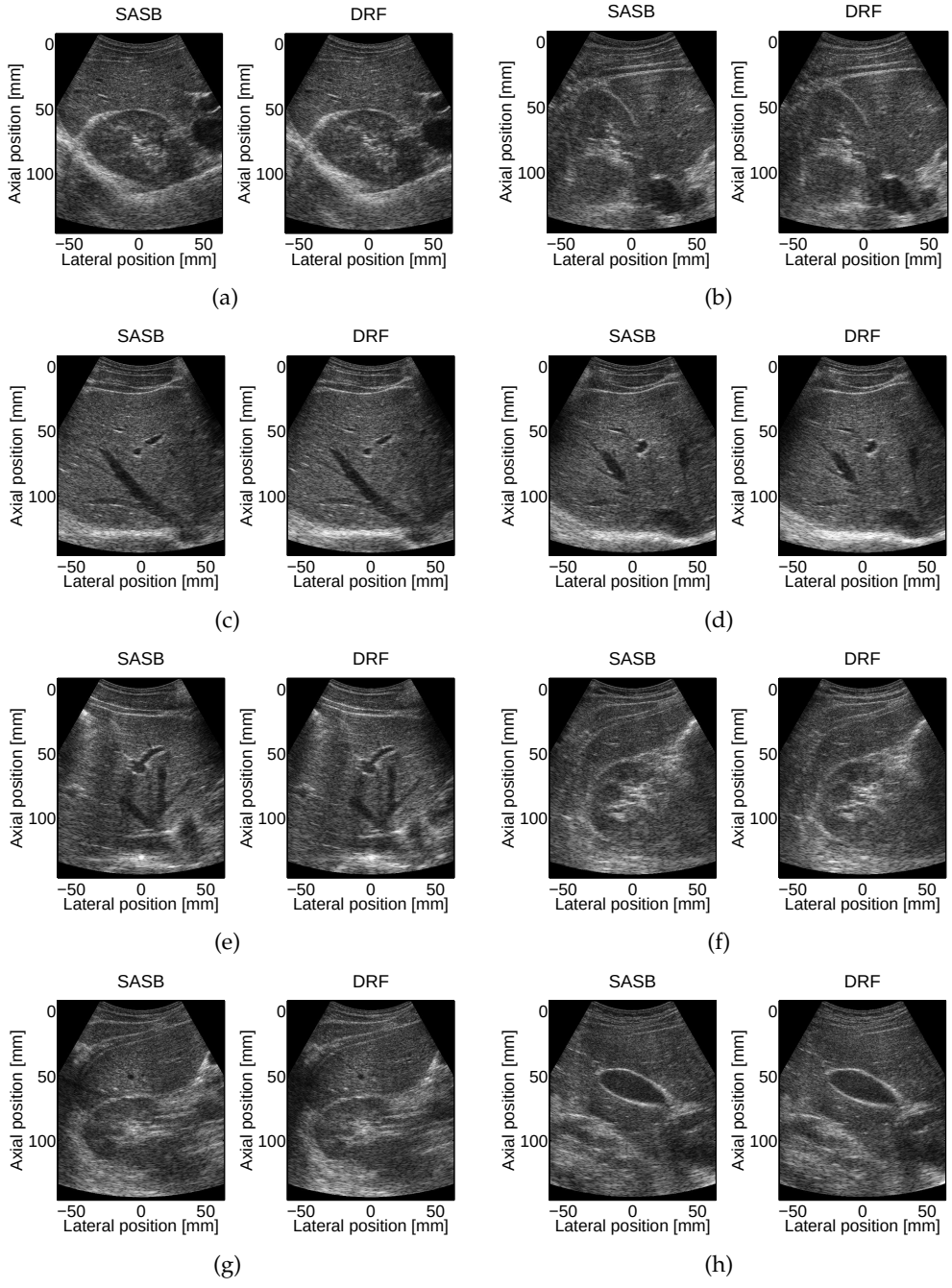
SASB
DRF
Axial position [mm]
Lateral position [mm]
0
50
100
−50
0
50
(a)
(b)
(c)
(d)
(e)
(f)
(g)
(h)

Figure B.2

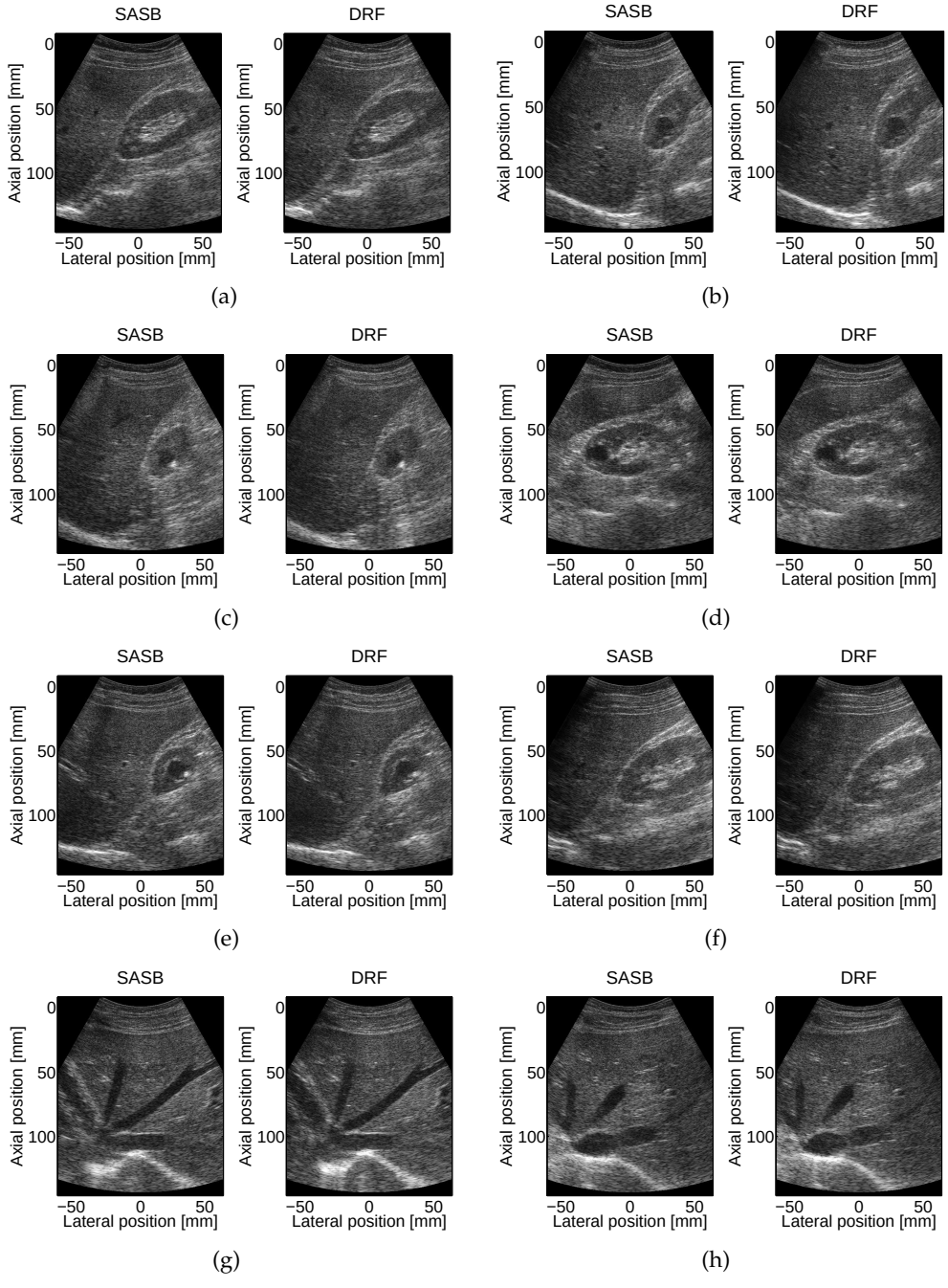
SASB
DRF
Axial position [mm]
Lateral position [mm]
0
50
100
−50
0
50
(a)
(b)
(c)
(d)
(e)
(f)
(g)
(h)

Figure B.3

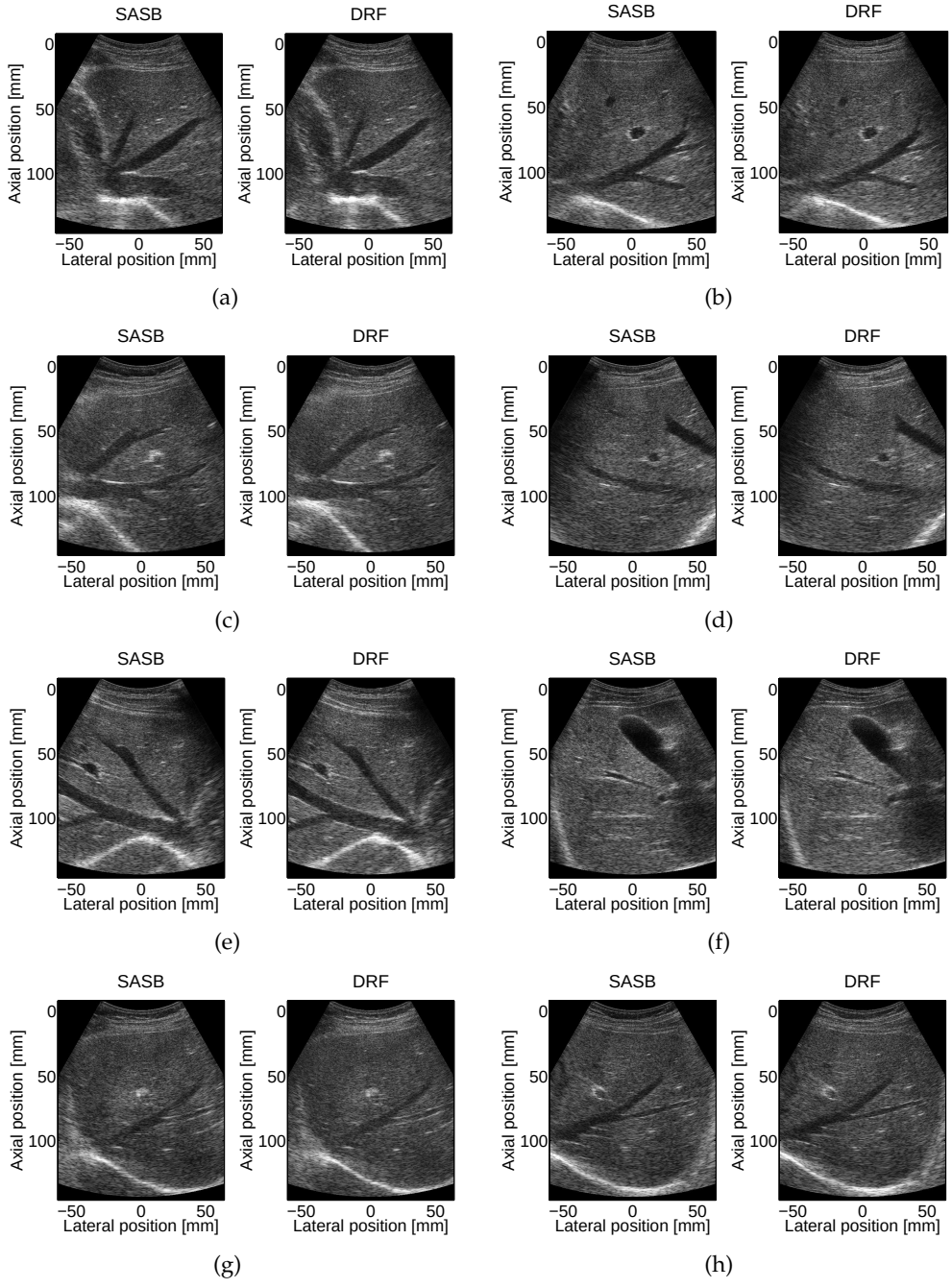
SASB
DRF
Axial position [mm]
Lateral position [mm]
0
50
100
−50
0
50
(a)
(b)
(c)
(d)
(e)
(f)
(g)
(h)

Figure B.4

APPENDIX

C

Data material used in the clinical trial

The following figures presents the first B-mode image in each of the 84 image sequences presented to the evaluators in the clinical trial.

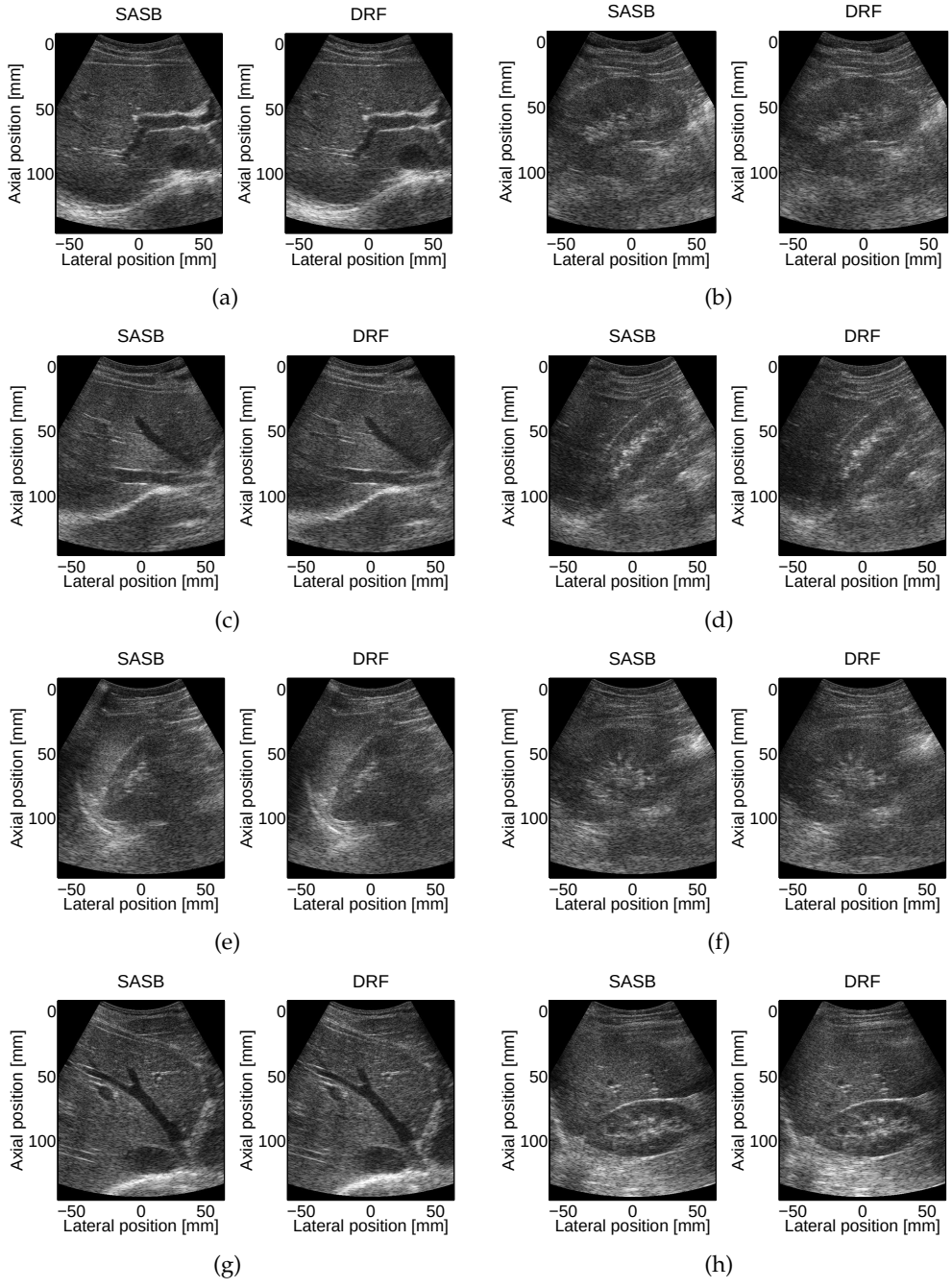
SASB
DRF
Axial position [mm]
Lateral position [mm]
0
50
100
−50
0
50
(a)
(b)
(c)
(d)
(e)
(f)
(g)
(h)

Figure C.1

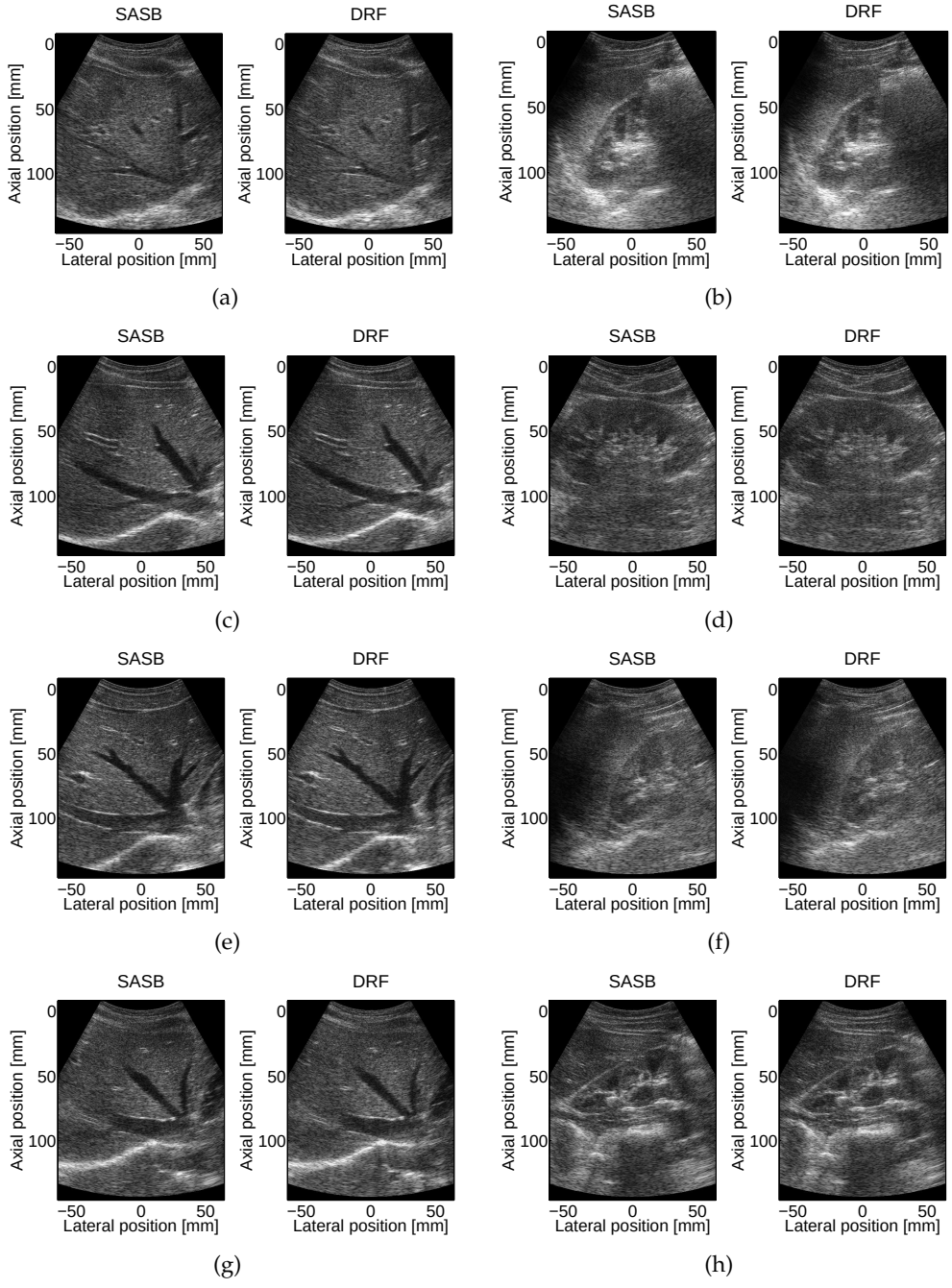
SASB
DRF
Axial position [mm]
Lateral position [mm]
0
50
100
−50
0
50
(a)
(b)
(c)
(d)
(e)
(f)
(g)
(h)

Figure C.2

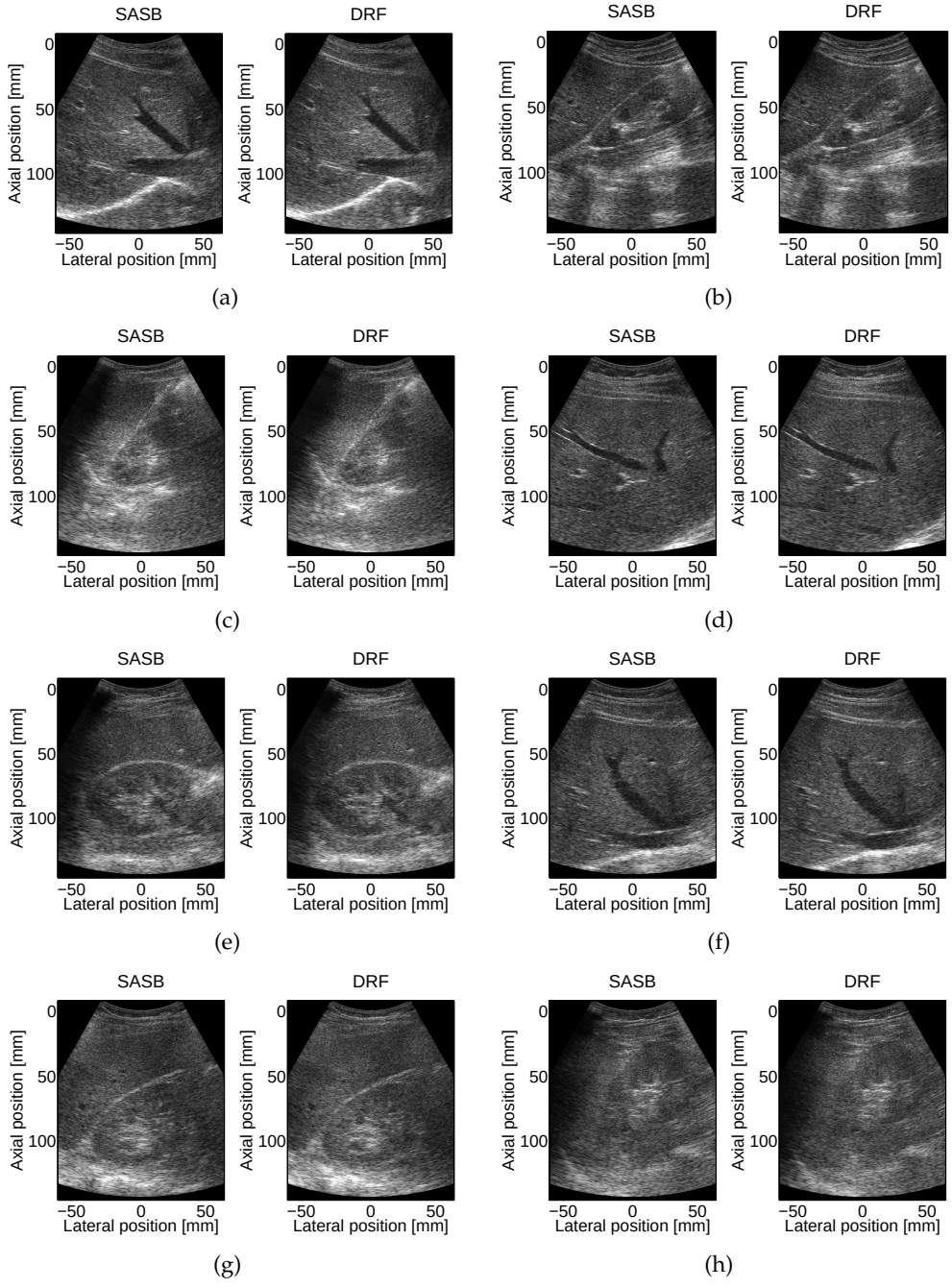
SASB
DRF
Axial position [mm]
Lateral position [mm]
0
50
100
−50
0
50
(a)
(b)
(c)
(d)
(e)
(f)
(g)
(h)

Figure C.3

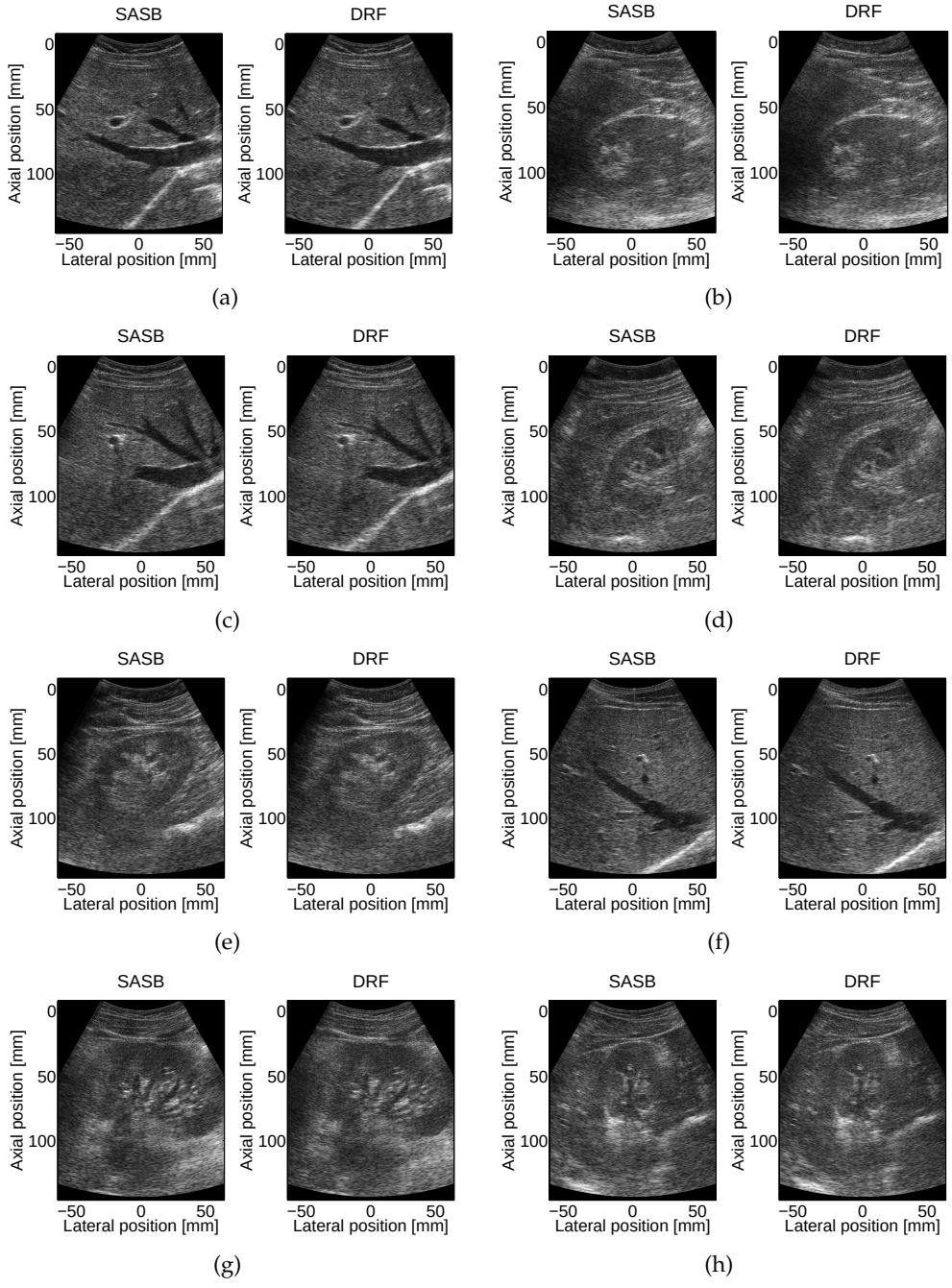
SASB
DRF
Axial position [mm]
Lateral position [mm]
0
50
100
−50
0
50
(a)
(b)
(c)
(d)
(e)
(f)
(g)
(h)

Figure C.4

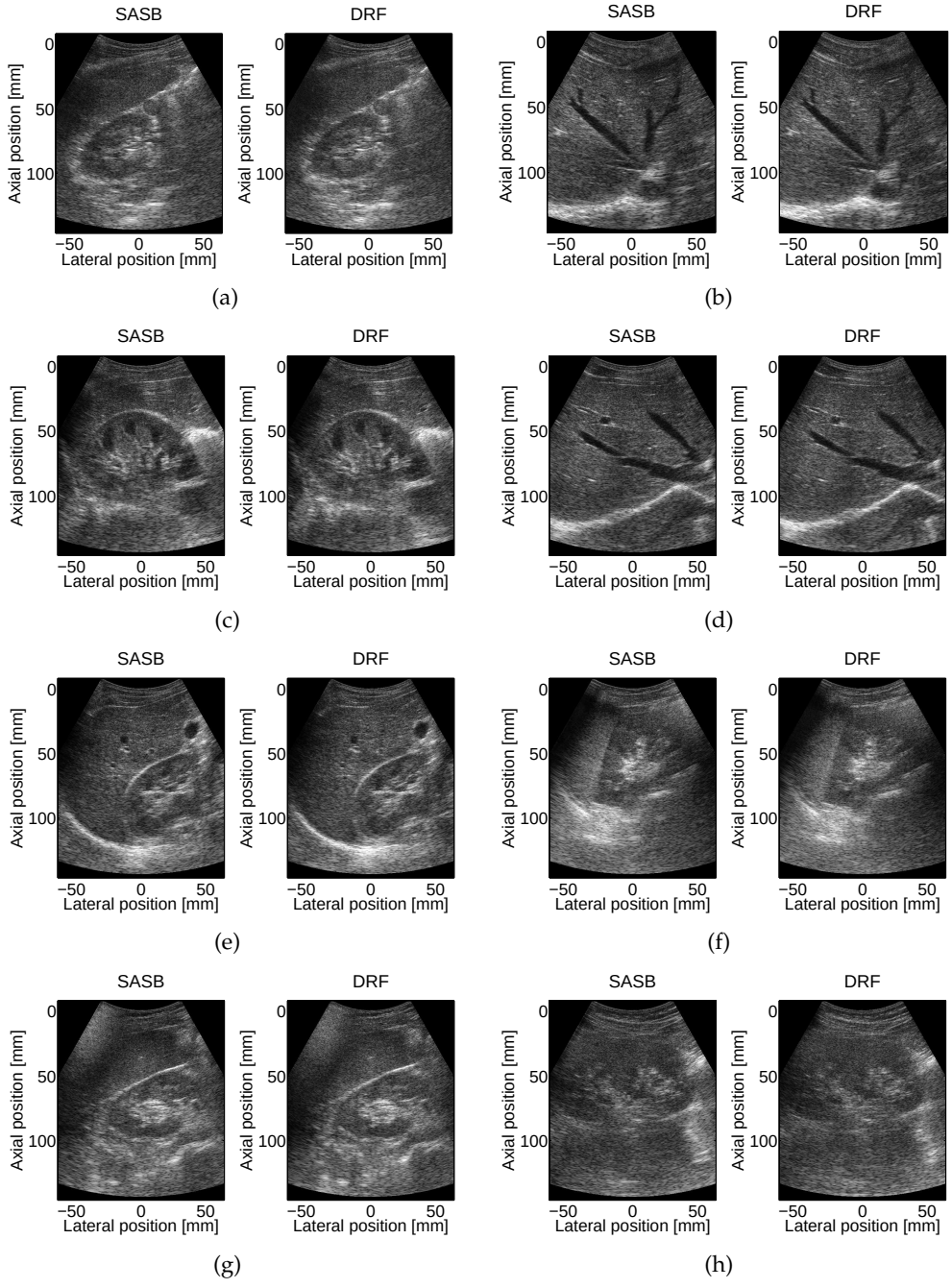
SASB
DRF
Axial position [mm]
Lateral position [mm]
0
50
100
−50
0
50
(a)
(b)
(c)
(d)
(e)
(f)
(g)
(h)

Figure C.5

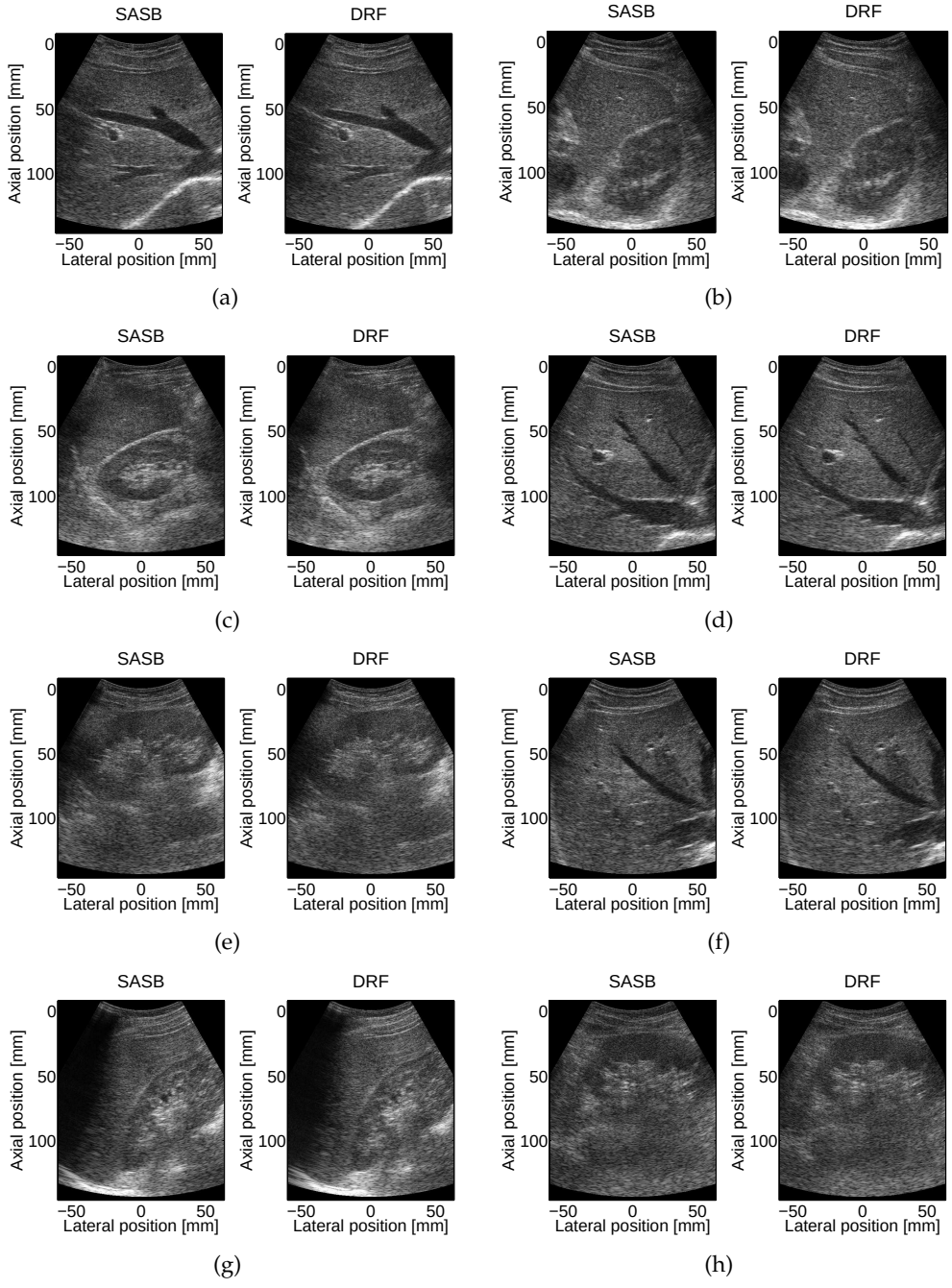
SASB
DRF
Axial position [mm]
Lateral position [mm]
0
50
100
−50
0
50
(a)
(b)
(c)
(d)
(e)
(f)
(g)
(h)

Figure C.6

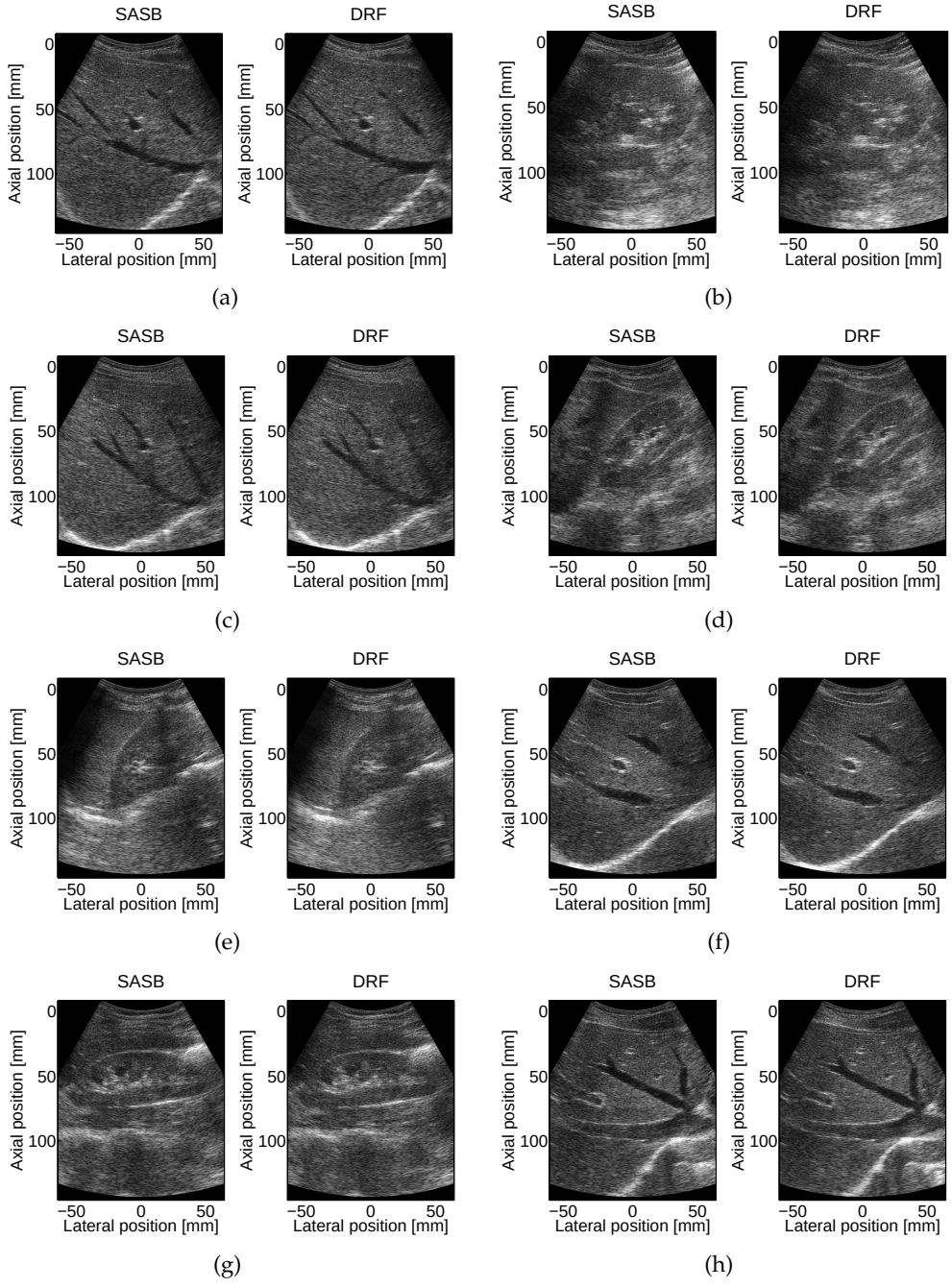
SASB
DRF
Axial position [mm]
Lateral position [mm]
0
50
100
−50
0
50
(a)
(b)
(c)
(d)
(e)
(f)
(g)
(h)

Figure C.7

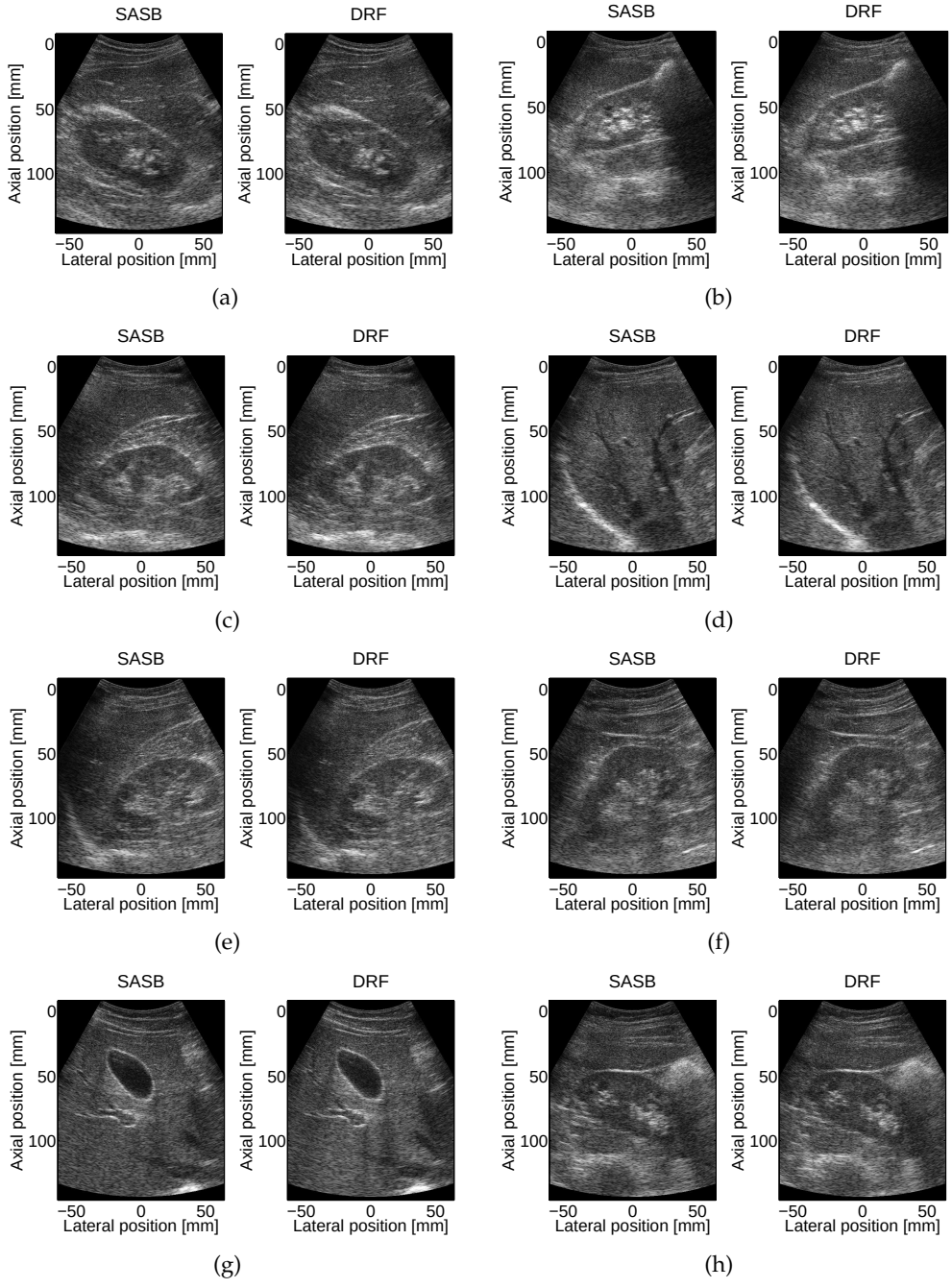
SASB
DRF
Axial position [mm]
Lateral position [mm]
0
50
100
−50
0
50
(a)
(b)
(c)
(d)
(e)
(f)
(g)
(h)

Figure C.8

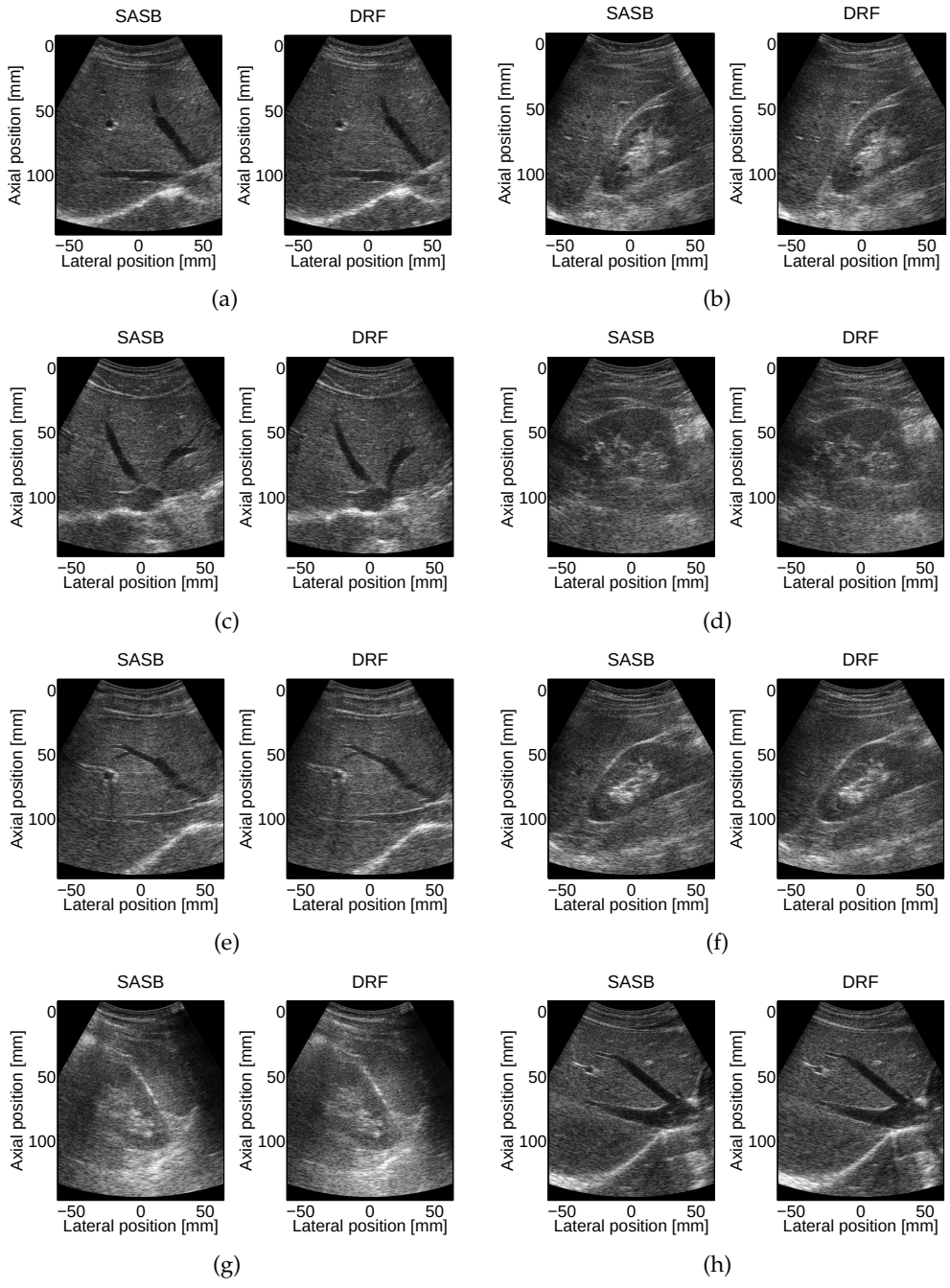
SASB
DRF
Axial position [mm]
Lateral position [mm]
0
50
100
−50
0
50
(a)
(b)
(c)
(d)
(e)
(f)
(g)
(h)

Figure C.9

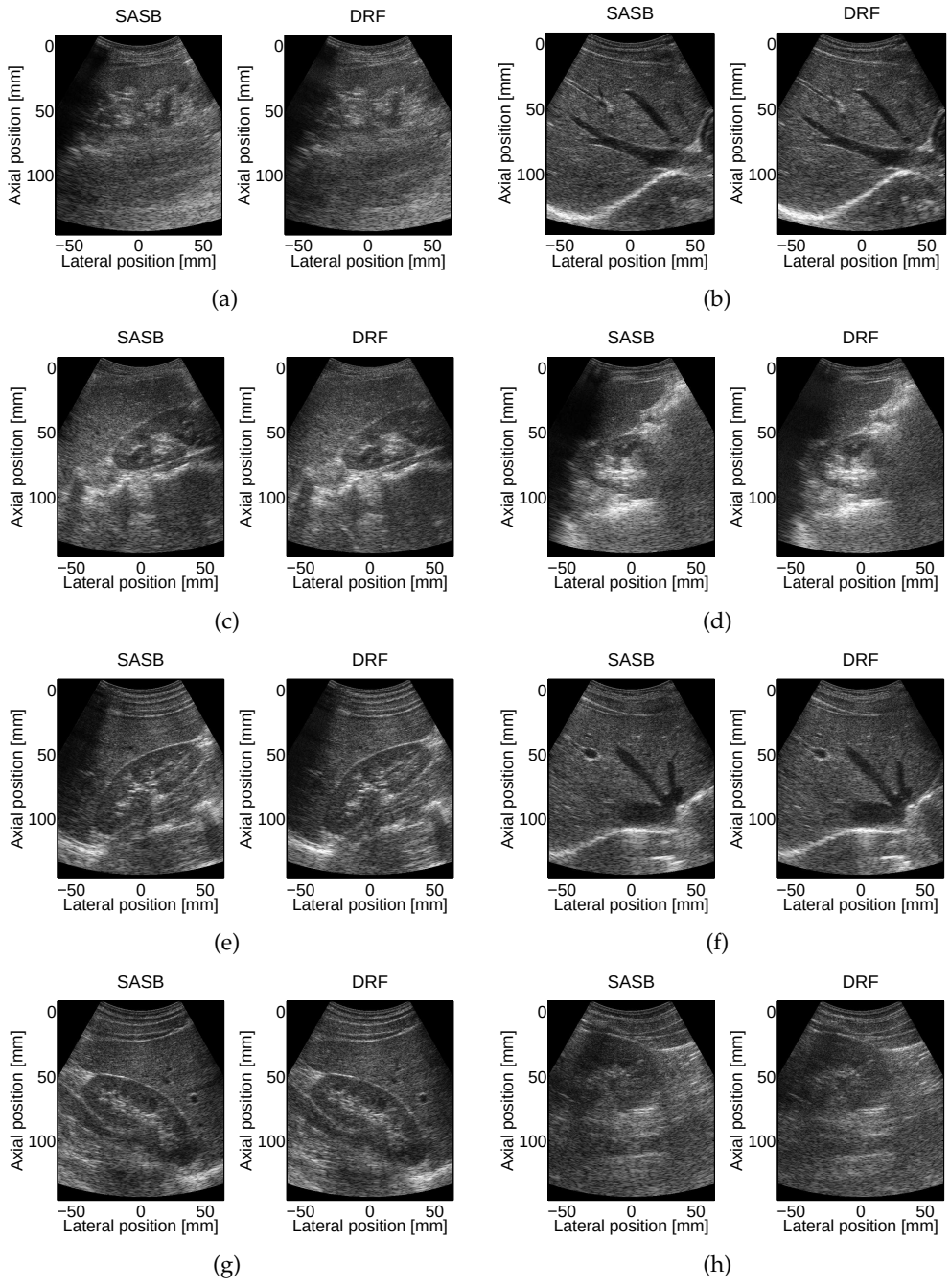
SASB
DRF
Axial position [mm]
Lateral position [mm]
0
50
100
−50
0
50
(a)
(b)
(c)
(d)
(e)
(f)
(g)
(h)

Figure C.10

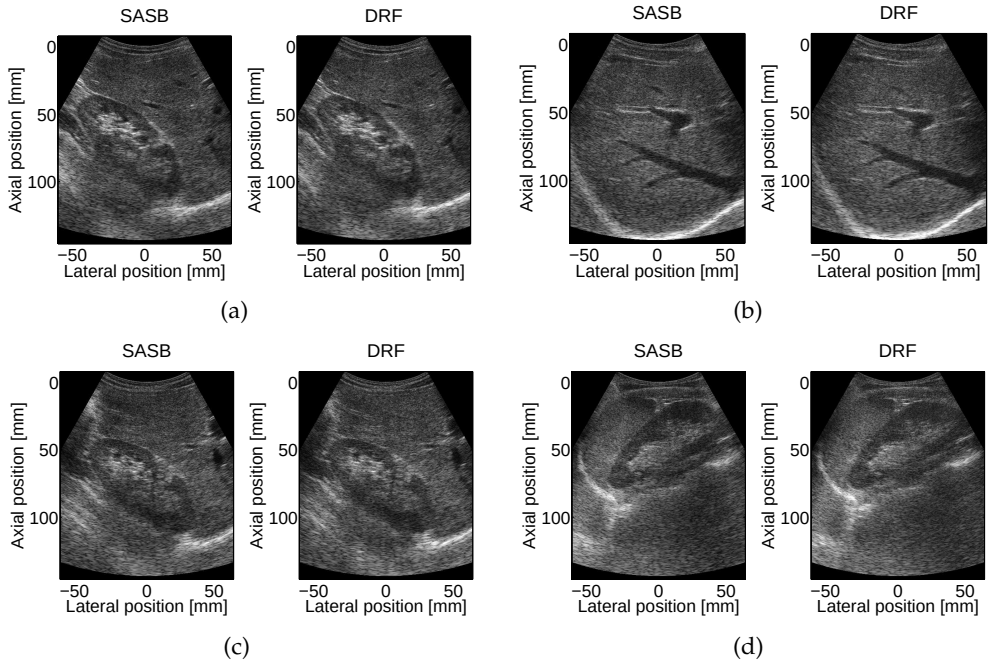
SASB
DRF
SASB
DRF
Axial position [mm]
0
50
100
−50
0
50
Lateral position [mm]
(a)
(b)
(c)
(d)

Figure C.11

_____